高燃焼度燃料および革新型燃料の熱流動設計評価における数値実験法の開発

（共同研究報告書）

２００３年３月

東京工業大学　原子炉工学研究所
核燃料サイクル開発機構　大洗工学センター

Ⓢ

高燃焼度燃料および革新型燃料の熱流動設計評価における数値実験法の開発

（東京工業大学・核燃料サイクル開発機構　共同研究報告書）

二ノ方　寿*、三沢　丈治*、Emilio Baglietto*、青木　尊之**、

A.P. Sorokin***、前川　勇****、大島　宏之*****、山口　彰*****

要　旨

湾曲、変形を想定した高燃焼度高速炉炉心燃料や稠密配列燃料格子燃料に対し、様々な運転条件下における燃料表面壁せん断応力や被覆管温度分布、冷却材および燃料の温度分布を詳細に評価して燃料の温度制限に対する適正な裕度を確認するとともに、Design by Analysis のツールとしての熱流動大規模数値シミュレーション手法を提案する。適用範囲に限界があるホットスポットファクターや実験に基づく経験論的なアプローチなどに代わり、数値シミュレーションによって、高燃焼度、長寿命、高信頼性、安全性、運転・保守の容易性、核廃棄物量の最少化などの諸要求条件を充たす高速炉炉心の熱流動設計の最適化を容易とする。

直交座標系と曲線座標系の間の座標変換を利用して、燃料集合体のような複雑形状を有する流路内の熱流動現象を詳細に解析する擬似乱流直接シミュレーションコードを開発し、座標変換前後の計算の妥当性について各種簡易形状流路内乱流熱伝達を計算して検証するとともに、物理量分布や乱流統計量などについて実験結果と比較し精度の確認を行った。また、擬似直接乱流シミュレーションを三角配列無限大本数ピン集合体に適用した結果の妥当性を、公開文献にある実験結果および汎用 CFD コード STAR-CD によるレイノルズ平均 N-S 方程式系の計算結果と比較して示すとともに、運動量・エネルギーの輸送プロセスに与える乱流の非等方性による二次流れの影響の重要性が強調された。さらに、円管形状に拘らない任意の新型高性能被覆管形状を考慮に入れて、熱流動の観点から最適の形状および配列を検討した。

*　　　東京工業大学原子炉工学研究所
**　　東京工業大学国際学術情報センター
***　　Institute of Physics and Power Engineering
****　　川崎重工業（株）パワープラント事業部
*****　大洗工学センター　要素技術開発部　流体計算工学グループ
*****　大洗工学センター　要素技術開発部　流体計算工学グループ

Development of a Numerical Experimentation Method for Thermal Hydraulics Design and Evaluation of High Burn-Up and Innovative Fuel Pins

Hisashi Ninokata[*], Takeharu Misawa[*], Emilio Baglietto[*], Takayuki Aoki[**], A.P. Sorokin[***]
Isamu Maekawa[****], Hiroyuki Ohshima[*****] and Akira Yamguchi[*****]

Abstract

A method of large scale direct numerical simulation of turbulent flows in a high burn-up fuel pin bundle is proposed to evaluate wall shear stress and temperature distributions on the pin surfaces as well as detailed coolant velocity and temperature distributions inside subchannels under various thermal hydraulic conditions. This simulation is aimed at providing a tool to confirm margins to thermal hydraulics design limits of the nuclear fuels and at the same time to be used in design-by-analysis approaches. The method will facilitate thermal hydraulic design of high performance LMFR core fuels characterized by high burn-up, ultra long life, high reliable and safe performances, easiness of operation and maintenance, minimization of radio active wastes, without much relying on such empirical approach as hot spot factor and sub-factors, and above all the high cost mock up experiments.

A pseudo direct numerical simulation of turbulence (DNS) code is developed, first on the Cartesian coordinates and then on the curvilinear boundary fit coordinates that enables us to reproduce thermal hydraulics phenomena in such a complicated flow channel as subchannels in a nuclear fuel pin assembly. The coordinate transformation is evaluated and demonstrated to yield correct physical quantities by carrying out computations and comparisons with experimental data with respect to the distributions of various physical quantities and turbulence statistics for fluid flow and heat transfers in various kinds of simple flow channel geometry. Then the boundary fitted pseudo DNS for flows inside an infinite pin array configuration is carried out and compared with available detailed experimental data. In parallel similar calculations are carried out using a commercial code STAR-CD to cross-check the DNS performances. As a result, the pseudo DNS showed reasonable comparisons with experiments as well as the STAR-CD results. Importance of the secondary flow influences is emphasized on the momentum and heat transfers mechanisms in a tight pitch lattice bundle. Also an attempt is made of optimizing heat and momentum transfers inside fuel pin bundles a possibility of adopting non-circular shape of fuel pins for better nuclear and thermal hydraulics performances.

[*] Tokyo Institute of Technology, Research Laboratory for Nuclear Reactors

[**] Tokyo Institute of Technology,

[***] Institute of Physics and Power Engineering

[****] Kawasaki Heavy Indudtry

[*****] O-arai Engineering Center

目　　次

表・図一覧

【3章】

1．はじめに

　将来のエネルギー資源を確保し、且つマイナーアクチナイド（MA）燃焼、核分裂生成物(FP)の消滅能力を併せ持つことより環境負荷低減に貢献できる原子炉として、高速炉が最も可能性を有している。しかしこの性能を発揮させるためには、安全性は無論のこと、同時に将来の軽水炉システムと比肩しうる経済性を有し、かつ核不拡散の要求に十分応えうる原子炉プラントを実現する必要がある。本来、原子炉とくに高速炉はベースロードに適しており、将来の基本路線として経済性の観点からは大型化・高燃焼度化の方向性が維持されるものと考えられる。一方、近年の傾向として、より融通性のある中小型炉心の提案が国内外で行われており、5年から20年にわたって燃料交換なしに運転を行える低出力密度の超長寿命炉心の設計例も提案されている。

　これらの路線や提案に共通する高燃焼度、長寿命、高信頼性、安全性、運転・保守の容易性、核廃棄物量の最少化などの諸要求条件を充たすナトリウム冷却高速増殖炉炉心を実現するためには、炉心物質組成、形状、サイズを最適化する必要があり、燃料要素の設計が大きなウェイトを占めることになる。とくに伝熱流動の視点からはナトリウムが冷却材として最も優れているが、新しい燃料の開発にはナトリウムを用いたモックアップ試験によるデータの積み重ねが必要で、結果として長期の開発リードタイムを必要とし、炉心の成立性を短期にかつ精度よく評価することは容易でない。

　以上の背景に鑑み、本研究では炉心燃料熱流動設計の観点から、炉心設計の自由度を大幅に増大させることを目的として、高燃焼度化や長寿命化を念頭に置いた通常の燃料形状および配置に対し、これまで培ってきた計算科学的手法をベースとする高度な熱流動評価手法を確立するとともに、超長寿命炉心に装荷する燃料集合体を念頭に、円管形状に拘らず任意の新型高性能被覆管形状を考慮に入れた熱流動の観点から、最適な燃料被覆管形状および配置を検討する。

2．燃料集合体内乱流解析

2．1 燃料集合体熱流動解析の実際

　原子炉プラントの設計や安全性評価に関わる熱流動研究の大部分は、通常運転時の定常条件下または過渡変化条件下における原子炉炉心燃料集合体や熱交換器のように複雑な形状を有する流路内の単相乱流や沸騰二相流、軽水炉のシビアアクシデントや高速炉の炉心損傷事故を想定した時の複雑な相変化や化学反応が共存した多相・多成分熱流動等を対象としている。このような研究の中で、解析コードを用いるシミュレーションの果たす役割は重要であり、とくに実機模擬装置などを用いて得られる実験データの解釈、実験的知見の実機条件への外挿、設計されたプラントが所期の性能を発揮するかどうかの確認、また過渡変化時・事故時のプラント応答評価などに頻繁に用いられている。

　これまで産業界で実用に供されてきた殆どの解析コードのアプローチは、プラント内の各コンポーネントを集中定数化したり、コンポーネント内を有限個のメッシュまたはコントロールボリューム（CV）に分割し、本来分布をもつ物理量をメッシュ上またはCVで体積積分して得られる平均量についてシステムの巨視的な挙動を説明する、いわゆる集中定数アプローチが中心である。原子炉炉心燃料集合体解析の分野ではサブチャネル解析がその代表例である。本サブチャネル解析手法は、これまでに単一燃料集合体全体内の3次元冷却材挙動を詳細に解析する上で、最も広範に用いられてきた。ただし、サブチャネルのサイズまたは等価直径に対応する代表長さが、解析で得られる分布の分解能、すなわち詳細さの限度である。つまり、下に述べるように、サブチャネル内の物理量分布については飽くまで平均化され、その詳細については別途詳細な解析に委ねられる。また、広範に用いられてきたにも拘らず、燃料集合体の熱流動設計において、サブチャネル解析コードは設計ツールの主流として用いられてきたのではなく、あくまでバックアップとしての位置づけに置かれていた。所謂 Design by Analysis のツールとしてサブチャネル解析コードは、モックアップ実験に置き換わるほどの信頼性を獲得していない、というのがその現実であろう。その理由を以下に述べる。

　原子炉炉心燃料集合体サブチャネル解析、炉心損傷事故を想定した時の安全解析などによく用いられる上記集中定数系コードは、基本的に、システムの時間的・空間的に巨視的な挙動を記述することに重点を置く。すなわち、集中定数系コードが解く方程式系は、着目するシステムの熱流動を支配する瞬時・局所保存式である偏微分方程式を、ある時間刻み幅およびコントロールボリューム（CV）上で時間・空間積分して得られる。したがって、これらの集中定数系解析においては、離散化数値精度とともに、積分の結果要求される多くの構成方程式、または構成方程式に応用される実験相関式が解析結果の質を左右する。Appendix A に集中定数系コードが解く方程式系の導出について、その概略を示す。

　このことから、コスト的にも高くつき適用範囲の観点からも制約の多い実験相関式を補完したり代替するために、実験的に詳細なデータを取得する努力と並行して、数値風洞的な CFD アプローチでミクロな情報を得て、より「機構論的」な構成方程式*を再構築し、その信頼性を高める必要性が喚起されてきた。この再構築により、サブチャンネル解析コードを Design by Analysis のツールとして確立するのが本研究の目標にある一方、さらに、構成方程式を必要とする集中定数系に代わり、偏微分方程式を直接解く分布定数系アプローチにより、直接集合体内全体の熱流動シミュレーションを実行することの実用化に対する期待が高まってきている。

２．２　分布定数系コードによる解析の現状

　一方、航空機空力設計や自動車のエンジンの設計などによく用いられている計算流体力学的手法(CFD: Computational Fluid Dynamics)を応用する研究も多く報告されているが、より複雑な形状流路を流れる流体を対象とする原子炉熱流動研究においては、その CFD 本来の解析能力を十分発揮しているとは考え難かった。これらは、主に計算機の演算処理量や記憶容量からくる制約に因るところが多い。例えば、サブチャンネル内の流速および温度分布を高精度で評価するためには、数 mm の水力等価直径を持つサブチャンネルをさらに細分化した計算メッシュを用いる必要がある。このため集合体サブチャンネルの三次元熱流動解析は、今もって実用的な計算時間および記憶容量の範囲内では実施できない状況にある。

　しかしながら計算機パワーの急激な増大によりこれらの制約が暫時無くなりつつある近年、原子炉内熱流動現象のさらなる高精度な解析を目指して、上記の設計や安全性評価に関わる熱流動研究が対象とする様々な複雑な現象について、微視的機構に着目した分布定数系シミュレーションの研究が進められている。その例として、直接乱流シミュレーション、大渦法（ＬＥＳ）の原理を用い、CFD に代表される連続体力学的手法に基づく超微細メッシュ法など、一般的に、実験的に取得困難な輸送現象の微細構造を明らかにする上で強力な手段を提供するものである。

---

　*　「機構論的」な構成方程式とは、CV 内の平均量で直接記述されない局所的かつ複雑な熱流動現象を規定する因果関係について、原因となる支配因子を選び出し、物理法則に即した素過程の組み合わせとして、数学的に一般化された表現を指す。このようなモデルを採用することにより、着目する現象に対しより一般的・普遍的なモデル化を達成し、集中定数系コードの適用範囲が、ある特定の実験結果によって制限されるといった従来コードの制約を取り除くことができるというものである。従って、このような機構論的な構成方程式（モデル）を構築する上で、いわゆる分布定数系数値シミュレーションの果たす役割は大きいといわざるをえない。

　従来用いられてきた乱流解析モデルの例として渦拡散モデル、k-εモデル、ＬＥＳなどが挙げられる。代表的な時間平均モデルは、瞬時の保存方程式の従属変数を時間平均値と変動成分に分ける、いわゆる Reynolds 分解を経て導出される。略して RANS (Reynolds averaged Navier-Stokes) モデルとも呼ばれるものである。渦拡散モデルは通常円管内流れに対する相間式を用いる場合が多く熱流動条件、流路形状に対し一般性がない。工業分野で最も広く一般的に用いられ、学術的にも検証が進んでいる RANS モデルは二方程式乱流モデルであり、近年では実験が困難な体系に対する数値実験ツールとして用いられるようになってきている。しかしながら最も広範に用いられている k-ε モデルでは、渦粘性の等方性を仮定しているため、速度変動成分の非等方性が強い現象への適用には不適切である。例えば非円形流路において、流れ方向を法線とする断面内に発生する二次流れ（第二種二次流れ）はその典型例であり、燃料集合体サブチャンネル内の流れがこれに該当する。

　またＬＥＳは壁近傍の層流境界層の扱いに難点があり、燃料ピン壁の影響を強く受けるサブチャネル内乱流には適用し難い現状がある。

　これらのことより、燃料集合体サブチャンネル内の分布定数系詳細熱流動解析には、計算機資源に対する制約がないとすれば、直接乱流シミュレーションが適しているのは自明である。本研究では、このような背景のもとに、直接乱流シミュレーション手法を実際に燃料集合体内乱流に適用する試みと実用化の可能性について述べるものである。

2．3　高燃焼燃料集合体熱流動設計

　　高燃焼度炉心燃料の湾曲、変形については、通常運転、過渡変化、自然循環除熱など様々な運転条件下における被覆管温度分布を詳細に評価して燃料の温度制限に対する裕度を保証することが要求される。

　　しかしながら、湾曲燃料、ピン接触などの高燃焼度条件下での燃料表面壁せん断応力分布や被覆管温度分布および冷却材温度分布を正確に計算した例はない。これは流路の非対称性が卓越する3次元乱流場を正確に予測することが極めて困難であること、とくに計測のみでなく計算上極めて予測困難な二次流れが乱流流速の分布に強く影響を及ぼしているためである。このことがさらには温度分布の正確な予測を困難にしている。現実の設計では、ホットスポットファクター、サブファクターなど統計量に基づくアプローチや、実験に基づく経験論的なアプローチによる評価によって、高燃焼度燃料の湾曲、変形による被覆管のホットスポット評価が行われるが、基本的には保守的な評価が中心であり改善の余地が多い。今後は実験に代わりうる、構成方程式を使わない直接シミュレーションまたはLES（大渦シミュレーション）による高質かつ大規模な計算機シミュレーションによって被覆管のホットスポット評価を行う普遍的な手法の確立が必要かつ急務である。

　　超長寿命炉心を設計する上では、燃料体積比率を高くすることにより内部転換比又は増殖比を高くできるが、従来の燃料設計におけるP／D比制限のために必ずしも核設計から要求される燃料体積比率を充たすことができない場合がある。また、これまでの燃料設計は円管形状の被覆管を前提としているが、これは製作の容易性、FPガス圧に耐えるという意味でプラスの側面を持つ一方、熱伝達という観点からは必ずしも最適形状とはいえない。すなわち、燃料形状を最適化することによって、燃料集合体の全サブチャネル内冷却材温度分布を可能な限り平坦化すること、被覆管周方向温度分布を平坦化すること、燃料中心温度を下げることができれば、定常時および過渡時の被覆管、燃料温度制限に対する余裕を大きく取ることができる。このように既存の燃料形状概念にとらわれず自由な発想に基づいて燃料形状を熱伝達、流体力学的見地から大事幅広く検討し、新形状燃料の成立性をみることは炉心設計の自由度を拡大する上で必要である。

２．４　直接乱流シミュレーションの実用化ニーズ

　高速炉燃料集合体サブチャネル内まで詳細に解析しうる解析コードについては、大洗工学センターで開発された有限要素法に基づく SPIRAL コードが代表的であるが、乱流モデル、計算時間、使いやすさの観点などからの改良が望まれている。並行して、東京工業大学原子炉工学研究所において有限差分法による２次元解析コード COOLFD が開発された。1998 年 4 月フランスＣＥＡグルノーブル研究所で開催された第 9 回国際水理学会新型炉ワーキンググループ会議におけるベンチマーク演習に参加した結果、COOLFD は高燃焼度燃料を模擬した変形バンドル内詳細 2 次元流速分布、温度分布予測に関する国際ベンチマーク問題を計算して、実験結果との概ね良好な一致を見るまでに至っているが、未だ二次流れの機構論的な予測モデルの構築までは至らず、3 次元乱流の詳細な計算が必要であることの知見が得られた。また、海外ではフランス CEA における TRIO コードなどを応用している例が見受けられるが、当該国際ベンチマークによる 3 次元乱流の詳細解析においては成功していない。

　本研究は、以上のような国内外の研究進捗状況と対比すると、乱流の非等方性が無視できないサブチャネル内乱流場、温度場の詳細解析について、より高精度かつ高信頼性のある計算結果を提供することに目的があり、本目的を達成することは極めて重要である。また、直接乱流シミュレーション手法を曲線座標系が要求される炉心燃料集合体のような複雑形状流路内乱流へ適用する本格的な乱流大規模シミュレーションとしては初の試みであり、この成果は高速炉のみでなく他の原子炉開発へも多大な貢献を行う。

　例えば、軽水炉ではあるが、超長寿命型原子炉に用いる燃料については、米国 DOE の NERI 公募型研究で採用された STAR-LWR 計画において様々な角度から検討を開始している。STAR-LWR 計画は、PWR と高速炉技術を融合した超長寿命中小型原子炉の開発研究で、コンパクトネス、核不拡散性、高転換率、受動安全性、経済性を強調した可搬型の軽水炉を狙っている。現在、東工大原子炉研二ノ方研究室では、将来の超高燃焼炉心オプションとしてのナトリウム冷却高速炉と並行して、高転換率を狙う水冷却稠密燃料格子集合体の熱流動設計の最適化を検討しているが、ともに狭隘流路部分を含む乱流熱伝達を精度よく予測し、設計の制限因子である被覆管温度制限と冷却材温度制限への尤度を定量化することが重要であるため、本研究で得られる直接乱流シミュレーションの実用化は新型炉開発にとっても、極めて強力な手段を提供することになる。

３．大規模シミュレーション解析コードの開発

３．１　　サブチャンネル内流速分布予測に対する２次流れの影響

　燃料集合体熱流動設計で重要なモデルは、流動に対する摩擦および形状圧損係数モデルおよび熱伝達係数で、これらのモデル導出にあたり燃料ピン表面上での壁せん断応力および温度分布の正確なデータが必要である。そのためには、乱流の非等方性に起因する第２種２次流れの重要性が指摘される（Appendix A）。したがって直接乱流シミュレーションによる同２次流れの予測が重要となる。

　すなわち、燃料集合体サブチャンネル内第二種二次流れの評価では、空間スケールが小さく、また主流方向を法線とする断面内の速度成分に着目する必要性から計測が困難となり、数値解析からの情報が特性把握を行う上での拠り所となる。

　三角配列のロッドバンドル内における冷却材流速の分布を、数値解析によって適切に評価するためには、乱流の非等方性に起因する２次流れの影響を考慮したモデルを用いる必要がある。ここでは、２次流れを考慮した計算と考慮しない計算を、実験結果[1]と比較することで、２次流れがバンドル内の流速分布に与える影響を検証する。

　図 3-1 に、計算領域となる２次元無限三角配列のロッドバンドルの基本対称セルを示す。充分発達した乱流に対する解くべき２次元レイノルズ方程式は以下の通りである。

$$u_j \frac{\partial u_i}{\partial x_j} = \frac{1}{\rho}\frac{\partial p}{\partial x_i} + \frac{\partial}{\partial x_j}\left(\nu\frac{\partial u_i}{\partial x_j} - \left\langle u_i' u_j' \right\rangle\right) \quad , \quad -\left\langle u_i' u_j' \right\rangle = \nu_i^{turb}\frac{\partial u_j}{\partial x_i} + \nu_j^{turb}\frac{\partial u_i}{\partial x_j} \quad (3\text{-}1)$$

ここでは、直管内の充分発達した非等方性乱流を予測する MSV (Multi-Scale-Viscosity) モデル[2]によって、レイノルズ応力を計算した。離散化手法には、EFD スキーム [2]を用いた。

　一例として、Reynolds 数=24000、P/D（P:燃料棒中心間距離、D:燃料棒直径）=1.2 のときの無次元化された軸方向流速分布の計算結果を図 3-2 (a),(b)、比較対象とする実験結果を(c)に示す。流路中心方向に沿った流速分布については、２次流れを考慮することにより、実験結果に示される傾向を予測しており、バンドル内の軸方向流速分布、とくに壁近傍の流速分布に対しては、２次流れの影響が大きいことが確認できる。

　Re=8,170 および Re=160,100 での二次流れ分布の比較を、それぞれ図 3-3 に示す。同結果によれば二次流れとして、Re=8,170、Re=160,100 の場合、それぞれ主流流速の約１％、0.2%と予測されている。基本的には矩形管の場合と同レベルの二次流れが生じるものと予想される。

　なお、これらの計算は十分に発達した乱流を想定し、基本的には渦拡散モデルに基づいており、燃料集合体内サブチャンネル間の３次元乱流揺らぎ成分に基づく運動量、エネルギー交換メカニズムを解明できない。また、２次流れ成分は主流（軸方向）成分の高々数％で、測

定困難な物理量のため、数値実験により求めなければならないことより、2次流れを含むサブチャネル内のより定量的な詳細乱流特性把握のためには、経験式に基づかない乱流3次元解析、すなわち直接乱流シミュレーションが必要である。

図3-1：計算体系

(a) 2次流れなし   (b) 2次流れあり

(c)実験結果

図3-2：無次元軸方向流速分布

Elementary cell

Re = 8170   Re = 160100
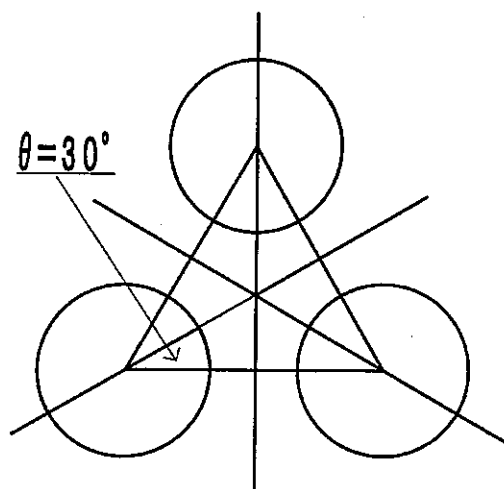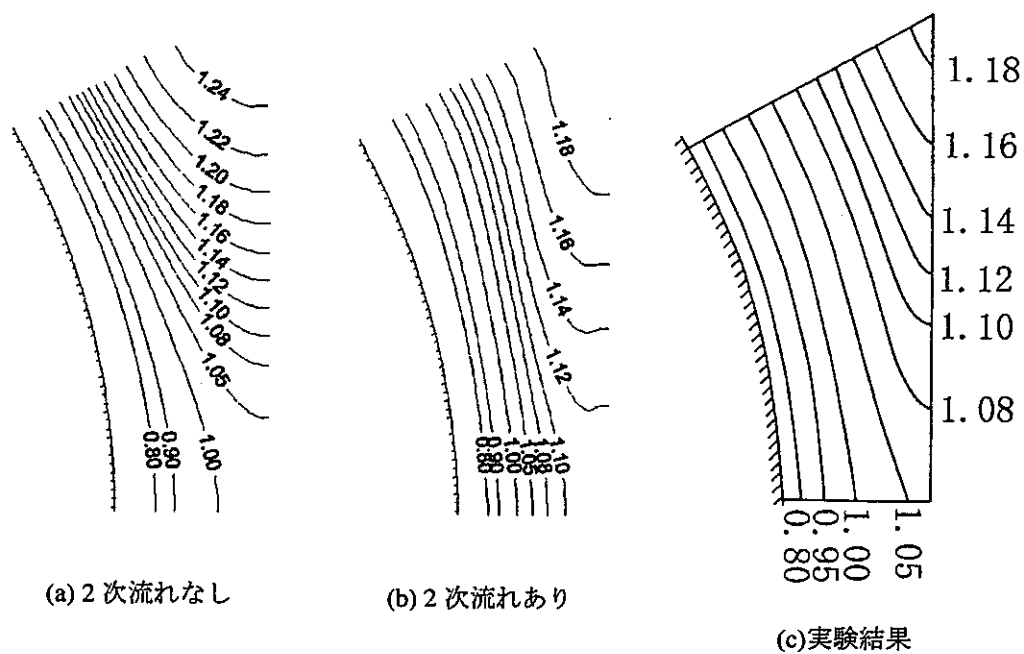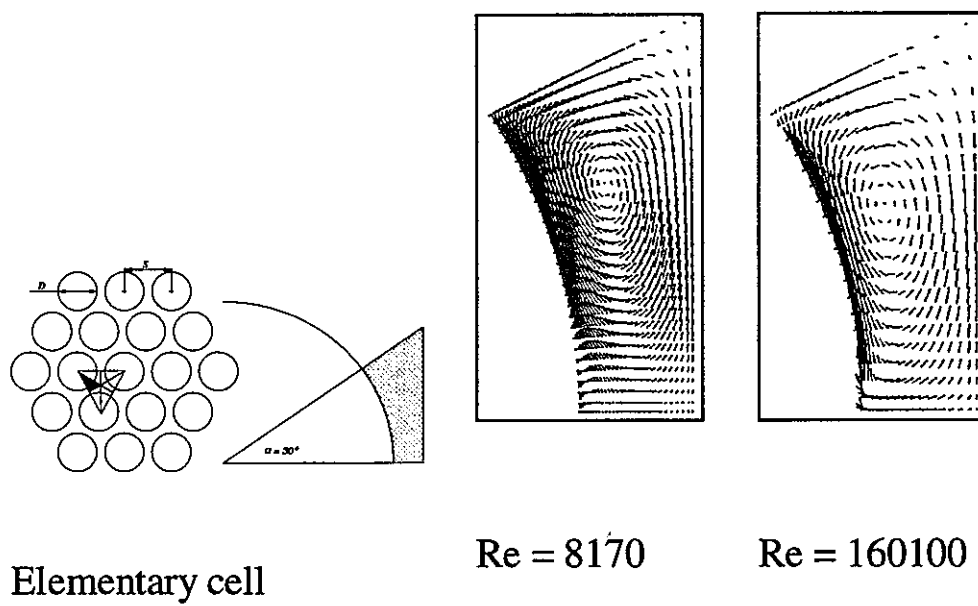
図 3-3 燃料集合体サブチャンネル内2次流れの流速ベクトル分布

3.2 直交座標系直接乱流シミュレーションコードの開発

以下に述べる内容は、これまでに直接乱流シミュレーション手法を燃料集合体体系に適用する例が内外ともになかったことに鑑み、様々な試行錯誤のプロセスにおいて判明した事実や課題、如何に課題を解決していったかなどを明確にすることを目的にして、基本的に開発の経過に沿った記述とする。前半部分、すなわち直交座標系における直接乱流シミュレーションのダクト内流れや平行平板流路のような簡易形状流路に対する応用は基本的に既に他の研究者により数多くの報告がある。しかしながら、これらの報告においては、多くのノウハウや、本質的な問題点や課題が明確に示されていない場合が多く、従って本報告で基礎的な直交座標系における直接乱流シミュレーションモデルの開発についても記述することは有意義であると考える。なお、後半部分の境界適合型曲線座標系における直接乱流シミュレーションは本報告が最初である。

3.2.1 開発の方針

燃料被覆管のホットスポット評価を行うために、等温場における強制対流域のみでなく、温度分布が流体挙動に強く影響を及ぼす混合対流領域における支配方程式を安定に解く必要性、および、直接シミュレーションへの適用性を勘案し、種々の数値解法の中から、運動量保存式中の対流項、拡散項は陽、質量およびエネルギー式の対流項を半陰的に扱い且つ全ての保存式を圧力方程式に集約して同時に解く修正ICE法を選定するとともに、当面、対流項については河原-桑原によるK-Kスキームを非等間隔メッシュに拡張適用し、時間差分スキームは2次の精度をもつアダムス・バシュフォース法、サブチャネル形状の模擬に対しては、一般曲線座標系を適用するものとした。計算フロー、構成するサブプログラム群を具体化し、膨大な計算データの格納、ポスト処理法を含めたコード基本設計方針を定めた。

コード基本設計方針に基づき、まず3次元デカルト座標系における非圧縮性流れの3保存式、すなわち質量、運動量、エネルギー保存式を差分化するとともに、ICCG法による行列解法を組み込み、基本コードの開発を行った。等温場における強制対流および非等温場自然対流条件下でのキャビティ流れなどの2次元体系における各種ベンチマーク計算問題に適用し、コードの基本性能を確認した（3.3.1 キャビティフロー関するベンチマーク解析参照）。

ロッドバンドル体系における熱流動解析の前段階として、本基本コードの精度検証、及び今後のバンドル体系への適用に対する見通しを明らかにすることを目的とする、Gabrilakis [3] による計算と同様な等温場における矩形ダクト内の乱流直接シミュレーションを試みた。その結果、十分発達した乱流（Re=4,400）に対し、K-Kスキームでは数値粘性の影響が大きく、クーラン数が0.1、ダクト断面に対し80x80または100x100程度のメッシュ分割では、層流底

層については理論解と一致するが乱流のプロファイルが得られないことが判明し、非等間隔メッシュシステムへの適用について経験が多い他の高次差分（QUICK 法や中心差分法）を試みた結果、中心差分による対流項差分が境界層から乱流コアへの遷移を与えることが示された。（3.3.2 矩形ダクト乱流直接シミュレーション参照）。ただし、中心差分に特有な数値的不安定性が影響している。基本的には、メッシュサイズをさらに細かくすれば乱流直接シミュレーションが可能であることは自明である。しかしながら、計算体系は微小な領域に限られる。計算資源は有限であり、現実の燃料集合体内の全流路をコルモゴロフスケール以下にメッシュ分割することは不可能であり、ここでは超大型計算となる燃料集合体への適用を考慮して、可能な限りメッシュ数は少なくて済む、より高次で安定な差分法を検討する。

　既往ベンチマーク問題等をもちいてコードの計算負荷負荷診断を実施した。現在、使用している計算機は、ワークステーションとしては最強の一つである VT-Alpha6 833 SW である。同計算機を用いて、上記の体系で計算を行った場合、*1 タイムステップ当たり、約 23 秒の* CPU 時間を要しており、その内 ICCG 行列計算が全体計算時間の *90%以上*を占めている。そのため、今後、より大容量のシミュレーション計算を行う為には、行列計算の高速化が課題として残ったが、別途超大型ベクトルマシーンでベクトル化して実行すると約 20－30 倍の計算速度が得られることが原理的に判っているため、東工大のスーパーコンピュータ SX-5 向けのベクトル化を並行して実施することとした。

３．２．２　３次元圧力ポアッソン方程式行列解法の高速化

　これまで行ってきた有限差分法による直接数値計算では、圧力ポアッソン方程式の行列計算が最も CPU 時間を占めていた。今後、より大規模メッシュ体系における計算を行う上で、この部分の計算時間の短縮化は急務である。よって、FFT（高速フーリエ変換）を用いた行列解法の改良を行った。以下に FFT を使用した行列ソルバー[4]の概要を述べる。
Nx×Ny×Nz メッシュ、Z 方向に周期境界条件、および等間隔メッシュを用いた体系を計算するものとする。解くべき方程式を以下に示す。

$$\frac{\phi_{i+1\,jk} - 2\phi_{ijk} + \phi_{i-1\,jk}}{\Delta x^2} + \frac{\phi_{ij+1k} - 2\phi_{ijk} + \phi_{ij-1k}}{\Delta y^2} + \frac{\phi_{ijk+1} - 2\phi_{ijk} + \phi_{ijk-1}}{\Delta z^2} = \rho_{ijk} \qquad (3\text{-}2)$$

以下に計算手順を示す。始めに、ρ_{ijk} のフーリエ級数

$$\rho_{ijk} = \frac{1}{2}\,\mathrm{Re}\,\overline{\rho}_{ij}(0) + \sum_{kw=1}^{\frac{N_z}{2}} \mathrm{Re}\,\overline{\rho}_{ij}(k_w)\cos(\frac{2\pi k_w}{N_z}k) + \sum_{kw=1}^{\frac{N_z}{2}-1} \mathrm{Im}\,\overline{\rho}_{ij}(k_w)\sin(\frac{2\pi k_w}{N_z}k) \quad (3\text{-}3)$$

より、FFT 計算コードを使用して、係数 $\mathrm{Re}\,\overline{\rho}_{ij}(k_w)$、$\mathrm{Im}\,\overline{\rho}_{ij}(k_w)$ を求める。次に、5 重対称行列

$$\frac{\mathrm{Re}\,\overline{\phi}_{i+1j}(k_w)-2\mathrm{Re}\,\overline{\phi}_{ij}(k_w)+\mathrm{Re}\,\phi_{i-1j}(k_w)}{\Delta x^2}+\frac{\mathrm{Re}\,\overline{\phi}_{ij+1}(k_w)-2\mathrm{Re}\,\overline{\phi}_{ij}(k_w)+\mathrm{Re}\,\overline{\phi}_{ij-1}(k_w)}{\Delta y^2}$$
$$-4\sin(\frac{\pi k_w}{N})\cdot\frac{\mathrm{Re}\,\overline{\phi}_{ijk}(k_w)}{\Delta z^2}=\mathrm{Re}\,\overline{\rho}_{ij}(k_w) \tag{3-4}$$

および

$$\frac{\mathrm{Im}\,\overline{\phi}_{i+1j}(k_w)-2\mathrm{Im}\,\overline{\phi}_{ij}(k_w)+\mathrm{Im}\,\phi_{i-1j}(k_w)}{\Delta x^2}+\frac{\mathrm{Re}\,\overline{\phi}_{ij+1}(k_w)-2\mathrm{Im}\,\overline{\phi}_{ij}(k_w)+\mathrm{Im}\,\overline{\phi}_{ij-1}(k_w)}{\Delta y^2}$$
$$-4\sin(\frac{\pi k_w}{N_z})\cdot\frac{\mathrm{Im}\,\overline{\phi}_{ij}(k_w)}{\Delta z^2}=\mathrm{Im}\,\overline{\rho}_{ij}(k_w) \tag{3-5}$$

を、ベクトル計算に適しているスケーリング付き共役勾配法(SCG 法)による解法で計算し、$\mathrm{Re}\,\overline{\phi}_{ij}(k_w)$、$\mathrm{Im}\,\overline{\phi}_{ij}(k_w)$ を求める。最後に、ϕ_{ijk} のフーリエ級数

$$\phi_{ijk}=\frac{1}{2}\mathrm{Re}\,\overline{\phi}_{ij}(0)+\sum_{kw=1}^{\frac{N_z}{2}}\mathrm{Re}\,\overline{\phi}_{ij}(k_w)\cos(\frac{2\pi k_w}{N_z}k)+\sum_{kw=1}^{\frac{N_z}{2}-1}\mathrm{Im}\,\overline{\phi}_{ij}(k_w)\sin(\frac{2\pi k_w}{N_z}k) \tag{3-6}$$

より、FFT 計算コードを使用して、ϕ_{ijk} が求まる。本手法の利点としては、Nx×Ny 要素の2次元ポアッソン方程式を Nz 個解くことになる為、Nx×Ny×Nz 要素の3次元ポアッソン方程式を計算する事に比べ、行列解法における反復回数が少なくてすみ、かつ今後、計算ルーチンの並列化も、より容易に行える事が挙げられる。

スカラー計算機である VT-Alpha6 833 SW (VisualTechnolocy) 上においては、$N_x x N_y x N_z = 64x64x64$ の格子数におけるポアッソン方程式の計算において、通常の ICCG 法による解法を用いた計算では、約 40 秒要していた計算時間が、Z 軸方向に FFT を用いた ICCG 法による解法では、約 1 秒台と、40 倍程度短縮された。

また、ベクトル計算機である SX-5 (NEC) 上においては、$N_x x N_y x N_z = 100x100x210$ の格子数におけるポアッソン方程式の計算では、ベクトル計算の特化された超平面法を適用した ICCG 法による解法を用いた計算でも約 12 秒要していた計算時間が、Z 軸方向に FFT を用いたスケーリング付 CG 法による解法では約 2.5 秒と、5 倍程度短縮された。

3．3　既往実験による直交座標系 DNS の検証

3．3．1　キャビティフローに関するベンチマーク解析

　キャビティ上部壁速度を与えた強制対流下における流速分布に関するベンチマーク解析を実施し、2 次元対流拡散方程式が正確に解かれていることの確認を行った。ベンチマーク問題の詳細は、Ghia ら[5]により与えられているが、計算体系は、上下左右が壁面に囲まれた、大きさが 1.0x1.0 の正方形キャビティである。上部壁面が移動壁であり、中身の流体は、速度 1.0 で移動する壁面に引きずられて、正方キャビティ内の流動場を循環する。この正方キャビティ内流動場の計算では、時間刻み幅Δt=1.0x10^{-3} とし、50x50 の等間隔メッシュを用いた。

　正方キャビティの辺の長さと移動壁の速度を、それぞれ代表長さ、代表速度とした Reynolds 数 Re=100 および 400 の流動場について計算を行った。対流項差分スキームの比較を行うために、それぞれの Reynolds 数について、3 次精度河村・桑原スキームを用いた計算と、比較のために 1 次精度風上差分スキームを用いた計算を実行した。

　図 3-4 に Reynolds 数 100 における計算結果を示す。横方向流速分布は、正方形キャビティを左右に 2 分割する線上における上部移動壁と平行な流速の分布であり、縦方向流速分布は、キャビティを上下に 2 分割する線上における上部移動壁と垂直な流速の分布である。両スキームともに、ベンチマークの結果と、ほぼ良好に一致している。

　図 3-5 に Reynolds 数 400 における計算結果を示す。一次風上差分スキームを用いた計算結果は、比較的数値粘性が大きいために、Reynolds 数が大きい流動場では、ベンチマークの結果と比べ、大きな差が認められるものの、河村・桑原スキームを用いた計算結果は、ベンチマークの結果と精度良く一致している。

　比較的少ない格子点数を用いたにも関わらず、良好な計算解が得られたことは、2 次精度中心差分形式であれば本ベンチマーク問題に対しては十分な精度で標準解と一致していることを示している。
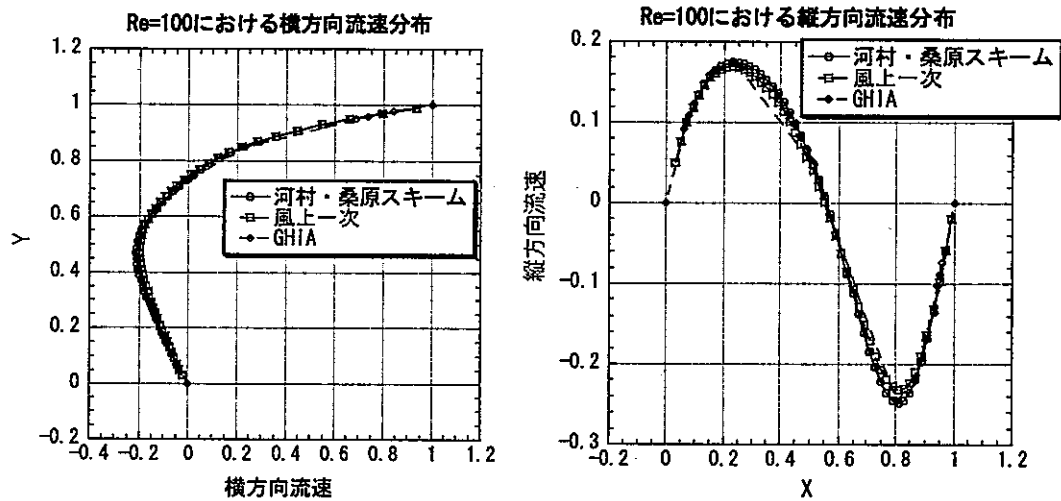
図 3-4　　Re=100 における流動分布
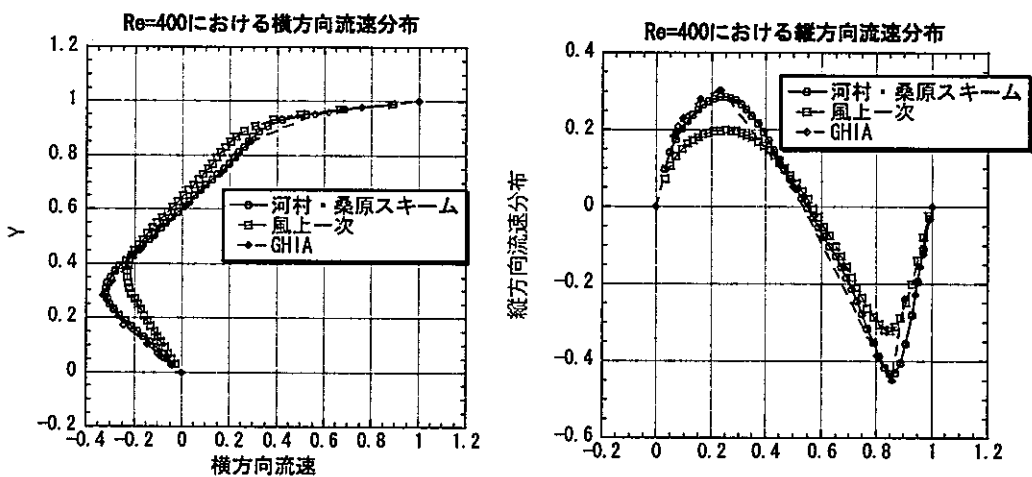
図 3-5　　Re=400 における流動分布

3.3.2 矩形ダクト乱流直接シミュレーション（I）

（1）メッシュ分割法

図3-6に、計算領域となる正方形管を示す。$1 \times 1 \times 2$ の計算領域をメッシュ数が $100 \times 100 \times 64$ メッシュの体系で、時間幅はクーラン数 0.1（典型的な値：$\Delta t \sim 10^{-4}$）として計算を行った。

粘性低層の厚さ y_0 は、摩擦流速 w_τ、動粘性率 ν とすると、以下の式を満たす。

$$y^+ = \frac{y_0 \cdot w_\tau}{\nu} \leq 5 \tag{3-7}$$

摩擦流速 w_τ の定義式は、摩擦係数 λ、流体密度 ρ、主流方向平均流速 w_B とすると

$$w_\tau = \sqrt{\frac{\overline{\tau_w}}{\rho}} \quad and \quad \overline{\tau_w} = \frac{D_h}{4}\frac{\Delta p}{\Delta L} = \frac{\lambda}{8}\rho w_B{}^2 \quad の関係から \quad w_\tau = \sqrt{\frac{\lambda}{8}}w_B \tag{3-8}$$

で与えられる。なお、摩擦係数は、ブラジウスの公式から、レイノルズ数 Re の関数として円管内乱流に対する次の式を用いた。

$$\lambda = \frac{0.3164}{Re^{-0.25}} \tag{3-9}$$

メッシュサイズ Δz は、軸方向摩擦流速 w_τ、動粘性率 ν としたとき、以下の式：

$$\Delta z^+ = \frac{\Delta z \cdot w_\tau}{\nu} \tag{3-10}$$

によって無次元化した値 Δz^+ が 9.4 となるように設定した。同様に無次元化した x、y 方向のメッシュサイズ Δx、Δy も同様に Δx^+、Δy^+ が 0.56 ～ 5. となるように設定した。ダクトの断面方向すなわち、x、y 両方向の非等間隔メッシュは、以下の式で求めた。

$$y_j = \frac{1}{2}(b-1)\left[\frac{a^{2j/N_y}-1}{a^{(2j/N_y-1)}+1}\right], \qquad j = 0,1,2,.....,N_y \tag{3-11}$$

上式で、N_y はメッシュ数であり、本計算では x、y 両方向ともに、$N_y=100$ としている。a は、$a = (b+1)/(b-1)$ で与えられる。b はメッシュ分割サイズを決定するパラメーターであり、1.05 とした。図3-7 に、x 軸上でのメッシュ分割の分布図を示す。

境界条件は、主流方向に平行な壁面には流速については non-slip 条件、圧力にはノイマン条件を適用し、主流方向の流出流入口には流速、圧力ともに周期境界条件を適用する。

数値解法は修正 ICE 法に従い、時間差分スキームはアダムス・バシュフォース法を用い

た。

　十分発達した乱流に対し、ダクト内乱流流速分布は、無次元化された軸方向流速 w^+ と無次元化された壁からの距離 y^+ の関係（壁法則）で記述される。すなわち数値解析結果を比較すべき乱流流速分布は以下の式で与えられる。

$$y^+ = \frac{y \cdot w_\tau}{\nu} \quad , \quad w^+ = \frac{w}{w_\tau} \tag{3-12}$$

で定義される y^+ と w^+ を用いて、壁法則に従う流速分布は、壁面近傍の粘性低層では線形則、

$$w^+ = y^+ \tag{3-13}$$

に従い、壁面から離れた乱流域では対数則、

$$w^+ = 3.2\ln(y^+) + 3.9 \tag{3-14}$$

に従う。

（2）　計算結果と考察

　三方向流速の初期条件は、軸方向流速 $w=14.7$、u 及び $v=0$ を計算領域内に一様に与えた速度分布に、軸方向平均初期流速分布の 1% を振幅として、$-1\sim1$ の間の一様乱数を掛けた値を擾乱として速度分布に足し合わせ、初期流速分布とした。

　図3-8に示すスタガードメッシュ上で用いたK-Kスキームでは数値粘性の影響が大きく、クーラン数が 0.1、ダクト断面に対し 80x80 または 100x100 程度のメッシュ分割では、層流底層については理論解と一致するが、乱流のプロファイルが得られないことが判明した。図3-9に、その計算結果（Re=4,400）の一例を示す。

　したがって K-K スキームに代えて、非等間隔メッシュシステムへの適用について経験が多い他の高次差分（QUICK 法や中心差分法）を試みた結果、中心差分による対流項差分が境界層から乱流コアへの遷移を与えることが示された。ここでは、2 次精度中心差分スキームを例として、$u\,\partial u/\partial x$ と $v\,\partial u/\partial y$ の差分式を示す。ただし u、v は x 方向、y 方向の流速で、これらの位置関係は図 3-8 に定義されている。

$$u\frac{\partial u}{\partial x}\bigg|_{i+1/2jk} = \frac{1}{\Delta x_i + \Delta x_{i+1}}\left[\Delta x_i \frac{u_{i+3/2jk}+u_{i+1/2jk}}{2}\frac{u_{i+3/2jk}-u_{i+1/2jk}}{\Delta x_{i+1}} + \Delta x_{i+1}\frac{u_{i+1/2jk}+u_{i-1/2jk}}{2}\frac{u_{i+1/2jk}-u_{i-1/2jk}}{\Delta x_i}\right] \tag{3-15}$$

$$v\frac{\partial u}{\partial x}\bigg|_{i+1/2jk} = \frac{1}{2}\left[\frac{\Delta x_{i+1}v_{i+1j+1/2k}+\Delta x_i v_{ij+1/2k}}{\Delta x_{i+1}+\Delta x_{i+1}}\frac{u_{i+1/2j+1k}-u_{i+1/2jk}}{(\Delta y_{j+1}+\Delta y_j)/2} + \frac{\Delta x_{i+1}v_{i+1j-1/2k}+\Delta x_i v_{ij-1/2k}}{\Delta x_{i+1}+\Delta x_{i+1}}\frac{u_{i+1/2jk}-u_{i+1/2j-1k}}{(\Delta y_j+\Delta y_{j-1})/2}\right] \tag{3-16}$$

同スキームを用いたときの、計算結果を以下に示す。図 3-10 は、Reynolds 数 $=4400$ のとき、壁を 2 等分する線に沿った軸方向流速分布で、比較のために、壁法則に従う流速分布も示した。計算結果は、7000 タイムステップ（時間間隔 $t_{interval}=0.8$）の間の流速分布を時間平均し

た値である。計算結果が境界層から乱流域への遷移を良好に再現できていることがわかる。図3-11に軸方向流速の乱流変動量であるRMS値の分布の計算結果とKimら[6]のスペクトル法による結果を示す。乱流変動量については、充分発達した安定な計算結果ではないが、Kimらの結果と傾向が一致している。

　　壁法則に従う流速分布と比較して計算結果は、管路中央部の平均流速に若干の差異が生じているが、その可能性としては、（1）2次の精度であるにもかかわらず、メッシュサイズが大きい事、（2）十分発達するまでの計算時間が不足している事、また、（3）周期境界条件に従うとするこの種の乱流直接シミュレーションにおいて、初期の流速分布および擾乱の与え方が初期値問題として解を求める場合に極めて重要な要因となっている事、などがあげられる。なお、（1）に関しては、ここで実施したメッシュサイズと同程度のスキームで充分乱流プロファイルが示されている報告があり[7]、残る可能性としては（3）の初期条件および境界条件の与え方に問題があると考えられるが、普遍的な理論はなく、あくまで経験的に追求することが必要である。

　　現在、使用している計算機は、VT-Alpha6 833 SW である。同計算機を用いて、上記の体系で計算を行った場合、1タイムステップ当たり、約23秒のCPU時間を要する。コード内で、圧力ポアソン方程式における行列計算にはICCG法による解法を使用しているが、この部分のみで約21秒を要し、全体計算時間の90%以上を占めている。従って、今後、上記（3）をパラメトリックに実施する為、また、より大容量のシミュレーション計算を行う為には、行列計算の高速化が最優先課題である。

　　以上より判明した成果および課題としては、壁法則を直接与えるなど、流速および擾乱の初期分布の与え方の最適化に一工夫あれば比較的はやく発達した乱流に到達すること、ベクトル化または並列化により計算速度の2桁の向上が可能となること、2次精度中心差分に代わる高次差分の導入の必要性の検討などが挙げられる。
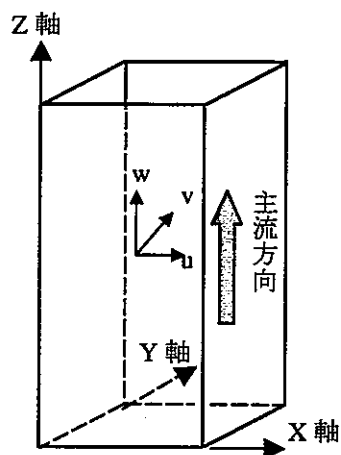
図 3-6 計算体系
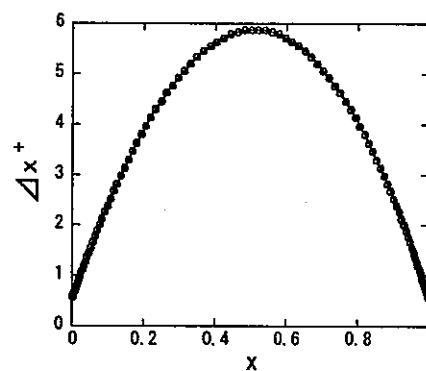
図 3-7 メッシュ分割分布
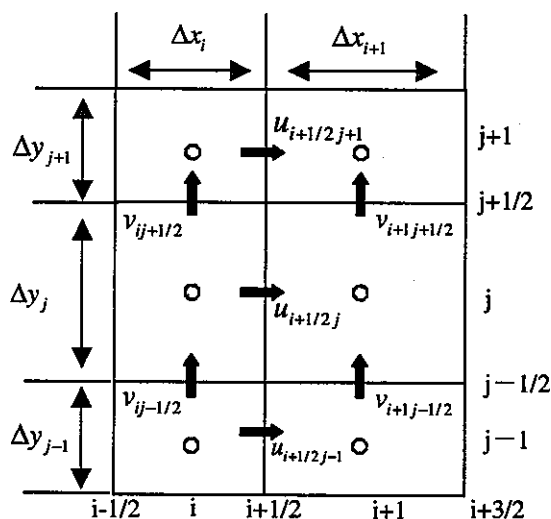
図 3-8 スタガードメッシュ
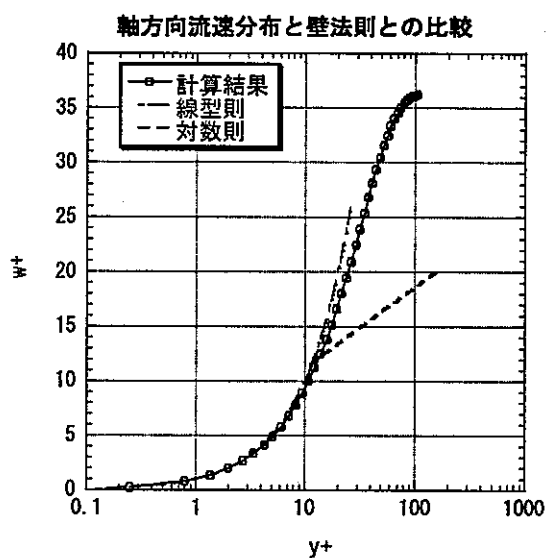
図 3-9 軸方向流速分布（河村桑原スキーム）
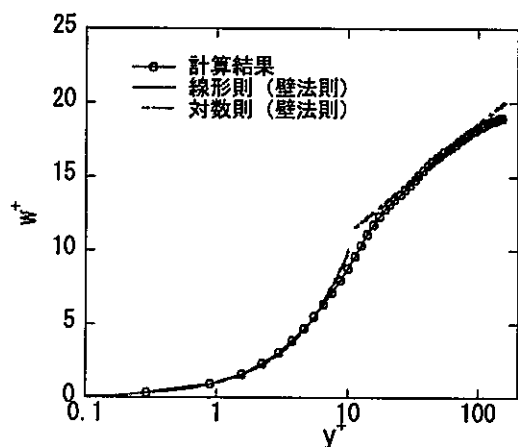
図 3-10 軸方向流速分布（中心差分スキーム）
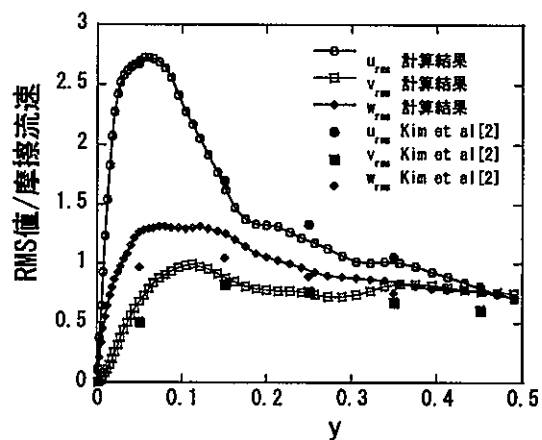
図 3-11 乱流変動量 RMS 値の分布

３．３．３　矩形ダクト乱流直接シミュレーション（II）

　　x，y，z 方向に*1×1×6.4*の矩形ダクト計算領域体系で、３．３．２　矩形ダクト乱流直接シミュレーション（I）で採用した非等間隔メッシュ分割法を適用し、時間幅はクーラン数 0.1（典型的な値：$\Delta t \sim 10^{-6}$）として、以下の表3-1にある４ケースについて乱流解析を実施した。境界条件は、主流方向に平行な壁面には流速についてはnon-slip条件、圧力にはノイマン条件を適用し、主流方向の流出流入口には流速、圧力ともに周期境界条件を適用する。ダクト計算Iは、対流拡散項のより高精度化されたもの、IIは基本的には３．３．２で実施した計算と同じ、IIIおよびIVはより詳細なメッシュを用いた計算である。

表3-1　計算条件

	Re τ	計算体系	メッシュ数	$\triangle$x+	$\triangle$y+	$\triangle$z+	対流項差分法 拡散項差分法
ダクト計算I	300	1.0×1.0×6.4	80×80×100	0.714〜7.34	0.714〜7.34	19.3	5次精度風上差分 6次精度中心差分
ダクト計算II	300	1.0×1.0×6.4	80×80×100	0.714〜7.34	0.714〜7.34	19.3	2次精度中心差分 2次精度中心差分
ダクト計算III	300	1.0×1.0×6.4	100×100×210	0.567〜5.87	0.567〜5.87	9.18	5次精度風上差分 6次精度中心差分
ダクト計算IV	300	1.0×1.0×6.4	100×100×210	0.567〜5.87	0.567〜5.87	9.18	2次精度中心差分 2次精度中心差分
Gavrilakis	300	1.0×1.0×64.0	127×127×1000	0.45〜4.6	0.45〜4.6	9.42	2次精度中心差分 2次精度中心差分

粘性低層の厚さ y_0 は、摩擦流速 w_τ、動粘性率 ν とすると、以下の式（再掲）を満たす。

$$y^+ = \frac{y_0 \cdot w_\tau}{\nu} \leq 5 \tag{3-7}$$

摩擦流速 w_τ の定義式は、摩擦係数 λ、流体密度 ρ、主流方向平均流速 w_B とすると

$$w_\tau = \sqrt{\frac{\overline{\tau_w}}{\rho}} \quad and \quad \overline{\tau_w} = \frac{D_h}{4}\frac{\Delta p}{\Delta L} = \frac{\lambda}{8}\rho w_B{}^2 \quad \text{の関係から} \quad w_\tau = \sqrt{\frac{\lambda}{8}}w_B \tag{3-8}$$

で与えられる。なお、摩擦係数は、ブラジウスの公式から、レイノルズ数 Re の関数として円管内乱流に対する次の式を用いた。

$$\lambda = \frac{0.3164}{Re^{-0.25}} \tag{3-9}$$

メッシュサイズΔzは、軸方向摩擦流速 w_τ、動粘性率 ν としたとき、以下の式：

$$\Delta z^+ = \frac{\Delta z \cdot w_\tau}{\nu} \tag{3-10}$$

によって無次元化した値Δz^+ を設定した。同様に無次元化した x, y 方向のメッシュサイズΔx、Δy も同様にΔx^+、Δy^+が *0.56 〜 7.*となるように設定した。

計算結果を図 3-12～図 3-19 に示す。ただし、軸方向流速分布では w_τ を無次元化に使用した。他の図中に用いられる記号などの説明を以下に記する。

$$W^+ = \frac{W}{w_\tau} \tag{3-17}$$

w_τ: 4壁面全体で平均化された摩擦速度

RMS 分布、レイノルズ応力分布では、W^*を無次元化に使用した。

$$W^* = \frac{W}{w^*} \tag{3-18}$$

w^*: 4壁面全体で平均化された摩擦速度

軸方向流速分布、RMS 分布、レイノルズ応力分布については、矩形断面において、壁面に垂直な 2 等分線上の値を平均化した。2 次流れ流速分布についても、矩形断面を 4 つの象限に区切ったときに、各象限での 2 次流れ流速を平均化した。

十分発達した乱流に対し、ダクト内乱流流速分布は、無次元化された軸方向流速 w^+ と無次元化された壁からの距離 y^+ の関係（壁法則）で記述される。すなわち数値解析結果を比較すべき乱流流速分布は以下の式で与えられる。

$$y^+ = \frac{y \cdot w_\tau}{\nu} \quad , \quad w^+ = \frac{w}{w_\tau} \tag{3-12}$$

で定義される y^+ と w^+ を用いて、壁法則に従う流速分布は、壁面近傍の粘性低層では線形則：

$$w^+ = y^+ \tag{3-13}$$

に従い、壁面から離れた乱流域では対数則：

$$w^+ = 3.2\ln(y^+) + 3.9 \tag{3-14}$$

に従う。

計算結果は、図 3-12 から図 3-19 を通して示されているとおり、疎メッシュから細メッシュになるにつれて、2 次精度による計算が Gavlirakis の結果と合う。とくに壁せん断応力（図 3-15）に関しては、細メッシュで中心差分を用いた結果が最も Gavlirakis[3]によるベンチマーク解と一致している。今回の計算では、5 次精度による計算は、メッシュを細かくしても精度良い計算結果が得られない。5 次精度のスキームが上流差分形式であることがその原因であることも考えられる。

ダクト計算 I   ダクト計算 II

ダクト計算 III   ダクト計算 IV
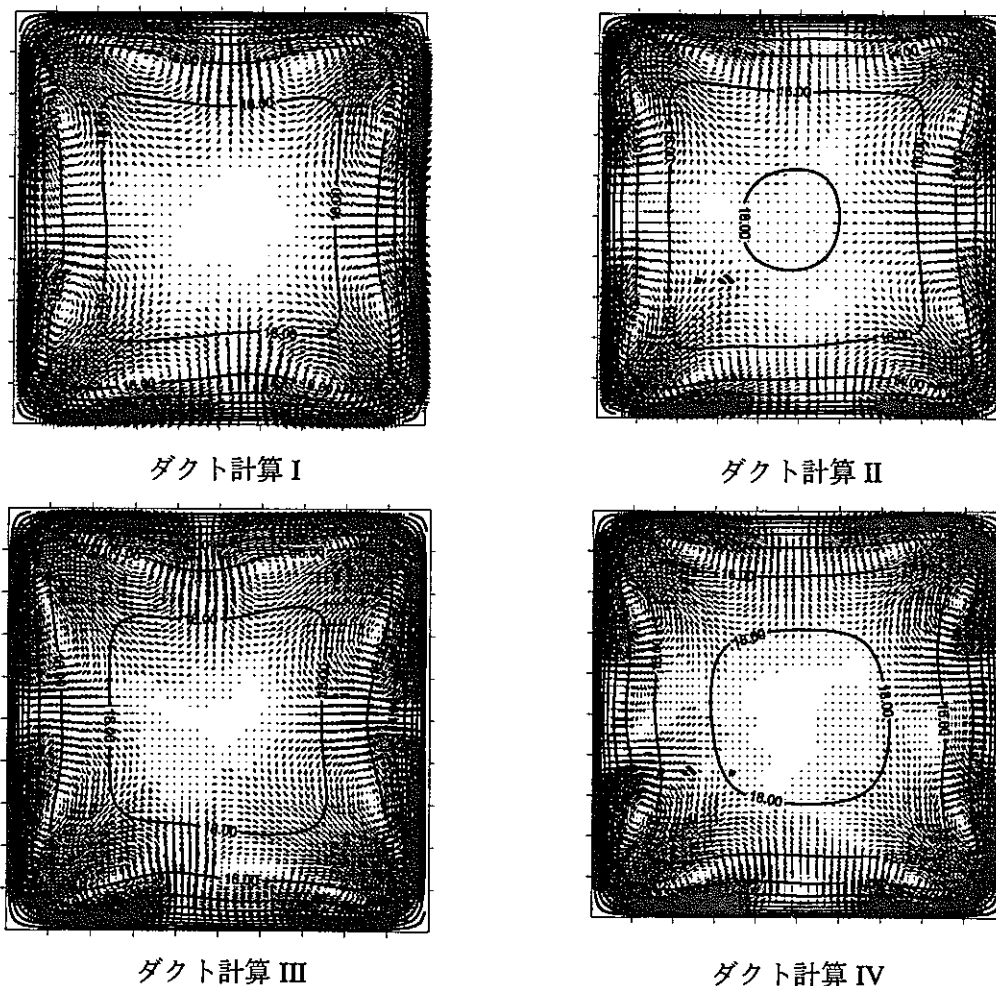
図 3-12　2 次流れ分布
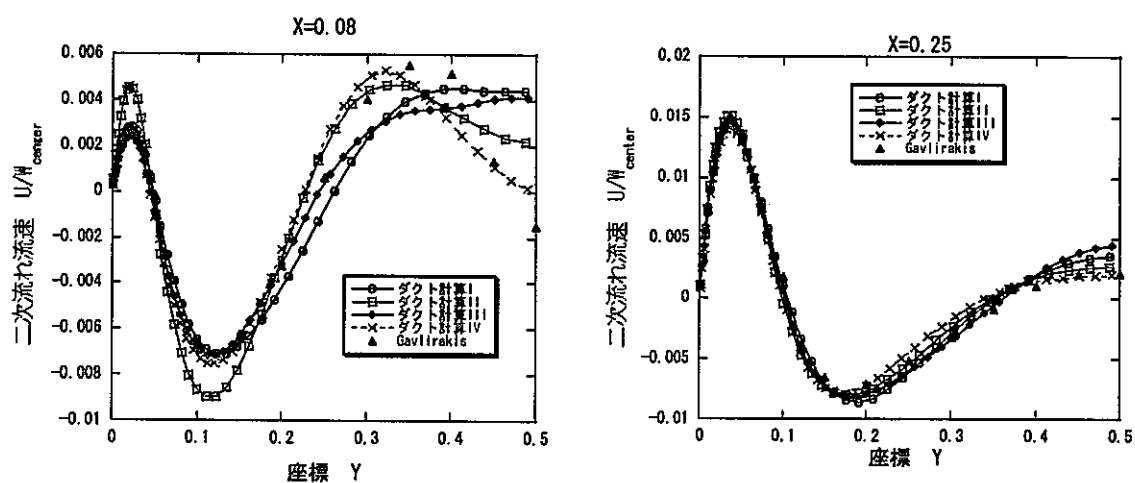
図 3-13　2 次流れ分布（Gavlirakis との比較）
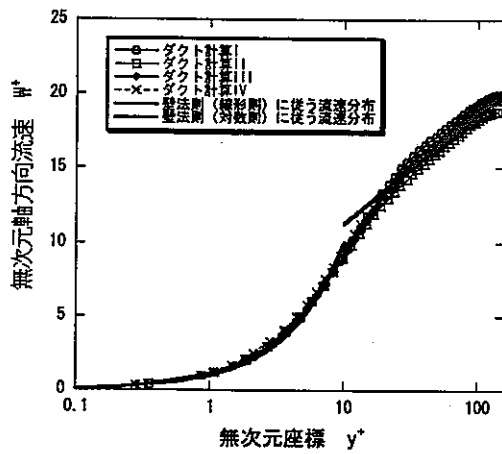
図 3-14　流速分布
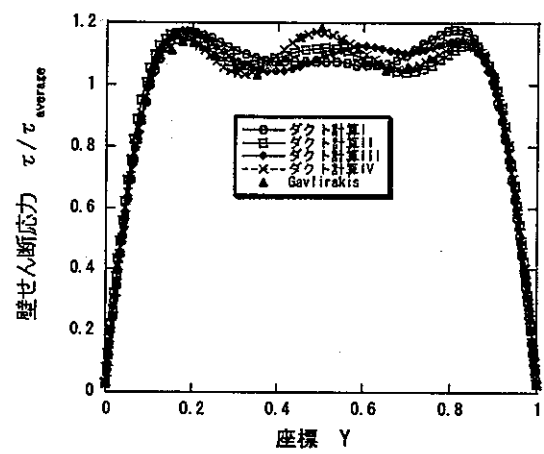
図 3-15　壁せん断応力分布
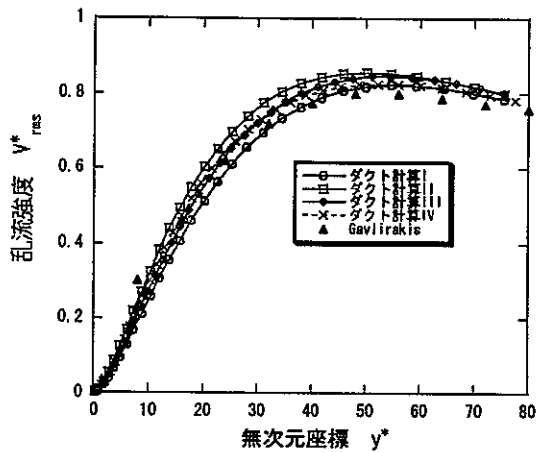
図 3-16　乱流強度 V*
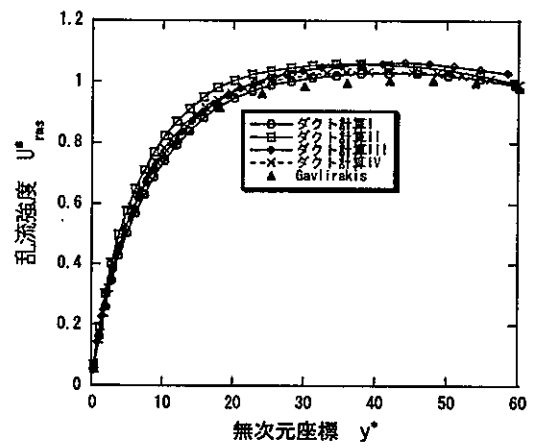
図 3-17　乱流強度 U*
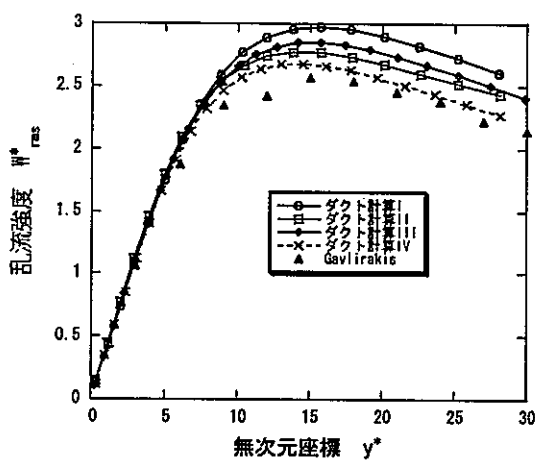
図 3-18　乱流強度 W*
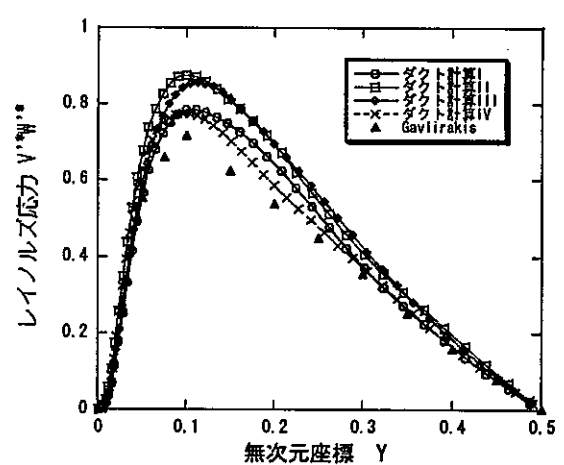
図 3-19　レイノルズ応力 V'*W'*

3．3．4　平行平板内非等温場乱流予測

　本節においては、平行平板内の発達した乱流場における熱伝達の問題を解き、直接乱流シミュレーションによって得られる熱伝達率と実験相間式との比較を行う。

　非等温乱流場におけるエネルギー保存式は以下の式で与えられる：

$$\frac{\partial T}{\partial t}+u_j\frac{\partial T}{\partial x_j}=\frac{\lambda}{\rho C_p}\frac{\partial^2 T}{\partial x_j^2} \tag{3-19}$$

　この場合、周期境界条件を課して運動量保存式を解いて得られる乱流場を求め、エネルギー保存式の対流項の流速は与えられるものとする。運動量保存の周期境界条件と整合性を保つため、次の式で与えられる変数変換を用いる：

$$T(x,y,z)=\frac{d\langle T_m\rangle}{dz}\cdot z-\theta(x,y,z) \tag{3-20}$$

$$\langle T_m\rangle=\frac{\int wTdy}{\int wdy} \tag{3-21}$$

　そうすると、解くべきエネルギー保存式は、

$$\frac{\partial \theta}{\partial t}+u_j\frac{\partial \theta}{\partial x_j}=\frac{\lambda}{\rho C_p}\frac{\partial^2 \theta}{\partial x_j^2}+w\cdot\frac{d\langle T_m\rangle}{dz} \tag{3-22}$$

$$\frac{d\langle T_m\rangle}{dz}=\frac{T_\tau\cdot w_\tau}{\delta}\frac{1}{\langle w\rangle}\quad\text{ただし}\quad\langle w\rangle=\frac{\int wdy}{\int dy} \tag{3-23}$$

より

$$\frac{\partial \theta}{\partial t}+u_j\frac{\partial \theta}{\partial x_j}=\frac{\lambda}{\rho C_p}\frac{\partial^2 \theta}{\partial x_j^2}+\frac{T_\tau\cdot w_\tau}{\delta}\frac{w}{\langle w\rangle} \tag{3-24}$$

となる。ただし

$$w_\tau=\sqrt{\frac{\tau_w}{\rho}} \tag{3-25}$$

$$T_\tau=\frac{q_w}{\rho C_p w_\tau} \tag{3-26}$$

$$q_w=\lambda\frac{\partial \theta}{\partial y}\bigg|_{wall} \tag{3-27}$$

以上より境界条件の与え方は次のとおりとなる。すなわち、

壁面境界条件 $\quad \theta(x, y=0, z)=\theta(x, y=L_y, z)=0$ (3-28)

周期境界条件 $\quad \theta(x+L_x, y, z)=\theta(x, y, z)$ (3-29)

$$\theta(x, y, z+L_z)=\theta(x, y, z)$$ (3-30)

　熱平板体系を図 3-20 に、計算結果の例を図 3-21～図 3-23 に示す。比較のために、河村らが行った同じ平板体系における直接数値シミュレーション[8]の結果も載せた。また、直接数値シミュレーションで得られた温度分布をもとに計算された Nu 数と、Dittus-Boelter の式[9]および Sebban の式[10]による値との比較を図 3-24 に示す。これらの値から、直接乱流シミュレーションによる熱伝達係数の予測の信頼性が高いといえる。

　なお Nu 計算には、平板間距離と軸方向の断面平均流速で定義される Re_b で 5500 を使用した。

　図 3-24 に比較される実験相関式は以下のとおりである。

Dittus-Boelter の式 :

$$Nu = 0.025 \, Re_b^{0.8} \, Pr^{0.4}$$ (3-31)

Seban の式 :

$$Nu = (5.8 + 0.01 \, Re_b^{0.8} \, Pr^{0.8})/c$$ (3-32)

だたし、式（3-32）において、c は補正係数である。

　図 3-21 で比較される Kader の式[11]を以下に示す。

$$\theta^+ = Pr \cdot y^+ \exp(-\Gamma) + \left\{ 2.12\ln\left[(1+y^+)\frac{2.5(2-y/\delta)}{1+4(1+y/\delta)^2} \right] + \beta(Pr) \right\} \exp(-1/\Gamma)$$ (3-33)

ただし、

$$\beta(Pr) = (3.85 \, Pr^{1/3} - 1.3)^2 + 2.12\ln Pr$$ (3-34)

$$\Gamma = \frac{10^{-2}(Pr \cdot y^+)^2}{1+5 \, Pr^3 \cdot y^+}$$ (3-35)
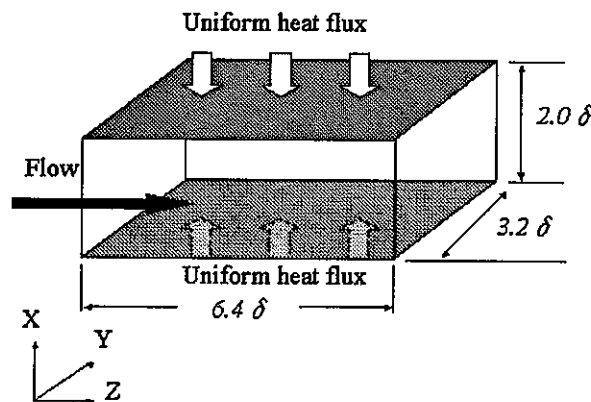
図 3-20 　平行平板体系
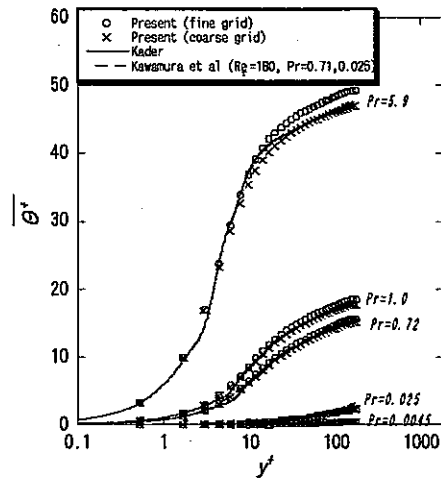
図 3-21　温度分布の比較
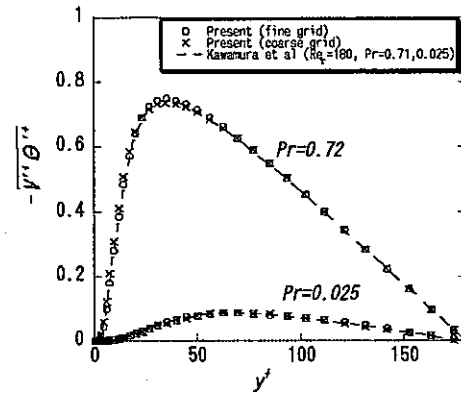
図 3-22　乱流熱流束分布の比較
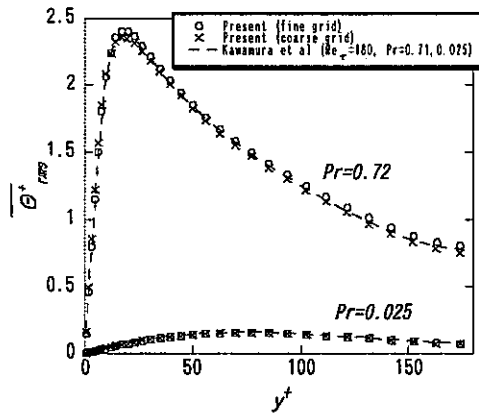
図 3-23　温度乱流強度分布の比較
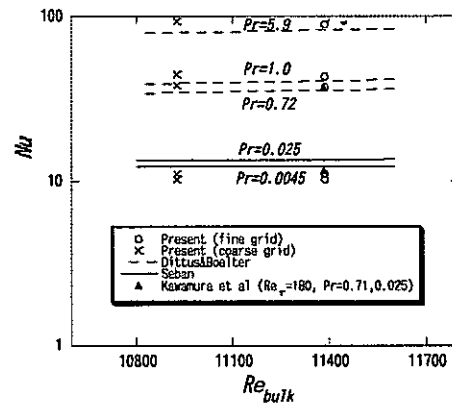
図 3-24　Nu 数の比較

3．4 曲線座標系での直接乱流シミュレーション

3．4．1 境界適合格子法を用いた基礎方程式と解法

　強制対流の非圧縮流体を計算するため、以下の基礎式（デカルト座標系 $x_j(x, y, z)$）から出発する。ここで u_j は i 方向の流速、ρ は密度、P は圧力、μ は粘性係数、T は温度、C_p は定圧比熱、λ は熱伝導率を示す。

質量保存式

$$\frac{\partial u_j}{\partial x_j} = 0 \tag{3-36}$$

運動量保存式

$$\rho \frac{\partial u_i}{\partial t} + \rho u_j \frac{\partial u_i}{\partial x_j} = -\frac{\partial P}{\partial x_i} + \mu \frac{\partial^2 u_i}{\partial x_j^2} \tag{3-37}$$

エネルギー保存式

$$\rho C_p \frac{\partial T}{\partial t} + \rho C_p u_j \frac{\partial T}{\partial x_j} = \lambda \frac{\partial^2 T}{\partial x_j^2} \tag{3-38}$$

以下に、上記基礎式の、デカルト座標系 $x_i(x, y, z)$ から境界適合座標系 $\xi_i(\xi, \eta, \zeta)$ への変換について示す。デカルト座標系において、スカラーf、ベクトル $F_i(F_x, F_y, F_z)$ が与えられたとき、勾配、発散、ラプラシアンは、以下のように変換される。

勾配

$$\frac{\partial f}{\partial x_i} = \frac{\partial \xi_j}{\partial x_i} \frac{\partial f}{\partial \xi_j} \tag{3-39}$$

発散

$$\frac{\partial F_i}{\partial x_i} = \frac{1}{J} \frac{\partial}{\partial \xi_j} \left(J \frac{\partial \xi_j}{\partial x_i} F_i \right) \tag{3-40}$$

ラプラシアン

$$\frac{\partial^2 f}{\partial x_j^2} = \frac{1}{J}\frac{\partial}{\partial \xi_j}\left[J\frac{\partial \xi_j}{\partial x_l}\left(\frac{\partial \xi_k}{\partial x_l}\frac{\partial f}{\partial \xi_k}\right)\right] = \frac{1}{J}\frac{\partial}{\partial \xi_j}\left(G^{jk}\frac{\partial f}{\partial \xi_k}\right) \tag{3-41}$$

ここで J はヤコビアン、G^{ij} は格子歪みテンソルを示し、以下のように与えられる。

$$J = \begin{vmatrix} \dfrac{\partial x}{\partial \xi} & \dfrac{\partial x}{\partial \eta} & \dfrac{\partial x}{\partial \zeta} \\[2mm] \dfrac{\partial y}{\partial \xi} & \dfrac{\partial y}{\partial \eta} & \dfrac{\partial y}{\partial \zeta} \\[2mm] \dfrac{\partial z}{\partial \xi} & \dfrac{\partial z}{\partial \eta} & \dfrac{\partial z}{\partial \zeta} \end{vmatrix} \tag{3-42}$$

$$G^{ij} = J\frac{\partial \xi_i}{\partial x_l}\frac{\partial \xi_j}{\partial x_l} \tag{3-43}$$

上記の関係式を使用して、デカルト座標系における非圧縮流体の基礎式を、以下のように変換することができる。

反変流速成分

$$U^i = J\frac{\partial \xi_i}{\partial x_j}u_j \tag{3-44}$$

質量保存式

$$\frac{\partial U^i}{\partial \xi_i} = 0 \tag{3-45}$$

運動量保存式

$$\frac{\partial u_i}{\partial t} + \frac{1}{J}U^j\frac{\partial u_j}{\partial \xi_j} = -\frac{1}{\rho}\frac{\partial \xi_j}{\partial x_i}\frac{\partial P}{\partial \xi_j} + \frac{\mu}{\rho}\frac{1}{J}\frac{\partial}{\partial \xi_j}\left(G^{jk}\frac{\partial u_i}{\partial \xi_k}\right) \tag{3-46}$$

エネルギー保存式

$$\frac{\partial T}{\partial t} + \frac{1}{J}U^j\frac{\partial T}{\partial \xi_j} = \frac{\lambda}{\rho C_p}\frac{1}{J}\frac{\partial}{\partial \xi_j}\left(G^{jk}\frac{\partial T}{\partial \xi_k}\right) \tag{3-47}$$

簡単のため、二次元体系のときのデカルト座標系と、境界適合座標系を図 3-25 に示す。U^j

は反変流速である。e_1、e_2 は、座標 x_1、x_2 の単位ベクトル、g_1、g_2 は、座標 ξ_1、ξ_2 の単位ベクトルを示す。ここでは、圧力 P、温度 T などのスカラー量を格子中心に配置し、ベクトル量である流速については、一般座標系で定義された反変流速 U^j を格子境界に配置し、デカルト座標系で定義された流速 u_i を格子中心に配置した、コロケート格子による差分式を適用した。

格子系としては他に、流速について、一般座標系で定義された U^j のみで定義したスタガード格子系も考えられるが、保存方差分式を構成するのが困難、計算が煩雑、メモリー増大などの問題がある。コロケート格子を用いれば、各タイムステップ毎に、流速のデカルト座標系成分から一般座標系成分への変換となり、手続きが増すが、保存式を離散的に実現するには、有利である。

計算手順を以下に示す。

手順1．格子中心において、対流項、粘性項より、仮の流速場 u_i^p を求める。

$$u_i^p = u_i^n + \Delta t \left[-\frac{1}{J} U^j \frac{\partial u_i}{\partial \xi^j} + \frac{\mu}{\rho J} \frac{\partial}{\partial \xi^j} \left(G^{jk} \frac{\partial u_i}{\partial \xi^k} \right) \right]^n \tag{3-48}$$

手順2．格子境界において、仮の反変流速 $\left(U^i\right)^p$ を、仮の流速場 u_i^p より補間して求める。

$$\left(U^i\right)^p = J \frac{\partial \xi_i}{\partial x_j} u_j^p \tag{3-49}$$

手順3．以下の圧力ポアッソン式を解く。

$$\frac{\Delta t}{\rho} \frac{\partial}{\partial \xi_i} \left(G^{ij} \frac{\partial P}{\partial \xi_j} \bigg|^{n+1} \right) = \frac{\partial}{\partial \xi_i} \left(U^i\right)^p \tag{3-50}$$

手順4．求まった P^{n+1} より、新しい時間における反変流速 $\left(U^i\right)^{n+1}$ と。流速場 u_i^{n+1} が修正されて求まる。

$$u_i^{n+1} = u_i^p - \frac{\Delta t}{\rho} \frac{\partial \xi^j}{\partial x_i} \frac{\partial P}{\partial \xi^j}\bigg|^{n+1} \tag{3-51}$$

$$\left(U^i\right)^{n+1} = \left(U^i\right)^p - \frac{\Delta t}{\rho} G^{ij} \frac{\partial P}{\partial \xi_j}\bigg|^{n+1} \tag{3-52}$$
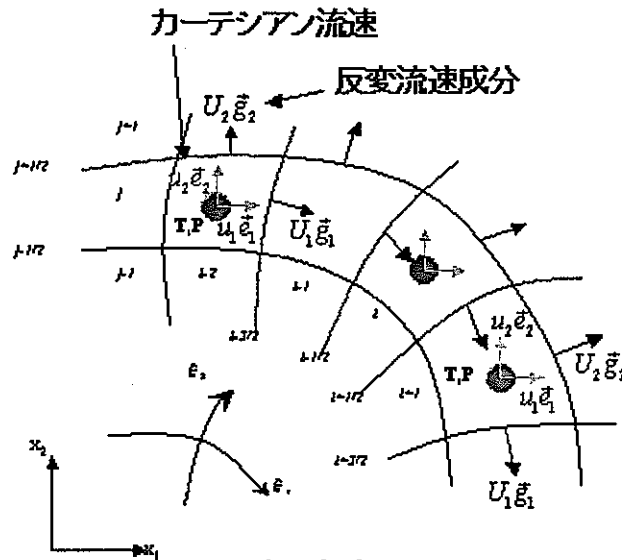
図 3-25　コロケート格子

３．４．２　燃料集合体内温度計算における基礎式

　軸方向に一様な流路を流れる十分発達した乱流について直接数値計算を実施する為には、十分発達した乱流を流入条件に適用する必要から、軸方向に周期境界を適用した。しかし、非等温乱流場計算においては、壁面に熱流束が与えられた場合、軸方向に進むにつれて、温度が上昇する。そのため、温度場にも軸方向に周期境界条件を適用するために、３．３．４節で示した平行平板内における十分発達した非等温場乱流計算では、温度 T を

$$T\left(x, y, z\right) = \frac{d\langle T_m \rangle}{dz} z - \theta\left(x, y, z\right) \tag{3-53}$$

とする変換を行い、ある座標 z における壁面からの温度差 θ を新たに定義することで、温度

場についても周期境界条件を適用することができた。ここで、$\langle T_m \rangle$ は、バルク温度である。バルク温度の軸方向の勾配は、平板上に一様な熱流束が与えられていると仮定することで求めることができる。

　上記の変換が成り立つ為には、下図 3-26 の右に示すとおり、ある高さの流路断面内においては、壁面温度は場所によらず一定であり、かつ乱流に起因する流体温度の揺らぎに対して不変である、との仮定が必要であった。

　しかし、燃料集合体内熱流動については、図 3-26 の左に示す平行平板内乱流とは異なり、流路が広い箇所と狭い箇所では平均流速は一定ではなく、それにより除熱量にも違いが生じ、壁面温度も周方向に分布を持つ。したがって壁面温度はあくまでも計算対象に含めるべきであり、境界条件として前もって与えることはできない。
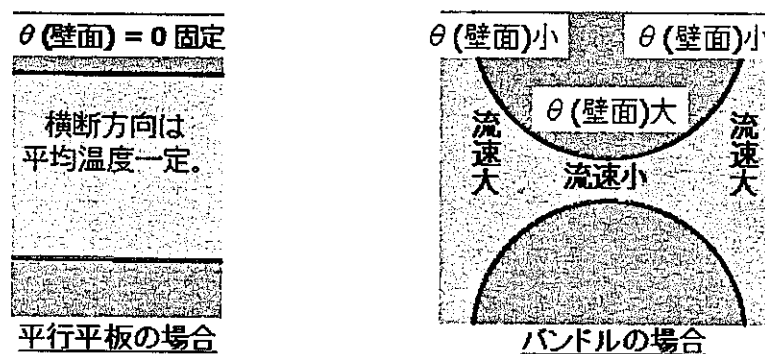
図 3-26　温度場計算における境界条件

　そのために、流体のエネルギー方程式を計算するだけではなく、固体内熱伝導についても計算を行うことで、固体壁面温度を計算することを可能にする。図 3-27 にバンドル内熱流動計算の計算体系の概略図を示す。図中の ξ^i（ξ^1=周方向、ξ^2=径方向、ξ^3=軸方向）は境界適合座標系を表す。
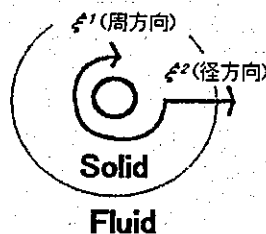
図 3-27　　　温度計算体系

図 3-27 の計算体系における流体、および固体の熱流動の基礎式を以下に示す。

流体エネルギー方程式

$$\frac{\partial T}{\partial t} = -\frac{1}{J}U^j\frac{\partial T}{\partial \xi^j} + \frac{1}{\rho_{fluid}C_{p\,fluid}J}\frac{\partial}{\partial \xi^j}\left[\lambda_{fluid}G^{jk}\frac{\partial T}{\partial \xi^k}\right] \qquad (3\text{-}54)$$

固体熱伝導方程式

$$\frac{\partial T}{\partial t} = \frac{1}{\rho_{solid}C_{p\,solid}J}\frac{\partial}{\partial \xi^j}\left(\lambda_{solid}G^{jk}\frac{\partial T}{\partial \xi^k}\right) + \frac{S_{heat}}{\rho_{solid}C_{p\,solid}} \qquad (3\text{-}55)$$

S_{heat} は固体内における単位体積あたりの発熱量である。

　ここで、周期境界条件を用いて運動量保存式を解いて得られる乱流場は与えられるものとして、温度 T について、次の式で与えられる変数変換を行う。

$$T = \frac{\partial \langle T_m \rangle}{\partial \xi^3}\xi^3 - \theta \qquad (3\text{-}56)$$

ただしバルク温度 $\langle T_m \rangle$ は、以下の式で与えられる。

$$\langle T_m \rangle = \frac{\displaystyle\sum_{fluid}\left(J \cdot U^3 T\right)}{\displaystyle\sum_{fluid}\left(J \cdot U^3\right)} \qquad (3\text{-}57)$$

その結果、解くべき方程式は、以下の式に変換される。

流体エネルギー方程式

$$\frac{\partial \theta}{\partial t} = -\frac{1}{J}U^j\frac{\partial \theta}{\partial \xi^j} + \frac{1}{\rho_{fluid}C_{p\,fluid}J}\frac{\partial}{\partial \xi^j}\left[\lambda_{fluid}G^{jk}\frac{\partial \theta}{\partial \xi^k}\right] + \frac{U^3}{J}\frac{\partial \langle T_m \rangle}{\partial \xi^3} \qquad (3\text{-}58)$$

<u>固体熱伝導方程式</u>

$$\frac{\partial \theta}{\partial t} = \frac{1}{\rho_{solid} C_{p\,solid} J} \frac{\partial}{\partial \xi^j}\left(\lambda_{solid} G^{jk} \frac{\partial \theta}{\partial \xi^k}\right) - \frac{S_{heat}}{\rho_{solid} C_{p\,solid}} \tag{3-59}$$

固体領域である燃料棒の中心において、境界条件を

$$\theta\left(\xi^2 = center\ of\ rod\right) = 0 \tag{3-60}$$

と設定し、かつ燃料棒中心における径方向の温度勾配はないと仮定することで、軸方向のバルク温度勾配を、次の式で与えることができる。

$$\frac{\partial T_m}{\partial \xi^3} = \frac{\displaystyle\sum_{solid}(J \cdot S_{heat})}{\rho_{fluid} C_{p\,fluid} \displaystyle\sum_{fluid} U^3} \tag{3-61}$$

３．４．３　境界適合座標系に基づく差分方式の精度評価

（１）精度評価の方法

　本章では、３．４．２節で示された境界適合座標系に拡張された有限差分法の、擬似直接数値計算への適応性を検証するために、非直交格子体系を用いた平行平板内乱流と、円管内乱流について、擬似直接数値計算を実施し、その精度評価を行った。

　平行平板内乱流計算については、同様の差分手法を用いた直交座標スタッガード格子系に基づく擬似直接数値計算による計算結果と比較することにより、境界適合座標系に拡張された手法との計算精度の検証、および格子歪みと格子サイズが計算結果に与える影響についての検証を行った。

　計算手法は Fractional Step 法に従った。空間差分としては、２次精度 Consistent スキーム[7]を対流項、他の項には２次精度中心差分スキームを適用した。ただし、壁面においては、粘性項に内側３点補間を用いた。時間進行については、対流項と粘性項に２次精度 Adamus-Bashforth 法を使用した。圧力 Poisson 方程式は、計算時間の短縮を行うために、３．２．２で述べた軸方向に FFT を使用するスケーリング付 CG 法によって解かれた。また、Cartesian 流速から反変流速への変換では、４次精度補間が適用された。

（２）平行平板内乱流計算：計算条件・体系

　図3-28に、計算体系となる平行平板を示す。3次元各方向の計算領域の大きさは、壁面垂直方向（y方向）の大きさを 2δ としたとき、スパン方向を 3.2δ、軸方向を 6.4δ に設定した。

　本計算では、格子歪みの影響を検証するために、図3-29に示す直交座標格子体系（Case1）と、スパン方向に格子を歪ませた非直交座標格子体系（Case2）の2通りの格子体系で計算を行った。

また、格子サイズが計算結果に与える影響を検証するために、Case1、Czse2それぞれの格子体系に対して、2通りに格子サイズを変えた計算を実行した。表3-2に、格子サイズ一覧を示す。ただし Δy^+ は、$\Delta y^+ = \Delta y \cdot \overline{w_\tau}/\nu$ で定義される壁座標である。x方向およびz方向は等間隔格子を使用している。y方向にのみ、壁面に格子を集中させる必要から、非等間隔格子を使用している。本計算では、細メッシュのケースでは、x、y、z各方向に、$128x64x128$ノード、疎メッシュのケースでは、x方向とz方向について、格子サイズを2倍粗くした、$64x64x64$ノードの計算を実行した。また、比較の為に、細メッシュ、および疎メッシュのケースについて、本計算と同じ空間差分法、時間進行法を用いた直交座標スタッガード格子に基づく擬似直接数値計算を実施した。時間刻み幅は、全てのケースともに、$\Delta t \cdot \overline{w_\tau}/\delta = 0.0005$ とした。
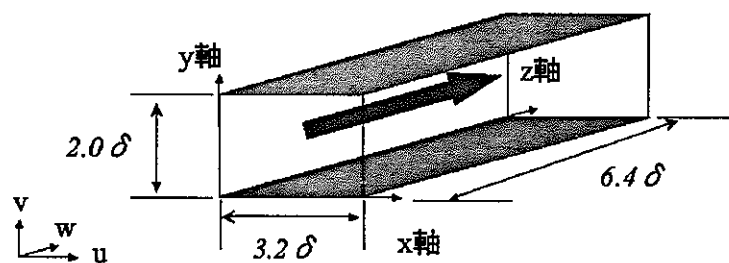
図 3-28　計算体系
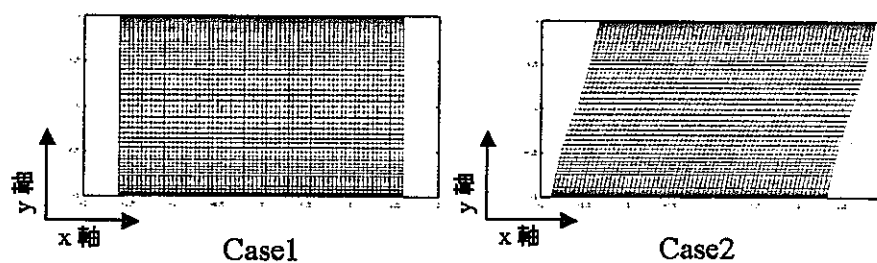
図 3-29　格子体系

表 3-2　計算ケース：基本条件

	y 一方向	
	メッシュ数 Ny	メッシュサイズ $\triangle y^+$
Case1（直交座標系計算）	64	1.1～11.0
Case2（曲線座標系計算）	64	1.1～11.8
直交座標スタッガード格子計算	64	1.1～11.0

表 3-2　計算ケース：細メッシュ計算（続き）

	細メッシュ計算			
	x 方向		z 方向	
	メッシュ数 Nx	メッシュサイズ $\triangle x^+$	メッシュ数 Nz	メッシュサイズ $\triangle z^+$
Case1（直交座標系計算）				
Case2（曲線座標系計算）	128	4.5	128	9.0
直交座標 スタッガード格子				

表 3-2　計算ケース：疎メッシュ計算（続き）

	疎メッシュ計算			
	x 方向		z 方向	
	メッシュ数 Nx	メッシュサイズ $\triangle x^+$	メッシュ数 Nz	メッシュサイズ $\triangle z^+$
Case1（直交座標系計算）				
Case2（曲線座標系計算）	64	9.0	64	18.0
直交座標 スタッガード格子				

（3）平行平板内乱流計算：計算結果

　以下に計算結果から得られた計算結果、および比較の為に、直交座標スタッガード格子に基づく擬似直接数値計算の結果と、Kim ら[6]が行ったスペクトル法に基づく計算の結果を示す。

　図 3-30 に、摩擦流速で無次元化されたレイノルズ応力分布を示す。直交座標スタッガード格子に基づく計算結果は、疎メッシュ、細メッシュともに Kim らのスペクトル法による結果と一致している。境界適合座標系に基づく計算においても、Case1、Case2 ともに、計算結果に違いが見られず、良好に、これらの結果と一致している。
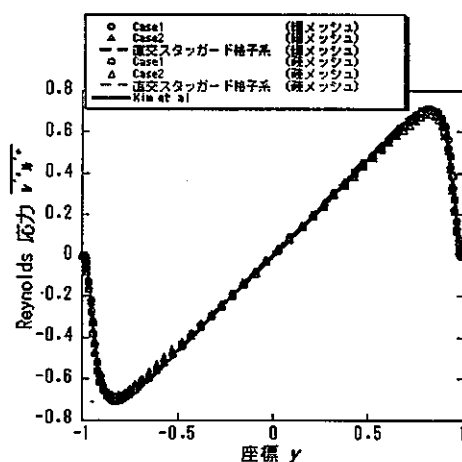
図 3-30　　レイノルズ応力分布

　図 3-31 に軸方向流速分布を、図 3-32〜図 3-34 に、x、y、z 各方向に流速乱流強度分布を示す。直交スタッガード格子に基づく計算結果は、細メッシュのケースは Kim らのスペクトル法による結果と良好に一致しているが、疎メッシュのケースは、スペクトル法による結果と比べ過少評価している。疎メッシュのケースでは、軸方向流速を評価するには十分な格子サイズではないことがわかる。一方、境界適合座標系に基づく計算では、疎メッシュ、細メッシュのそれぞれのケースにおいて、Case1、Case2 ともに、直交スタッガード格子に基づく計算結果と一致している。

図 3-31　　　軸方向流速分布

$$u'^+_{rms} = \frac{\sqrt{u'^2}}{w_z}$$

図 3-32　　　x 方向流速乱流強度分布

$$v'^+_{rms} = \frac{\sqrt{v'^2}}{w_z}$$

図 3-33　　　y 方向流速乱流強度分布

$$w^+_{rms} = \frac{\sqrt{\overline{w'^2}}}{w_z}$$
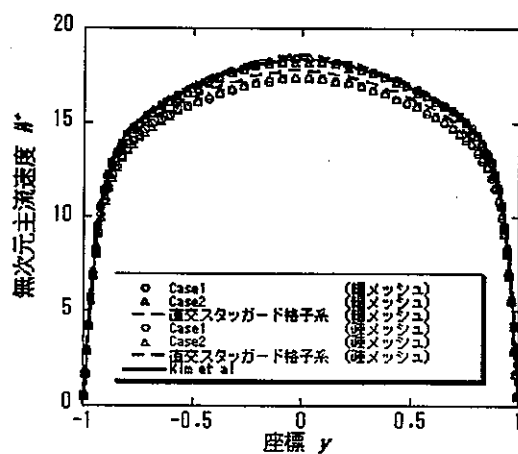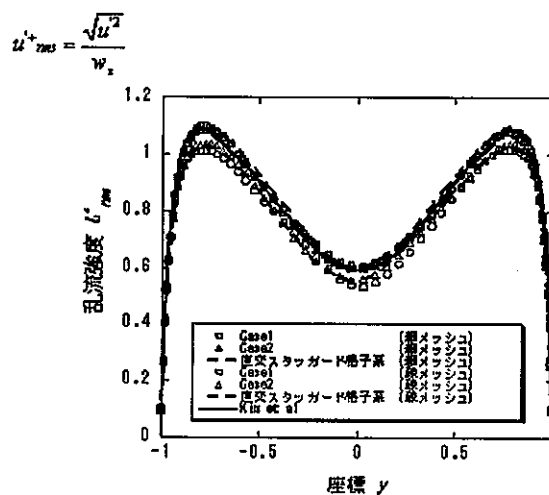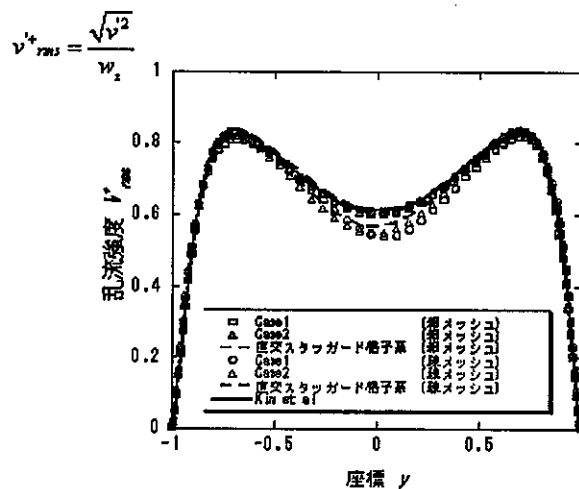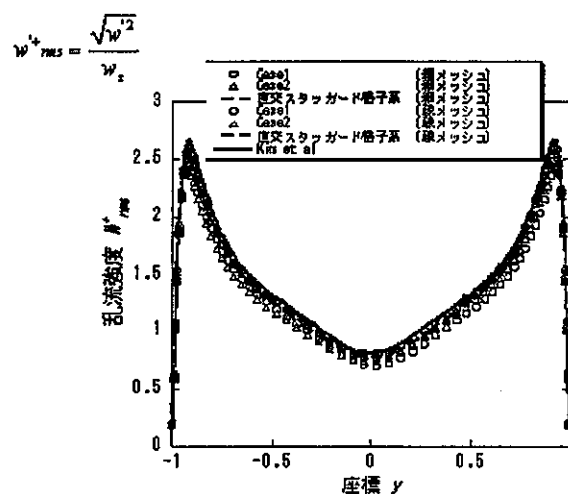
図 3-34 z 方向流速乱流強度分布

　図 3-35 に、平板垂直方向流速の歪み度分布を示す。直交座標スタッガード格子に基づく計算では、細メッシュのケースでも、Kim らの結果とは一致していないことから、今回設定した範囲内では、歪み度を精度良く評価するには、格子サイズ、または差分精度が不足している事がわかる。境界適合座標系に基づく計算では、軸方向流速、乱流強度と同様に、格子歪みが計算結果に与える影響は見られず、疎メッシュ、細メッシュのケースともに、直交座標スタッガード格子に基づく計算と良好に一致している。
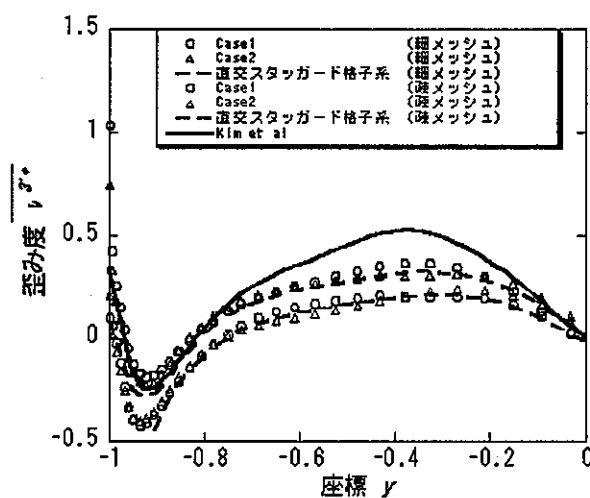
図 3-35 y 方向流速歪み度分布

　以上のことから、本手法に基づく計算は、今回設定した格子範囲内においては、格子歪み

が計算結果に与える影響は殆ど見られなかった。また、同じ差分手法、時間進行法による直交座標スタッガード格子に基づく計算の結果と、ほぼ同程度の格子サイズ依存性をもつことを確認した。

４．燃焼度燃料および革新型燃料開発への応用

４．１　三角配列稠密燃料格子内乱流

　　燃料集合体内流れによる壁せん断応力分布はサブチャネル内の二次流れ、すなわち乱流の非等方性に依存する。流速分布、従って被覆管の温度分布も同様で、直接乱流シミュレーションの重要性が強調される。P/D が 1.2 より小さい稠密燃料格子においては乱流の非等方性はより強く、必ずしも壁せん断応力分布、熱流束分布は単調な形状から離脱し、下段落に述べるように特異な挙動を示す。また低 Re 数乱流においては狭隘部における乱流から層流への遷移も発生する可能性もあり、通常の RANS 適用において破綻を来たす場合が多い所以である。

　　例えば、図４－１は 19 ピン集合体中心ピン＃１が、照射または熱変形しピン＃７に近接した状況を模擬したものである。本来ならば、このように単一ピンが変位したのみで対象性が崩れる場合、19 本ピン集合体全体を直接乱流シミュレーションによって計算するのが理想である。4.2 節以降では、計算機資源の制約により、現状では狭隘部における熱流動現象を計算するために狭隘部のギャップ幅で配列された無限大本数のピン束を仮定して解析を行う。ここでは COOLFD による 19 本ピン集合体全体の二次元解析の知見に基づいて、一本のピンが変位した場合の三角配列燃料格子内乱流の特徴について述べる。
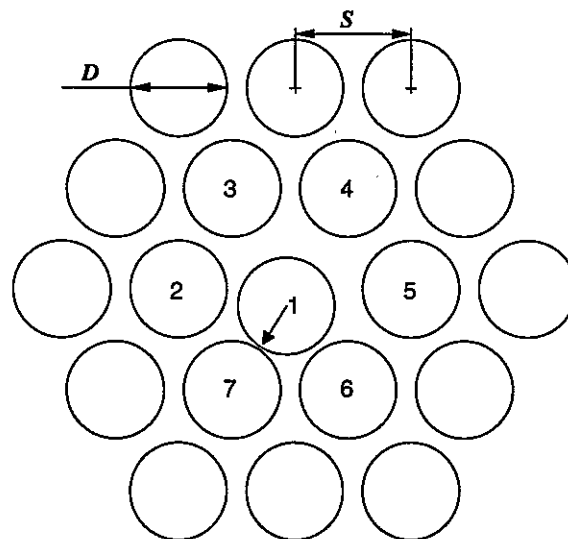
図４－１実験体系

　　図４－２に、チェコ原研にて詳細流速を測定した位置を示す(Heina, et al[12])。測定結果によると、一般的に、ピン表面法線がピン－ピン間のギャップ（０°）から離れ、サブチャネル中心部に向かう位置（30°）に達したときに壁せん断応力は最大となる。図４－３に示す

ピン＃6の周囲の壁せん断応力分布は単調な変化を示す。このことは、P/D>1.2で、とくにノミナル形状の場合に当てはまる。この傾向は、数値解法としてEFDスキーム、乱流モデルとしてMSV（Appendix B参照）を用いたCOOLFDによる2次元解析で適切に予測可能であることが示されている。

　しかしながら、P/Dが1.05以下の場合（図4－1でピン＃1とピン＃7ギャップ近傍）、狭隘部の近くでせん断応力が一旦増加し、ギャップ部で再び減少するという逆W形を示すことが、実験的に得られている（図4－4参照）。COOLFDの予測によると、狭隘ギャップ部において、むしろW字型の壁せん断応力が得られており、乱流モデルに起因することは予想されても、これまでのところその原因は特定されていない。
チェコ原研で実施した詳細流束分布測定実験と相似側を考慮してセットアップした発熱ピン体系でのナトリウム実験がロシアIPPEで実施されている(Ushakov, et al [13])。

　本実験によると、ピン＃1またはピン＃7の最狭隘部における被覆管温度分布は、冷却材の高熱伝導率に因り比較的スムーズで、低プラントル数流体の優れた熱伝達特性のためにホットスポットの温度上昇も比較的低く抑えられているのが示されている。以上のような実験的な観察を裏づけするCOOLFDによる19本ピン集合体全体の二次元解析による三角配列燃料集合体内乱流運動量、エネルギー交換に関する知見の詳細はAppendix Bに示す。
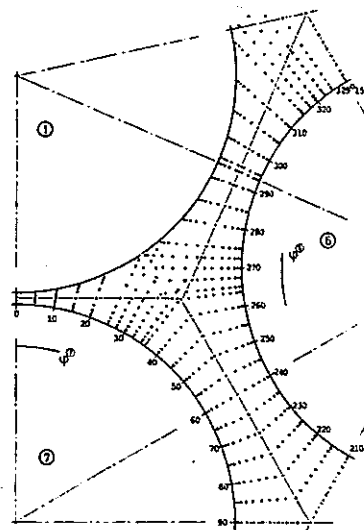
図4－2　流束測定点（Heina, et al [12]）
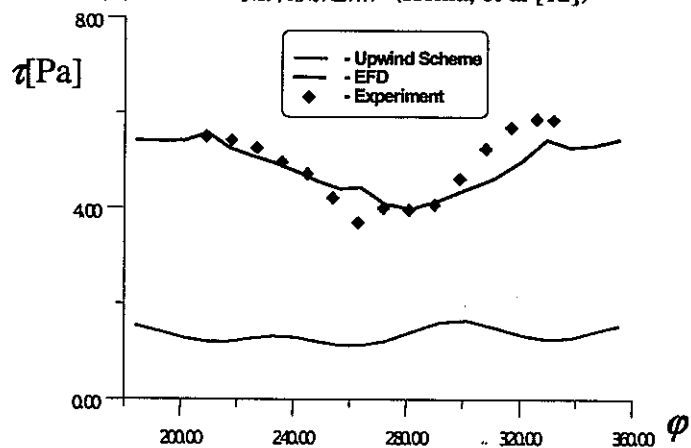
図4－3　ピン＃6周辺壁せん断応力分布（角度φは図4－2参照）
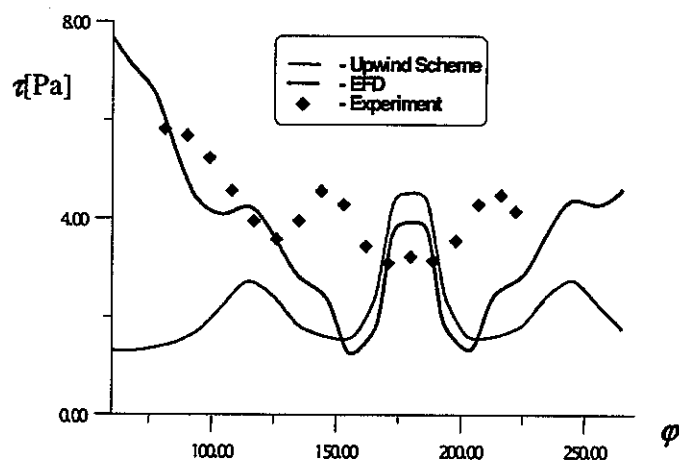
図4－4　ピン＃1周辺壁せん断応力分布（角度φは図4－2参照）

４．２　曲線座標系直接乱流シミュレーションの応用

　本章では、無限大本数燃料集合体内における十分発達した乱流について、境界適合座標系に拡張された有限差分法に基づく擬似直接乱流シミュレーション（DNS）数値計算を実施し、実験との比較を行う。

４．２．１　無限大燃料ピン束体系のシングルブロック計算

　有限本数の燃料集合体全体に直接乱流シミュレーションを適用するには、現時点で最も高性能な超並列マシンを以ってしても記憶容量の絶対的不足且つ天文学的な計算時間がかかることが予測される。したがって、ここでは形状の対称性を最大限活用できる無限大本数の燃料ピンからなる仮想的な無限大燃料集合体について直接乱流シミュレーションを実施するものとする。本研究においては、以下の（１）に述べるごとく、４つの最小単位セルを組み合わせた計算領域（ブロック）、及び２つの最小単位セルを組み合わせた計算領域について、単一 CPU で直接乱流シミュレーションを行う。将来、実際の有限本数燃料集合体に対して適用する場合は、これらのブロックを必要数だけ結合し適切な境界条件を与え、高性能並列計算機の利用によるマルチブロック計算を提案する。

　なお、三角配列の燃料集合体内詳細流束分布の測定例は過去にいくつか報告されているが、いずれも高レイノルズ数乱流のものであり、現状直接乱流シミュレーションで実施できる最高のレイノルズ数が約１０，０００程度であることを勘案すると、厳密な意味で必ずしも既往実験データとの比較による検証とはいえないが、計算と実験によるデータの傾向の比較により定性的な評価が可能である。厳密な意味での検証を行うには、より低いレイノルズ数における詳細な乱流データの取得が今後の課題として指摘される。

（１）計算体系

　図 4-5 の中央図に、計算対象となる燃料集合体を示す。三角配列の、軸方向に一様な、無限配列のピンバンドルを仮定している。本計算では、燃料棒直径を D、燃料棒中心間距離を P としたときに、$P/D = 1.2$ の集合体を計算対象とした。

　バンドル内乱流を精度良く再現するためには、最大サイズの渦を表現することができる十分な計算領域を確保することが望まれるが、そのためには、計算コードの並列化を含めた、よりいっそうの計算速度の高速化が必要である。本計算では、その前段階として、バンドル内の対称性を考えて、図中の最小単位セルを組み合わせた流路について、擬似直接数値計算

を実行した。

　図4-5の右図及び左図に、本計算で解析する最小単位セルを4セル組み合わせた流路についての計算（以下、4セル計算）、及び2セル組み合わせた流路についての計算（以下、2セル計算）の計算体系を示す。軸方向をz軸、燃料棒中心を結ぶ軸をy軸、z軸およびy軸ともに垂直な軸をx軸とする。軸方向を流れる流体は十分発達した乱流を仮定している。

　計算体系の軸方向長さ　*Lz* は、4セル計算、2セル計算共に、*3.2Dh*、または、*1.9D*とした。ただし、*Dh*(= *4S/Lw*、*S*=流路断面積、*Lw*=濡れぶち長さ)は、以下の式で定義される、無限配列集合体の等価直径である。

$$\frac{D_h}{D} = \frac{2\sqrt{3}}{\pi}(P/D)^2 - 1 \tag{4-1}$$
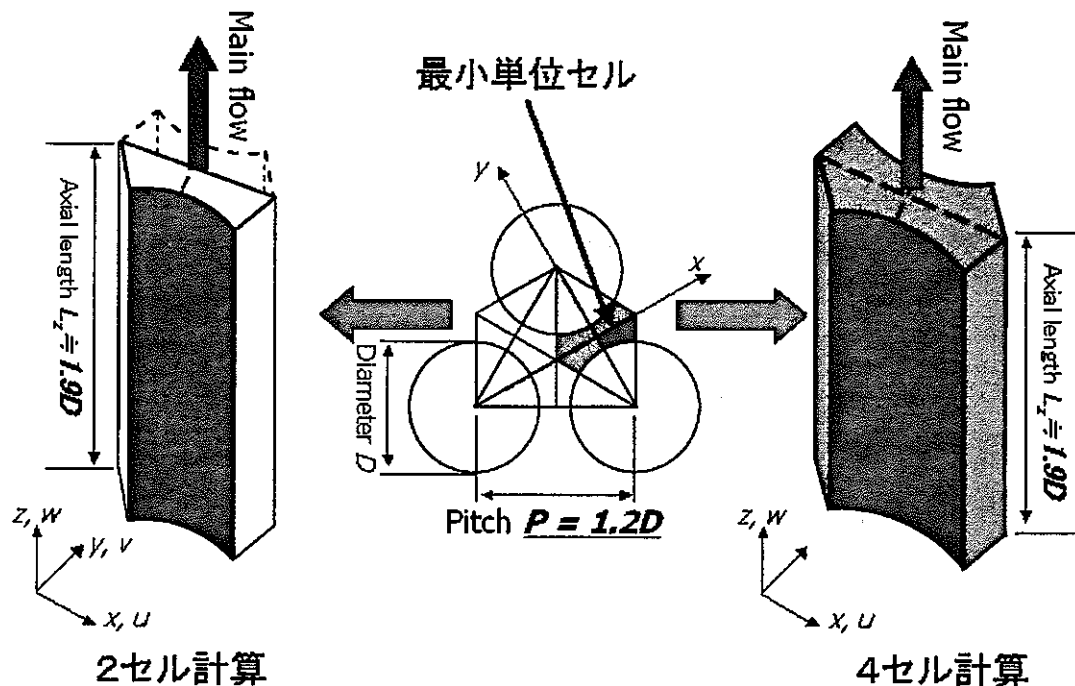
図4-5　計算体系

（2）境界条件について

　図4-6に、軸方向に垂直な断面についての境界条件を示す。4セル計算では、燃料棒壁面に滑りなし境界条件を適用し、軸方向（z軸方向）の境界面には、十分発達した乱流場を流速場の境界条件として与える為に、周期境界条件を適用した。周方向（x軸方向）の境界面

についても、同様の理由から、周期境界条件を適用した。ただし、境界面の向き及び形状が一致していないため、軸方向の境界と同様の周期境界条件を適用することができない。その為、図4-6の左図に示すようにx軸上に接する対称面を境に、周方向の境界面を2領域に分け、それぞれの境界面について、周回方向に周期性を満たす境界条件を設定した。例えば、y＜0、x＞0に属する境界面を通過して流出した流体は、その流速ベクトルのx方向成分及びy方向成分を、反時計回りに60度回転変換した後、y＜0、x＜0に属する境界面を通過して流入する。また、y＞0、x＞0に属する境界面を通過して流出した流体は、同様に流速ベクトルの向きを、時計回りに60度回転変換した後、y＞0、x＜0に属する境界面を通過して流入する。

　2セル計算では、燃料棒壁面に滑りなし境界条件を、x軸に接している対称面に、鏡面対称境界条件を適用した。軸方向の境界面には周期境界条件を適用し、周方向の境界面には、4セル計算と同様の流速ベクトルの回転変換を伴う境界条件を適用した。

　4セル計算の体系では、x軸に接する対称面に仮定を用いる必要がないが、周方向の境界面を、x軸を境に2領域に分けて、それぞれについて別個の周期境界条件を適用しなくてはならない。一方2セル計算の体系では、対称面に鏡面境界条件を用いなくてはならないが、4セル計算のように、周方向の境界面を分ける必要はない。
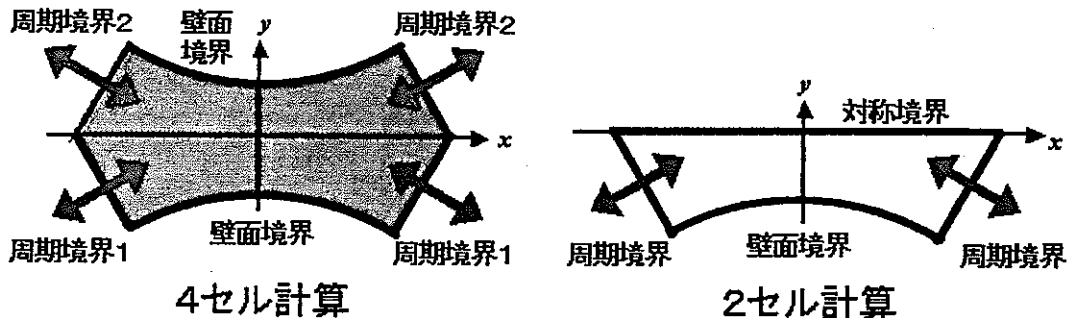
図4-6　境界条件

（3）計算条件

　本計算では、平均摩擦流速 $\overline{w_\tau}$ と等価直径 D_h で定義される摩擦Reynolds数 $Re_\tau=600$ の乱流について、直接計算を実行した。ただし、平均摩擦流速 $\overline{w_\tau}$ は以下の式で定義される。

$$\overline{w_\tau} = \sqrt{\frac{\overline{\tau_{wall}}}{\rho}} \tag{4-2}$$

ここで、ρ は密度、$\bar{\tau}_{wall}$ は、計算領域に接している壁面表面全体について平均化された軸方向流速の壁面せん断応力である。

本計算では、軸方向バルク流速 $\bar{w}_{bulk}$ と等価直径 D_h で定義されるバルク Reynolds 数 Re_{bulk} が約 10000 の乱流について直接数値計算を実行することを試みた。$Re_{bulk}=10000$ としたとき、以下の円管内乱流場における、$\bar{\tau}_{wall}$ を導出する式

$$\bar{\tau}_{wall} = \frac{\lambda}{8}\rho \bar{w}_{bulk}^{2} \tag{4-3}$$

及び

$$\lambda = 0.3164 \cdot Re_{bulk}^{-1.4} \tag{4-4}$$

より求められた摩擦レイノルズ数 Re_τ は、約 600 程度に相当する。

4．2．2　計算手法

（1）支配方程式と解法

本計算では、バンドル内を通過する非圧縮性流体は、軸方向平均圧力勾配 *dP/dZ* によって駆動される。ただし、*dP/dZ* と、平均壁面せん断応力 $\overline{\tau}_{wall}$ または平均摩擦流速 $\overline{w_\tau}$ の関係は、以下の通りである。

$$\overline{\tau}_{wall} = \rho\,\overline{w}_\tau^{\,2} = -\frac{D_h}{4}\frac{dP}{dZ} \tag{4-5}$$

流体の支配方程式である運動量保存式と質量保存式は、境界適合座標系において、以下のように拡張される(Zang et al[14])。

$$\frac{\partial u_i}{\partial t} = -\frac{1}{J}U^j\frac{\partial u_i}{\partial \xi^j} - \frac{1}{\rho}\frac{\partial \xi^j}{\partial x_i}\frac{\partial p}{\partial \xi^j} - \frac{dP}{dz}\delta_{iz} + \frac{\nu}{J}\frac{\partial}{\partial \xi^j}\left(G^{jk}\frac{\partial u_i}{\partial \xi^k}\right) \tag{4-6}$$

$$\frac{\partial U^j}{\partial \xi^j} = 0 \tag{4-7}$$

ここで、$x_i\left(x_1=X, x_2=Y, x_3=Z\right)$ は Cartesian 座標、$\xi^i\left(\xi^1=\xi, \xi^2=\eta, \xi^3=\zeta\right)$ は境界適合座標である。本計算では、周方向を ξ 方向、径方向を η 方向、軸方向を ζ 方向とした。ν は動粘性率、p は軸方向平均圧力勾配 *dP/dZ* からの変動成分である。

計算格子はコロケート格子を用いた。この格子上では、Cartesian 流速：

$$u_i\left(u_1=u, u_2=v, u_3=w\right)$$

と　圧力 *p* を格子中心で定義され、反変流速

$$U^i\left(U^1=U, U^2=V, U^3=W\right)$$

は格子面上で定義される。反変流速は、以下の式で定義される。

$$U^i = J\frac{\partial \xi^i}{\partial x_j}\cdot u_j \tag{4-8}$$

ここで、*J* はヤコビアンである。

$$J = \begin{vmatrix} \dfrac{\partial x}{\partial \xi} & \dfrac{\partial x}{\partial \eta} & \dfrac{\partial x}{\partial \zeta} \\[8pt] \dfrac{\partial y}{\partial \xi} & \dfrac{\partial y}{\partial \eta} & \dfrac{\partial y}{\partial \zeta} \\[8pt] \dfrac{\partial z}{\partial \xi} & \dfrac{\partial z}{\partial \eta} & \dfrac{\partial z}{\partial \zeta} \end{vmatrix} \tag{4-9}$$

また G^{ij} は、以下の式で定義される格子歪みテンソルである。

$$G^{ij} = J \frac{\partial \xi^i}{\partial x_l} \frac{\partial \xi^j}{\partial x_l} \tag{4-10}$$

解法は Fractionalstep 法に従った。空間差分としては、2次精度 Consistent スキーム (Kawamura et al[7])を対流項、他の項には2次精度中心差分スキームを適用した。時間進行については、対流項と粘性項に2次精度 Adamus-Bashforth 法を使用した。圧力 Poisson 方程式は、計算時間の短縮を行うために、軸方向に FFT を使用したスケーリング付 CG 法によって解かれた。

直交座標スタッガード格子体系に基づく平行平板内乱流について、上記の空間差分、時間進行法を使用した擬似直接数値計算を実行し、スペクトル法に基づく計算と良好に一致する計算が行えることを、既に確認している。

Cartesian 流速から反変流速への変換では、4次精度補間が適用された。

（２）計算格子体系について

図 4-7 に、4セル計算、及び2セル計算における流路断面の計算格子を示す。この格子体系では、粘性低層を解像するために、壁面近傍に格子を集中させた。壁面境界に接する格子は、式(4-7)、(4-8)の壁面境界における扱いを容易にするために、境界面に対して垂直な格子を適用した。周方向境界に接する格子についても、同様に境界面に垂直な格子を適用した。

使用した計算格子点数は、周方向、径方向、軸方向の順に、4セル計算においては、64x64x128 ノード（520,000 ノード）、2セル計算においては、64x32x128 ノード（260,000 ノード）の格子を適用した。計算格子サイズについては、4セル計算、2セル計算ともに、同様の格子分布を適用した。壁面に接している格子は、周方向に一様に、径方向格子サイズ $\Delta y^+=1.0$、周方向格子サイズ $\Delta x^+=8.4$ とした。ただし Δy^+ は、 $\Delta y^+ = \Delta y \cdot \overline{w_\tau} / \nu$ で定義される壁座標である。X 軸に接している格子は、$\Delta y^+=9.4 \sim 21.2$、周方向格子サイズ $\Delta x^+=10.8 \sim 11.2$ と定義した。

軸方向格子サイズは、一様に $\Delta z^+ =15.0$ と定義した。時間刻み幅 Δt については、4セル計算、2セル計算ともに、$\Delta t \cdot \overline{w_\tau}/D_h =0.00030$、または $\Delta t \cdot \overline{w_\tau^2}/\nu =0.18$ と定義した。

４セル計算　　　　　　　　　２セル計算
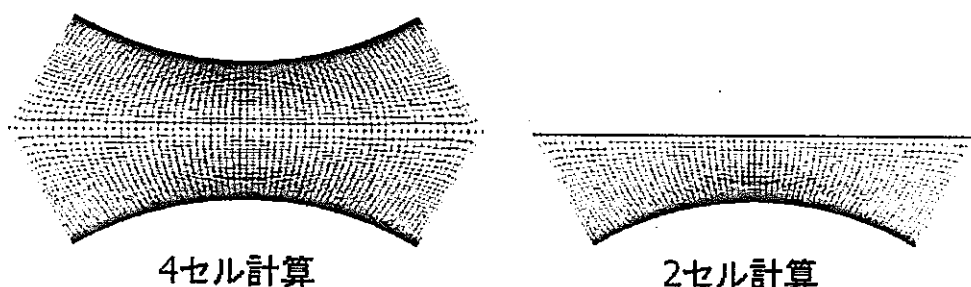
図4-7　断面内計算格子

（３）計算手順

　バンドル内の直接数値計算を実行する前に、平行平板内乱流について、同じ格子数を適用した直交座標スタッガード格子に基づく擬似直接数値計算を実行した。平板内乱流が、安定な十分発達した乱流に到達した後に、計算領域内における瞬時の流速分布を初期条件として用いた。

　4セル計算については、$\Delta t \cdot \overline{w_\tau}/D_h =30$、または流体が流路内を約 $450D_h$ 通過する事に相当する時間、2セル計算については、$\Delta t \cdot \overline{w_\tau}/D_h =27$、または流体が流路内を約 $400D_h$ 通過する事に相当する時間だけ計算を実行し、計算領域内の乱流エネルギーが十分定常な状態になり、流路内流体が十分発達した乱流に到達したことを確認した。

　その後、4セル計算については $\Delta t \cdot \overline{w_\tau}/D_h =430$、または流体が流路内を $6500D_h$ 通過することに相当する時間、2セル計算については $\Delta t \cdot \overline{w_\tau}/D_h =160$、または流体が流路内を $2400D_h$ 通過することに相当する時間だけの時間平均、及び軸方向に空間平均を行い、計算結果が得られた。本計算では計算マシンとして、ベクトルマシンである SX-5(NEC)上を使用した。計算結果が得られるまでに、4セル計算では約520時間、2セル計算では約140時間、の計算時間を要した。

4．2．3　計算結果と評価

　得られた計算結果は、計算領域の x 軸および y 軸に対する対称性を考え、最小単位セルに平均化された。

　計算結果より得られた摩擦 Reynolds 数は、4 セル計算では $Re_\tau=604.7$、2 セル計算では $Re_\tau=604.8$ であり、両計算ともに設定した値 $Re_\tau=600$ と 1%以内で一致している。バルク Reynolds 数は、4 セル計算では $Re_{bulk}=9090$、2 セル計算では $Re_{bulk}=9000$ であった。

　図 4-8 に、計算結果から得られた、バルク流速で無次元化された軸方向流速等高線分布の計算結果を示す。

　2 セル計算の流速分布は、4 セル計算の流速分布と異なり、x 軸に接する対称面と流速等高線の交叉角が垂直ではない。これは、2 セル計算において、対称面に鏡面境界を適用したためと考えられる。

　一方で、2 セル計算の流速等高線は、4 セル計算の分布と比較して、センター領域で疎の分布になっており、ギャップ領域においては逆に密な分布になっている。このことは、最小単位セル内を反時計回りに循環する第二種二次流れによる移流効果は、2 セル計算の方が強い傾向にあることを示している。

4セル計算　　　　　　2セル計算
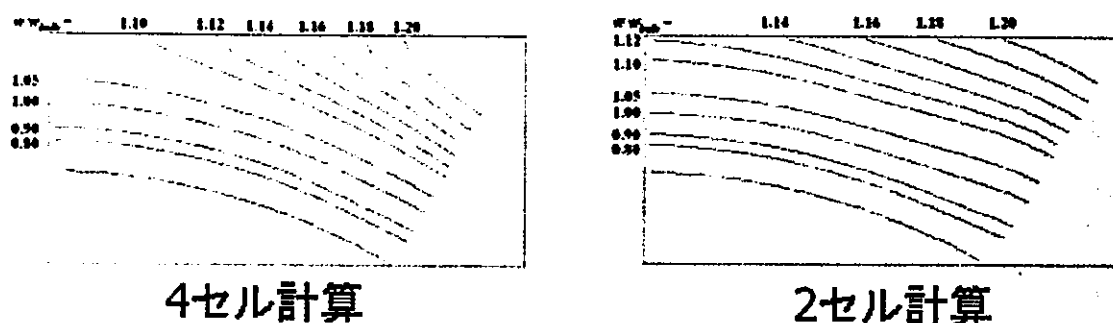
図 4-8　　軸方向流速等高線分布

　図 4-9 に、y 軸上（$\theta=0°$）、及び周方向周期境界面（$\theta=30°$）における、平均摩擦流速と動粘性率で無次元化された軸方向流速分布の計算結果と、Trupp らが、$Re_{bulk}=11680$ における実験結果より得られた流速分布を元に最小 2 乗法により導出された対数則

$$\overline{w}/\overline{w_\tau} = 1.95 \cdot \ln\left(y_w \overline{w_\tau}/v\right) + 7.01 \tag{4-11}$$

に基づく流速分布を示す。
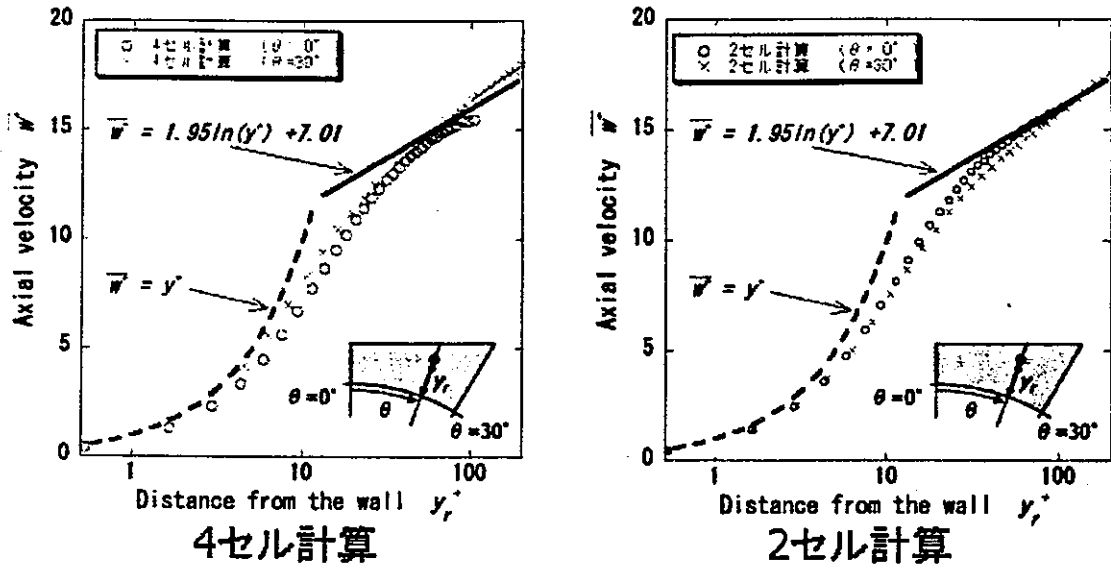
図 4-9　　　軸方向流速分布

Trupp らの実験では、(4-11)の対数則を導出する際に、平均摩擦流速 $\overline{w_\tau}$ を、以下の相関式より求めている。

$$\overline{w_\tau} = \left(f \cdot \overline{w}_{bulk}^2 \middle/ 8\right)^{1/2} \tag{4-12}$$

$$f = C \operatorname{Re}_{bulk}^{-n} \tag{4-13}$$

ただし

$$C = 0.287\left(\frac{D_h}{D} - 0.30\right)^{-1/2} \tag{4-14}$$

$$n = 0.368\left(P/D\right)^{-1.358} \tag{4-15}$$

計算結果から得られた流速分布も、(4-11)の対数則に従う流速分布と比較するために、(4-12)

～(4-15)の相関式より求められた摩擦流速で整理された。　4セル計算、2セル計算ともに、対数則に従う流速分布に良好に一致している。また、ギャップ領域（θ=0°）とセンター領域（θ=30°）における2セル計算の流速分布は、お互いに近づいており、軸方向等速線分布と同様の傾向が見られる。

　図4-10に、壁面せん断応力分布の計算結果、及びTruppらの$Re_{bulk}=23760$における実験結果を示す。2セル計算の分布は、実験結果と良好に一致している。しかし、4セル計算の分布は、実験結果と比べ、ギャップ領域では過小評価しており、センター領域では過大評価している。第二種二次流れは、センター領域では速度勾配を減少させ、ギャップ領域では増加させる。4セル計算の結果は、2セル計算の結果と比べ、第二種二次流れによる移流効果が弱いために、実験結果と一致しなかったと考えられる。
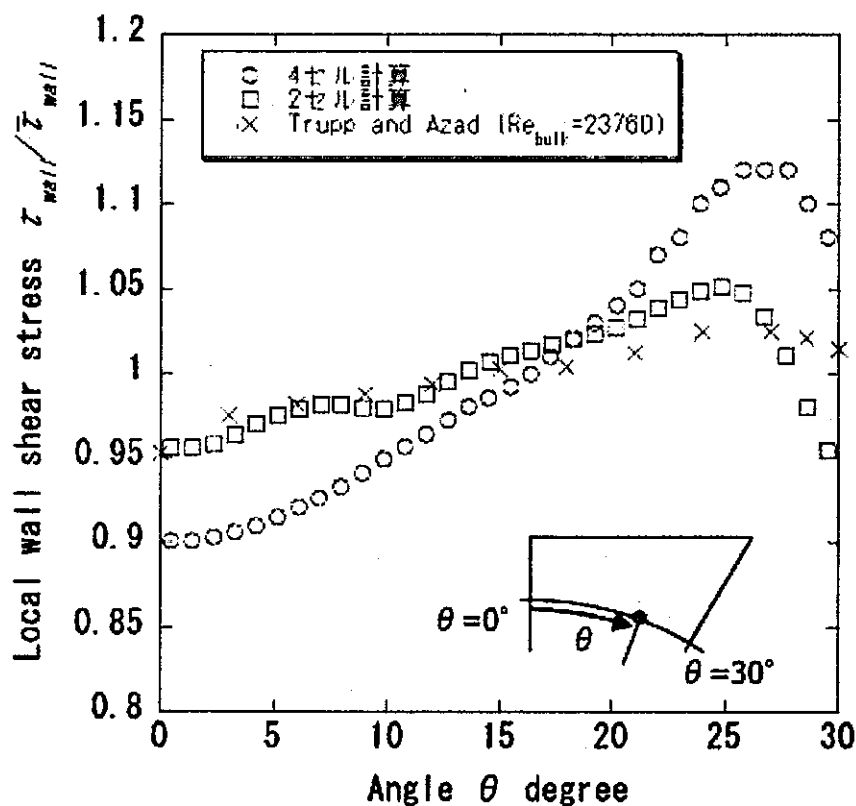
図4-10　　壁面せん断応力分布

　図4-11に、二次流れ流速分布を示す。2セル計算の分布は、最小単位セル内を循環する第二種二次流れを良好に再現できている。4セル計算の分布の分布も、同様の分布が見られるが、センター領域の壁面近傍で小さな渦が発生している。この小さな渦は、計算領域の各々

の象限においても、同様の箇所に発生していた。

　第二種二次流れの平均値とバルク流速との比　$\overline{V}_{sec}/w_{bulk}$　で定義される二次流れ強度は、4セル計算で 0.14%、2セル計算で 0.38%であった。2セル計算の二次流れ強度は、4セル計算の二次流れ強度よりも約2.7倍程度大きく、この結果は、軸方向流速分布、壁面せん断応力分布の傾向と一致する。

4セル計算　　　　　　　　**2セル計算**
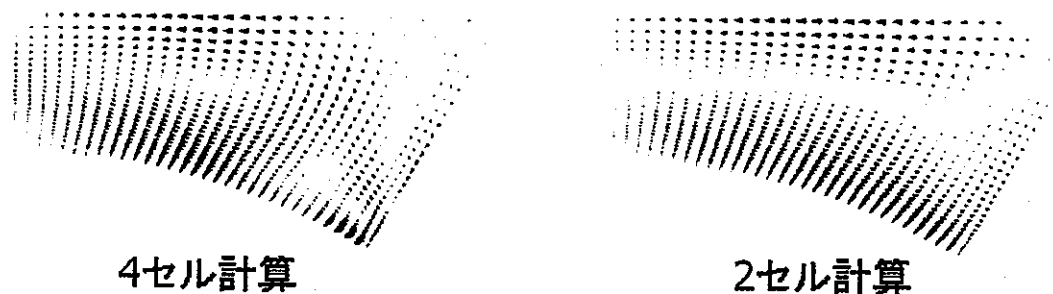
図4-11　　第二種二次流れ流速分布

　図4-12に、計算結果から得られた、以下の式

$$\Omega = \frac{\partial \overline{u}}{\partial y} - \frac{\partial \overline{v}}{\partial x} \tag{4-16}$$

で定義される渦度分布を示す。渦度分布の白い部分は正の渦度、灰色の部分は負の渦度を示す。渦度等高線の増加分は 0.5 である。2セル計算の結果は、壁面近傍を除いて、単一符号の渦度が、それぞれの最小単位セルを占めている事がわかる。壁面近傍にて異なる符号の渦度が見られるのは、滑りなし境界条件の影響であると考えられる。一方、4セル計算の結果は、2セル計算の渦度分布と異なり、壁面近傍以外に、周方向境界面近傍においても、異なる符号の渦度が見られる。この原因として、周方向の境界面を、x軸に接する対称面を境にして分岐する周期境界条件が起因している可能性が考えられる。周方向周期境界条件が起因して、周方向境界面近傍で異なる符合の渦度分布が発生し、その結果、二次流れ強度が弱まったと思われる。

4セル計算　　　　　　　　　　　　2セル計算
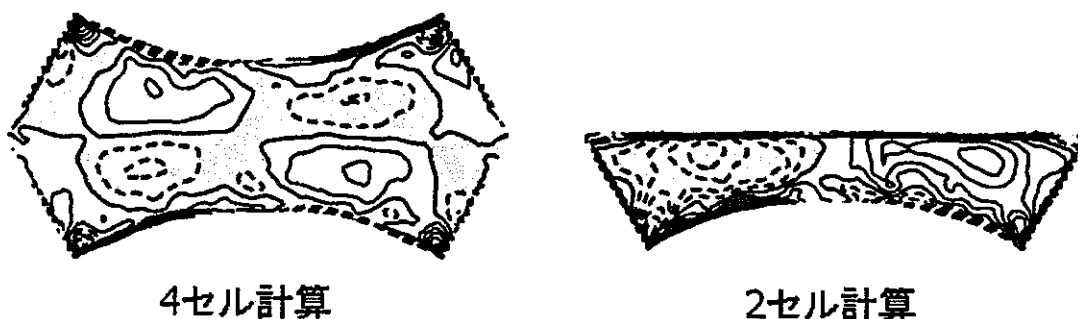
図 4-12　　　渦度分布

乱流の二次モーメントを調べるために、以下に示す渦度方程式の検討を行った。

$$-u\frac{\partial \Omega}{\partial x}-v\frac{\partial \Omega}{\partial y}+\nu\left(\frac{\partial^2}{\partial x^2}+\frac{\partial^2}{\partial y^2}\right)\Omega+\frac{\partial^2}{\partial x\partial y}\left(\overline{v'^2}-\overline{u'^2}\right)+\left(\frac{\partial^2}{\partial x^2}-\frac{\partial^2}{\partial y^2}\right)\overline{u'v'}=0 \quad (4\text{-}17)$$

渦度方程式の第一項及び第二項は、対流項及び粘性項である。第三項及び第四項は、Reynolds normal stress、及び Reynolds shear stress の勾配である。共に乱流の非等方性に起因する項であり、渦度方程式の生成項の役割を担っている。

　これらの生成項が図 4-12 の渦度分布に与える影響を見ることを試みた。本来ならば、勾配も含めて検証すべきだが、境界適合座標系上で勾配を含めて生成項を求めるのは困難の為、本稿では、Reynolds shear stress $\overline{u'v'}$、及び Reynolds normal stress $\overline{v'^2}-\overline{u'^2}$ の分布を調べた。

　図 4-13 に、計算結果から得られた Reynolds shear stress $\overline{u'v'}$ を示す。4 セル計算及び 2 セル計算を比較して、センター領域の対称面近傍で若干の違いが見られるものの、それ以外では大きな違いが見られなかった。

4セル計算　　　　　　　　　　　　2セル計算
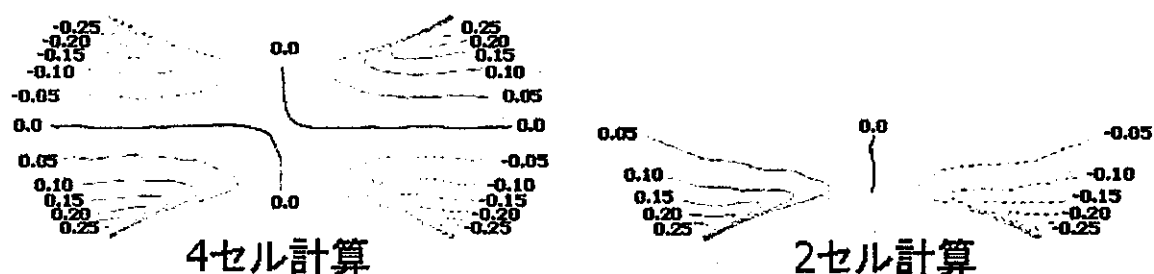
図 4-13　　　Reynolds shear stress 分布　　（$\overline{u'v'}$）

図4-14に、計算結果から得られたReynolds normal stress $\overline{v'^2}-\overline{u'^2}$ を示す。壁面近傍については、2セル計算と4セル計算の分布に大きな違いは見られない。しかし、x軸上に接する対称面近傍では、2セル計算の分布は、4セル計算の分布とは異なり、径方向に向かって大きな勾配を持つことが分かる。これは、2セル計算では、鏡面境界を適用した為である。それにも関わらず、2セル計算の方が良好な二次流れが再現でき、その結果、壁面せん断応力が実験結果と良好に一致したということは、対称面近傍のReynolds normal stress分布が第二種二次流れに与える影響は大きくない可能性が考えられる。
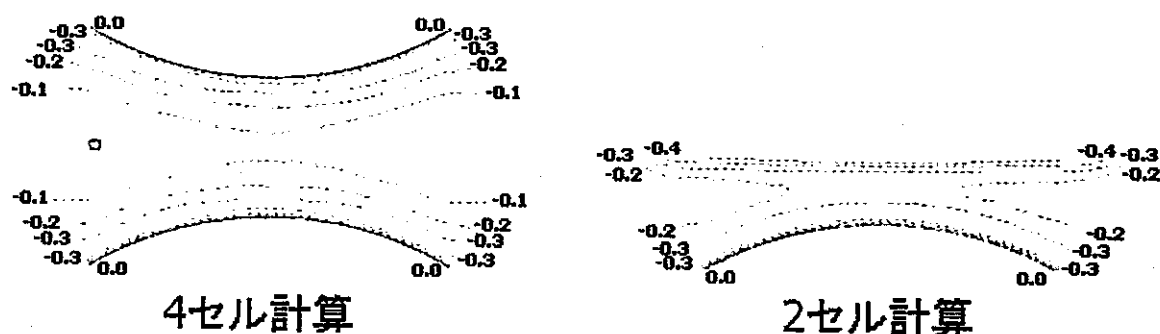
図4-14   Reynolds normal stress 分布 $(\overline{v'^2}-\overline{u'^2})$

　以上より、4セル計算では、x軸に接する対称面を境に分岐した周方向周期境界を適用しなければならず、そのことが起因して、過去に得られた知見とは異なる二次流れ分布が得られ、また二次流れ強度が弱まったと考えられる。2セル計算では、x軸に接する対称面に鏡面境界を適用したにも関わらず、壁面せん断応力分布、2次流れ分布において、少なくとも4セル計算よりも良好な結果を得ることができた。しかし、鏡面境界面近傍における軸方向流速分布及びReynolds normal stress分布は、妥当な分布とは言えない。

　今後、三角配列燃料集合体内サブチャンネルにおける乱流場に対してより精度の良い擬似直接数値計算を実施する為には、今回実施した計算の体系よりも更に多くの最小単位セルで構成される計算領域を確保することにより、対称境界条件を用いず且つ4セル計算で適用した周方向周期境界を用いる必要のない計算体系を適用する必要がある。その為には、並列計算を含めたシミュレーション計算の高速化が急務である。

４．３　汎用解析コードによる乱流解析

　４．２節で報告した直接乱流シミュレーションによるシングルブロック計算を、汎用流体解析コード STAR-CD による計算結果と比較して、評価を行った。Appendix C に STAR-CD の概要、組み込まれている乱流モデル、離散化手法の説明について示す。以下評価の概要を示す。

　三角配列無限大本数燃料集合体内における十分発達した乱流に対し、標準的な k-ε モデル，線型および非線形 k-ε モデル（Quadratic model と Cubic model）について、計算メッシュ数（非線形モデルの場合 10,000～160,000）、Re 数、P/D をパラメーターとして計算を行った。なお、非線形モデルとは、応力とひずみの間に非線形の関係を仮定して乱流の非等方性を考慮するもので、通常の k-ε モデルでは予測できない二次流れを計算することができる。なお、Appendix D、Appendix E において STAR-CD 乱流モデルの評価の詳細を述べる。

４．３．１　流速および温度分布

　計算で得られた三角配列（P/D=1.17）集合体内流速分布をピン壁表面からの距離に対してプロットして実験値と比較すると、線型モデルで 8~9%の誤差、非線形モデルで 2~3%の誤差で流速プロファイルが予測されていることがわかる（Appendix D : Figs. 11-13 ; Appendix E : Figs: 12-14）。壁せん断応力分布の比較は Appendix E の Figs. 8-10 に示すが、これらの図は前節４．２．３の図４－１３に示す直接乱流シミュレーションの結果と略同じ傾向の分布を示している。ただし、直接乱流シミュレーションは図４－１３に見られるようにφ＝３０°の近傍で応力が減少している傾向を捕捉しているのに比べ、STAR-CD では単調にφ＝３０°まで増加している。いずれの計算結果がより正しいか否かはここでは未だ十分な判定材料がない。、また、実験データが存在しないため直接の比較はできないが、非線形モデルにより、乱流の非等方性と二次流れはある程度模擬が可能であることが確認された。なお、STAR-CD によるこれらの傾向の計算メッシュ数に対する依存性は比較的小さいことが判明した。

　Appendix F に、P/D=1.05, 1.1, 1.15 の３種類の無限大本数三角配列格子の最小対称ユニット内の Re~40,000 の乱流に対し、流速分布および集合体出入り口温度差が一定になるような一様熱流束分布を与えた場合の温度分布を STAR-CD コードで計算した結果を示す。乱流モデルは低レイノルズ数 k-ω モデルを採用した。P/D が大きいほど狭隘部での壁近傍流速勾配が急峻で管内流れに近い形状を示すが、P/D が 1.05 に対しては局所的に低レイノルズ数流れに近くなる傾向が確かめられた。温度分布についても P/D が小さくなるほどギャップ狭隘部での温度上昇が顕著で、流速分布の影響が明らかである。ただしこれらの計算結果は実験と比較

するためのものではなく、分布の定性的傾向を見るためであり、詳細な検討は今後の課題である。

　Appendix G にドイツ FZK で実施された矩形ダクト内に一列に組み込まれた４本ロッド発熱試験結果（TEGENA）に対する STAR－CD によるロッド表面近傍の流体温度分布計算結果を示す（Figs. 8-11）。いずれの図も非線形 k-ε モデルによる予測が線形 k-ε モデルによるものよりも良い一致を示すことが確かめられた。

４．３．２　摩擦圧損係数比較

　積分パラメーターである摩擦圧損係数について、直接乱流シミュレーションと STAR-CD で求めたものを比較した。ただし、直接乱流シミュレーションの計算結果は P/D=1.2 のみで、かつ二次流れ分布が未だに静定していないことから、必ずしも定量的な比較が不可能である。
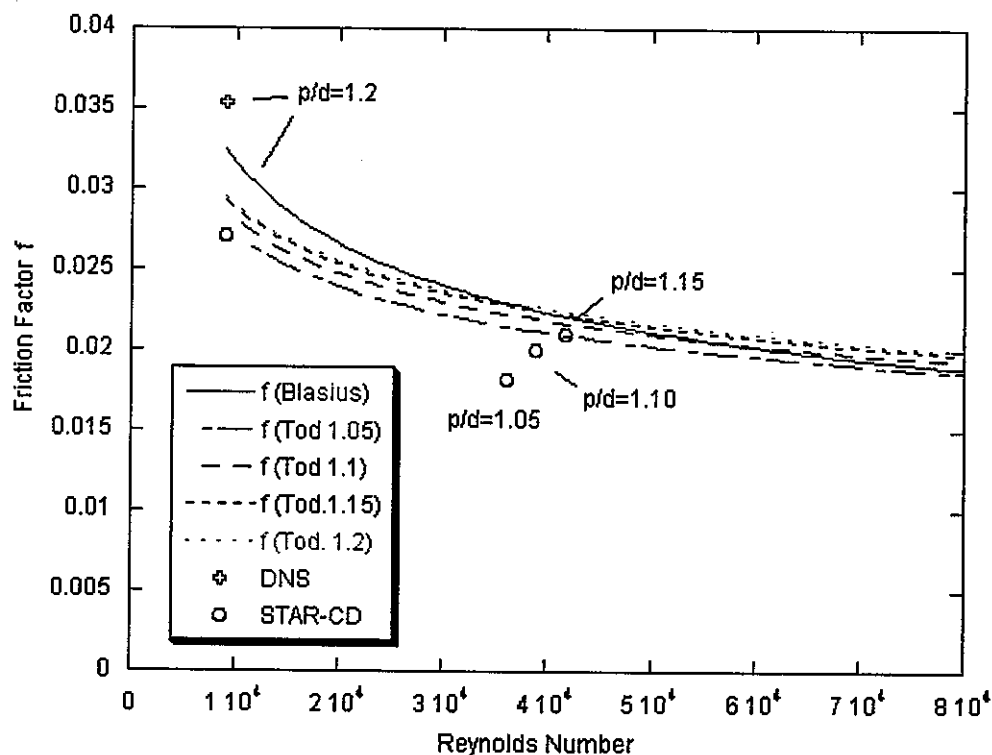
図 4-15　摩擦圧損係数の比較

　図４－１５に、円管内乱流に対する摩擦圧損係数 Blasius 式、P/D（1.05, 1.1, 1.15, 1.2）を考慮した Chen-Todreas によるバンドル圧損係数モデルを、Re 数を横軸に示す。STAR-CD で得られた流速分布と壁せん断応力をもとに求められた摩擦圧損係数の値は Chen-Todreas 式で

与えれるものよりは低めにプロットされているが相関式で与えられる傾向を捉えている。一方、直接乱流シミュレーションによる摩擦圧損係数は P/D＝1.2 に対し、過大に評価しているのが現状である。このことは、直接乱流シミュレーションによる計算が比較的粗大メッシュで行われていることが大きな要因と考えられる。また、未だ十分に発達した乱流に至っていない可能性があることも挙げられる。これらのことを勘案して、摩擦圧損および熱伝達係数ともに、今後とも計算を継続してより定量的な評価を実施していく予定である。

4.4　革新型燃料形状の検討

　本節では、通常の円柱型燃料稠密配列における狭隘部ホットスポットを回避を目的として、非円柱形状の燃料による熱流動特性評価を述べる。ただし評価は COOLFD による2次元解析による。非円柱形状の選択の基準は、被覆管温度分布が平坦となること、燃料中心温度が低く抑えられること、サブチャネル内の流速分布および温度分布が一様であること、摩擦圧損増加を極力抑えることなどが挙げられる。これらの要求条件を可能な限り満足させるための形状を求めるために、出力密度、流量、入り口サブクーリングなどの原子炉運転条件に対応して、冷却材体積比率、ポンピングパワー、被覆管周方向温度分布、燃料ピン中心最高温度、沸騰温度までの余裕などそれぞれの評価項目関数を定義し、これらの相乗積としての評価関数を定義した（Figure of Merit）。その結果、評価関数を最小化する形状は、6角柱形状のロッドであり、また構造上応力集中を防ぐ上で考案されたのが Multi-Lobe 型ロッドである。

(a) 円柱型燃料ロッド　　　　　　　　　　(b) Multi-Lobe 型ロッド
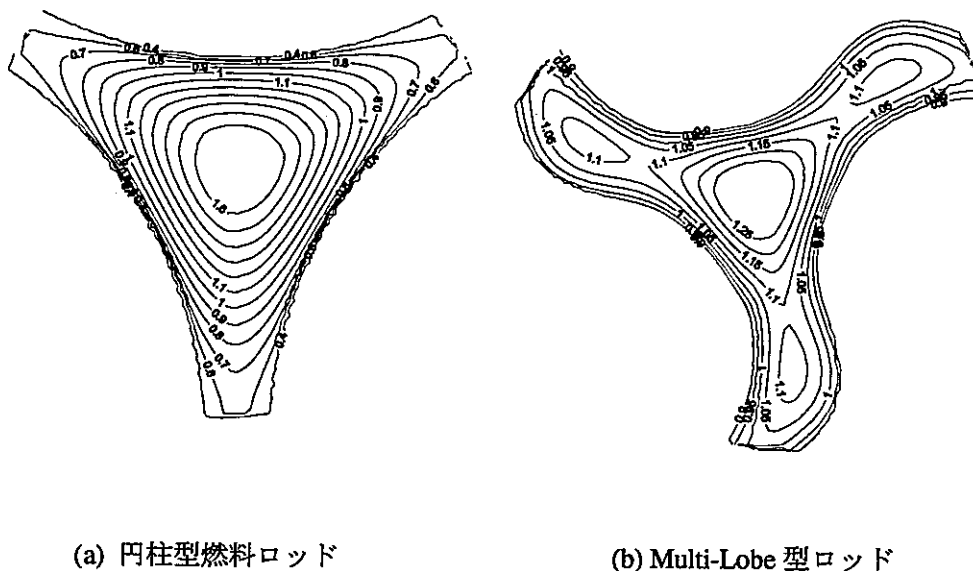
図4－16　サブチャネル内流速分布　（Re=90,000）

　図4－16に標準的な P/D=1.1 の円柱型燃料ロッドと対応する Multi-Lobe 型ロッドの三角配列に対する流速分布、表4－1に平均熱流束、ロッド表面温度とバルク流体温度差の最大値、被覆管表面温度の最高値の計算結果を示す。同じ熱伝達量に対し、Multi-Lobe 型ロッドの被覆管表面温度の最高値（Hot Spot）が水冷却の場合約20℃低下していることが認められる。なおここでは高転換型軽水炉を念頭に、冷却材は水を想定した。ナトリウム冷却の場合は、フィルムドロップの低下およびサブチャネル内冷却材温度分布がより平坦になるが、

ここで示した計算結果と同様な傾向が得られることはいうまでもない。一方、等価直径の減少に伴う圧力損失の増加は約 13%である。

表4－1　P/D=1.1 円柱型燃料ロッドと対応する Multi-Lobe 型ロッドの比較

	Regular Array	Multi-Lobe Array
Flow Area Fraction	25%	25%
P/D (P/Lmax)	1.1	--
Power, [W/rod]	12250	
Mean Heat Flux [W/m^2]	328400	297770 (-9%)
Center:rod　<tw> - <tf> = Δt °C	13	7
Center rod: tmax , Δt (wall) °C	33	11

本節では 2 次元計算のみ紹介したが、今度 STAR-CD による詳細計算と並行して、直接乱流シミュレーションによるより信頼性の高い計算を実施していく予定である。

5．おわりに

　本報告書は、燃料集合体サブチャネル内の詳細流速、温度分布を評価するために直接乱流シミュレーション手法の適用と実用化の試みを行ったものである。直接乱流シミュレーションは、矩形ダクトや円管形状のような簡単な流路形状に対して適用され、乱流現象の解析に適用された例は多く、その計算結果の信頼性は高いことが知られている。しかしながら、燃料集合体のように複雑形状流路内乱流に適用された例はなく、また一般的に工学的な応用を意識した公開コードが存在しないために、デカルト座標系における直接乱流シミュレーションコードの開発から実施する必要があり、開発に多くの困難が予想された。本研究期間においては、曲線座標上の乱流直接数値シミュレーションを可能とし、無限大本数ロッドバンドル内の対称性を考慮した最小計算セルを４つ組み合わせた計算体系及び２つ組み合わせた計算体系内の乱流計算を行ったことが多大な成果として挙げられる。また、集合体内の乱流非等方性の影響は予想以上に大きく、第二種二次流れの正確な予測の重要性が再確認された。

　以下に本研究期間に実施した開発を通して得られた課題を述べる。

　４・２節で示された無限大燃料ピン束体系のシングルブロック計算では、限られた計算領域内における計算であり、必ずしも十分な計算領域を確保した計算ではない。そのため、シングルブロック計算で対象とした計算領域よりも大きいサイズの渦が流速分布等の形成に影響を与えていることは否定できない。また、燃料ピン中心に対する周回方向の境界条件は、必ずしも適切な条件とは言えない。これらの課題を解決する為には、図５－１に示す六角形の計算領域にて計算を実行することが必要である。この体系であれば、シングルブロック計算で適用した計算領域の12倍の大きさで計算を行うことができる。また、六角形の向かい合う境界面同士を周期境界に設定すれば、流速の回転変換を伴うような適切とはいえない境界条件を設定する必要もない。

　図５－１の計算体系で高い信頼性のある直接数値シミュレーションを実行するために、今後クリアすべき課題を以下に示す。
1.　計算体系のマルチブロック化
　　構造格子で構成される計算空間で、図５－１について格子体系を形成するのは困難である。構成する24個の正三角形のブロックについて構造格子を用いた格子体系を形成し、最終的にブロック間を結合させる、いわゆる計算領域のマルチブロック化を適用した方が、計算格子の歪みを最小限に抑え、かつ任意な計算体系を形成することができる。その為に、計算領域のマルチブロック化が必要である。

2. 並列計算の適用

　図5－1の体系を適用した計算は、莫大な計算コストを必要とする。このことは、3・2・2節にて示された圧力ポアッソン方程式行列解法の高速化だけでは不十分であることを示している。この問題を解決できる有力な手段として、莫大な計算コストを複数のCPUに分散させる並列計算の適用が挙げられる。これまで行ってきた計算は全て単CPUによるものであり、更なる大規模計算を行うためには、計算コードを並列計算に対応させることは不可欠である。
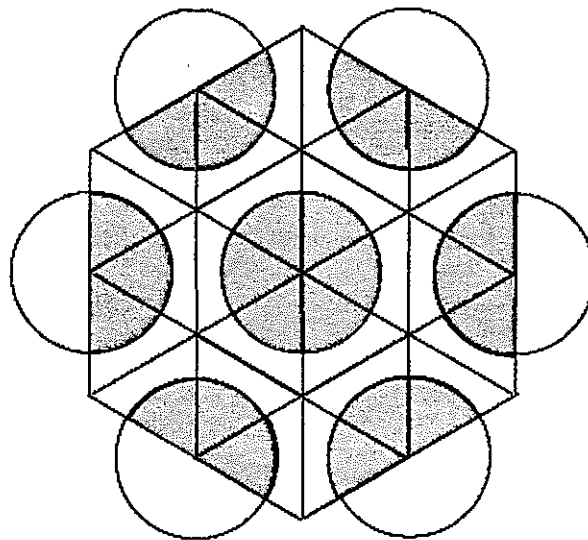
図5－1　マルチブロック体系

3. 差分手法の高次精度化

　本稿で示された直接数値シミュレーションは、基本的に2次精度中心差分スキームを用いた計算であった。十分な空間解像度、すなわち計算格子点数を確保すれば、二次精度中心差分スキームを用いた計算でも高い精度の計算結果が得られることは既に示された。また、直接乱流シミュレーションの本質は、微細格子を採用することにより、空間分解能を可能な限り高めることにある。そのため、本研究の微細メッシュと二次精度差分法の組み合わせは方向性として正しい。しかしながら、より大きな計算領域、より高い Reynolds 数における計算で、高い精度の計算結果を得る為に、莫大な数の計算格子点を確保には限界がある。与えられた計算資源の制約の中で数値シミュレーションを可能とするためには、2 次精度差分よりも高次精度の差分スキームを適用し、2 次精度差分スキームの計算で用いた格子よりも粗い格子サイズで、2 次精度差分スキームと同じ精度の結果を得ることができれば、結果的に

計算コストの節約に繋げることができるのは理屈である。しかしながら、格子サイズがコル
モゴロフスケールから大きく逸脱することで微細な渦生成・消滅の機構や乱流の詳細構造を
喪失してしまうため、擬似直接乱流シミュレーションにおける格子サイズは乱流現象に与え
る悪影響を最小限に抑える限界を押さえた上で、その範囲内で計算を実施する必要がある。

　最終的には、直接乱流シミュレーション手法を図4－2に示すような実験体系に適用し、
高燃焼度燃料の湾曲や変位を確実に計算してホットスポット評価を行うことである。しかし
ながら、地球シミュレータで供給される計算機資源をもってしても、有限本数集合体全体を
計算することは不可能で、当面は変位ロッド近傍のサブチャネルからなる無限大本数集合体
を仮定して、その対称セルについて直接乱流シミュレーションを行うことになる。

本研究期間に発表した国際会議論文、ジャーナル論文のリストを以下に示す。また、文献 10、
7、11、6 については巻末に Appendices D, E, G, H に添付する。

1． Misawa, T., Maekawa, I., and Ninokata, H., "Basic Study on the Detail Turbulent Analysis in a Square Duct", 2001 Fall Meeting of the Atomic Energy Society of Japan, Sapporo, Japan, September 19-21, 2001

2． Misawa, T., Maekawa, I., and Ninokata, H., "Calculation of Heat Transfer Coefficients on a Flat Plate by Pseudo Direct Numerical Simulation of Turbulence ", 2002 Fall Meeting of the Atomic Energy Society of Japan, Iwaki, Japan, September 14-16, 2002

3． Misawa, T., Maekawa, I., and Ninokata, H., "Calculation of Heat Transfer Coefficients on a Flat Plate by Pseudo Direct Numerical Simulation of Turbulence" , Third Korea-Japan Symposium on Nuclear Thermal Hydraulics and Safety, Kyeongju, Korea, October 13-16, 2002

4． E. Baglietto, H. Ninokata, "Study of Steam Generator Overheating Tube Failure in FBR Reactors" Third Korea-Japan Symposium on Nuclear Thermal Hydraulics and Safety, Kyeongju, Korea, October 13-16, 2002

5． Misawa, T., Maekawa, I., Akamatsu, M., and Ninokata, H., "Application of Pseudo Direct Numerical Simulation to Subchannel Analysis(1), Verification of Adaptability of Boundary Fit Coordinate Scheme", 2003 Spring Meeting of the Atomic Energy Society of Japan, Sasebo, Japan, March 27-29, 2003

6． Misawa, T., Maekawa, I., and Ninokata, H., "Calculation of Heat Transfer Coefficients on a Flat Plate by Pseudo Direct Numerical Simulation of Turbulence". (submitted to JNST).

7． E. Baglietto, H. Ninokata, "Selection of an Appropriate Turbulence Model to Evaluate Performances of Novel Fuel Geometries for the "IRIS" Reactor". 4th ASME/JSME Joint Fluids Engineering Conference, Honolulu, Hawaii, 2003

8． Misawa, T., Maekawa, I., and Ninokata, H., "Calculation of Detailed Velocity and Temperature Distributions in a High-Burnup Fuel Subassembly using Pseudo Direct Numerical Simulation", 2003 Mechanical Engineering Congress, Tokushima, Japan, August 5-8, 2003

9． E. Baglietto, H. Ninokata, "Selection of an Appropriate Turbulence Modeling in a CFD code for an Ultra-long Life Core for the "IRIS" Reactor", GENES4/ANP2003, Kyoto, JAPAN, 2003

1 0. Misawa, T., Maekawa, I., and Ninokata, H., "Calculation of Detailed Velocity and Temperature Distributions in a High-Burnup Fuel Subassembly using Pseudo Direct Numerical Simulation", NURETH-10, Seoul, Korea, 2003.

1 1. E. Baglietto, H. Ninokata, "Turbulence Models Evaluation For Heat Transfer Simulation In Tight Lattice Fuel Bundles", NURETH-10, Seoul, Korea, 2003

参考文献

[1] Trupp, A.C., and Azad, R.S., (1975). "The Structure of Turbulent Flow in Triangular Array Rod Bundles", Nucl.Engng.Des., 32, 47-84

[2] Kriventsev, V. and Ninokata, H., J.Nucl.and Tech., Vol.37, No.8, p.646, 2000

[3] Gavrilakis, S., (1992), "Numerical Simulation of Low-Reynolds-Number Turbulent Flow through a Straight Square Duct", J.Fluid.Mech., 244, p.101-129

[4] "乱流の数値シミュレーション",梶島岳夫著,,養賢堂,99 年 8 月初版発行

[5] Ghia, U., Ghia, K.N., and Shin, C.T., (1982),"High-Re Solutions for Incompressible Flow Using the Navier-Stokes Equations and a Multigrid Method", Journal of Computational Physics 48, 387-411

[6] Kim, J., Moin, P. & Moser, R., (1987), "Turbulence statistics in fully developed channel flow at low Reynolds number", J.Fluid Mech., 177, 133

[7] Suzuki, T. and Kawamura, N.,. (1994). "Consistency of Finite-Difference Scheme in Direct Numerical Simulation of Turbulence", Trans. JSME, 60,578, (in Japanese)

[8] Kawamura, H., Ohsaka, K., Abe, H., Yamamoto, K., (1998), "DNS of turbulent heat transfer in channel flow with low to medium-high Prandtl number", Int.J.Heat. Fluid. Flow, 19, pp. 482-491

[9] Dittus, F. W.,and Boelter, L. M. K., (1947), "Transfer in Automobile Radiators of the Turbulent Type", Univ. of California Publications in Engineering

[10] Seban, R. A., (1950), "Heat Transfer to a Fluid Flowing Turbulently between Parallel Walls with Asymmetric Wall Temperatures", Trans. ASME, vol.72, pp.789

[11] Kader, B. A,, (1981), "Temperature and concentration profiles in fully turbulent boundary layers", Int.J.Heat. Mass. Transfer., vol.24, No.9, pp.1541-1544

[12] Heina, J., Chervenka, J., Mantlik, F., (1977), "Result of Local Measurements of Hydraulic Characteristic in Deformed Pin Bundle", UJV4156-T, part.1, Rzez, Czech Republic

[13] Ushakov, P.A., Zhukov, A.V., et al, Mantlic, F., Heina, J., et al, (1978), "Investigation of Thermodynamics in Regular and Deformed Bundle of Pins", CEMR, Moscow (in Russian).

[14]   Zang, Y., Street, R.L., and Koseff, J.R., (1994). "A Non-staggered Grid, Fractional Step Method for Time-Dependent Incompressible Navier-Stokes Equation in Curvilinear Coordinates", J. Comput. Phys., 114   18-33.

Appendix A

集中定数系コードが解く方程式系の導出

代表的なサブチャネル解析における保存方程式の例として、エネルギー保存式の導出について述べる。次式は、エネルギー保存式の積分表示である。（各項の意味については表1参照）

$$A_{fi}\frac{\partial}{\partial t}[<\rho h>_i]+\frac{\delta}{\delta z}[\dot{m}_i h_i]=<q_i^{'''}>_{rb}-\sum_{j=1}^{J}W_{ij}^{*H}[h_i-h_j]-\sum_{j=1}^{J}W_{ij}\{h^*\}+A_{fi}\left\langle\frac{Dp_i}{Dt}\right\rangle \tag{1}$$

表1

記　号	説　　明
〈　〉	体積積分平均
δ	差分オペレータ
D/Dt	物質微分オペレータ (substantial differential operator)
A_{fi}	サブチャネル i の流路断面積
・	流体密度
h	流体エンタルピー
$\dot{m}_i$	軸方向質量流束
$<q_i^{'''}>_{rb}$	燃料要素からの熱伝達量
W_{ij}^{*H}	サブチャネル i-j 間のエネルギー乱流混合係数（粘性拡散を含む）
W_{ij}	単位体積あたりクロスフロー質量流量 (= ・$u_{ij}s_{ij}$) [Note: u_{ij}=サブチャネル間ギャップにおける横方向流速（クロスフロー流速）; s_{ij} = ギャップ幅] いわゆる diversion crossflow と呼ぶ。
h^*	サブチャネル (i) に流入または (i) から流出するエンタルピー
p	圧力
t	時間
Δz	軸方向コントロールボリューム高さ（軸方向メッシュサイズ）

（1）式を導き出すにあたって軸方向の熱の拡散や粘性効果による熱の散逸などを無視してある。以下に各項の意味を簡単に示す。

　　　　左辺第一項：サブチャネル内エンタルピの時間変化

　　　　　第二項：z方向対流によるエンタルピの出入り

　　　右辺第一項：燃料要素から入る熱量

　　　　　第二項：サブチャネル (i) – (j) 間のエンタルピ乱流混合量

　　　　　第三項：横方向対流によるエンタルピの出入り

　　　　　第四項：圧力による仕事

（1）式の導出にあたっては、以下の手順が踏まれている。すなわち、φを輸送される物理量とすると、瞬時局所の輸送方程式は偏微分方程式として（2）式のように表される：

$$\frac{\partial}{\partial t}\rho\phi + \nabla \cdot \rho\vec{u}\phi = -\nabla \cdot \vec{J} + \rho S(\phi) \tag{2}$$

（2）式は着目する CV DV 上で体積積分され、

$$\frac{1}{\Delta V_f}\int_{\Delta V_f}dV\frac{\partial}{\partial t}\rho\phi + \frac{1}{\Delta V_f}\int_{\Delta V_f}dV\nabla \cdot \rho\vec{u}\phi = -\frac{1}{\Delta V_f}\int_{\Delta V_f}dV\nabla \cdot \vec{J} + \frac{1}{\Delta V_f}\int_{\Delta V_f}dV\rho S(\phi) \tag{3}$$

となるが、（3）式は、さらに

$$\frac{\partial}{\partial t}<\rho\phi> + \frac{1}{\Delta V_f}\int_{A_{ff}}\rho\phi\vec{u}\cdot\vec{n}dA = -\frac{1}{\Delta V_f}\int_{A_{ff}}\vec{J}\cdot\vec{n}dA - \frac{1}{\Delta V_f}\int_{A_{fs}}\vec{J}\cdot\vec{n}dA + <\rho S> \tag{4}$$

ただし、以下の定義を用いてある：

$$<\Psi> \equiv \frac{1}{\Delta V_f}\int_{\Delta V_f}\Psi dV \tag{5}$$

$$\left\langle\frac{\partial\rho\phi}{\partial t}\right\rangle = \frac{\partial}{\partial t}<\rho\phi> \tag{6}$$

$$<\nabla\cdot\Psi> = \frac{1}{\Delta V_f}\int_A \Psi\cdot\vec{n}dA \tag{7}$$

$$A = A_{ff} + A_{fs} \tag{8}$$

$$<\nabla\cdot\rho\phi\vec{u}> = \frac{1}{\Delta V_f}\int_{A_{ff}}\rho\phi\vec{u}\cdot\vec{n}dA \tag{9}$$

ϕ、$\vec{u}$ については、各々の面 Aff 上での平均 ϕ_{av}、$\vec{u}_{av}$ と平均からの"ずれ" ϕ'、$\vec{u}'$ の和である。

$$\phi = \phi_{av} + \phi' \tag{10}$$

$$\vec{u} = \vec{u}_{av} + \vec{u}' \tag{11}$$

従って、

$$\rho\phi\vec{u} = \rho(\phi_{av}\vec{u}_{av} + \phi_{av}\vec{u}' + \phi'\vec{u}_{av} + \phi'\vec{u}') \tag{12}$$

$$\int_{A_{ff}}\phi_{av}\vec{u}'\cdot\vec{n}dA = \int_{A_{ff}}\phi'\vec{u}_{av}\cdot\vec{n}dA = 0 \tag{13}$$

であるから、（9）式対流項のみに限って示せば、実際には平均からの"ずれ" ϕ'、$\vec{u}'$ のクロスタームの存在が指摘される：

$$< \nabla \cdot \rho \, \phi \bar{u} > = \frac{\rho}{\Delta V_f} \int_{A_{ff}} \phi_{av} \bar{u}_{av} \cdot \bar{n} dA + \frac{\rho}{\Delta V_f} \int_{A_{ff}} \phi' \bar{u}' \cdot \bar{n} dA \tag{14}$$

（１４）式右辺第 2 項は通常サブチャネル解析では省略されており、サブチャネル内の物理量が分布を持つときは、本項は無視できない場合がある。とくに（4）式右辺第 1 項、第 2 項の拡散項においては重要で、その例としては、サブチャネル境界における運動量、エネルギーの乱流混合、および壁と流体との交換としての摩擦圧損、熱伝達が挙げられる。とくに摩擦圧損の正確な評価には、壁近傍の極めて正確な流束分布を与える必要があり、とくに壁の影響を強く受ける稠密燃料配列の場合は第 2 種 2 次流れの正確な予測が前提となる。

限界の認識

サブチャネル解析手法そのものは、1960 年代頃から開発されてきており、燃料集合体多次元解析として最善の手法として確立されている。一方、下記のようなモデル上の制約があることを念頭におくべきである。

1) サブチャネル内に分布する物理量は平均化され一様分布

2) 局所的な現象は平均化の操作の過程で消失

3) 局所的な現象はこれらの平均量の関数として代数的な関係式（構成方程式）

4) 分解能は、サブチャネルのサイズ

5) より詳細なサブチャネル内の物理量分布を求めたい場合は、分布定数系解析

6) サブチャネル間の物理量の交換

7) クロスフローは、ギャップから遠去かるにつれて、そのベクトルの向きが曖昧

8) 　　　　　　の制約は、上記の如く大きな問題を呈することはないが、クロスフローが比較的重要になる箇所、とくにスペーサ近傍では、横方向運動量の完全な対流輸送を考慮する必要がある。

Appendix B

Calculation of Detailed Velocity and Temperature Distributions in a Rod Bundle of Nuclear Reactor

Ninth International Topical Meeting on Nuclear Reactor Thermal Hydraulics
(NURETH-9)
San Francisco, California, October 3 - 8, 1999

CALCULATION OF DETAILED VELOCITY AND TEMPERATURE DISTRIBUTIONS IN A ROD BUNDLE OF NUCLEAR REACTOR

Vladimir Kriventsev and Hisashi Ninokata
Research Laboratory for Nuclear Reactors
Tokyo Institute of Technology
2-12-1 O-okayama, Meguro-ku, Tokyo 152-8550, JAPAN
kriventsev@writeme.com   hninokat@nr.titech.ac.jp

KEY WORDS

Computational Fluid Dynamics (CFD); Finite-Difference Method (FDM); Anisotropy of Turbulence; Rod Bundle

ABSTRACT

This paper presents several results of numerical simulation of fluid flow and heat transfer in hexagonal rod bundles including those with disturbed structure. The experimental data were available for local velocity and wall shear stress distributions from experiments of Heina and Mantlik (1977) at NRI, Czech Republic. Second, we describe a result for a series of the sodium experiments carried out at the IPPE, Russia (Ushakov, 1978) that provide detailed data on the wall temperature profiles. Both experiments provide complete sets of data for comparison with the results of numerical simulation.

Here the Reynolds and energy conservation equations have been discretized by the Efficient Finite Difference (EFD) scheme. These equations are solved for steady-state fully developed turbulent incompressible flow in two-dimensional orthogonal coordinate system. Regarding the averaged energy conservation equation, the use of anisotropic turbulent conductivity coefficients based on the axial velocity distribution has been made.

Comparison of calculated results and experimental data is presented for distributions of the local shear stress, axial velocity and the wall temperature in the "geometrically disturbed" region around dislocated rod. Overall, the results of numerical calculation show satisfactory agreement with experimental data for both flow and temperature distributions.

1.   INTRODUCTION

In rod bundle thermal hydraulics analysis in nuclear fuel rod subassemblies, two approaches are common:

  i)   lumped parameter analysis (LPA) approach represented by subchannel analysis and

  ii)   distributed parameter analysis (DPA) approach.

The subchannel analysis method is well established, and current emphasis is placed on modeling for the constitutive relationships, which are a result of the integration

process of a set of local instantaneous flow conservation equations over subchannel control volumes. In order to support the subchannel model development, it is necessary to have local information on fluid flow and heat transfer in a rod bundle. In this regard, a new DPA code development is an on-going effort based on a new Efficient Finite Difference (EFD) scheme for single-phase convection-diffusion equations in a rod bundle and on the Object-Oriented Programming (OOP) technique.

The EFD scheme is further development of "locally exact in one-dimension" analytical methods. It gives much more accurate numerical solution than other popular methods even using a mesh system with fewer grid points. This fact is important in view of calculation of three-dimensional velocity and temperature distributions of the coolant in a rod bundle that requires far more computing power than that most advanced current super computers available to date can provide.

A rod bundle geometry is modeled using components of the Computational Object-Oriented Library for Fluid Dynamics (COOLFD) which is a new-generation programming tool being aimed at improving the development of the CFD application for complex calculation areas such as a rod bundle of a nuclear reactor.

2. PROBLEM OF METHOD AND ALGORITHM VERIFICATION

It is extremely important in numerical analysis that computational methods and algorithms, as well as the computer code itself are verified not only on an "abstract" idealized problems like flows in straight tube, plane and square channels, etc. but on real problems investigated by accurate and careful experimental measurements. As for turbulent flow and heat transfer in a rod bundle of a nuclear reactor, such experimental data were collected in co-operative research of Czech and Soviet institutions sponsored by the former Council for Mutual Economic Aid (COMECON).

2.1 Experimental Data Available For Comparison

First, a series of velocity and wall shear stresses measurements were performed by Mantlik, Heina, et al. (1977) at NRI, Czech Republic. Hexagonal rod bundles of fast reactor were investigated under "nominal" and "deformed" geometry as rod bundles with geometrical "disturbances" such as single/multiply rods dislocations. These experiments were performed with air as working fluid.

Follow-up experiments on the heat transfer in the rod bundles with the same type of geometrical disturbance were performed at IPPE, USSR, by Ushakov, et al. (1978) and Zhukov, et al. (1985). Electrically heated fuel element imitators were assembled into the rod bundle fulfilled by sodium coolant. In different sets of experiments, some of rods were dislocated from the original positions for different distances including the case of the direct contact. Wall temperature distributions around some "interesting" pins were measured at the axial locations corresponding to the fully-developed flow and heat transfer.

The two sets of experiments above provide consistent database on velocity and temperature distributions to be compared with the data of numerical analysis. The generalized results of these experimental can be found in the recent IAEA surveying report (Bogoslovskay, 1999) in English.

Moreover, experimental data above on velocity distribution (Heina, 1977) had been selected for benchmark exercises at 9th IAHR Working Group Meeting on Advanced Nuclear Reactors Thermal Hydraulics at CEA-Grenoble, April 7-9, 1998.

In this paper, the single type of the rod bundle geometry with only dislocated central rod has been chosen for numerical analysis. In addition to the axial velocity calculations as in the benchmark problem above, the temperature distributions have been calculated as well. Those have been compared with corresponding temperature fields available from the experiments on heat transfer at IPPE (Ushakov, 1978).

2.2 Experimental Rod Bundle With Geometrical Disturbance

In this section, the geometry of the experimental rod bundle is described. As was mentioned above, from the variety of hydraulic experiments (Heina, 1977) a rod bundle with dislocated central pin has been chosen for numerical analysis and comparison. The cross section of general layout is shown in Fig. 1. The central rod No 1 is displaced in direction of rod No 7 keeping the gap between them as small as *3.16* mm. It changes the pitch-to-diameter ratio to *1.026* while the average "nominal" value is *1.17* – which correspond to the regular fuel assembles of the BN-600 reactor. Pins were not wrapped with wire and no displacers were used in such a rod bundle. The total number of rods is 19, which makes it possible to neglect the influence of the peripheral effects. The air physical properties were measured as density $\rho = 1.31 \ kg/m^3$ and kinematic viscosity as $v = 1.591E\text{-}5 \ m^2/sec$. The main series of the experiments was performed for Reynolds number $Re = 151660$ (calculated for the flow subchannel between rods Nos. 1, 6 and 7.

The locations of the measured axial velocities are shown in Fig. 2. In addition, shear stress distributions along the wetted surfaces were measured for rods Nos. 1, 6 and 7 in the central zone.

Similar geometry was modeled in the heat transfer experiments of IPPE (Ushakov, 1978) with sodium as a coolant. Those experiments kept the same relative values of pitch-to-diameter ratio and the corresponding Reynolds number.

In numerical calculations of fluid flow and heat transfer, the rod bundle with the same geometry is used.
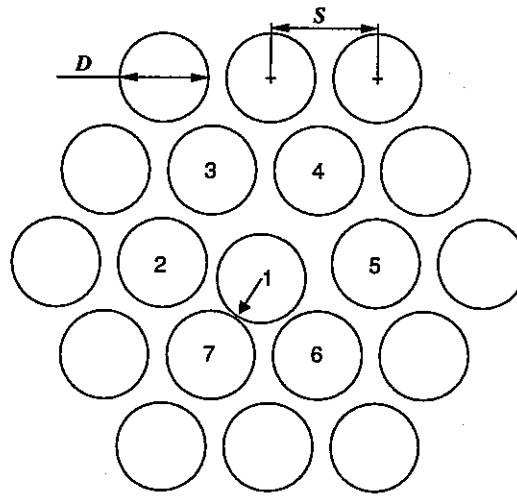
Fig. 1   Experimental rod bundle with "geometrical disturbance": the central rod is dislocated from the original position. Pin diameter $D = 120.0$ mm; pitch $S = 140.4$ mm
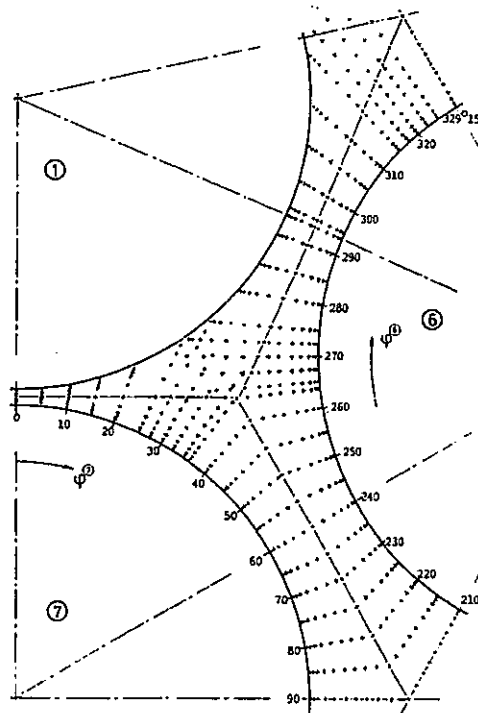
Fig. 2   Detailed location of points where axial velocity components were measured in the experiment (Heina, 1977)

3. PROBLEM DEFINITION AND NUMERICAL METHOD

3.1 Governing Equations

Reynolds equation for steady-state fully developed turbulent incompressible flow in two-dimensional orthogonal coordinate system can be written for axial velocity component as the following:

$$\frac{\partial}{\partial x_1}\left(\left(v+v_1^T\right)\frac{\partial W}{\partial x_1}\right) + \frac{\partial}{\partial x_2}\left(\left(v+v_2^T\right)\frac{\partial W}{\partial x_2}\right) = -\frac{1}{\rho}\frac{\partial P}{\partial z},\qquad(1)$$

where W is the axial velocity component; v is the kinematic viscosity; v_1^T and v_2^T are the components of anisotropic turbulent eddy viscosity used in Boussinesq model; ρ is the density; P is the pressure and x_1 and x_2 are the dimensions of an orthogonal coordinate system. Here, W is an unknown dependent variable. There are no other two (U and V) components of velocity vector in Eq. (1) following the assumption that no secondary flows exist.

Non-slipping boundary conditions are applied as zero velocities on the walls and zero shear stresses on the outer symmetry lines. Pressure drop $\dfrac{\partial P}{\partial z}$ in axial direction (which is supposed to be a constant in case of the fully developed flow) depends on wall shear stress distribution and, therefore, should satisfy a flow distribution with the mean velocity measured in the experiment. The latest is defined by the Reynolds number $Re = 185700$ (calculated with values, averaged over the whole rod bundle). Thus, some kind of iterative procedure is required. First, an initial estimation of pressure drop is given. Then, after calculation of velocity distribution and averaging its value over the calculation area, a new Reynolds number is calculated. Based on its difference from the latest value, a new pressure gradient is estimated. These outer iterations are repeated until the given accuracy is not reached.

After the velocity distribution is found with some accuracy, an equation for temperature can be solved. The following equation of energy conservation for steady-state fully developed incompressible flow in two-dimension is used:

$$\rho c_p W(x_1,x_2)\frac{\partial T}{\partial z} = \frac{\partial}{\partial x_1}\left(\left(\lambda+\varepsilon_1^T\right)\frac{\partial T}{\partial x_1}\right) + \frac{\partial}{\partial x_2}\left(\left(\lambda+\varepsilon_2^T\right)\frac{\partial T}{\partial x_2}\right),\qquad(2)$$

where T is the fluid temperature; λ is the thermal conductivity; ε_1^T and ε_2^T are the components of anisotropic turbulent eddy thermal conductivity those are defined using turbulent Peclet number as

$$Pe_T = v^T/\varepsilon^T \quad \text{and} \quad \varepsilon_i^T = \frac{v_i^T}{Pe_T}.\qquad(3)$$

As it was mentioned, no secondary flows are considered in this analysis. The reason is not only additional complexity of numerical simulation of full-components Navier-Stokes equations but also uncertainty of the definition of turbulent shear stresses. Formulas for the coefficients of turbulent viscosity and conductivity were derived to fit experimental velocity distributions. However, for the most data available it is not clear, whether Boussinesq turbulent eddy viscosity includes the effect of secondary flows or not. It should be noted here, that for those rod bundle flow experiments where the only axial velocity component is measured it is impossible (in principal) to calculate turbulent eddy viscosity components correctly.

3.2 Finite-Difference Discretization

A finite-difference method based on the "locally exact" scheme was applied in this work. Detailed description of the Efficient Finite-Difference (EFD) scheme was given by Kriventsev and Ninokata (1997). In this section, let us consider an application of the EFD discretization to the governing equations (1) and (2). The main idea of the EFD scheme is based on the use of the exact analytical solution of a simplified one-dimensional convection-diffusion equation for the area limited by two neighboring grid points. This exact solution makes it possible to estimate more accurately (in terms of finite-difference discretization) fluxes of the transported quantity on the interfaces of the control volume. Regarding to the problem considered here, these fluxes are shear stresses in case of the momentum equation (1) and heat fluxes for energy equation (2).

The simplified one-dimensional equation above can be written for every control volume in each direction. All remaining terms of the original convecton-diffusion equation including physical volume source terms like pressure gradient, transport terms from other directions and transient term are collected by an extra-source term. In doing so, with EFD, it is assumed that both the extra-source term and the diffusion coefficients (turbulent viscosity and conductivity in Eqs. (1) and (2) correspondingly) are distributed linearly within the neighboring grid points. For example, in x_1 direction, this simplified one-dimensional equation can be written as follows:

$$\frac{\partial}{\partial x_1}\left(\left(V_1\left(x_1^{i-1}, x_2^j\right) + \frac{V_1\left(x_1^i, x_2^j\right) - V_1\left(x_1^{i-1}, x_2^j\right)}{x_1^i - x_1^{i-1}}\left(x - x_1^{i-1}\right)\right)\frac{\partial W}{\partial x_1}\right) = \quad (4)$$

$$= S_1\left(x_1^i, x_2^j\right) - S_1\left(x_1^{i-1}, x_2^j\right)$$

where $\qquad V_1(x_1, x_2) = V + V_1^T(x_1, x_2),$

and $\qquad S_1(x_1, x_2) = -\frac{\partial}{\partial x_2}\left(\left(V + V_2^T(x_1, x_2)\right)\frac{\partial W}{\partial x_2}\right) - \frac{1}{\rho}\frac{\partial P}{\partial z}.$

Giving the values of the transported quantity at i and $i-1$ points as boundary conditions one can solve Eq. (4) analytically. Then, using this analytical solution, expressions for the shear stress and heat flux at the interface in between i and $i-1$ control volumes can be derived. Those expressions include the values of the transported

quantity at two neighboring grid points and being applied to the all sides of the control volume, result in the finite-difference approximation of governing equations in the given control volume.

For simplicity of presentation, let us consider slightly simplified case where the extra-source term is assumed to be a constant (instead of linear) in the area in between two corresponding grid nodes. In this case, implementing the EFD procedure above, the shear stress can be estimated by the following finite difference:

$$
\rho\tau = \left(v + v_1^T\right)\frac{\partial W}{\partial x_1} = \left(\frac{v_1^i - v_1^{i-1}}{\log\dfrac{v_1^i}{v_1^{i-1}}}\right)\frac{W_i - W_{i-1}}{x_1^i - x_1^{i-1}}
$$

$$
+ \left(x_1 - x_1^{i-1}\right)S_1\left(\frac{v_1^i + v_1^{i-1}}{2\left(v_1^i - v_1^{i-1}\right)} - \frac{1}{\log\dfrac{v_1^i}{v_1^{i-1}}}\right),
\tag{5}
$$

On the other side, the regular upwind scheme (in fact, the central-difference scheme in this particular case, because the convection term is zero without secondary flow) results in the following:

$$
\rho\tau = \frac{v_1^i + v_1^{i-1}}{2}\frac{W_i - W_{i-1}}{x_1^i - x_1^{i-1}}.
\tag{6}
$$

When expressions for shear stresses above are substituted to the original governing equation (1) integrated over the corresponding control volume as described, for example in (Patankar, 1980), the resulting finite-difference discretization can be written as follows:

$$
a_{ij}W_{i,j} + b_{ij}^+ W_{i+1,j} + b_{ij}^- W_{i-1,j} + c_{ij}^+ W_{i,j+1} + c_{ij}^- W_{i,j-1} + d_{ij} = 0,
\tag{7}
$$

which results in a system of linear equations with five-diagonal matrix of coefficients. Such a system can be resolved by a series of iterative matrix solvers available. In this work, even simple Gauss-Zaidel iterations converged very fast. In addition, line-by-line sweeping including as an internal part the Three-Diagonal Matrix Algorithm (TDMA) can be recommended to reduce CPU time.

The finite-difference discretization given by simplified EFD formula (5) differs from regular central-difference discretization (6) in corrected diffusion coefficient and an extra source term (the last in the right-hand side of Eq. (5)). The latest includes terms from other directions and, therefore, depends on the velocity distribution itself. Thereby, it must be adjusted demanding an additional iteration procedure. Nevertheless, as was shown in (Kriventsev, 1997) the accuracy of the discretization given by Eq. (5) is much higher than one of ordinary schemes even using meshing system with fewer grid nodes.

Thereby, additional computational efforts per node are well compensated by high accuracy and lower number of grid points to achieve that accuracy.

Expression (5) is used in this work for finite-difference discretization, as well as for the calculation of the shear stresses at the rod walls.

Discretization formula, similar to Eq. (5) can been easily derived for the energy conservation equation (2), as well as for calculations of heat fluxes on the pin wall.

The finite-difference method, briefly described here, can be applied to the governing equations written for any *orthogonal* coordinate system. The construction of such a system faces certain difficulties and has specific features to be discussed in the following section.

3.3 Meshing System

In a construction of the mesh system for rod bundle geometry with dislocated rods, an orthogonal coordinate transformation is used. This transformation is performed using the grid generation components of the Computational Object-Oriented Library (COOLFD) that was described in (Kriventsev, 1998). First, separate meshing systems are generated for every "typical" elementary rod including surroundings as shown in Fig. 3.

All these "elementary" mesh components are assembled together to fit the whole rod bundle area to be calculated. In doing so, other visual components of the COOLFD library are used. The sample is shown in Fig. 4.
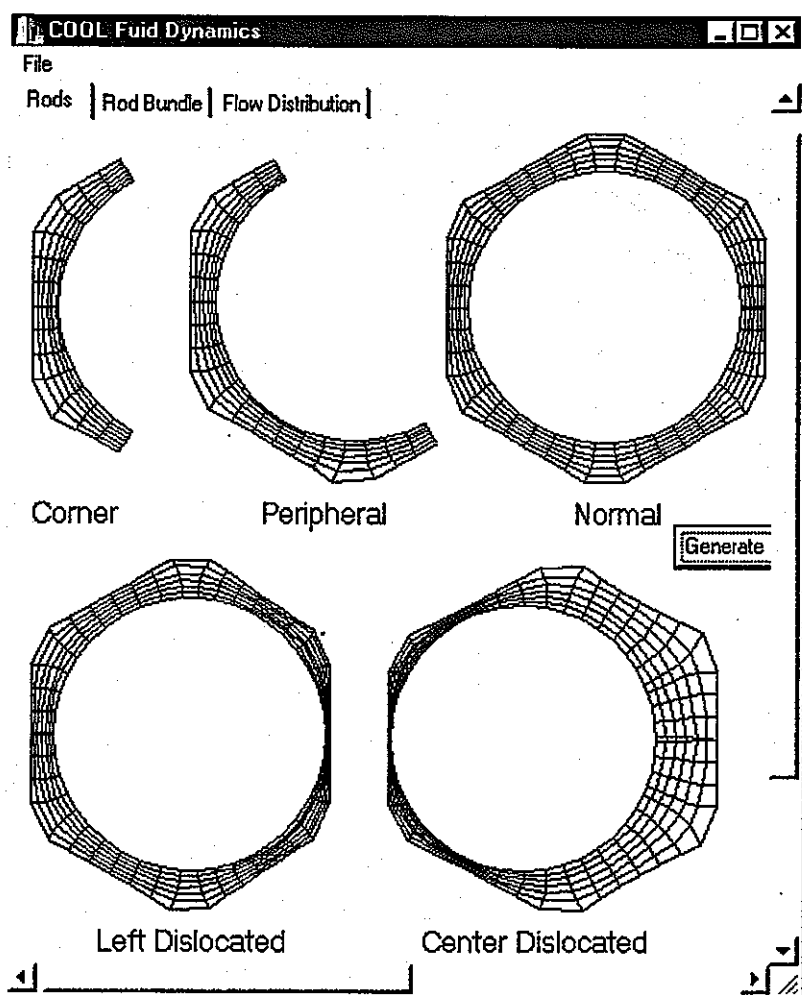
Fig. 3 Elementary grid components calculated for corner, peripheral, and central rods: regular, left-side neighbor of dislocated rod and central dislocated rod
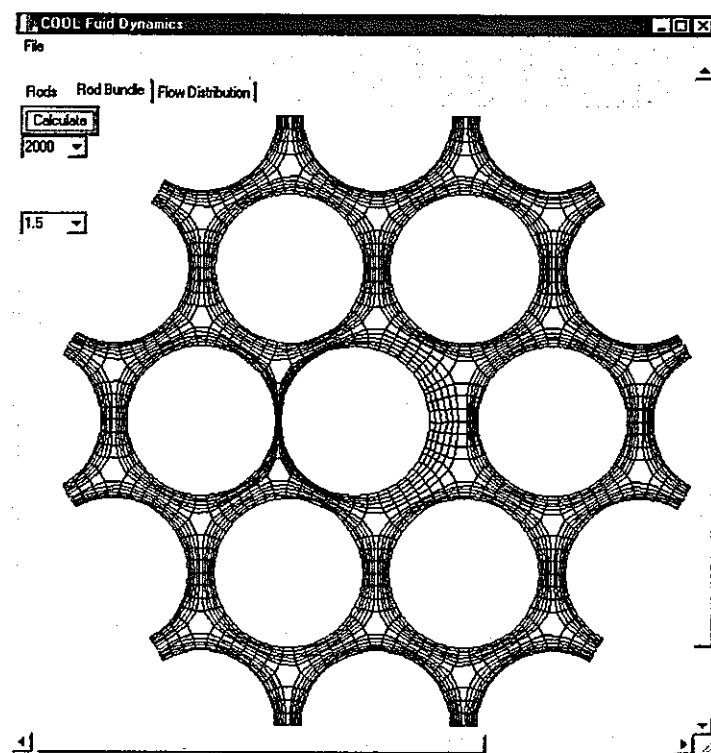
Fig. 4　　Elementary grid components assembled in the rod bundle

The orthogonal meshing system has great benefits as follows:

- Avoiding mixing derivatives in the governing equations those result in specific difficulties in the finite-difference discretization and reduce the numerical accuracy;

- The possibility to fit grid lines as close to the walls as necessary to describe this most important region with higher accuracy

However, orthogonal systems bring some disadvantages in computational aspects.

First, it takes additional computational efforts to construct such complicated systems. Laplace-type equations should be solved to calculate orthogonal grid lines. Nevertheless, the numerical solution is much simple in this case then solution of the main system of Navies-Stocks and energy equations. It is simple because of both the natural simplicity (relatively) of Laplace equation and the possibility to solve these equations for the elementary subdomains only but not for the whole calculation area. Then, these elementary subdomains can be assembled to fit the calculation region as shown in Fig. 3 and Fig. 4.

Second problem, as one can see in Fig. 4, some "hole" control volumes of hexagonal shape appear at the centers of subchannel. These control volumes seam to be too "big" relatively to the others. However, the fine resolution of mesh is not so necessary at subchannel centers close to the symmetry lines where derivatives are usually negligibly small. Furthermore, some evident improvements can be proposed to refine

these hexagonal control volumes. One of them is to consider these control volumes as additional elementary subdomains where its own internal mesh system can be generated. However, the application of this idea has not been implemented yet.

Despite the difficulties above, authors believe the benefits of the orthogonal meshing system outweigh these disadvantages significantly (in terms of CPU time and overall computational resources). The latest will be discussed in the following sections.

3.4 Eddy Diffusivity Coefficients

The coefficient of turbulent viscosity in radial direction is used from the data of Nijsing and Eifler (1971) as follows:

$$\frac{v_r}{u^* y^+} = \left[1 - \exp\left(-0.407\frac{y}{y^+}\right)\right]\exp\left(-e\frac{y}{y^+}\right),$$ (8)

where y is the distance to the wall,

$$e = \log\left[\frac{1 - \exp(-0.407)}{0.07}\right], \qquad y^+ = \frac{yu^*}{v},$$

and the friction velocity $\quad u^* = \sqrt{\tau_w/\rho}$

The expression of Neelen (1986) is used for eddy diffusivity in azimuthal direction:

$$\frac{v_r}{u^* y^+} = \exp\left(u_1 \exp\left[u_2\frac{y^+}{R} + u_3\right] + u_4\right)$$

$$\times \left[1 + A_r\left(B_r^2 - B_r + \frac{1}{3}\right) - A_r\left(B_r - \frac{y}{y^+}\right)^2\right],$$ (9)

where R is the distance from the wall to the maximum velocity line, and

$$u_1 = 0.118; \quad u_2 = -13.8;$$

$$u_3 = \left(\frac{2d_h}{d}\right)^{0.238} + 3.52;$$

$$u_4 = 0.215\left(\frac{2d_h}{d}\right) + 5.1\left(\frac{s}{d}\right)^{0.149} - 6.94;$$

$$A_r = 3.0; \quad B_r = 0.6$$

It should be noted, the relations above were obtained for radial and azimuthal directions in polar system that center coincides with one of the rod. Despite that, they are used here directly even in the case of the orthogonal system as v_1 and v_2 correspondingly. As one can see in Fig. 4, the grid lines of the orthogonal meshing system are practically coincide with polar coordinate system near the wall. However, for the region in the center

of subchannel, correct radial and azimuthal directions cannot be defined clear for any coordinate system. Again, it should be noted that areas around subchannel centers are not so important because of the symmetry (derivatives are negligibly small).

3.5 Numerical Procedure

The computational part of the COOLFD library is used to calculate numerical solution. At this stage, the simple Gauss-Zaidel method is used to predict the solution on each inner iteration loop. Dynamic velocities u^* were recalculated for all local wall points and then, all the values of turbulent eddy viscosity and thermal conductivity are recalculated for the entire region. An outer iteration loop was used to adjust the pressure gradient which should generate the flow distribution with mean velocity as given by experimental conditions in (Heina, 1977) ($<W> = 48.34m/s$).

The calculation of the flow distribution in the 19-pin rod bundle divided into the 8808 control volumes takes about three minutes of CPU time on personal computer with Intel Pentium-II 400Mhz processor. In addition, the calculation of temperature distribution with energy conservation equation demands about one minute of CPU time more. Two samples of the COOLFD visual components that serve to control the calculation process and represent the numerical solution graphically are shown in Fig. 5 and Fig. 6. The first sample screen was captured during flow calculation while the latest demonstrates a temperature map calculated by energy equation iterations.

4. RESULTS OF CALCULATION

The results of numerical simulation of fluid flow were compared with experimental data (Heina, 1977). The local shear stress distributions calculated on the wall of rods No 6, 1, and 7 are shown in Fig. 7, Fig. 8 and Fig. 9 correspondingly.

Here, one can see that traditional upwind scheme underestimates the wall shear stresses significantly (in times!) while EFD scheme generate quite satisfactory results.

The samples of the axial velocities profiles around rods No 6 and 7 are shown in Fig. 10 and Fig. 11 correspondingly. These results are shown for EFD only.

Again, agreement with experimental values of axial velocity is not perfect but satisfactory.

The main source of the numerical error is possibly related to the implementation of the experimental relations of turbulent eddy viscosity. While both formula (8) of Nijsing and Eifler (1971) and Eq. (9) of Neelen (1986) were derived for regular rod bundle geometry, they are directly used for geometrically "disturbed" subchannel in this work because of lack of detailed experimental data. In addition, it is believed that secondary flows contribute an important part in the velocity distribution developing. Still, even using significant simplification above, the model presented in this work can predict

velocity and wall shear stress distributions in satisfactory agreement with the experimental data available for such sophisticated geometry.

On the next stage of calculations, velocity field is used for finite-difference representation of the energy equation (2) that is discretizated with the EFD scheme again on the same mesh system. Then, the resulting system of linear equations is calculated. Numerically predicted temperature distribution was compared with the liquid metal experiments performed in IPPE (Ushakov, 1978). In these experiments, the wall temperatures were measured by single thermocouple located on the wall of the central rod that was turned around. Thus, the single thermocouple could measure the temperature distributions around the wall and those results are available for comparison with calculated ones.

Two samples of comparison of calculated temperature distributions around central dislocated rod No 1 with those from experimental data are shown in Fig. 12 and Fig. 13 for Peclet numbers 218 and 58 correspondingly.
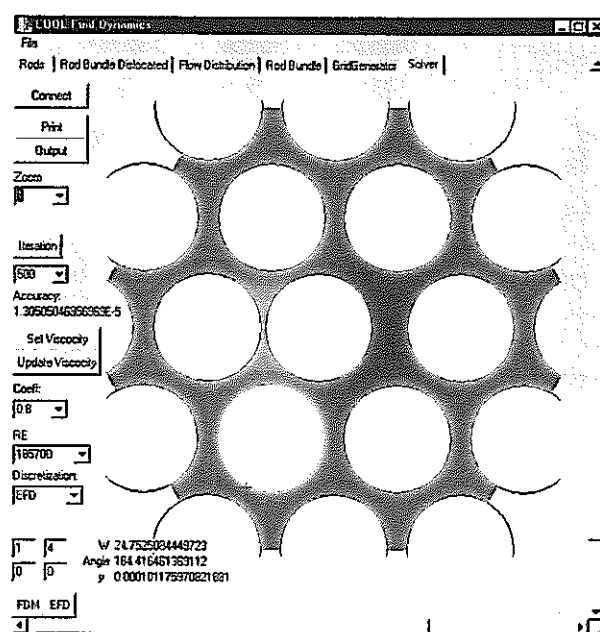
Fig. 5 Sample of flow distribution at the experimental 19-pin rod bundle with disclocated central rod
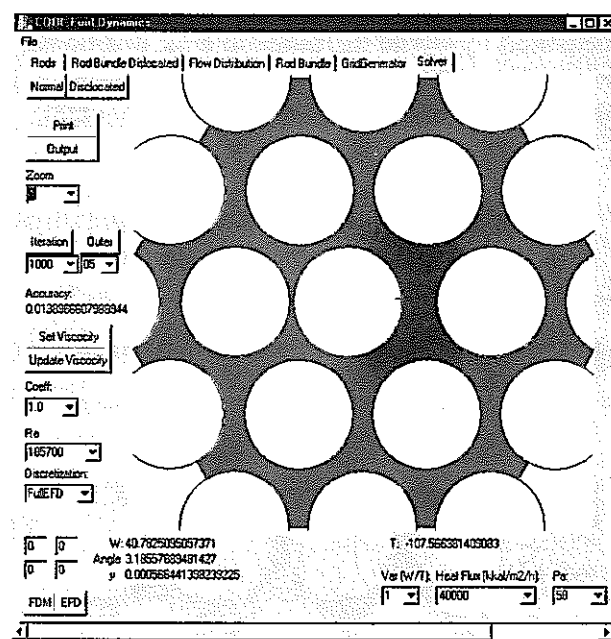
Fig. 6   Sample of temperature distribution at the 19-pin rod bundle with dislocated central rod
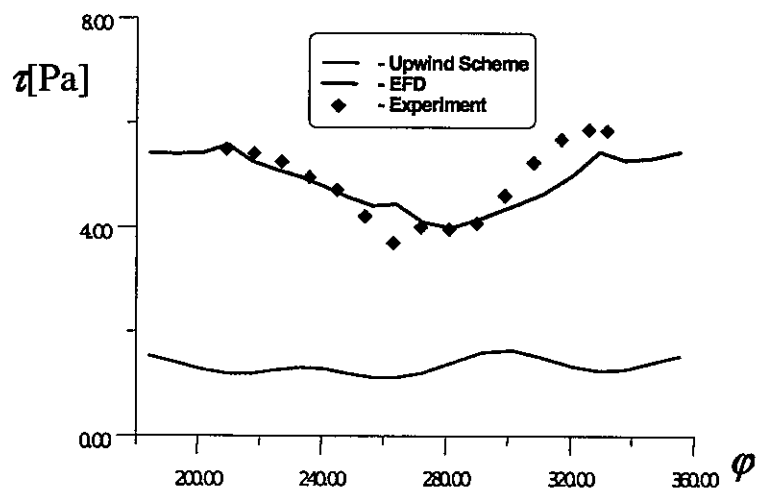
Fig. 7   Wall shear stress distribution; Rod No 6
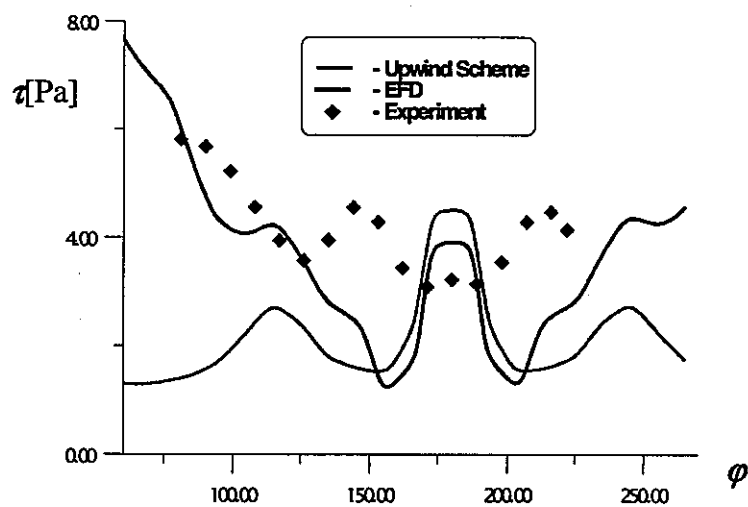
Fig. 8   Wall shear stress distribution; Rod No 1
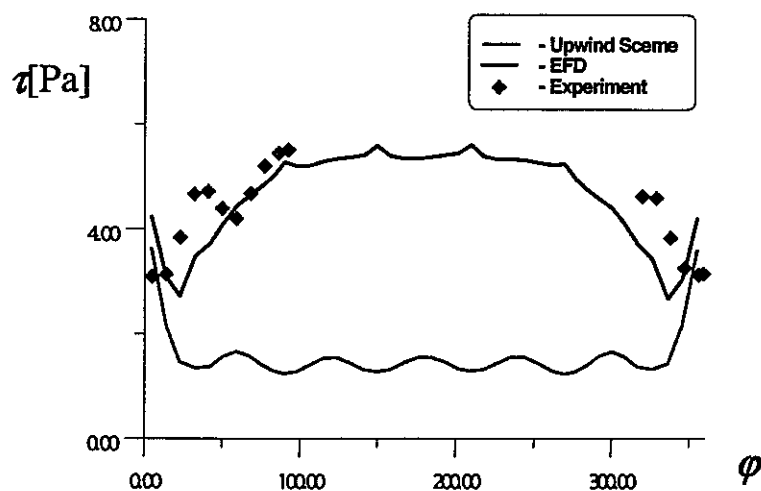
Fig. 9   Wall shear stress distribution; Rod No 7
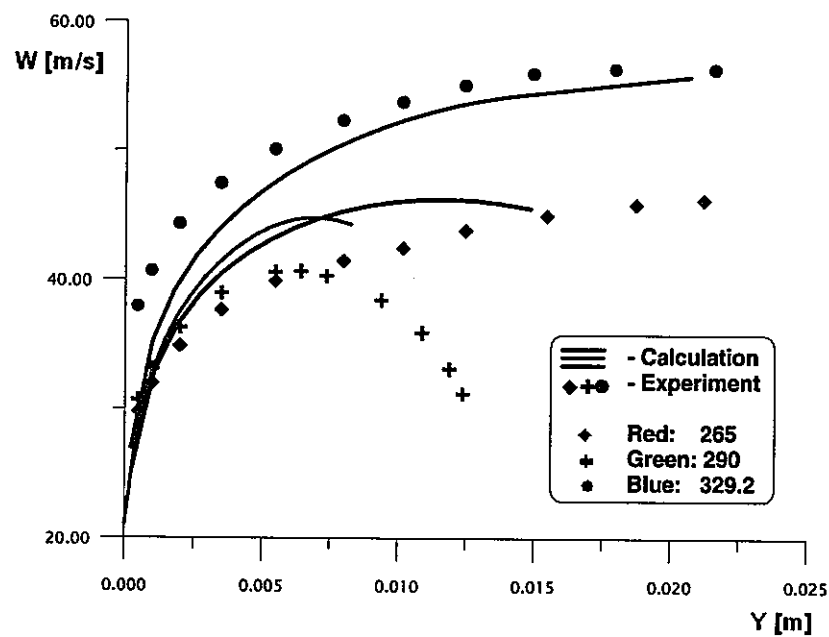
Fig. 10   Axial velocity distribution vs. distance to the wall; Rod No 6 in direction of angle $\varphi = 265°, 290°$, and 329.2 degrees.
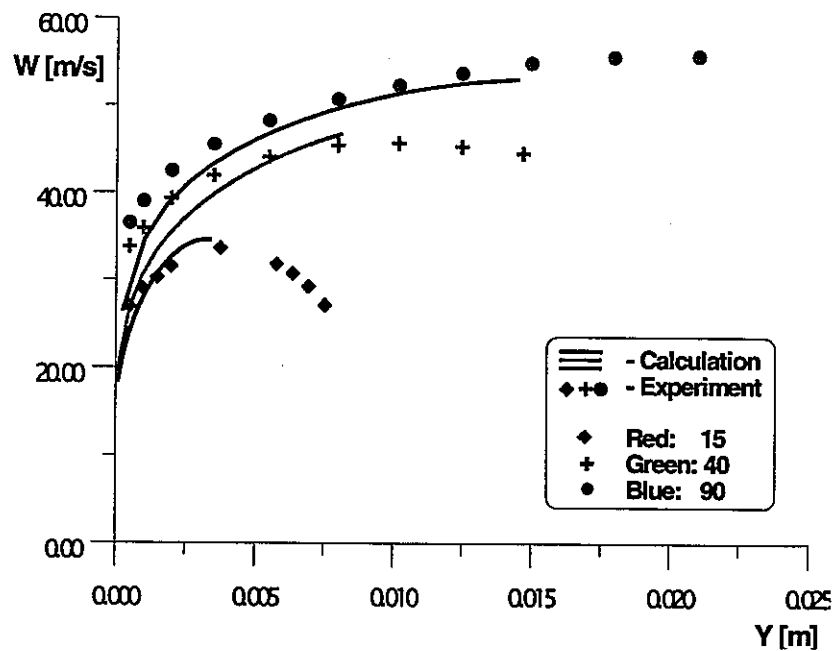
Fig. 11   Axial velocity distribution vs. distance to the wall; Rod No 7 in direction of angle $\varphi = 15°, 40°$, and 90 degrees.
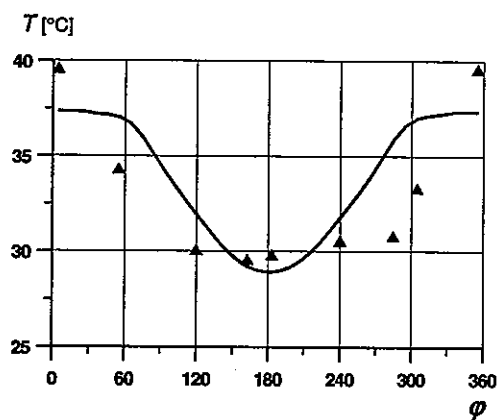
Fig. 12 Wall temperature distribution around the central rod; $Pe = 218$
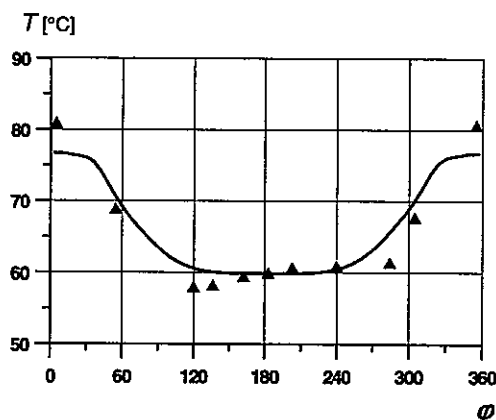
Fig. 13 Wall temperature distribution around the central rod; $Pe = 58$

5. CONCLUSIONS

In this work, detailed velocity and temperature distributions in a "geometrically disturbed" rod bundle of a nuclear reactor have been calculated numerically using the Efficient Finite Difference (EFD) scheme and Computational Object-Oriented Library for Fluid Dynamics (COOLFD). The data for comparison were available for local velocity and shear stress distributions from experiments of Heina and Mantlik (1977) and for wall temperature distributions from follow-up experiments of (Ushakov, 1978) and (Zhukov, 1985).

The system of momentum, continuity and energy equations has been solved numerically for fully developed incompressible flow in two dimensions. A calculation area has included the whole internal region of a 19-pin rod bundle. Secondary flows have been assumed negligibly small and only axial velocity component has been calculated.

An orthogonal mesh system has been generated. The calculation area has been assembled by elementary mesh components calculated for every typical subdomain.

The results of numerical simulation show satisfactory agreement with experimental data both for flow and temperature distribution. Thereby, we consider that the applicability of the COOLFD library and the EFD scheme for simulation of fluid flow and heat transfer in complex regions has been demonstrated.

To improve the accuracy, the simulation of secondary flows is necessary. Whereas the simple Boussinesq hypothesis cannot predict the secondary flows, an accurate model of turbulence should be developed.

REFERENCES

Bogoslovskay, G.P., Cevolani, S., Ninokata, H., Rinejski, A.A., Sorokin, A.P., Zhukov, A.V., 1999. LMFR Core and Heat Exchanger Thermohydraulic Design:

Former USSR and Present Russian Approaches, IAEA-TECDOC-1060, January 1999, pp. 167-233

Heina, J., Chervenka, J., Mantlik, F. Results of Local Measurements of Hydraulic Characteristic in Deformed Pin Bundle. UJV-4156-T, part 1, Rzez, Czech Republic, 1977.

Kriventsev V. and Ninokata H., 1997. An Effective Finite-Difference Scheme For Transient Problems of Heat and Mass Transfer, Proc. 8th Int. Topical Meeting on Nuclear Reactor Thermal-Hydraulics (Nureth8), Kyoto, 1, 572-580.

Kriventsev V. and Ninokata H., 1998. An Application of Object-Oriented Programming in Numerical Simulation of Fluid Dynamics in Complex Geometry, Proc. Spring Meeting of the JSME, Tokyo

Neelen, N., 1986. Modeling of Transport of Momentum in Parallel Turbulent Flow Through a Rod Bundle, Dr. Eng. Thesis, TU Braunschweig, Germany.

Nijsing, R. and Eifler, W., 1971. Temperature Fields in Liquid-Metal-Cooled Rod Assemblies, *Progress in Heat and Mass Transfer 7*, 115-149.

Patankar, S.V., 1980. *Numerical Heat Transfer and Fluid Flow*, Hemisphere, Washington, D.C.

Ushakov, P.A., Zhukov, A.V., et al. (USSR), Mantlik, F., Heina, J., et al. (CSFR), 1978 *Investigation of Thermodynamics in Regular and Deformed Bundles of Pins*, CEMR, Moscow (in Russian)

Zhukov, A.V., Kirillov, P.L., Matuhin, N.M., Sorokin, A.P., et al, 1985. *Thermal Hydraulics Analysis of Fuel Assemblies of Fast Reactor cooled by liquid metal*, Moscow, Energoatomizdat (in Russian).

Appendix C

STAR-CD コード概要

STAR-CD

Introduction

The STAR-CD system is produced by Computational Dynamics Limited. The system comprises the main analysis code, STAR (the name STAR stands for Simulation of Turbulent flow in Arbitrary egions), and the pre-processor and post-processor code, PROSTAR. A parallel-running version of the system, called STAR-HPC (for High Performance Computing) is available as a separate product (not purchased by our laboratory).

Capabilities of Star-CD

STAR operates by solving the governing differential equations of the flow physics by numerical means on a computational mesh, for quite general circumstances, as described below and illustrated by examples included at the end of this section. For very large problems, the code (in its STAR-HPC form) is also capable of running in parallel computing mode, thus greatly extending the size of models that can be handled and enormously reducing the time needed to obtain a solution. The types of flow phenomena currently represented include:

• **Steady and Transient** — efficient, optimised finite-volume solution algorithms are used for each class.

• **Laminar and Turbulent** — in the turbulent case, a number of turbulence models are available, including low-Reynolds-number, two-layer, non-linear, RNG and LES-based models.

• **Newtonian and Non-Newtonian** — laminar non-Newtonian flows are catered for, through built-in constitutive relations and facilities for user coding of alternative functions.

• **Incompressible and Compressible** — within the compressible regime, the solution algorithms allow all flow speeds to be handled, including transonic and supersonic.

• **Heat Transfer (Convection, Conduction and Radiation)** — these mechanisms can exist individually or collectively. For example, conjugate heat transfer problems, involving simultaneous fluid convection and solid conduction, can be addressed. Radiation modelling simulates the effect of any transparent solid regions within the model as well as taking into account the radiative properties of the intervening fluid medium and any solid particles present in it.

• **Mass Transfer** —the code caters for mixtures of gases or liquids containing up to 50 chemical species.

• **Chemical Reaction (including combustion)** — several built-in options are available for calculating chemically-reacting flows, including those controlled by chemical kinetics and/or turbulent mixing. In the latter case, the emphasis is on turbulent combustion and contemporary models thereof. A number of special-purpose models for simulating coal combustion processes are also available.

• **Distributed Resistances (porous media)** — volume and planar resistance modelling is provided to enable representation of flows in porous media, heat exchangers, chemical reactors, etc. The resistance may be non-isotropic.

• **Buoyancy and Rotation** — the code has built-in provision for calculating flows subject to such body forces, as well as user-coding facilities to enable addition of other forces. The rotation option is one of several features that make the code particularly suitable for rotating machinery applications.

• **Free Surface Flows and Cavitation** — STAR may be used for problems requiring

the simultaneous CFD analysis of a heavy and a light fluid domain in contact with each other. The simulation accounts for surface tension forces and employs a special discretisation scheme that preserves sharp interfaces. Cavitation problems are modelled using an extension of the free-surface algorithms.

• **Multiple Streams** — STAR has the ability to simultaneously calculate multiple independent streams, each of which may be a different fluid, and all of which may communicate thermally through dividing walls. Typical applications would be heat exchangers.

• **Dispersed Multi-Phase Flows** — multi-phase systems comprising particles, bubbles or droplets in a continuous fluid phase may be calculated, with full account of interphase heat, mass and momentum transfer. The mesh-related features include:

• **Unstructured Meshes** — these are body-fitted, non-orthogonal and may be composed of a mixture of hexahedra, tetrahedra and triangular prisms, all connected in an arbitrary pattern, in the finite-element fashion.

• **All-tetrahedral Meshes** —allows flow calculations to be made on arbitrarily complex tetrahedral grids imported from mesh generators such as ICEM CFD Tetra.

• **Arbitrary polyhedral cell shapes** — generated by the Pro*am package through automatic cell trimming. This also produces regular surface-layer meshes linked to an efficient structured grid in the main flow region.

• **Mesh Movement** — here the entire mesh or portions thereof can be dynamically distorted in a user-prescribed fashion, so as to accommodate moving boundaries or some other requirement.

• **Arbitrary Interfaces** — enables different parts of a model to be meshed independently in the most convenient way and then joined together in an arbitrary manner along a special interface, with no requirement for mesh continuity.

• **Embedded Refinement** —allows mesh cells to be subdivided in an arbitrary fashion, to achieve local or global refinement with relative ease. Various numerical accuracy criteria, including a built-in error estimation algorithm, may be used to guide the user towards those parts of the mesh that are most in need of refinement.

• **Sliding Interface** — the treatment enables two or more adjacent mesh zones to slide relative to each other, while retaining full implicit coupling between the zones. This feature, when employed in conjunction with rotating meshes, opens the door to a wide range of applications, such as stirred mixing vessels, pumps and turbomachinery.

• **Multiple Rotation Zones** — simulates relative rotational motion between two or more adjacent mesh zones in an approximate fashion (exact undersome circumstances). This enables steady-state simulations of large, complex rotating machines to be performed, such as multi-stage gas turbines or multi-impeller stirred mixers.

• **Dynamic Cell Addition/Deletion** —this facility enables cells to be added or deleted during the course of a transient calculation as in, for example, the combustion chamber of a reciprocating engine.

Additional flexibility is offered through user programming facilities: STAR's capabilities can be further extended through user programmability. This feature allows special body force terms, boundary conditions, thermofluid properties, etc. to be inserted using FORTRAN coding.

Code Description

Flow Field

The mass and momentum conservation equations solved by STAR-CD for general incompressible and compressible fluid flows and a moving coordinate frame (the 'Navier Stokes' equations) are, in Cartesian tensor notation:

$$\frac{1}{\sqrt{g}}\frac{\partial}{\partial t}\left(\sqrt{g}\rho\right)+\frac{\partial}{\partial x_j}\left(\rho\tilde{u}_j\right)=s_m \tag{1}$$

$$\frac{1}{\sqrt{g}}\frac{\partial}{\partial t}\left(\sqrt{g}\rho u_i\right)+\frac{\partial}{\partial x_j}\left(\rho u_j\tilde{u}_i-\tau_{ij}\right)=-\frac{\partial p}{\partial x_i}+s_i \tag{2}$$

where

t — time
x_i — Cartesian coordinate $(i = 1, 2, 3)$
u_i — absolute fluid velocity component in direction
u_j — u_j-u_{cj} relative velocity between fluid and local (moving) coordinate frame that moves with velocity u_{cj}
p — piezometric pressure
ρ — density
τ_{ij} — stress tensor components
s_m — mass source
s_i — momentum source components
$\sqrt{g}$ — determinant of metric tensor

  and repeated subscripts denote summation.

This specialisation of the above equations to a particular class of flow involves:

• Application of ensemble or time averaging if the flow is turbulent.
• Specification of a constitutive relation connecting the components of the stress tensor τ_{ij} to the velocity gradients.
• Specification of the 'source', s_m, which represents the sum of the body and other external forces, if present.

We will not present all code options, but only discuss those of our interest. In particular, since our attention is concentrated on the turbulence modeling, we next present the closure formulations.

Turbulence Models

Introduction

It is well known that among the various turbulence models, the k-ε is currently the most popular and applicable to a large variety of flow cases with reasonable prediction accuracy. However, there still are fundamentals problems that need to be resolved. In particular, it is well known that the usual formulations of the model assume an isotropic eddy diffusivity in modeling the Reynolds stress tensor. One important deficiency of such a model is the fact that anisotropic effects are not accounted for. In simple terms, since the viscosity is a scalar, each component of the stress affects its strain to the same extent. For this reason, flows where turbulent intensity gradients, and hence the augmentation effects of secondary strain rates, are important cannot be accurately predicted. The most quoted example is the secondary flow that originates in a square duct due to the gradients of the turbulent shear stresses.

Due to this important limitation, Reynolds Stress Models (RSM) are often used instead, because they offer a greater potential for predicting the anisotropic phenomena correctly. Anyhow, although the second moment transport equations can be derived in exact forms, the higher order correlations need to be modeled with some drastic assumption of unknown validity; even the principles and basic techniques for their modeling have not been established yet, at least, in the near wall region, as stated by Myong and Kasagi. The simultaneous solution of a set of highly non-linear coupled differential equations for each individual component of the Reynolds stress tensor has also a very high computational cost and often leads to unstable computations. In this respect the use of algebraic rather then differential equations for the Reynolds stresses, which leads to the Algebraic Reynolds Stress Model (ARSM), offers a more solid solution scheme. These models are anyhow up to date far from being assessed and the solutions often rely heavily on the user assumptions, making them not appealing for our research.

Our attention in this work is therefore directed towards a different approach to realistically simulate the effects of anisotropy in the flow, which consists of a non-linear extension of the stress-strain relation. This approach forms a Non-Linear Eddy Viscosity Model (NLEVM) sometimes also refereed to as an explicit ARSM. Although the idea of a NLEVM emerged in the 70's) only recently they have seen practical applications. These models have shown promising capabilities in successfully reproducing turbulence driven secondary flows.

The capabilities of these models to correctly predict shear stress and velocity distributions in a tight lattice fuel bundle are evaluated in comparison with the classic EVM.

Further in our fuel design we will also have to challenge the thermal analysis of the fuel bundle. For this reason we also analyzed the model performances on a benchmark dealing with a heated rod bundle. In this case it is fundamental not only to study the prediction capabilities of the various models, but also to consider which offer a good balance between accuracy, robustness and calculation cost requirement. We therefore considered two alternative approaches, the k-ω and the Shear Stress Transport (SST) model. The k-ω model, in place of the dissipation rate, ε, adopts an equation for the turbulent frequency, ω, of the large scales. The ω-equation is claimed to have significant advantages near the surface and to accurately predict the turbulent length scale which should improve wall shear stress and heat transfer predictions. Moreover, the model has a very simple Low-Reynolds formulation, which does not require additional non-linear wall damping terms. The main advantage of the model has therefore shown to be its robustness, and the reduced resolution demands for integration to the wall. The SST model instead combines the use of the k-ω model near the wall with the k-ε model away from the wall where the k-ω has shown some weakness.

Near Wall Treatment

The commonly used high Reynolds number versions of the k-ε model, as well known, cannot be applied near the vicinity of the wall since the model neglects the effects of viscosity. The typical approach to avoid modeling these effects is through the use of empirical wall functions, to bridge the gap between the solid boundary and the turbulent core. However, the universality of such functions breaks down for complex flows. Another common approach is the use of a two-layer formulation, where the ε-equation is only solved in the outer part of the boundary layer, whereas the inner portion of the logarithmic layer, and the viscous sub-layer, are treated by a mixing length formulation. Again, for complex flows, the coupling between the mixing length and the ε-equation becomes problematic, and the solution depends strongly on the specification of the matching location; the uniqueness of the solution can therefore not be guaranteed.

Since our study deals with analyzing novel fuel geometries, both these approaches cannot be considered acceptable for our intent. Hence, near wall k-ε models or low Reynolds number models, which attempt to model the direct influence of viscosity, are the only suitable approach.

This formulation uses the standard transport equation for k, but augments the equation for ε with an extra term, which depends on the distance to the wall, to render the model valid up to solid wall. It is anyhow computationally more intensive and in particular requires the values of the y+ in the near wall cell to be of the order of 1. This condition produces extremely high meshing requirements making the simulation of large geometries problematic. For this reason, in the work, particular attention is posed on the balance between accuracy and mesh requirements of the different low Reynolds approaches, as compared to the high Reynolds form.

A particularly attracting wall treatment is represented by the V2F model developed by Durbin. The V2F model avoids explicit low-Re terms in the e equation by using an elliptic relaxation equation near the wall. In addition, an equation for the fluctuating v_2 is introduced. This model does not require the calculation of wall distance, and does not require the use of dumping functions or wall functions to adjust the behavior of turbulence quantities. It is claimed to have reduced computational overhead and to produce better friction and heat transfer predictions through the correct modeling of the viscous sub-layer. This model is not evaluated in this work but will be tested in the near future.

Low Reynolds k-ε

We do not illustrate the standard k-ε model, we present only the closure equations for the low Reynolds number formulation especially pointing out the difference between the linear and non-linear models.

Turbulence energy

$$\frac{1}{\sqrt{g}}\frac{\partial}{\partial t}\left(\sqrt{g}\,\rho k\right)+\frac{\partial}{\partial x_j}\left(\rho\tilde{u}_j k-\frac{\mu_{eff}}{\sigma_k}\frac{\partial k}{\partial x_j}\right)=\mu_t(P+P_B)-\rho\varepsilon-\frac{2}{3}\left(\mu_t\frac{\partial u_i}{\partial x_i}+\rho k\right)\frac{\partial u_i}{\partial x_i}+\mu_t P_{NL}$$

(3)

where

$$\mu_{eff}=\mu+\mu_t$$

(4)

and the turbulent viscosity μ_t is linked to k and ε via:

$$\mu_t=f_\mu\frac{C_\mu\rho k^2}{\varepsilon}$$

(5)

$$P \equiv 2 s_{ij} \frac{\partial u_i}{\partial x_j} \tag{6}$$

$$P_B \equiv -\frac{g_i}{\sigma_{h,t}} \frac{1}{\rho} \frac{\partial \rho}{\partial x_i} \tag{7}$$

$$P_{NL} = -\frac{\rho}{\mu_t} \overline{u_i' u_j'} \frac{\partial u_i}{\partial x_j} - \left[P - \frac{2}{3}\left(\frac{\partial u_i}{\partial x_i} + \frac{\rho_k}{\mu_t}\right)\frac{\partial u_i}{\partial x_i} \right] \tag{8}$$

$P_{NL}= 0$ for linear models and $._k$ is an empirical coefficient. The first term on the right-hand side of equation (3) represents turbulent generation by shear and normal stresses and buoyancy forces, the second viscous dissipation, and the third amplification or attenuation due to compressibility effects. The last term accounts for the non-linear contributions.

Turbulence dissipation rate

$$\frac{1}{\sqrt{g}} \frac{\partial}{\partial t}\left(\sqrt{g} \rho \varepsilon\right) + \frac{\partial}{\partial x_j}\left(\rho \tilde{u}_j \varepsilon - \frac{\mu_{eff}}{\sigma_\varepsilon}\frac{\partial \varepsilon}{\partial x_j}\right) = C_{\varepsilon 1} \frac{\varepsilon}{k}\left[\mu_t (P + P') - \frac{2}{3}\left(\mu_t \frac{\partial u_i}{\partial x_i} + \rho k\right)\frac{\partial u_i}{\partial x_i}\right] + C_{\varepsilon 3}\frac{\varepsilon}{k}\mu_t P_B$$

$$-C_{\varepsilon 2}\left(1 - 0.3 e^{-R_t^2}\right)\rho \frac{\varepsilon^2}{k} + C_{\varepsilon 4}\rho \varepsilon \frac{\partial u_i}{\partial x_i} + C_{\varepsilon 1}\frac{\varepsilon}{k}\mu_t P_{NL} \tag{9}$$

where $..$, $C.1$, $C.2$, $C.3$ and $C.4$ are empirical coefficients whose values are given in Table 1. The right-hand side terms represent analogous effects to those described above for the k equation.

Table 1: Values Assigned to Model Coefficients

C.	.k	..	.h	.m	C_1	C_2	C_3	C_4	k	E
0.09	1.0	1.22	0.9	0.9	1.44	1.92	1.44	-0.33	0.42	9.0

The term P' is given by:

$$P' = 1.33\left[1 - 0.3 e^{-R_t^2}\right]\left[P + 2\frac{\mu}{\mu_t}\frac{k}{y^2}\right] e^{-0.00375 Re_y^2} \tag{10}$$

μ_t is defined in equation (5) with f_μ given by

$$f_\mu = \left[1 - e^{-0.0198 Re_y}\right]\left(1 + \frac{5.29}{Re_y}\right) \tag{11}$$

in which

$$Re_y = \frac{y\sqrt{k}}{\nu} \tag{12}$$

R_t is the turbulent Reynolds number given by

$$R_t = \frac{k^2}{\nu \varepsilon} \tag{13}$$

The equation for dissipation is not solved at the near-wall cell. Rather, the dissipation, ε_P, at the near-wall cell is fixed as follows:

$$\varepsilon_P = \frac{2vk}{y^2}$$

(14)

where y+ for the near-wall cell is of the order of 1.0.

Linear and Non-linear Constitutive Relations

Linear Model

The turbulent Reynolds stresses and scalar fluxes are linked to the ensemble averaged flow properties as follows

$$-\overline{\rho}\,\overline{u_i' u_j'} = 2\mu_t s_{ij} - \frac{2}{3}\left(\mu_t \frac{\partial u_k}{\partial x_k} + \rho k\right)\delta_{ij}$$

(15)

$$\overline{\rho}\,\overline{u_j' h'} = -\frac{\mu_t}{\sigma_{h,t}}\frac{\partial h}{\partial x_j}$$

(16)

$$\overline{\rho}\,\overline{u_j' m_m'} = -\frac{\mu_t}{\sigma_{m,t}}\frac{\partial m_c}{\partial x_j}$$

(17)

where

$$k \equiv \frac{\overline{u_i' u_i'}}{2}$$

(18)

is the turbulent kinetic energy, μ_t is the turbulent viscosity, and $\sigma_{n,t}$, $\sigma_{m,t}$ are the turbulent Prandtl and Schmidt numbers, respectively. The turbulent viscosity μ_t is, as said, linked to k and ε via the equation (5) while $f\mu$ is given by equation (11).

We can notice in the above relationships that each component of the shear stress influences only one component of the velocity gradient, and therefore anisotropy cannot be accounted for. Non linear models try to cater for this defect by adopting non-linear relationships between Reynolds stresses and the rate of strain.

Quadratic model

For the quadratic model, the constitutive relations for the Reynolds stresses are as follows:

$$-\overline{\rho}\frac{\overline{u_i' u_j'}}{k} = \frac{2}{3}\left(\frac{\mu_t}{k}\frac{\partial u_k}{\partial x_k} + \rho\right)\delta_{ij} - \frac{\mu_t}{k}S_{ij} + C_1\frac{\mu_t}{\varepsilon}\left[S_{ik}S_{kj} - \frac{1}{3}\delta_{ij}S_{kl}S_{kl}\right] + C_2\frac{\mu_t}{\varepsilon}\left[\Omega_{ik}S_{kj} + \Omega_{jk}S_{ki}\right] +$$
$$C_3\frac{\mu_t}{\varepsilon}\left[\Omega_{ik}\Omega_{jk} - \frac{1}{3}\delta_{ij}\Omega_{kl}\Omega_{kl}\right]$$

(19)

where

$$C_1 = \frac{c_{NL1}}{(c_{NL6} + c_{NL7} S^3) C_\mu}, C_2 = \frac{c_{NL2}}{(c_{NL6} + c_{NL7} S^3) C_\mu}, C_3 = \frac{c_{NL3}}{(c_{NL6} + c_{NL7} S^3) C_\mu}$$

(20)

and

$$C_\mu = \frac{A_0}{A_1 + A_2 S + A_3 \Omega}$$

(21)

where A_0, A_1, A_2, A_3, c_{NL1}, c_{NL2}, c_{NL3}, c_{NL6}, c_{NL7} are empirical coefficients whose values are shown in table 2. Once again the turbulent viscosity   is defined in equation (5).
Sij and Ωij are elements of the mean strain and vorticity tensors, respectively, and are given by

$$S_{ij} = \frac{\partial u_i}{\partial x_j} + \frac{\partial u_j}{\partial x_i}$$

(22)

$$\Omega_{ij} = \frac{\partial u_i}{\partial x_j} - \frac{\partial u_j}{\partial x_i}$$

(23)

The other two terms required to complete the definition of C_μ are as follows:

$$S = \frac{k}{\varepsilon} \sqrt{\frac{1}{2} S_{ij} S_{ij}}$$

(24)

$$\Omega = \frac{k}{\varepsilon} \sqrt{\frac{1}{2} \Omega_{ij} \Omega_{ij}}$$

(25)

Cubic model

The constitutive equation for the cubic model is obtained by adding a high order term to the equation (19). The final expression is

$$-\overline{\rho \frac{u_i' u_j'}{k}} = \frac{2}{3}\left(\frac{\mu_t}{k}\frac{\partial u_k}{\partial x_k} + \rho\right)\delta_{ij} - \frac{\mu_t}{k} S_{ij} + C_1 \frac{\mu_t}{\varepsilon}\left[S_{ik} S_{kj} - \frac{1}{3}\delta_{ij} S_{kl} S_{kl}\right] + C_2 \frac{\mu_t}{\varepsilon}\left[\Omega_{ik} S_{kj} + \Omega_{jk} S_{ki}\right] +$$

$$C_3 \frac{\mu_t}{\varepsilon}\left[\Omega_{ik}\Omega_{jk} - \frac{1}{3}\delta_{ij}\Omega_{kl}\Omega_{kl}\right] + C_4\mu_t\frac{k}{\varepsilon^2}(S_{ki}\Omega_{lj} + S_{kj}\Omega_{li})S_{kl} + C_5\mu_t\frac{k}{\varepsilon^2}(S_{kl}S_{kl} - \Omega_{kl}\Omega_{kl})S_{ij}$$

(26)

where

$$C_4 = c_{NL4} C_\mu^2$$

(27)

$$C_5 = c_{NL5} C_\mu^2$$

(28)

the turbulent viscosity μ_t is defined in equation (5), c_{NL4}, c_{NL5} are empirical coefficients given in table 2.

Table 2: Values Assigned to Coefficients

A_0	A_1	A_2	A_3	c_{NL1}	c_{NL2}	c_{NL3}	c_{NL4}	c_{NL5}	c_{NL6}	c_{NL7}
0.667	1.25	1.0	0.9	0.75	3.75	4.75	-10.0	-2.0	1000	1.0

Low Reynolds k-ω

For the k-ω model, the general forms of the k and ω equations are as follows:

Turbulence Energy

$$\frac{1}{\sqrt{g}}\frac{\partial}{\partial t}\left(\sqrt{g}\,\rho k\right)+\frac{\partial}{\partial x_j}\left(\rho\tilde{u}_j k-\left(\mu+\frac{\mu_t}{\sigma_k^\omega}\right)\frac{\partial k}{\partial x_j}\right)=\rho P_k-\rho\beta^* k\omega \tag{29}$$

Specific dissipation rate

$$\frac{1}{\sqrt{g}}\frac{\partial}{\partial t}\left(\sqrt{g}\,\rho\omega\right)+\frac{\partial}{\partial x_j}\left(\rho\tilde{u}_j\omega-\left(\mu+\frac{\mu_t}{\sigma_\omega^\omega}\right)\frac{\partial\omega}{\partial x_j}\right)=\rho\alpha\frac{\omega}{k}P_k-\rho\beta\omega^2+\rho S_\omega \tag{30}$$

Standard

For the standard model the closure coefficients and auxiliary relations are:

$$\alpha=\frac{13}{25}\;,\;\;\beta=\beta_0 f_\beta\;,\;\;\beta^*=\beta_0^* f_\beta^*\;,\;\;\sigma_k^\omega=\sigma_\omega^\omega=2\;,$$

$$\beta_0=\frac{9}{125}\quad,\quad f_\beta=\frac{1+70\chi_\omega}{1+80\chi_\omega}\quad,\quad \chi_\omega=\left|\frac{\omega_{ij}'\omega_{jk}'s_{ki}'}{\left(\beta_o^*\omega\right)^3}\right|\;,$$

$$\beta_0=0.09\quad,\quad f_\beta^*=\begin{cases}1 & ,\;\chi_k\le 0\\[4pt]\dfrac{1+680\chi_k^2}{1+400\chi_k^2} & ,\;\chi_k>0\end{cases}\;, \tag{31}$$

$$\chi_k=\frac{1}{\omega^3}\frac{\partial k}{\partial x_j}\frac{\partial\omega}{\partial x_j}\quad,\quad S_\omega=0$$

where $s_{ij}'=\frac{1}{2}S_{ij}$ and the eddy viscosity is given by

$$\mu_t=\rho\frac{k}{\omega} \tag{32}$$

SST model

The SST model implemented is that proposed by Menter (1993), the coefficients in this case are expressed in the following general form:

$$C_\phi=F_1 C_{\phi 1}+\left(1-F_1\right)C_{\phi 2} \tag{33}$$

where

$$F_1=\tanh\left(\arg_1^4\right) \tag{34}$$

$$\arg_1=\min\left[\max\left(\frac{\sqrt{k}}{0.09\omega y};\frac{500\nu}{y^2\omega}\right);\frac{4\rho k}{\sigma_{\omega 2}^\omega CD_{k\omega}y^2}\right] \tag{35}$$

$$CD_{k\omega} = \max\left(\frac{2\rho}{\omega\sigma_{\omega2}^{\omega}}\frac{\partial k}{\partial x_j}\frac{\partial \omega}{\partial x_j} , 10^{-20}\right) \tag{36}$$

The coefficient set 1 is

$$\sigma_{k1}^{\omega} = 1.176 \quad , \quad \sigma_{\omega1}^{\omega} = 2 \quad , \quad \beta_1 = 0.075 \quad , \quad \beta_1^* = 0.09 \quad ,$$

$$\alpha_1 = \frac{\beta_1}{\beta_1^*} - \frac{1}{\sigma_{\omega1}^{\omega}}\frac{\kappa^2}{\sqrt{\beta_1^*}} \quad , \quad \kappa = 0.41 \tag{37}$$

and the coefficient set 2 is

$$\sigma_{k2}^{\omega} = 1 \quad , \quad \sigma_{\omega2}^{\omega} = 1.176 \quad , \quad \beta_2 = 0.0828 \quad , \quad \beta_2^* = 0.09 \quad ,$$

$$\alpha_2 = \frac{\beta_2}{\beta_2^*} - \frac{1}{\sigma_{\omega2}^{\omega}}\frac{\kappa^2}{\sqrt{\beta_2^*}} \quad , \tag{38}$$

$$S_\omega = 2\left(1 - F_1\right)\frac{1}{\sigma_{\omega2}^{\omega}}\frac{1}{\omega}\frac{\partial \omega}{\partial x_j}\frac{\partial k}{\partial x_j} \tag{39}$$

The eddy viscosity for this model is

$$\mu_t = \rho\frac{a_1 k}{\max\left(a_1\omega, \Omega^* F_2\right)} \tag{40}$$

where

$$a_1 = 0.31 \quad , \quad F_2 = \tanh\left(\arg_2^2\right) \quad , \arg_2 = \max\left(2\frac{\sqrt{k}}{0.09\omega y}, \frac{500\nu}{y^2\omega}\right)$$

$$\Omega^* = \sqrt{\frac{1}{2}\Omega_{ij}\Omega_{ij}} \tag{41}$$

k-ω Wall Treatment

Both k-ω models are adopted in the low Reynolds number form, for which ω at the near-wall cell is fixed algebraically according to:

$$\omega_p = \frac{60\nu}{\beta_1 y^2} \tag{42}$$

where ν is the kinetic viscosity, y the normal distance from the wall and $\beta_1 = 0.075$.

Discretization Practices

Introduction

The differential equations governing the conservation of mass, momentum, energy, etc. within the fluid, are discretised by the finite volume (FV) method. Thus, they are first integrated over the individual computational cells (and over a finite time increment, in the case of transient problems) and then approximated in terms of the cell-centred nodal values of the dependent variables. This approach has the merit, amongst others, of ensuring that the discretised forms preserve the conservation properties of the parent differential equations.

Spatial Flux Discretisation

The manner in which the convective and diffusive fluxes are expressed in terms of nodal φ values is one of the key factors determining accuracy and stability, for both steady-state and transient calculations. At the high Reynolds numbers often encountered in practice, the choice of convective flux approximation is particularly important.

There are essentially two main classes of convective flux approximation in widespread use, namely:

1. 'Low-order' schemes, which characteristically generate discretised equation forms that are easy to solve, produce solutions which obey the expected physical bounds, but sometimes give rise to smearing of gradients. The latter effect has come to be known as 'numerical diffusion'. This is a form of truncation error that diminishes as the grid is refined, but at an increased cost of calculation.

2. 'Higher-order' schemes, which better preserve steep gradients, but may result in equations that are more difficult to solve (and, in extreme cases, may provoke numerical instabilities) and/or have solutions exhibiting non-physical spatial oscillations ('wiggles'). These oscillations may, in some cases, lead to spurious values, e.g. negative species concentration or turbulent kinetic energy. This phenomenon is often termed 'numerical dispersion' . It too can be diminished by grid refinement or by using monotone schemes (e.g. a blending methodology).

The present practice in STAR-CD is to offer alternative user-selected schemes from each of the above categories.

Spatial Flux Discretisation

The manner in which the convective and diffusive fluxes are expressed in terms of nodal φ values is one of the key factors determining accuracy and stability, for both steady-state and transient calculations.

Upwind differencing (UD)

This form of interpolation preserves the correct physical bounds on ϕ under all conditions, but can lead to numerical diffusion.

Linear upwind differencing (LUD)

This is a specially adapted, second-order accurate scheme formulated for non-structured meshes and derived from a scheme originally proposed for structured meshes. It results in less numerical smearing than the UD scheme, but can produce solutions that are outside the physical bounds on ϕ (i.e. numerical dispersion).

Central differencing (CD)

The CD scheme, which is also second-order, simply interpolates linearly on nearest neighbour values, irrespective of flow direction. This scheme also produces less numerical diffusion, but can be dispersive

Quadratic upstream interpolation of convective kinematics (QUICK)

This is a third order scheme which fits a parabola through two points upstream and one point downstream to get an interpolated value. Note that this scheme should not be used for all-tetrahedral meshes and that it can be dispersive. MARS is a multidimensional second-order accurate differencing scheme that operates in two separate steps:

1. Reconstruction

A set of monotone gradients are computed using a multidimensional Total Variation Diminishing (TVD) scheme. The cell flow properties and the gradients completely define a second-order accurate spatial discretisation.

2. Advection

The reconstructed cell-face flow properties are used to compute the face fluxes for all advected properties using a monotone and bounded advection scheme. This incorporates a variable compression level which controls the amount of second-order upwinding of the scheme without affecting the order of accuracy of the spatial discretisation.

MARS does not rely on any problem dependent parameters to work properly and it can automatically handle all flow problems and mesh types supported by STAR-CD. However, the user can control the ability of the advection scheme to accurately capture sharp discontinuities in the flow by setting the scheme's compression level to a value between 0 and 1. Low values for this parameter result in a computationally efficient scheme at the expense of sharpness of resolution. High values improve the resolution but result in an increased number of iterations when steady flows are computed. The default value for this parameter is 0.5 which is a compromise between accuracy and convergence rate. MARS may also be used for the calculation of density. In this case, the implementation includes only the reconstruction step. This procedure can improve the solution accuracy for compressible flows.

Of all schemes available, MARS possesses the least sensitivity of solution accuracy to the mesh structure and skewness.

Self-filtered central differencing (SFCD)

This scheme, as the name implies, is effectively central differencing with a built-in adaptive filter to remove non-physical extrema whenever they would arise. This is achieved by locally blending the CD and UD schemes.

Gamma differencing scheme

This scheme, like SCFD, is effectively central differencing with a built-in adaptivefilter to remove non-physical extrema whenever they arise. This is achieved by locally blending CD and UD schemes.

Blended differencing

The method here is similar to that of the SFCD scheme, in that a higher-order, non-monotone scheme like CD (or LUD or QUICK) is blended with the lower-order UD scheme to suppress dispersion. However, the blending factor γ is now user-specified and, for this to be practicable, is taken to be uniform over the field.

Appendix D

Selection of an Appropriate Turbulence Modeling in a CFD code for an Ultra-long Life Core for the "IRIS" Reactor

Selection of an Appropriate Turbulence Modeling in a CFD code for an Ultra-long Life Core for the "IRIS" Reactor

Emilio Baglietto[1*], Hisashi Ninokata[1]

[1]Research Laboratory for Nuclear Reactors, Tokyo Institute of Technology, Tokyo, 152-8550, Japan

A comparative study of different turbulence models is presented, to select which could be adopted for the evaluation of thermo-hydraulic performances of innovative ultra-long life core designs. Various models are briefly outlined and discussed. Linear and non-linear low Reynolds k-e turbulence closures are applied on an isothermal benchmark to evaluate the capabilities to correctly predict wall shear stresses and velocity distribution in the channel. Capabilities to analyze problems involving heat transfer is also estimated, on a benchmark in a heated channel involving liquid sodium coolant. Two alternative approaches are considered for this case, the k-ω and the Shear Stress Transport model. The relative performances of the different models is assessed. The results show in both cases that the capability to account for anisotropic effects is the key requirement for a correct modeling in a rod bundle. In this respect non-linear models present promising capabilities but require further improvement for an accurate prediction.

KEYWORDS: Turbulence, anisotropic k-ε, secondary flow

I. Introduction

The International Reactor Innovative and Secure (IRIS) is an advanced, Generation IV [1], light water reactor being developed by an international consortium of industry, laboratory, university and utility establishments, led by Westinghouse. Its design is based on proven LWR technology, so that no new technology development is needed and near term deployment is possible [2]. At the same time evolutionary core solutions are being developed for future reloads [3].

The first IRIS core will employ standard <5% UO2 fuel and a standard PWR fuel assembly design, therefore not foreseeing licensing issues. At the same time work is ongoing to address the desirable target of a high conversion-ratio ultra-long life core.

Such a core will be characterized by a very tight lattice, with relatively small water volume fraction. In order to successfully tackle this challenge we must introduce innovative fuel configurations, to obtain a more uniform utilization of the coolant. A main undesirable aspect of classic triangular lattice is in fact the non-homogeneous distribution of water around fuel pins, which results in a non-uniform circumferential clad temperature and wall shear stress distribution [4]. The target is therefore to minimize the maximum clad and fuel centerline temperatures, keeping at the same time the pressure drops through the core as low as possible.

A first comparison between various fuel geometries have been performed by Romano and Todreas [5], who introduced a performance index methodology to assess thermo-hydraulic parameters such as core pressure drop, fuel centerline temperature and clad surface temperature distribution. This preliminary work shows the possibility of highly increasing fuel performances through the introduction

of novel designs.

A large range of arrangements are taken into considerations for the future core, and need to be assessed with a detailed analysis capable of correctly modeling three dimensional phenomena. Classical lumped parameters codes adopted in nuclear industries, such as sub-channel analysis codes are not appropriate for our purpose, being calibrated on specific geometries and operational conditions. As it is well known, the finest instruments for modeling turbulence are DNS and LES. The computing requirements however are extremely high; in the DNS case for example they scale as $Re^{9/4}$, making them, at the moment, unsuitable for our analysis [6]. Modern CFD codes of practical use are based on the so-called Reynolds Averaged Navier Stokes equations (RANS) models, where the terms representing turbulence interactions are modeled in terms of the mean flow variables, as for example in the widely used k-e approach. However, the reliability and accuracy of the results cannot easily be assured [7]. Turbulence modeling is usually considered the weakest point in CFD analysis.

For this reason a profound analysis of available models has been carried out and the models which showed promising characteristics have been tested and evaluated against isothermal and heated channel benchmarks for tight lattice geometries.

II. Turbulence models

It is well known that among the various turbulence models, the k-ε is currently the most popular and applicable to a large variety of flow cases with reasonable prediction accuracy. However, there still are fundamentals problems that need to be resolved. In particular, it is well known that the usual formulations of the model assume an isotropic eddy diffusivity in modeling the Reynolds stress tensor

* Corresponding author, Phone/Fax +81-3-5734-3056, E-mail: 01d51276@nr.titech.ac.jp

(EVM). One important deficiency of such a model is the fact that anisotropic effects are not accounted for. In simple terms, since the viscosity is a scalar, each component of the stress affects its strain to the same extent. For this reason, flows where turbulent intensity gradients, and hence the augmentation effects of secondary strain rates, are important cannot be accurately predicted. The most quoted example is the secondary flow that originates in a square duct due to the gradients of the turbulent shear stresses [8].

Due to this important limitation, Reynolds Stress Models (RSM) are often used instead, because they offer a greater potential for predicting the anisotropic phenomena correctly. Anyhow, although the second moment transport equations can be derived in exact forms, the higher order correlations need to be modeled with some drastic assumption of unknown validity; even the principles and basic techniques for their modeling have not been established yet, at least, in the near wall region, as stated by Myong and Kasagi [9]. The simultaneous solution of a set of highly non-linear coupled differential equations for each individual component of the Reynolds stress tensor has also a very high computational cost and often leads to unstable computations. In this respect the use of algebraic rather then differential equations for the Reynolds stresses, which leads to the Algebraic Reynolds Stress Model (ARSM), offers a more solid solution scheme. These models are anyhow up to date far from being assessed and the solutions often rely heavily on the user assumptions, making them not appealing for our research.

Our attention in this work is therefore directed towards a different approach to realistically simulate the effects of anisotropy in the flow, which consists of a non-linear extension of the stress-strain relation. This approach forms a Non-Linear Eddy Viscosity Model (NLEVM) sometimes also refereed to as an explicit ARSM. Although the idea of a NLEVM emerged in the 70's [10-11] only recently they have seen practical applications [12-13]. These models have shown promising capabilities in successfully reproducing turbulence driven secondary flows.

The capabilities of these models to correctly predict shear stress and velocity distributions in a tight lattice fuel bundle are evaluated in comparison with the classic EVM.

Further in our fuel design we will also have to challenge the thermal analysis of the fuel bundle. For this reason we also analyzed the model performances on a benchmark dealing with a heated rod bundle. In this case it is fundamental not only to study the prediction capabilities of the various models, but also to consider which offer a good balance between accuracy, robustness and calculation cost requirement. We therefore considered two alternative approaches, the k-w [14] and the Shear Stress Transport (SST) model [15]. The k-ω model, in place of the dissipation rate, ε, adopts an equation for the turbulent frequency, ω, of the large scales. The ω-equation is claimed to have significant advantages near the surface and to accurately predict the turbulent length scale which should improve wall shear stress and heat transfer predictions. Moreover, the model has a very simple Low-Reynolds formulation, which does not

require additional non-linear wall damping terms. The main advantage of the model has therefore shown to be its robustness, and the reduced resolution demands for an integration to the wall. The SST model instead combines the use of the k-ω model near the wall with the k-ε model away from the wall where the k-ω has shown some weakness.

1. Wall Treatment

The commonly used high Reynolds number versions of the k-ε model, as well known, cannot be applied near the vicinity of the wall since the model neglects the effects of viscosity. The typical approach to avoid modeling these effects is through the use of empirical wall functions, to bridge the gap between the solid boundary and the turbulent core. However, the universality of such functions break down for complex flows. Another common approach is the use of a two-layer formulation, where the ε-equation is only solved in the outer part of the boundary layer, whereas the inner portion of the logarithmic layer, and the viscous sub-layer, are treated by a mixing length formulation [16]. Again, for complex flows, the coupling between the mixing length and the ε-equation becomes problematic, and the solution depends strongly on the specification of the matching location; the uniqueness of the solution can therefore not be guaranteed.

Since our study deals with analyzing novel fuel geometries, both these approaches cannot be considered acceptable for our intent. Hence, near wall k-ε models or low Reynolds number models, which attempt to model the direct influence of viscosity, are the only suitable approach.

These formulation uses the standard transport equation for k, but augments the equation for ε with an extra term, which depends on the distance to the wall, to render the model valid up to solid wall. It is anyhow computationally more intensive and in particular requires the values of the y+ in the near wall cell to be of the order of 1. This condition produces an extremely high meshing requirements making the simulation of large geometries problematic. For this reason, in the work, particular attention is posed on the balance between accuracy and mesh requirements of the different low Reynolds approaches, as compared to the high Reynolds form.

A particularly attracting wall treatment is represented by the V2F model developed by Durbin [17]. The V2F model avoids explicit low-Re terms in the e equation by using an elliptic relaxation equation near the wall. In addition, an equation for the fluctuating $\overline{v_2}$ is introduced. This model does not require the calculation of wall distance, and does not require the use of dumping functions or wall functions to adjust the behavior of turbulence quantities. It is claimed to have reduced computational overhead and to produce better friction and heat transfer predictions through the correct modeling of the viscous sub-layer. This model is not evaluated in this work but will be tested in the near future.

III. Model Descriptions
1. Linear and Non-Linear Turbulence Closure

The calculations have been performed with the commercial code Star-CD version 3.15. The formulation of the k-ε model has been published in many papers and will not be repeated here for conciseness, but can be found in reference [18]. We instead briefly describe the turbulence closure formulations for the linear and non linear models, which are of main interest.

Linear model

For the standard linear k-ε model, the constitutive relations for the Reynolds stresses are as follows:

$$-\overline{\rho u_i' u_j'} = 2\mu_t S_{ij} - \frac{2}{3}\left(\mu_t \frac{\partial u_k}{\partial x_k} + \rho k\right)\delta_{ij} \qquad (1)$$

where, due to the linear correlation, each component of the shear stress influences only one component of the velocity gradient, therefore being unable to account for anisotropy. Non linear models try to cater for this defect by adopting non-linear relationships between Reynolds stresses and the rate of strain.

Quadratic model

For the quadratic model, the constitutive relations for the Reynolds stresses are as follows:

$$-\overline{\rho}\frac{u_i' u_j'}{k} = \frac{2}{3}\left(\frac{\mu_t}{k}\frac{\partial u_k}{\partial x_k} + \rho\right)\delta_{ij} - \frac{\mu_t}{k}S_{ij} +$$

$$C_1\frac{\mu_t}{\varepsilon}\left[S_{ik}S_{kj} - \frac{1}{3}\delta_{ij}S_{kl}S_{kl}\right] + C_2\frac{\mu_t}{\varepsilon}\left[\Omega_{ik}S_{kj} + \Omega_{jk}S_{ki}\right] + \qquad (2)$$

$$C_3\frac{\mu_t}{\varepsilon}\left[\Omega_{ik}\Omega_{jk} - \frac{1}{3}\delta_{ij}\Omega_{kl}\Omega_{kl}\right]$$

where

$$C_1 = \frac{c_{NL1}}{\left(c_{NL6} + c_{NL7}\, S^3\right)C_\mu} \qquad (3)$$

$$C_2 = \frac{c_{NL2}}{\left(c_{NL6} + c_{NL7}\, S^3\right)C_\mu} \qquad (4)$$

$$C_3 = \frac{c_{NL3}}{\left(c_{NL6} + c_{NL7}\, S^3\right)C_\mu} \qquad (5)$$

and

$$C_\mu = \frac{A_0}{A_1 + A_2 S + A_3 \Omega} \qquad (6)$$

where A_0, A_1, A_2, A_3, c_{NL1}, c_{NL2}, c_{NL3}, c_{NL6}, c_{NL7} are empirical coefficients whose values are shown in table 1. S_{ij} and Ω_{ij} are elements of the mean strain and vorticity tensors, respectively, and are given by:

$$S_{ij} = \frac{\partial u_i}{\partial x_j} + \frac{\partial u_j}{\partial x_i} \qquad (7)$$

$$\Omega_{ij} = \frac{\partial u_i}{\partial x_j} - \frac{\partial u_j}{\partial x_i} \qquad (8)$$

The other two terms required to complete the definition of $C\mu$ are as follows:

$$S = \frac{k}{\varepsilon}\sqrt{\frac{1}{2}S_{ij}S_{ij}} \qquad (9)$$

$$\Omega = \frac{k}{\varepsilon}\sqrt{\frac{1}{2}\Omega_{ij}\Omega_{ij}} \qquad (10)$$

the introduction of these quadratic terms has shown to be able to successfully reproduce turbulence driven secondary flows in various case. Anyhow the various quadratic models have shown limits in the sensitivity to minor strains. The quadratic models in particular do not have sensitivity to streamline curvature.

Cubic model

In order to capture the streamline curvature effects it is necessary to introduce further cubic terms. A cubic term is therefore added to correlation (2) ,as follows:

$$-\overline{\rho}\frac{u_i' u_j'}{k} = \frac{2}{3}\left(\frac{\mu_t}{k}\frac{\partial u_k}{\partial x_k} + \rho\right)\delta_{ij} - \frac{\mu_t}{k}S_{ij} +$$

$$C_1\frac{\mu_t}{\varepsilon}\left[S_{ik}S_{kj} - \frac{1}{3}\delta_{ij}S_{kl}S_{kl}\right] + C_2\frac{\mu_t}{\varepsilon}\left[\Omega_{ik}S_{kj} + \Omega_{jk}S_{ki}\right] + \qquad (11)$$

$$C_3\frac{\mu_t}{\varepsilon}\left[\Omega_{ik}\Omega_{jk} - \frac{1}{3}\delta_{ij}\Omega_{kl}\Omega_{kl}\right] + C_4\mu_t\frac{k}{\varepsilon^2}\left(S_{ki}\Omega_{lj} + S_{kj}\Omega_{li}\right)S_{kl} +$$

$$+ C_5\mu_t\frac{k}{\varepsilon^2}\left(S_{kl}S_{kl} - \Omega_{kl}\Omega_{kl}\right)S_{ij}$$

$$C_4 = c_{NL4}C_\mu^2 \qquad (12)$$

$$C_5 = c_{NL5}C_\mu^2 \qquad (13)$$

C_4 and C_5 are again empirical coefficients given in table 1.

Table 1 Coefficient for turbulence closures

A_0	A_1	A_2	A_3	c_{NL1}	c_{NL2}	c_{NL3}	c_{NL4}	c_{NL5}	c_{NL6}	c_{NL7}
0.667	1.25	1.0	0.9	0.75	3.75	4.75	-10.0	-2.0	10.00	1.0

k-ω models

For the k-ω model, as implemented in Star-cd, the general forms of the k and ω equations are as follows:

Turbulence Energy

$$\frac{1}{\sqrt{g}}\frac{\partial}{\partial t}\left(\sqrt{g}\,\rho k\right) + \frac{\partial}{\partial x_j}\left(\rho \tilde{u}_j k - \left(\mu + \frac{\mu_t}{\sigma_k^\omega}\right)\frac{\partial k}{\partial x_j}\right) = \qquad (14)$$

$$\rho P_k - \rho\beta^* k\omega$$

Specific dissipation rate

$$\frac{1}{\sqrt{g}}\frac{\partial}{\partial t}\left(\sqrt{g}\,\rho\omega\right)+\frac{\partial}{\partial x_j}\left(\rho\tilde{u}_j\omega-\left(\mu+\frac{\mu_t}{\sigma_\omega^\omega}\right)\frac{\partial\omega}{\partial x_j}\right)=$$ (15)

$$\rho\alpha\frac{\omega}{k}P_k-\rho\beta\omega^2+\rho S_\omega$$

Standard

For the standard model the closure coefficients and auxiliary relations are:

$$\alpha=\frac{13}{25}\ ,\quad \beta=\beta_0 f_\beta\ ,\quad \beta^*=\beta_0^* f_\beta^*\ ,\quad \sigma_k^\omega=\sigma_\omega^\omega=2\ ,$$

$$\beta_0=\frac{9}{125}\ ,\quad f_\beta=\frac{1+70\chi_\omega}{1+80\chi_\omega}\ ,\quad \chi_\omega=\left|\frac{\omega_{ij}'\omega_{jk}'s_{ki}'}{\left(\beta_0^*\omega\right)^3}\right|\ ,$$

$$\beta_0^*=0.09\ ,\quad f_\beta^*=\begin{cases}1 & ,\ \chi_k\le 0\\ \dfrac{1+680\chi_k^2}{1+400\chi_k^2} & ,\ \chi_k>0\end{cases}\ ,$$ (16)

$$\chi_k=\frac{1}{\omega^3}\frac{\partial k}{\partial x_j}\frac{\partial\omega}{\partial x_j}\ ,\quad S_\omega=0$$

where $s_{ij}'=\dfrac{1}{2}S_{ij}$ and the eddy viscosity is given by

$$\mu_t=\rho\frac{k}{\omega}$$ (17)

SST model

For the SST model, the coefficients are expressed in the following general form:

$$C_\phi=F_1 C_{\phi 1}+(1-F_1)C_{\phi 2}$$ (18)

where

$$F_1=\tanh\left(\arg_1^4\right)$$ (19)

$$\arg_1=\min\left[\max\left(\frac{\sqrt{k}}{0.09\omega y};\frac{500\nu}{y^2\omega}\right);\frac{4\rho k}{\sigma_{\omega 2}^\omega CD_{k\omega}y^2}\right]$$ (20)

$$CD_{k\omega}=\max\left(\frac{2\rho}{\omega\sigma_{\omega 2}^\omega}\frac{\partial k}{\partial x_j}\frac{\partial\omega}{\partial x_j},10^{-20}\right)$$ (21)

The coefficient set 1 is

$$\sigma_{k1}^\omega=1.176\ ,\quad \sigma_{\omega 1}^\omega=2\ ,\quad \beta_1=0.075\ ,\quad \beta_1^*=0.09\ ,$$

$$\alpha_1=\frac{\beta_1}{\beta_1^*}-\frac{1}{\sigma_{\omega 1}^\omega}\frac{\kappa^2}{\sqrt{\beta_1^*}}\ ,\quad \kappa=0.41$$ (22)

and the coefficient set 2 is

$$\sigma_{k2}^\omega=1\ ,\quad \sigma_{\omega 2}^\omega=1.176\ ,\quad \beta_2=0.0828\ ,\quad \beta_2^*=0.09\ ,$$

$$\alpha_2=\frac{\beta_2}{\beta_2^*}-\frac{1}{\sigma_{\omega 2}^\omega}\frac{\kappa^2}{\sqrt{\beta_2^*}}\ ,$$ (23)

$$S_\omega=2(1-F_1)\frac{1}{\sigma_{\omega 2}^\omega}\frac{1}{\omega}\frac{\partial\omega}{\partial x_j}\frac{\partial k}{\partial x_j}$$ (24)

The eddy viscosity for this model is

$$\mu_t=\rho\frac{a_1 k}{\max\left(a_1\omega,\Omega^* F_2\right)}$$

where

$$a_1=0.31\ ,\quad F_2=\tanh\left(\arg_2^2\right)\ ,\arg_2=\max\left(2\frac{\sqrt{k}}{0.09\omega y},\frac{500\nu}{y^2\omega}\right)$$

$$\Omega^*=\sqrt{\frac{1}{2}\Omega_{ij}\Omega_{ij}}$$ (25)

For the low Reynolds number adopted, ω at the near-wall cell is fixed algebraically according to:

$$\omega_p=\frac{60\nu}{\beta_1 y^2}$$ (26)

where ν is the kinetic viscosity, y the normal distance from the wall and $\beta_1=0.075$.

IV. Benchmark Problems Description
1. Air flow in a tight lattice rod bundle

The first benchmark, adopted for the turbulence models, refers to the evaluation of shear stress, and velocity field distribution, in an hexagonal tight lattice rod bundle. The p/d ratio of the lattice is 1.17 [19].

The experiments were performed in a wind tunnel using a 19-rods model of the fuel assembly. Geometrical data of the model cross section are shown in figure 1. Length of the model is 6 m. Only a short description of the results is given in this work but a more detailed analysis can be found in reference [20].
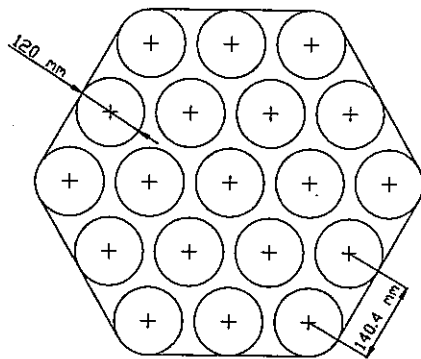
Fig.1 Rod Bundle Geometry

Measurement in the experiment have been performed in the region of hydraulically fully developed turbulent flow and without the back effect of outlet cross-section change. Data refer to the middle-cell, and we therefore assume that the influence of the walls around the rod bundle is negligible. Shear stress and axial mean velocities have been obtained with Pitot and Preston probes.

The following table shows the physical parameters of the experiment.

Table 2 Physical parameters

Fluid	Density	Kinematic Viscosity	Reynolds Number
Air	1.131 kg/m³	1.591e-5 m²/s	64300

2. Temperature distribution in a rod bundle with sodium flow

The second benchmark regards a heated bundle with sodium flow. The experiment, named TEGENA [21], was performed at the Karlsruhe Institute. Once again we present only a short description of the results, while a complete report will be published in future work.

The test geometry is presented in fig. 2. It consists of 4 heater rods of 25 mm in diameter and 6 m in length, with a p/d ratio of 1.147, suspended vertically in a rectangular channel.

The temperature values of the sodium have been measured in an horizontal plane, 29 mm ahead of the end of the rectangular channel, in the zone of thermally fully developed flow.

The main physical parameters are listed in table 3.

Table 3 Tegena parameters

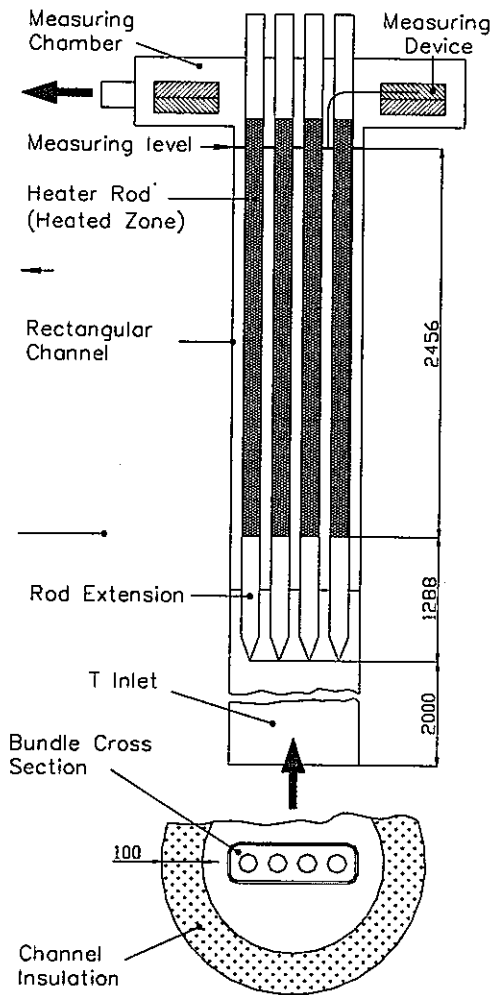| Fluid	Re	Pe	Sodium Flow	Heat Flux at rod surface
Sodium	60100	352.52	3.13 kg/s	50 W/cm²

Fig.2 Tegena test geometry

V. Numerical Simulation

1. Numerical procedure

The differential equations governing the conservation of mass, momentum, energy, etc. within the fluid, are discretized in the code by the finite volume (FV) method. The discretized equations are solved in a segregated manner with the SIMPLE (Semi-Implicit Method for Pressure-Linked Equations) algorithm [22].

For the spatial discretization a first order upwind differencing (UD) scheme has shown sufficient, but a quadratic upstream interpolation of convective kinematics (QUICK) has also been applied in all cases to assess the independency of results from discretization practices. Description of these methods can be found in reference [23].

2. Computational grid

In our simulations, particular attention is always posed on the dependency of the results on the grid resolution, to demonstrate the grid-convergence of the solution. For this reason, after preliminary sensitivity studies, three different grid resolutions are adopted for every geometry. Figures 4 and 5 show the various grids respectively for the first and

second benchmark. The grids shown are the one adopted for the low-Re number models, where the y+ value for the first cell is of the order of 1. For the first case, due to the symmetry of the problem we it has been sufficient to describe the elementary cell, as showed in figure 3, with the appropriate symmetry boundaries.
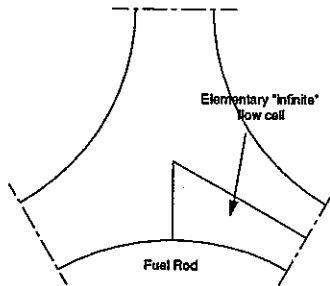

Fig.3 Benchmark 1 elementary cell

Refined mesh
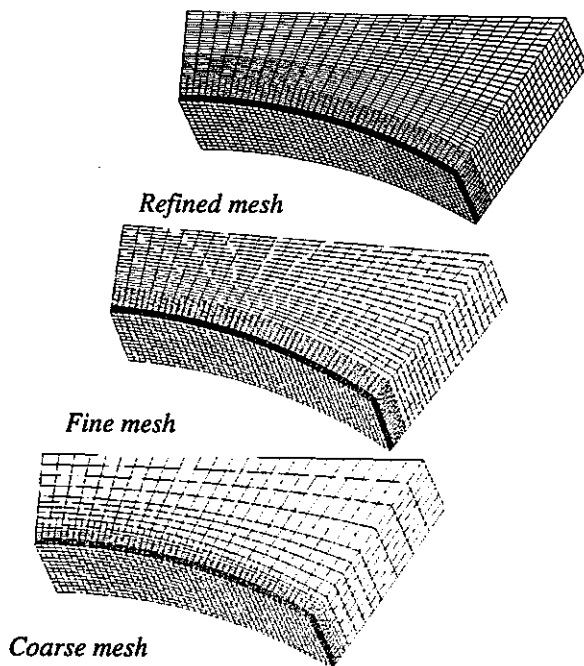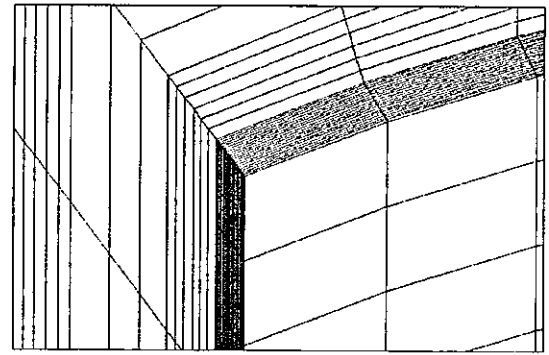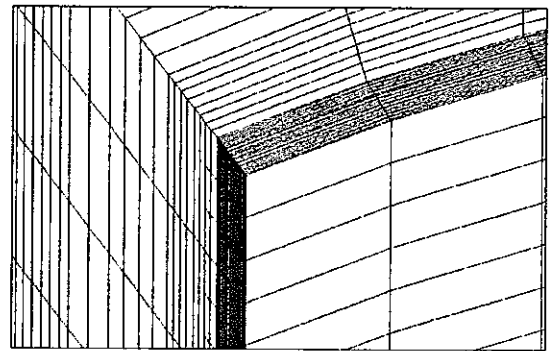
Fine mesh

Coarse mesh
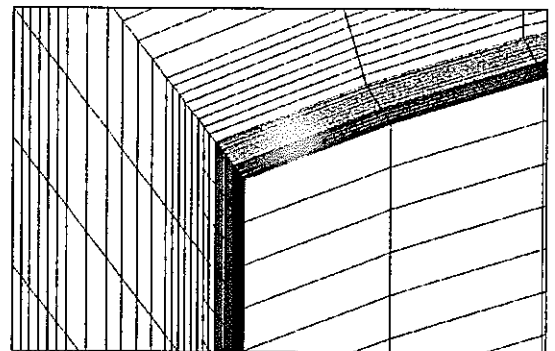
Fig.4 Benchmark 1 grids

In the second benchmark, the minimum symmetric geometry modeled is represented by one fourth of the bundle section. We show a particular, to appreciate the different mesh finesse.

Coarse mesh

Fine mesh

Refined mesh

Fig.5 Benchmark 2 grids

VI. Presentation and Discussion of Results

In both benchmarks, grid convergence of the results, and independence of the results from discretization methods, have been assessed with the methodology previously presented, but will not be presented for brevity.

1. Benchmark 1

Regarding benchmark 1, experimental data were available for the wall shear stress distribution along the wetted surface of the rod, versus the azimuth φ, as shown in fig. 6.
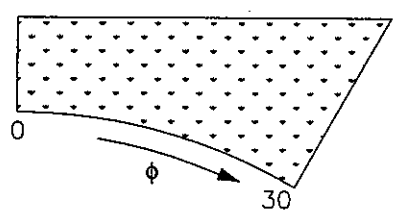
Fig.6 Stress distribution

These data are compared to those calculated from the simulation for the different turbulent models. Figure 7 and 8 present respectively the predictions of the linear and nonlinear models.
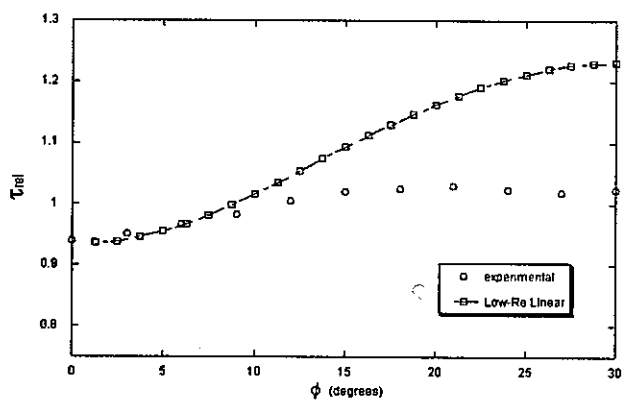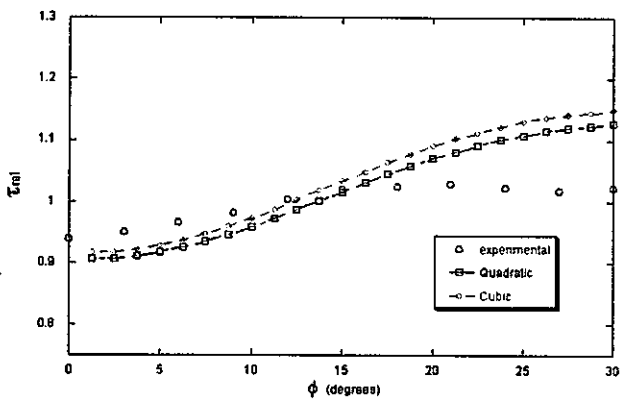

Fig.7 Linear low-Re model

Fig.8 Non-linear low-Re models

We clearly see that the standard k-e model, even though correctly predicting the shear stress in the small gap region, highly over predicts the values in the large gap region. In this respect the non-linear model shows a much flatter distribution, obtaining an acceptable quantitative agreement with experimental data. This is due to the ability of these models to account in some extent for anisotropic effects, thus predicting secondary flow in the channel, as shown in fig. 9. Still these models can not qualitatively reproduce the distribution flattening typical of the experimental data,

towards the center of the channel. This might be related to the fact that the velocity scale of the secondary motion is only less than 1% of the axial velocity.
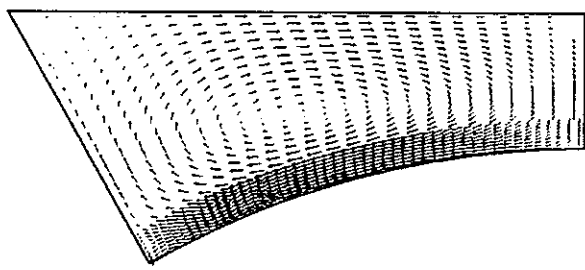

Fig.9 Secondary velocity field

Experimental velocity profiles were also available at three different locations, at 0, 15 and 30 degrees location, as shown in fig. 10. Comparisons again with the linear and non-linear models are shown in figures 11,12 and 13.
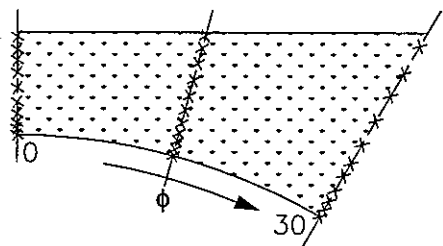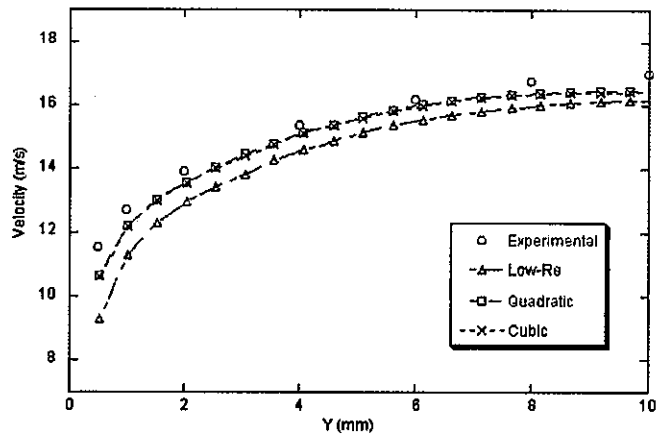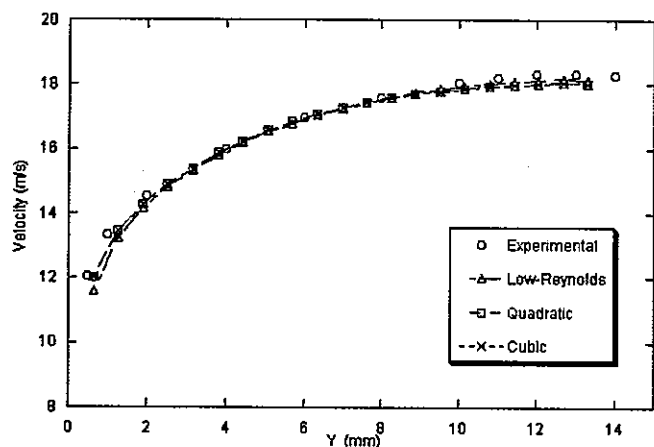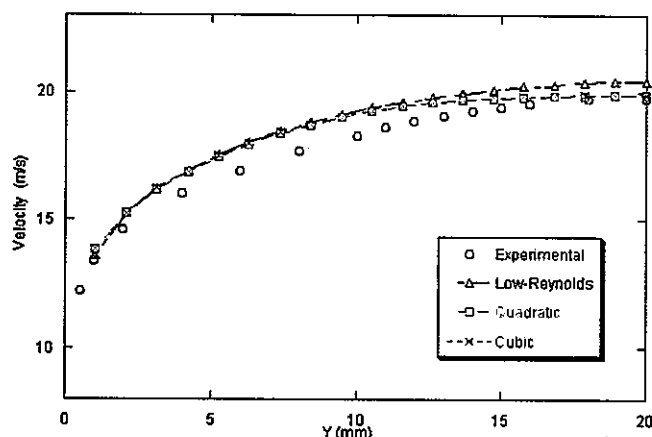

Fig.10 Velocity sensors location

Fig.11 Velocities at $\phi=0$ location

Fig.12 Velocities at φ=15 location

Fig.13 Velocities at φ=30 location

The comparison shows how the non-linearity in the models allows to better describe the velocity distributions in the flow. In particular this is clear in the narrow gap region (0 degrees), while at the 15 degrees location all models give good predictions. A particular discussion is related to the velocity distribution at the 30 degrees location. As shown, the non-linear models are able to correctly predict velocities in the near wall and bulk region but show a different behavior in between these two points. The experimental distribution is very flat in this zone in contrast with the calculated values. This might be a limitation of the models, but some doubts exist about the correctness of the experimental data.

1. Benchmark 2

Regarding benchmark 2, experimental distribution of the sodium temperatures is available along the line shown in fig.14.
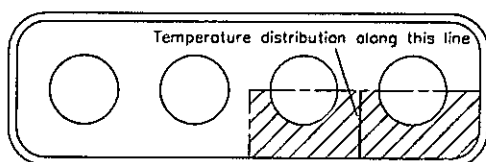
Fig.13 Temperature measurement location

In the following figures the predictions of the various models simulation are presented. The sodium temperature minus the flow averaged temperature in the measuring plane is graphed against the distance from the channel wall.
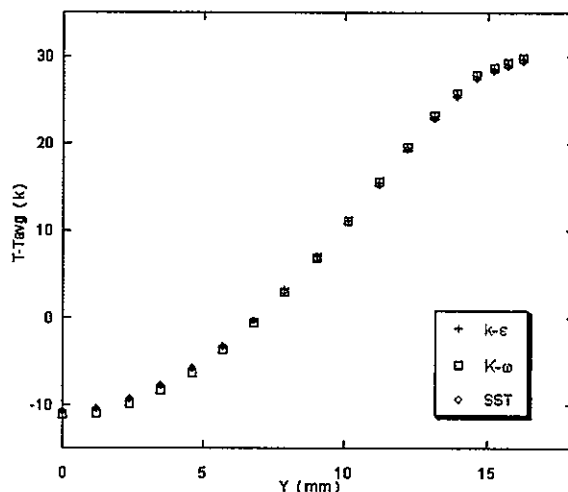
Fig.14 Temperature measurement location
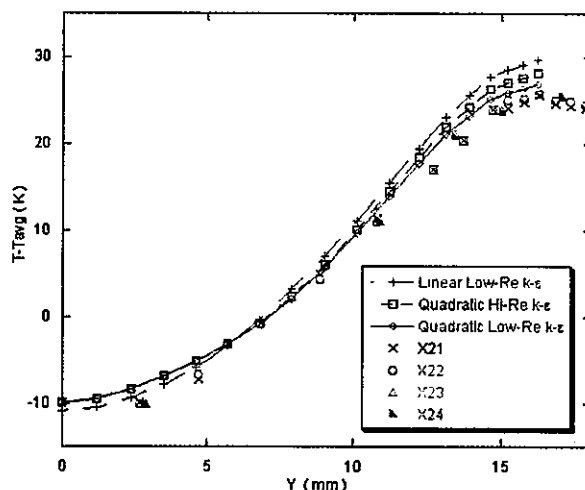
Fig.15 Temperature measurement location

Figure 14 shows how the low-Reynolds form of k-ε, k-ω and the SST model produce the same predictions for the sodium temperature distribution, and therefore only the k-ε is presented in the comparison with the experimental data. All these models over predict in the same measure the temperature values in the small gap region between pins. Only the non linear models are capable of producing a closer agreement with the experimental data (only the result of the quadratic low-Reynolds model are shown, since they present no difference from the cubic one). The figure also shows how, the hi-Reynolds form of the quadratic model, with the use of a law-of-the-wall, can benefit from the anisotropic modeling.

The various linear models show therefore a strong consistency, but at the same time, being unable to account for anisotropy, cannot produce a qualitatively correct

prediction, in this respect the non-linear modeling correctly captures the trend but still cannot get a close agreement in the narrow gap region.

VII. Conclusion

A large number of isothermal, and heat transfer simulations have been carried out to test the performances of numerous turbulence models. The results have clearly shown that to correctly model flow in tight lattice bundle it is necessary to adopt an approach capable of describing anisotropic turbulence. Comparisons show that the secondary flow, that arises from this anisotropy, seems to be responsible of an homogenization of velocity and temperature distribution in the channel. In particular experimental data show a strong flattening of the wall shear stress towards the channel center, which numerical predictions could not correctly reproduce. In all cases the non-linear models could therefore show improved predictions, due to their ability to reproduce in some extent the turbulence driven secondary motion, but improvements to the models are needed for a better agreement.

From the point of view of computational requirements, all low-Re form of the models have shown to require very fine grids in the near wall region to obtain a correctly converged solution. This requirement does not allows us, at the moment, to adopt these models for the simulation of large geometries involving heat transfer, as for instance a complete assembly. For the benchmark 2 case for example, the model of ¼ of the channel, for a height of 150 hydraulic diameters required the use of almost 3 million cells, which showed to be an upper limit for our computations.

High Reynolds number version of the non-linear model is still the only available approach for large geometries. In this regard we intend to test the performances of the V2F approach in a near future being claimed to produce a correct modeling of the viscous sub-layer with reduced computational requirements.

References
1) W. D. Magwood, "DOE NERI Agenda: Moving Forward on Generation IV Reactor Design," *Proc. PHYSOR 2000*, Pittsburgh, PA, May 2000 (2000).
2) M. D. Carelli, K. Miller, C. V. Lombardi, N. Todreas, E. Greenspan, H. Ninokata, F. Lopez, L. Cinotti, J.Collado, F.Oriolo, "IRIS: Proceeding Towards the Preliminary Design " *Proceedings of the 10th International Conference on Nuclear Engineering*, Arlington, VA, April 14-18, 2002, 10-22947 (2002).
3) B. Petrovic, M. D. Carelli, E. Greenspam, M. Milosevic, J. Vujic, E. Padovani, F. Ganda "First Core and Refueling Options for IRIS" *Proceedings of the 10th International Conference on Nuclear Engineering*, Arlington, VA, April 14-18, 2002, 10-22581 (2002).
4) A. Romano, V. Kriventsev, H. Ninokata, N.E. Todreas "Novel Fuel Geometries for the Generation IV IRIS Reactor" *Proceedings of the 9th International Conference on Nuclear Engineering*, Nice, France, April 8-12, 2001 (2001).
5) A. Romano, N. E. Todreas, *"Analysis of Novel Fuel Geometries for the Geneartion IV "IRIS" Reactor "* Department of Nuclear Engineering, Massachusetts Institute of Technology, MIT-ANP-TR-073 (2000).
6) C. J. Cheng, J. Shenq-Yuh, *"Fundamentals of Turbulence Modeling"* Taylor and Francis, (1998).
7) C. J. Freitas, "Selected Benchmarks from Commercial CFD Codes" *Journal of Fluid Engineering* 117, (1995).
8) H. K. Myong, "Numerical Investigation of Fully Developed Turbulent Fluid Flow and Heat Transfer in a Square Duct" *Int. J. Heat and Fluid Flow*, Vol. 12, No. 4, (1991).
9) H. K. Myong, N. Kasagi, "Prediction of Anisotropy of the Near Wall Turbulence with an Anisotropic Low-Reynolds-Number K-ε Turbulence Model" Journal of Fluids Engineering, Vol. 112, pp 521-524, (1990).
10) J. L. Lumley, "Toward a Turbulent Constitutive Relation", *J. Fluid Mechanics*, 41-2, pp. 413-434, (1970).
11) S. Pope, "A More General Effective-Viscosity Hypothesis", *J. Fluid Mechanics*, 72, pp. 331-340, (1975).
12) T. J. Craft, B. E. Launder, K. Suga, "Prediction of Turbulent Transitional Phenomena with a Non-Linear Eddy-Viscosity Model", J. of Heat and Fluid Flow18, pp. 15-28, (1997).
13) K. Suga, "Recent Developments in Eddy Viscosity Modelling of Turbulence", *R&D Review of Toyota CRDL*, Vol. 33, No 1. (1998).
14) D. C. Wilcox, *"Turbulence Modelling for CFD"*, 2nd edition, DCW Industries, Inc. (1998).
15) F. R. Menter, "Zonal two equation k-ω turbulence models for aerodynamic flows", *Proc. 24th Fluid Dynamics Conf.*, Orlando, Florida, USA, 6-9 July, Paper No. AIAA 93-2906, (1993).
16) V. C. Patel, W. Rodi, G. Scheuerer, "Turbulence Models for Near-Wall and Low Reynolds Number Flows – a review", *AIAA Journal* 23, 1308, (1985).
17) P. A. Durbin, "Separated Flow Computations with the k-e-v2f model", *AIAA Journal*, Vol. 33, No. 4, (1995).
18) B. E. Launder, D.B. Spalding, 'The numerical computation of turbulent flows', *Comp. Meth. in Appl. Mech. and Eng.*, 3, pp. 269-289, (1974).
19) "Benchmark Problem Task 1" *9th IAHR Working Group on Advanced Nuclear Reactor Thermal Hydraulics*, Grenoble, France, (1998).
20) E.Baglietto, H. Ninokata "Selection of an Appropriate Turbulence Model to Evaluate Performances of Novel Fuel Geometries for The "IRIS" Reactor", *4TH ASME_JSME Joint Fluids Engineering Conference* Honolulu, Hawaii, USA, FEDSM2003-45429 (2003).
21) R. Moller, *"TEGENA: Detailed Experimental Investigations of Temperature and Velocity Distributions in Rod Bundle Geometries with Turbulent Sodium Flow"*, Kernforschungszentrum Karlsruhe, (1989).

22) S.V. Patankar, D.B. Spalding, 'A Calculation Procedure For Heat, Mass And Momentum In Three-Dimensional Parabolic Flows', *Int. J. Heat Mass Transf*, 15, (1972).
23) *"STAR-CD Version 3.10 Manual, Methodology"* Computational Dynamics Limited, (1999).

Appendix E

Selection of an Appropriate Turbulence Model to Evaluate Performances of Novel Fuel Geometries for The "Iris" Reactor

SELECTION OF AN APPROPRIATE TURBULENCE MODEL TO EVALUATE PERFORMANCES OF NOVEL FUEL GEOMETRIES FOR THE "IRIS" REACTOR

Emilio Baglietto and Hisashi Ninokata
Research Laboratory for Nuclear Reactors
Tokyo Institute of Technology
Tokyo, Japan

ABSTRACT

A comparative study of different turbulence models is presented to select the most appropriate one for the evaluation of thermo-hydraulic performances of innovative core designs. The standard k-ε and different, linear and non linear, low Reynolds k-ε models are applied to fully developed flow in a triangular lattice rod bundle. Shear stresses and velocity distributions are evaluated using the commercial code Star-CD. The relative performance of the models is assessed indicating different predictions between linear and non linear turbulence closures. The results show that the capability of non linear models to account for anisotropic effects leads to better performances in modeling turbulent flow in tight lattice rod bundles. This capability is clearly shown by the existence of a secondary flow field in the plane normal to the flow direction.

INTRODUCTION

The International Reactor Innovative and Secure (IRIS) is an advanced, Generation IV [1], light water reactor being developed by an international consortium of industry, laboratory, university and utility establishments, led by Westinghouse. Its design is based on proven LWR technology, so that no new technology development is needed and near term deployment is possible [2]. At the same time evolutionary core solutions are being developed for future reloads [3].

An ultra long life, high conversion core design is currently under development. This core will be characterized by a very tight lattice, with relatively small water volume fraction. To obtain such a result we must introduce innovative fuel configurations to obtain a more uniform utilization of the coolant. A main undesirable aspect of classic triangular lattice in fact is the non-homogeneous distribution of water around fuel pins, which results in non-uniform circumferential clad temperature and wall shear stress distribution [4]. To address these goals we aim to enhance turbulence and flow-mixing, keeping at the same time the pressure drops through the core as low as possible.

To evaluate the performances of the novel configurations we must employ a suitable method able to model 3-dimensional thermal hydraulics of complex geometries. Classical codes used in nuclear industries, such as sub-channel analysis codes are not appropriate for our purpose, being calibrated on specific geometries and operational conditions. As it is well known, the finest instruments for modeling turbulence are DNS and LES. The computing requirements however are extremely high; in the DNS case for example they scale as $Re^{9/4}$, making them, at the moment, unsuitable for our analysis [5]. Modern CFD codes of practical use are based on the so-called Reynolds Averaged Navier Stokes equations (RANS) models, where the terms representing turbulence interactions are modeled in terms of the mean flow variables, as for example in the widely used k-ε approach. However, the reliability and accuracy of the results cannot easily be assured [6]. Turbulence modeling is usually considered the weakest point in CFD analysis. This work intends to systematically assess the turbulence models available and determine if they could be used to successfully evaluate the thermo-hydraulic performances of the new geometries. In particular we intend to evaluate the importance of anisotropy in modeling flow inside fuel bundles.

THE IRIS PROJECT

Reactor Design

IRIS (International Reactor Innovative and Secure) is being developed by an international consortium of industry, laboratory, university and utility establishments, led by Westinghouse. The consortium currently includes 20 members from 9 countries. The IRIS design addresses key requirements associated with advanced reactors, including enhanced safety, improved proliferation resistance, competitive electricity production cost, and improved waste management. This reactor design is based on proven LWR technology, so that no new

technology development is needed. As a result, IRIS has potential for near term deployment, around 2012. IRIS is a modular, medium size (335 MWe) PWR with an integral pressure vessel configuration (Fig. 1).

In contrast to loop PWRs where the primary system components are located outside the reactor pressure vessel, these components are either eliminated (large external loop pipes) or relocated (reactor coolant pumps, pressurizer, steam generators) in the IRIS integral configuration. This may be exploited to improve safety characteristics as well as to reduce the containment size. Indeed, one of the main reasons for the attractiveness of IRIS is its improved safety, which is achieved through the Safety by Design approach [7] [8].
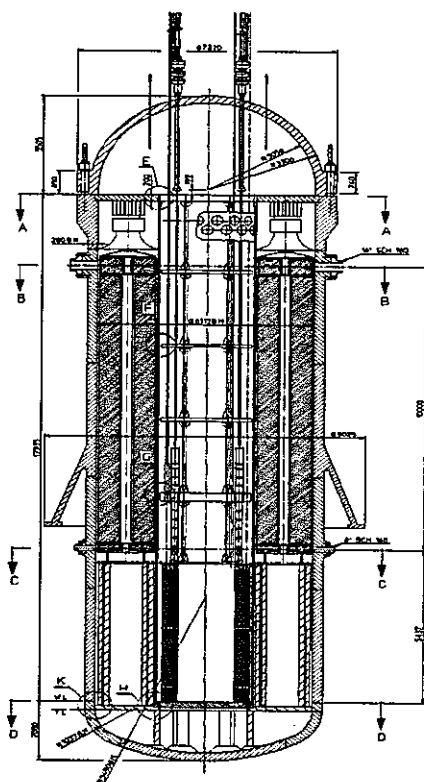

Figure 1 – IRIS Integral Primary System

Long and Ultra-Long Life Core

The reactor design is, as already stated, based on proven technology but, at the same time, aim was to introduce improvements as compared to present PWRs. These opposing requirements resulted in an evolutionary approach to fuel and core design, balancing new features and the need to avoid extensive testing and demonstration programs.

Most of the present power reactors operate on a 12-month or 18-month multi-batch refueling cycle. Objective for IRIS is to extend the cycle length significantly, to four or more years and to operate in a straight burn (single batch) mode. In particular, to avoid licensing issues, improved fuel utilization is required instead of an increased fissile content.

Fuel utilization may be improved in LWRs either via enhanced conversion achieved by reduced moderation, or via enhanced thermal neutron utilization achieved by increased

moderation [9][10]. The second option has been selected for the first deployment of the reactor. In place of the typical 17x17 PWR fuel assembly, IRIS adopts a 15x15 assembly with an increased fuel to moderator volume ratio, and a reduced soluble boron concentration to retain a negative moderator temperature coefficient (MTC).

At the same time an ultra long life core design is pursued. In order to increase core life to over 10 years, a very tight lattice design is necessary, capable of consistently increasing fuel utilization. This new core represents a strong engineering challenge, requiring introduction of innovative solutions and will require licensing because of its higher enrichment. Thus it can be envisioned as a reload option available after 2020.

Novel Geometries

As stated, in order to achieve a life of over ten years it is necessary to adopt a tight lattice design core, with a p/d ratio of ~1.1, respecting of course important constraints as:
 - Same power as the open lattice core
 - Fitted in the same envelope
 - Negative void coefficient
 - Economically competitive

It is known that a tightly pack design presents diverse drawbacks, both on neutronics and thermo-hydraulics. The attention in this first stage is directed to the thermo-hydraulic design which presents obstacles that have to be overcome before proceeding in the design.

Preliminary comparisons have shown that novel fuel shapes, as for example hexagonal pins, could improve the coolant utilization and reduce the fuel centerline temperature in comparison to the classical cylindrical pins solution. In turn, these solutions, which also require the presence of spacers, induce unacceptably high pressure drops through the core.

To overcome this limitations very innovative shapes are envisioned to achieve better coolant utilization through increased turbulence, and in particular to highly reduce the hot-channel problem typical in tight geometries. Moreover this new designs eliminate the need for spacers through a self-standing solution.

TURBULENCE MODELING

It is undeniable that CFD has become an irreplaceable tool for thermo-hydraulics. However, the turbulence modeling is up-to-date an unsolved issue. There is no generally applicable modeling strategy that has satisfactory accuracy in arbitrary flow problems [11]. Commercial codes offer several turbulent closure models already implemented and the code that we adopt, in particular, Star-CD, offers various forms of low and high Reynolds number k-ε models. This work intends to systematically assess the turbulence models available and determine if they could be used to successfully evaluate the thermo-hydraulic performances of the new geometries.

The classical approach to CFD analysis is through the high Reynolds number form of the k-ε. One important deficiency of such a model is the fact that anisotropic effects are not accounted for. In simple terms, since the viscosity is a scalar, each component of the stress affects its strain to the same extent. For this reason, flows where turbulent intensity gradients, and

hence the augmentation effects of secondary strain rates, are important cannot be accurately predicted. The most quoted example is the secondary flow that originates in a square duct due to the gradients of the turbulent shear stresses [12]. This kind of secondary flows will originate in some extent also in a tight lattice sub-channel, and could be important for a correct evaluation of the convective heat transfer. For this reason we select a benchmark that refers to such geometry, to evaluate the different closure relationships.

Another limit of the standard approach, based on the high Reynolds formulation of the k-ε model, is that it cannot be applied in the immediate vicinity of the wall, thus requiring the use of empirical wall functions to bridge the gap between the solid boundary and the turbulent core. The universality of such functions however breaks down for complex flows, and therefore low Reynolds formulations are preferable for our analysis

Low Reynolds number model

We do not illustrate the standard k-ε model, which can be found in reference [13]. We present only the closure equations for the low Reynolds number formulation especially pointing out the difference between the linear and non-linear models.

Turbulence energy

$$\frac{1}{\sqrt{g}}\frac{\partial}{\partial t}\left(\sqrt{g}\,\rho k\right)+\frac{\partial}{\partial x_j}\left(\rho\tilde{u}_j k-\frac{\mu_{eff}}{\sigma_k}\frac{\partial k}{\partial x_j}\right)=$$

(1)

$$\mu_t(P+P_B)-\rho\varepsilon-\frac{2}{3}\left(\mu_t\frac{\partial u_i}{\partial x_i}+\rho k\right)\frac{\partial u_i}{\partial x_i}+\mu_t P_{NL}$$

where

$$\mu_{eff}=\mu+\mu_t$$

(2)

and the turbulence viscosity μ_t is linked to k and ε via:

$$\mu_t=f_\mu\frac{C_\mu\rho k^2}{\varepsilon}$$

(3)

$$P\equiv 2s_{ij}\frac{\partial u_i}{\partial x_j}$$

(4)

$$P_B\equiv-\frac{g_i}{\sigma_{h,t}}\frac{1}{\rho}\frac{\partial\rho}{\partial x_i}$$

(5)

$$P_{NL}=-\frac{\rho}{\mu_t}\overline{u_i'u_j'}\frac{\partial u_i}{\partial x_j}-\left[P-\frac{2}{3}\left(\frac{\partial u_i}{\partial x_i}+\frac{\rho_k}{\mu_t}\right)\frac{\partial u_i}{\partial x_i}\right]$$

(6)

$P_{NL}=0$ for linear models and σ_k is an empirical coefficient. The first term on the right-hand side of equation (1) represents turbulent generation by shear and normal stresses and buoyancy forces, the second viscous dissipation, and the third

amplification or attenuation due to compressibility effects. The last term accounts for the non-linear contributions.

Turbulence dissipation rate

$$\frac{1}{\sqrt{g}}\frac{\partial}{\partial t}\left(\sqrt{g}\,\rho\varepsilon\right)+\frac{\partial}{\partial x_j}\left(\rho\tilde{u}_j\varepsilon-\frac{\mu_{eff}}{\sigma_\varepsilon}\frac{\partial\varepsilon}{\partial x_j}\right)=$$

(7)

$$C_{\varepsilon1}\frac{\varepsilon}{k}\left[\mu_t(P+P')-\frac{2}{3}\left(\mu_t\frac{\partial u_i}{\partial x_i}+\rho k\right)\frac{\partial u_i}{\partial x_i}\right]+C_{\varepsilon3}\frac{\varepsilon}{k}\mu_t P_B$$

$$-C_{\varepsilon2}\left(1-0.3e^{-R_t^2}\right)\rho\frac{\varepsilon^2}{k}+C_{\varepsilon4}\rho\varepsilon\frac{\partial u_i}{\partial x_i}+C_{\varepsilon1}\frac{\varepsilon}{k}\mu_t P_{NL}$$

where σ_ε, $C_{\varepsilon1}$, $C_{\varepsilon2}$, $C_{\varepsilon3}$ and $C_{\varepsilon4}$ are empirical coefficients whose values are given in Table 1. The right-hand side terms represent analogous effects to those described above for the k equation.

Table 1: Values Assigned to Model Coefficients

C_μ	σ_k	σ_ε	σ_b	σ_m	$C_{\varepsilon1}$	$C_{\varepsilon2}$	$C_{\varepsilon3}$	$C_{\varepsilon4}$	k	E
0.09	1.0	1.22	0.9	0.9	1.44	1.92	1.44	-0.33	0.42	9.0

The term P' is given by:

$$P'=1.33\left[1-0.3e^{-R_t^2}\right]\left[P+2\frac{\mu}{\mu_t}\frac{k}{y^2}\right]e^{-0.00375Re_y^2}$$

(8)

μ_t is defined in equation (3) with f_μ given by

$$f_\mu=\left[1-e^{-0.0198Re_y}\right]\left(1+\frac{5.29}{Re_y}\right)$$

(9)

in which

$$Re_y=\frac{y\sqrt{k}}{\nu}$$

(1 0)

R_t is the turbulent Reynolds number given by

$$R_t=\frac{k^2}{\nu\varepsilon}$$

(1 1)

The equation for dissipation is not solved at the near-wall cell. Rather, the dissipation, ε_P, at the near-wall cell is fixed as follows:

$$\varepsilon_P = \frac{2vk}{y^2}$$

(1   2   )

where y+ for the near-wall cell is of the order of 1.0.

Linear and Non-linear Constitutive Relations

Linear model

The turbulent Reynolds stresses and scalar fluxes are linked to the ensemble averaged flow properties as follows

$$-\overline{\rho u_i' u_j'} = 2\mu_t S_{ij} - \frac{2}{3}\left(\mu_t \frac{\partial u_k}{\partial x_k} + \rho k\right)\delta_{ij}$$

(1   3   )

$$\overline{\rho u_j' h'} = -\frac{\mu_t}{\sigma_{h,t}}\frac{\partial h}{\partial x_j}$$

(1   4   )

$$\overline{\rho u_j' m_m'} = -\frac{\mu_t}{\sigma_{m,t}}\frac{\partial m_c}{\partial x_j}$$

(1   5   )

where

$$k \equiv \frac{\overline{u_i' u_i'}}{2}$$

(1   6   )

is the turbulent kinetic energy, μ_t is the turbulent viscosity, and $\sigma_{n,t}$, $\sigma_{m,t}$ are the turbulent Prandtl and Schmidt numbers, respectively. The turbulent viscosity μ_t is, as said, linked to k and ε via the equation (3) while f_μ is given by equation (9).

We can notice in the above relationships that each component of the shear stress influences only one component of the velocity gradient, and therefore anisotropy cannot be accounted for. Non linear models try to cater for this defect by adopting non-linear relationships between Reynolds stresses and the rate of strain.

Quadratic model

For the quadratic model, the constitutive relations for the Reynolds stresses are as follows:

$$-\overline{\rho}\frac{\overline{u_i' u_j'}}{k} = \frac{2}{3}\left(\frac{\mu_t}{k}\frac{\partial u_k}{\partial x_k} + \rho\right)\delta_{ij} - \frac{\mu_t}{k}S_{ij} +$$

$$C_1\frac{\mu_t}{\varepsilon}\left[S_{ik}S_{kj} - \frac{1}{3}\delta_{ij}S_{kl}S_{kl}\right] + C_2\frac{\mu_t}{\varepsilon}\left[\Omega_{ik}S_{kj} + \Omega_{jk}S_{ki}\right] +$$

(17)

$$C_3\frac{\mu_t}{\varepsilon}\left[\Omega_{ik}\Omega_{jk} - \frac{1}{3}\delta_{ij}\Omega_{kl}\Omega_{kl}\right]$$

where

$$C_1 = \frac{c_{NL1}}{\left(c_{NL6} + c_{NL7}S^3\right)C_\mu}, \quad C_2 = \frac{c_{NL2}}{\left(c_{NL6} + c_{NL7}S^3\right)C_\mu}$$

(1   8   )

$$C_3 = \frac{c_{NL3}}{\left(c_{NL6} + c_{NL7}S^3\right)C_\mu}$$

and

$$C_\mu = \frac{A_0}{A_1 + A_2 S + A_3 \Omega}$$

(1   9   )

where A_0, A_1, A_2, A_3, c_{NL1}, c_{NL2}, c_{NL3}, c_{NL6}, c_{NL7} are empirical coefficients whose values are shown in table 2. Once again the turbulent viscosity μ_t is defined in equation (3).

S_{ij} and Ω_{ij} are elements of the mean strain and vorticity tensors, respectively, and are given by

$$S_{ij} = \frac{\partial u_i}{\partial x_j} + \frac{\partial u_j}{\partial x_i}$$

(2   0   )

$$\Omega_{ij} = \frac{\partial u_i}{\partial x_j} - \frac{\partial u_j}{\partial x_i}$$

(2   1   )

The other two terms required to complete the definition of C_μ are as follows:

$$S = \frac{k}{\varepsilon}\sqrt{\frac{1}{2}S_{ij}S_{ij}}$$

(2   2   )

$$\Omega = \frac{k}{\varepsilon}\sqrt{\frac{1}{2}\Omega_{ij}\Omega_{ij}}$$

(2   3   )

Cubic model

The constitutive equation for the cubic model is obtained by adding a high order term to the equation (17). The final expression is

$$-\overline{\rho}\frac{\overline{u_i' u_j'}}{k} = \frac{2}{3}\left(\frac{\mu_t}{k}\frac{\partial u_k}{\partial x_k} + \rho\right)\delta_{ij} - \frac{\mu_t}{k}S_{ij} +$$

$$C_1\frac{\mu_t}{\varepsilon}\left[S_{ik}S_{kj} - \frac{1}{3}\delta_{ij}S_{kl}S_{kl}\right] + C_2\frac{\mu_t}{\varepsilon}\left[\Omega_{ik}S_{kj} + \Omega_{jk}S_{ki}\right] +$$

(24)

$$C_3\frac{\mu_t}{\varepsilon}\left[\Omega_{ik}\Omega_{jk} - \frac{1}{3}\delta_{ij}\Omega_{kl}\Omega_{kl}\right] + C_4\mu_t\frac{k}{\varepsilon^2}\left(S_{ki}\Omega_{lj} + S_{kj}\Omega_{li}\right)S_{kl} +$$

$$+ C_5\mu_t\frac{k}{\varepsilon^2}\left(S_{kl}S_{kl} - \Omega_{kl}\Omega_{kl}\right)S_{ij}$$

where

$$C_4 = c_{NL4} C_\mu^2$$

$$(\qquad 2 \qquad\qquad 5 \qquad\qquad)$$

$$C_5 = c_{NL5} C_\mu^2$$

$$(\qquad 2 \qquad\qquad 6 \qquad\qquad)$$

the turbulent viscosity μ_t is defined in equation (3), c_{NL4}, c_{NL5} are empirical coefficients given in table 2.

Table 2: Values Assigned to Coefficients

A_0	A_1	A_2	A_3	c_{NL1}	c_{NL2}	c_{NL3}	c_{NL4}	c_{NL5}	c_{NL6}	c_{NL7}
0.667	1.25	1.0	0.9	0.75	3.75	4.75	-100	-2.0	1000	1.0

BENCHMARK PROBLEM

The benchmark selected for our work refers to the evaluation of shear stress and velocity field distribution in an hexagonal tight lattice rod bundle. The p/d ratio of the lattice is 1.17 [14].

The experiments were performed in a wind tunnel using a 19-rods model of the fuel assembly. Geometrical data of the model cross section are shown in figure 2. Length of the model is 6m. The wetted model perimeters for the assumed flow regimes can be taken as hydraulically smooth.
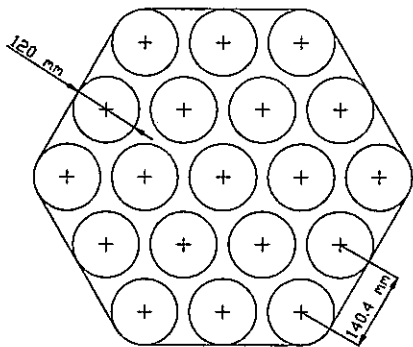

Figure 2 – Benchmark Geometry

Measurements have been performed inside the bundle at a distance of 5600 mm from the model inlet and 400 mm from the outlet, that is in the region of hydraulically fully developed turbulent flow and without the back effect of outlet cross-section change. Data refer to the middle-cell, and we therefore assume that the influence of the walls around the rod bundle is negligible. Shear stress and axial mean velocities have been obtained with Pitot and Preston probes.

The following table shows the physical parameters of the experiment.

Table 3 – Physical Parameters

Fluid	Density	Kinematic Viscosity	Reynolds Number
Air	1.131 kg/m³	1.591e-5 m²/s	64300

SIMULATION MODEL

As stated before the code Star-CD has been used for the

simulation. Due to the symmetry of the problem we do not need to simulate the complete bundle. It is sufficient to describe the elementary cell, as showed in figure 3, with the appropriate symmetry boundaries.
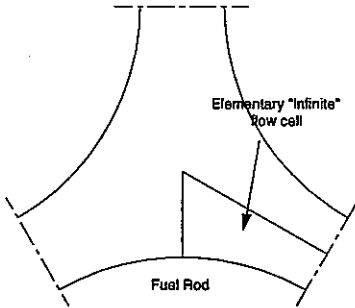

Figure 3 – Elementary Cell

In the axial direction, as the flow is fully developed, periodic conditions can be applied to limit the mesh number. The simulated cell has a height of 15mm.

Numerical Procedure

The differential equations governing the conservation of mass, momentum, energy, etc. within the fluid, are discretized in the code by the finite volume (FV) method. The discretized equations are solved in a segregated manner with the SIMPLE (Semi-Implicit Method for Pressure-Linked Equations) algorithm [15].

For the spatial discretization a first order upwind differencing (UD) scheme is considered sufficient, but a quadratic upstream interpolation of convective kinematics (QUICK) is also applied to assess the independency of results from discretization practices. Description of these methods can be found in reference [13].

Computational Grids

It is very important to study the dependency of the results on the grid resolution, to demonstrate the grid-convergence of the solution, as also the Journal of Fluid Engineering has invoked in the new policy statement on numerical uncertainty. For this reason three different grid resolutions have been used in our analysis as shown in figure 4.
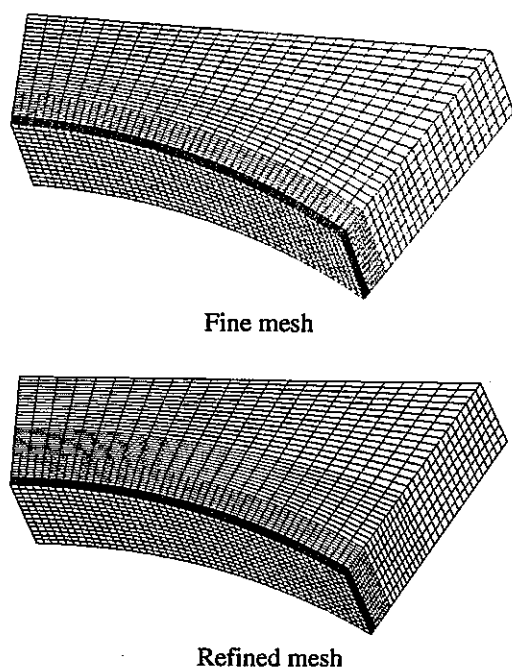

Coarse mesh
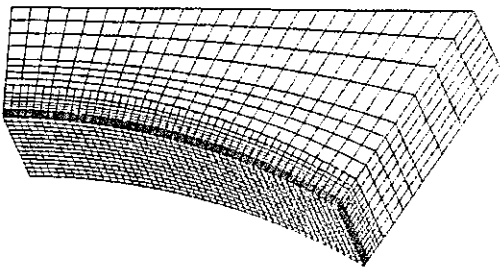
Fine mesh

Refined mesh

Figure 4 – Grid resolutions

As shown in the figures, in the near wall region the grid is very fine. For low Reynolds number models indeed this region is in most respects treated in the same way as the interior flow, with the no-slip condition imposed at the boundary cell faces. Prescription is nevertheless that the y+ value in the first cell be around 1.0.

In the case instead of standard high Reynolds model, laws-of-the-wall are adopted in the near wall region, and thus the y+ value of the first cell should be >20. If y+ values are too low, the point where the logarithmic velocity profile starts is too close to the wall and hence the velocity gradient is too high. Figure 5 shows the corresponding fine mesh for the high Reynolds number case.
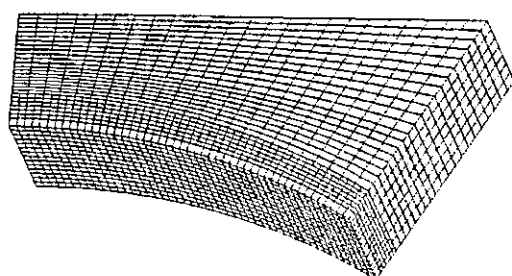

Figure 5 – Standard Method Grid

The total number of cells varies from 10,000 for the coarse grid, to 16,000 for the finest one in the case of low Reynolds models, and from 4,000 to 7,000 for the standard method.

RESULTS

Convergence and Grid Dependence
All turbulence models have been tested on the different

meshes to analyze grid dependency. In general, for all models the results obtained for the fine and refined grids provided the same values, showing that the fine grid is satisfactory for our case. In particular the standard method exhibited very low dependency on grid resolution, presenting very close results for the coarse mesh as well.

a) Standard (UD)   b) Low-Re (UD)

c) Cubic (UD)   d) Cubic (QUICK)
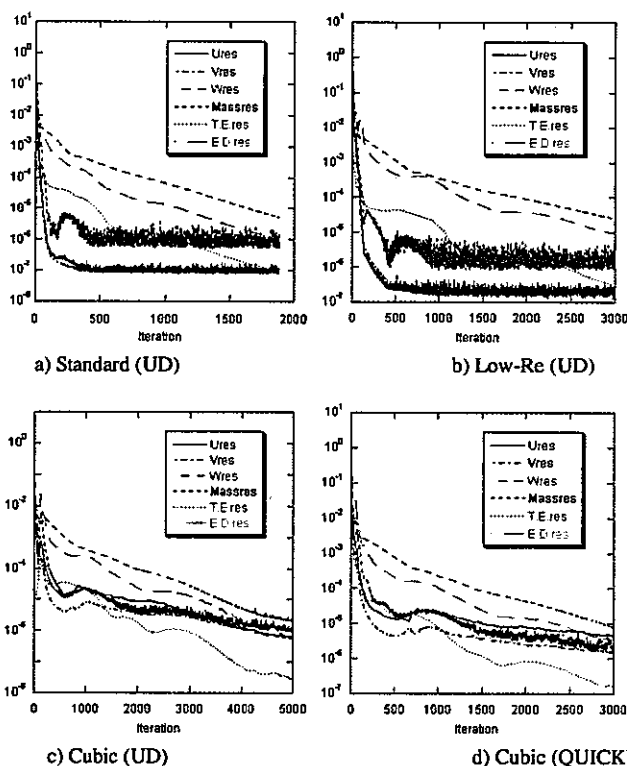
Figure 6 – Convergence histories for velocities, mass, k and ε dissipation residuals

The comparison between the first order upwind difference and the QUICK discretization schemes showed no dependency of the results upon the numerical technique. Figure 6 shows the residual histories, normalized by their values at the first iteration, for the various methods.

It is clear that the number of iterations needed to reach convergence increases with the complexity of the model. The use of a higher order scheme anyhow can accelerate the convergence as shown by the comparison between c) and d).

Shear Stress
Experimental data are available for the shear distribution along the wetted surface of the rod versus the azimuth φ, as shown in figure 7.
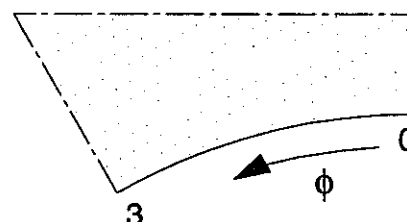
Figure 7 – Stress Distribution

These data are compared to those calculated from the simulation for the different turbulence models. Figure 8 shows that, as expected, the standard k-ε model cannot correctly follow the flattening of the shear stress towards the center of the channel, being unable to account for anisotropic effects, but can obtain quantitatively good predictions. The next figure shows the results of the linear low Reynolds k-ε model. The behavior is clearly the same as that for the standard method, but the quantitative disagreement is higher. The difference can be explained by the fact that in the standard model, the code uses an algebraic law-of-the-wall that is adjusted to give optimal average predictions, on the contrary the low Reynolds model solves the standard equations also in the near wall regions, retaining validity in any geometry, but thus showing the limits of isotropic modeling, which can predict correctly the narrow region, but completely ignore the flattening due to anisotropy.

Figure 10 shows the results of the two non-linear models. As we can see the curve is flatter in this case, since some anisotropy is accounted for, and even if the qualitative agreement is still limited, quantitatively the agreement is satisfactory.
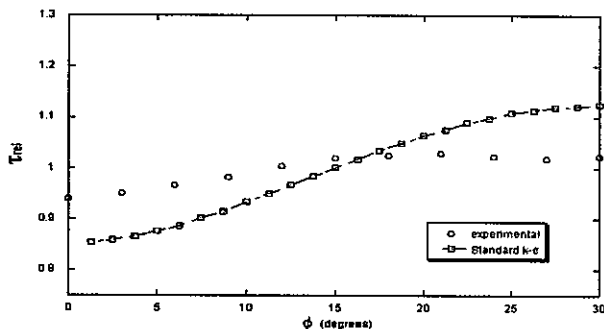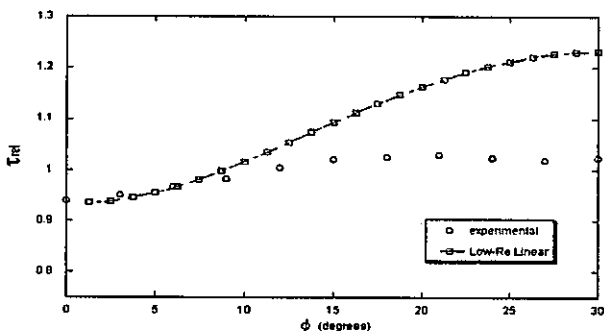

Figure 8 – Standard k-ε

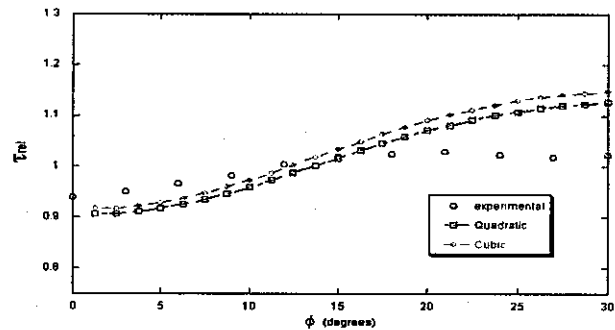**Figure 9 – Linear Low Reynolds**

Figure 10 – Non-linear Low Reynolds

Velocity Distribution

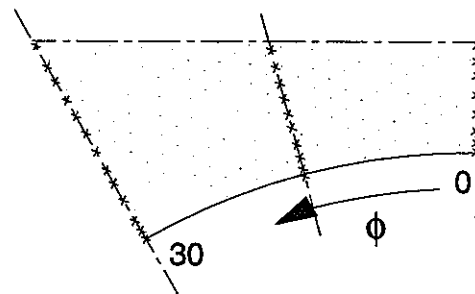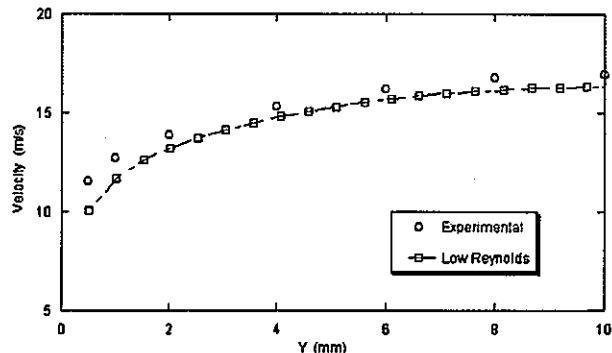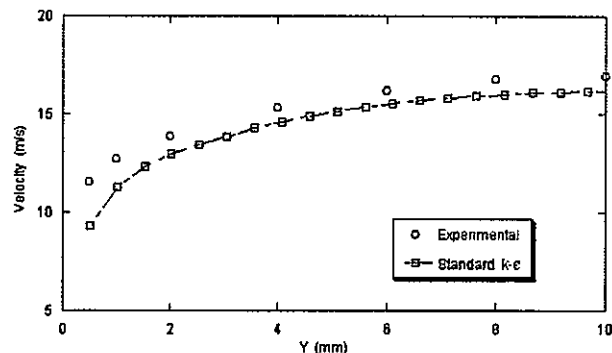Velocity profiles are compared with experimental data for three lines normal to the rod surface as shown in figure 11.
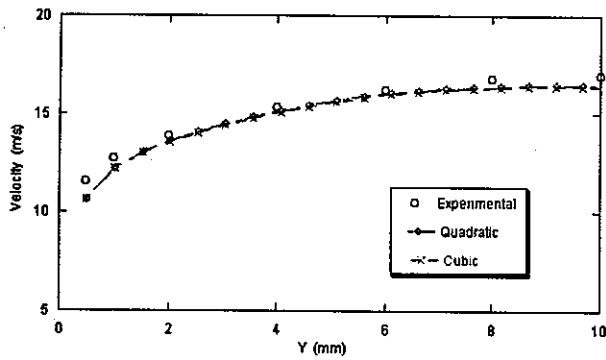

Figure 11 – Velocity sensors location

Figures 12, 13 and 14 show the results for the 0, 15 and 30 degrees location.

Figure 12 – Velocity at φ=0 degrees
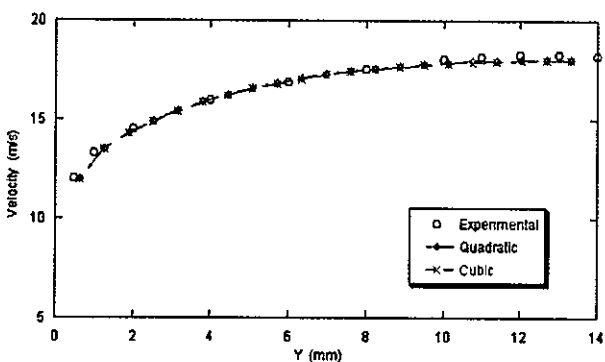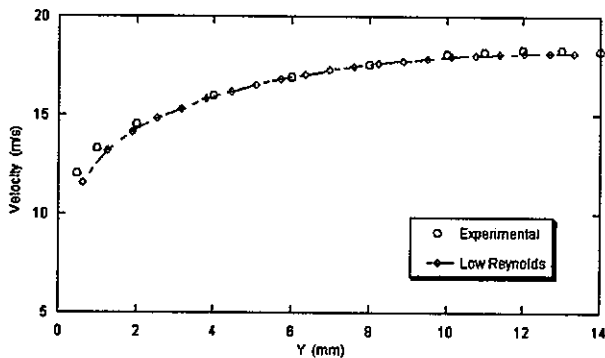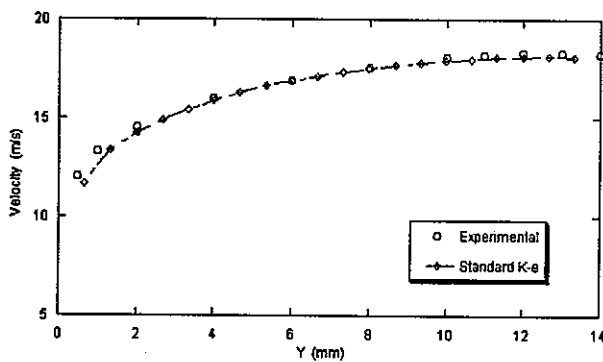
Figure 13 – Velocity at φ=15 degrees
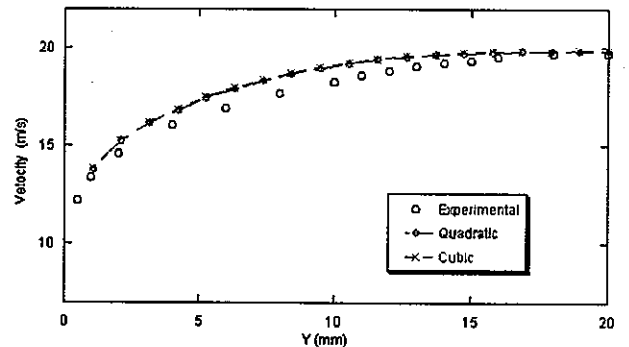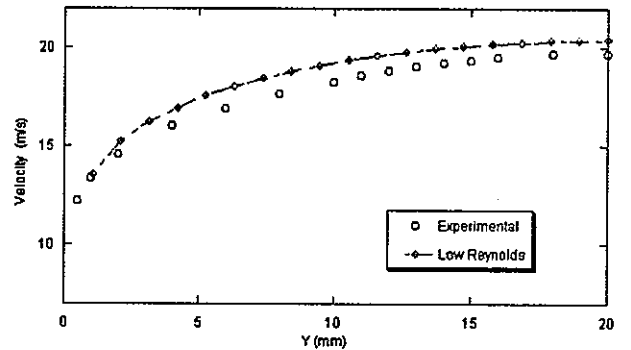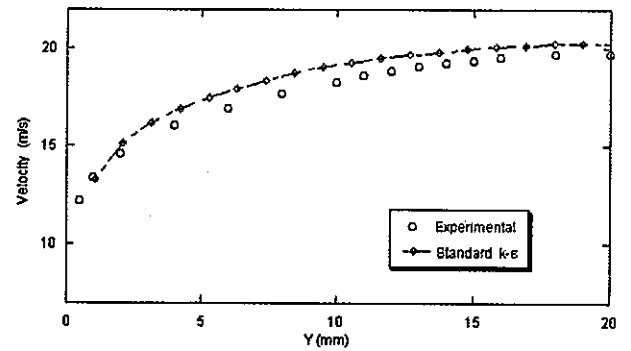
Figure 14 – Velocity at φ=30 degrees

The comparison with the experimental values shows how, adopting linear k-ε models, the simulations are underpredicting the velocity in the narrow area while overpredicting the distribution towards the center of the channel. This behavior is clearly explained by the inability of such models to account for anisotropy. The predictions of low and high Reynolds numbers are very similar, but we can see that near the wall, the use of law-of-the-wall gives poor qualitative and quantitative predictions. As expected, the non linear models provide more accurate predictions, still showing some underprediction in the narrow part of the channel. These models indeed are, as said, able to account for some anisotropy and this is evident in the formation of a secondary velocity field, as shown in figure 16. Here the velocity scale of the motion is about 0.5% of the axial velocity.

A particular discussion is related to the velocity distribution at the 30 degrees location. As shown the non-linear models are able to correctly predict velocities in the near wall and bulk region but show a different behavior in between these two

points. The experimental distribution is very flat in this zone as can be seen in figure 15. This might be a limitation of the models, but some doubts exist about the correctness of the experimental data.
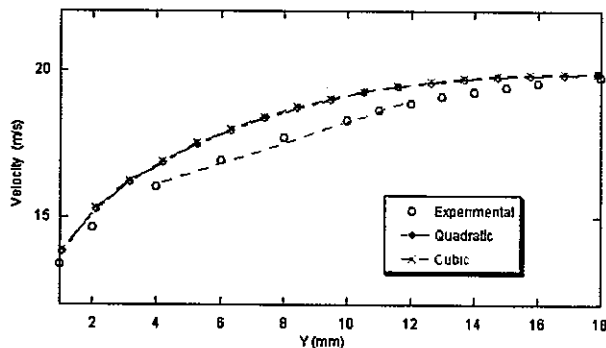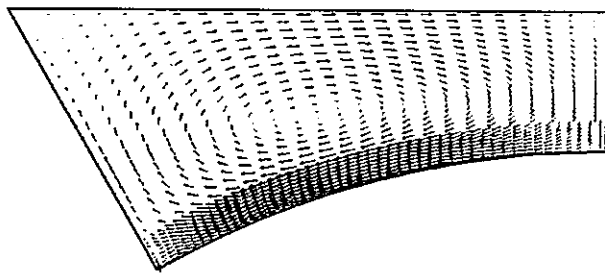

Figure 15– Flat velocity distribution

Figure 16– Mean secondary velocity field

CONCLUSIONS

A comparison of shear stress and velocity distribution predictions of different turbulence models has been presented for the case of fully developed flow in a tight triangular lattice assembly. Four models have been used, the standard k-ε, and three low Reynolds versions, linear quadratic and cubic. Grid convergence has been demonstrated with the use of three different resolutions. Accuracy of the spatial discretization has been evaluated with comparisons between a first and a third order accuracy method.

Evaluations have shown that all methods show limits in the shear stress predictions towards the center of the channel but have, in general, a reasonable quantitative agreement, in particular for the non linear models. Velocity fields predictions have shown that linear models, being incapable to account for anisotropy, cannot provide qualitatively accurate predictions, but can in general obtain an acceptable quantitative agreement, within 8-9% error. The standard method though exhibits limitations in the near wall region due to the use of an algebraic law-of-the-wall. Non linear models are instead able to account in some extent for anisotropy as shown by the existence of a secondary velocity field, thus providing much better qualitative and quantitative agreement capturing the correct velocity distributions within a 2-3%.

In the selection of an appropriate tool, for innovative geometries performance evaluation, we can conclude that the linear models showed limits in predicting the near wall region velocity distribution, that will be essential when evaluating the heat transfer coefficients and temperature distributions in the sub-channel. In this respect the accuracy of the non linear models showed to be much higher, making them, at the moment, our choice for performance evaluation. The case analyzed anyhow is fairly simple and it will be necessary to test such models on more complex flow problems, such as swirling flows, before proceeding further.

The work has in addition shown that low Reynolds models involve the use of a fine grid, which in our case required about 13,000 cells to obtain a convergent solution. This makes the requirement absolutely too high for studying a complete assembly, and limits the use of such models, for the moment, to smaller sections. On the opposite side lies the standard method, which even if incapable of correctly modeling anisotropic effects, showed a very low dependency on grid size, obtaining quasi-convergent results with very coarse meshes. This characteristic makes it suitable for modeling very complex geometries, up probably to a full core, with a number of cells around 10 millions.

REFERENCES

[1] Magwood, W. D., 2000, "DOE NERI Agenda: Moving Forward on Generation IV Reactor Design," *Proc. PHYSOR 2000*, Pittsburgh, PA, May 2000.

[2] Carelli, M. D., K. Miller, C. V., Lombardi, Todreas, N., E. Greenspan, H. Ninokata, F. Lopez, L. Cinotti, J.Collado, F.Oriolo,G. "IRIS: *Proceeding Towards the Preliminary Design*" *Proceedings of the 10th International Conference on Nuclear Engineering*, Arlington, VA, April 14-18, 2002.

[3] Petrovic, B., Carelli, M. D, E. Greenspam, M. Milosevic, J. Vujic, E. Padovani, F. Ganda "First Core and Refueling Options for IRIS" *Proceedings of the 10th International Conference on Nuclear Engineering*, Arlington, VA, April 14-18, 2002.

[4] Romano, A., V. Kriventsev, H. Ninokata, N.E. Todreas "Novel Fuel Geometries for the Generation IV IRIS Reactor" *Proceedings of the 9th International Conference on Nuclear Engineering*, Nice, France, April 8-12, 2001.

[5] Cheng, C. J., Shenq-Yuh, J., "Fundamentals of Turbulence Modeling" *Taylor and Francis*, 1998.

[6] Freitas, C. J. "Selected Benchmarks from Commercial CFD Codes" *Journal of Fluid Engineering* 117, 1995.

[7] Carelli, M. D., L. E. Conway, B. Petrovic, D. V. Paramonov, M. Galvin, N. E. Todreas, C. V. Lombardi, F. Maldari, M. E. Ricotti and L. Cinotti, "IRIS Reactor Conceptual Design," *Intl. Conf. On the Back-End of the Fuel Cycle (Global 2001)*, Paris, France, September 9- 13, 2001.

[8] Carelli, M. D., L. E. Conway, G. L. Fiorini, C. V. Lombardi, M. E. Ricotti, L. Oriani, F. Berra and N. E. Todreas, "Safety by Design: A New Approach to Accident Management in the IRIS Reactor," *IAEA-SR-218- 36, IAEA Intl. Seminar on Status and Prospects of Small and Medium Sized Reactors*, Cairo, Egypt, May 27-31, 2001.

[9] Carelli, M., L. Conway, B. Petrovic, D. Paramonov, M. Galvin, N. Todreas, C. Lombardi, F. Maldari and L. Cinotti, 2001, "Status of the IRIS Reactor Development", *Intl. Conf. on the Back-End of the Fuel Cycle (Global 2001)*, Paris, France, September 9-13, 2001.

[10] Petrovic, B., E. Greenspan, J. Vujic, T-p. Lou, G. Youinou, P. Dumaz and M. Carelli "International Collaboration and Neutronic Analyses in Support of the IRIS Project," 2000, *Trans. Am. Nucl. Soc.*, 83, pp. 186-187.

[11] Rautaheimo, P. P., et alt. "The Importance of Turbulence Modeling-Examples of Practical Flows" *ECCOMAS 2000*, Barcelona, September 11-14, 2000

[12] Hrenya, C.M. et alt. "Comparisons of Low Reynolds Number k-ε Turbulence Models in Predicting Fully Developed Pipe Flow" Chemical Engineering Science, Vol.50 Num.12, 1995.

[13] "STAR-CD Version 3.10 Manual, Methodology" *Computational Dynamics Limited*, 1999.

[14] "Benchmark Problem Task 1" *9th IAHR Working Group on Advanced Nuclear Reactor Thermal Hydraulics*, Grenoble, France, April 1998

[15] Patankar, S.V., and Spalding, D.B.1972.'A calculation procedure for heat, mass and momentum in three-dimensional parabolic flows', *Int. J. Heat Mass Transf*, 15.

Appendix F

STAR-CD コードによる稠密燃料格子の計算

Predictions on sodium cooled subchannel for various P/Ds

Introduction

Calculations adopting the low-Reynolds k-ε model have been performed on tight lattice subchannels with sodium cooling. The considered cases are p/d = 1.15, 1.10, and 1.05.
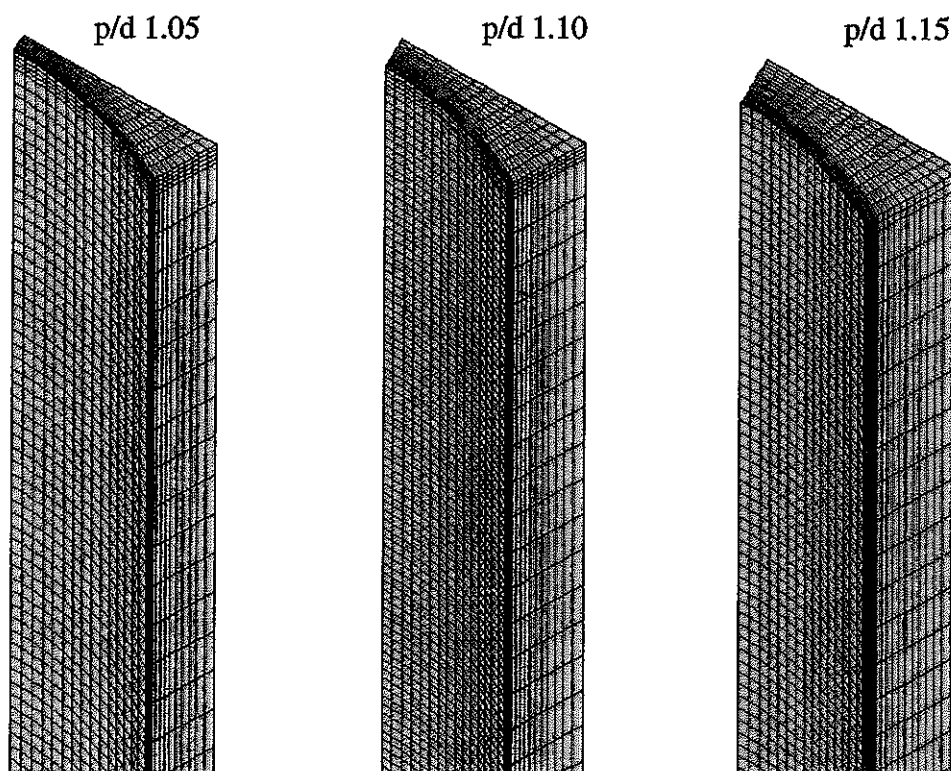
For all three cases the flow conditions are such to obtain a Re ~ 40,000 and the same total ΔT. The table presents the main flow parameters.

The following results are preliminary and not subject to quantitative assessment yet. Nevertheless a qualitative trend of velocity and temperature distributions is depicted and in general the friction factor in tight lattice bundles is calculated by STAR-CD in good agreement with Chen-Todreas model as shown in 4.3.2.

Flow conditions for the three cases

p/d = 1.15		p/d = 1.10		p/d = 1.05	
D equi (m)	2.978E-03	D equi (m)	2.172E-03	D equi (m)	1.4019E-03
Re	41839.000	Re	38893.000	Re	36223.000
Mass Flux (kg/s)	4.195E-03	Mass Flux (kg/s)	3.884E-03	Mass Flux (kg/s)	3.574E-03
Heat Flux(W/m^2)	1.816e5	Heat Flux(W/m^2)	1.681e5	Heat Flux(W/m^2)	1.547e5
T out	770.914	T out	770.923	T out	770.978
V out	4.08838	V out	5.23189	V out	7.64017

Velocity Distributions

p/d 1.10

STAR
PROSTAR 3.10

30-Apr-03
VELOCITY MAGNITUDE
M/S
ITER = 1870
LOCAL MX= 6.227
LOCAL MN= 0.0000

6.227
5.782
5.337
4.893
4.448
4.003
3.558
3.113
2.669
2.224
1.779
1.334
0.8896
0.4448
0.1786E-06

p/d 1.15

STAR
PROSTAR 3.10

30-Apr-03
VELOCITY MAGNITUDE
M/S
ITER = 1910
LOCAL MX= 4.738
LOCAL MN= 0.0000

4.738
4.400
4.061
3.723
3.385
3.046
2.708
2.369
2.031
1.692
1.354
1.015
0.6769
0.3385
0.5960E-07
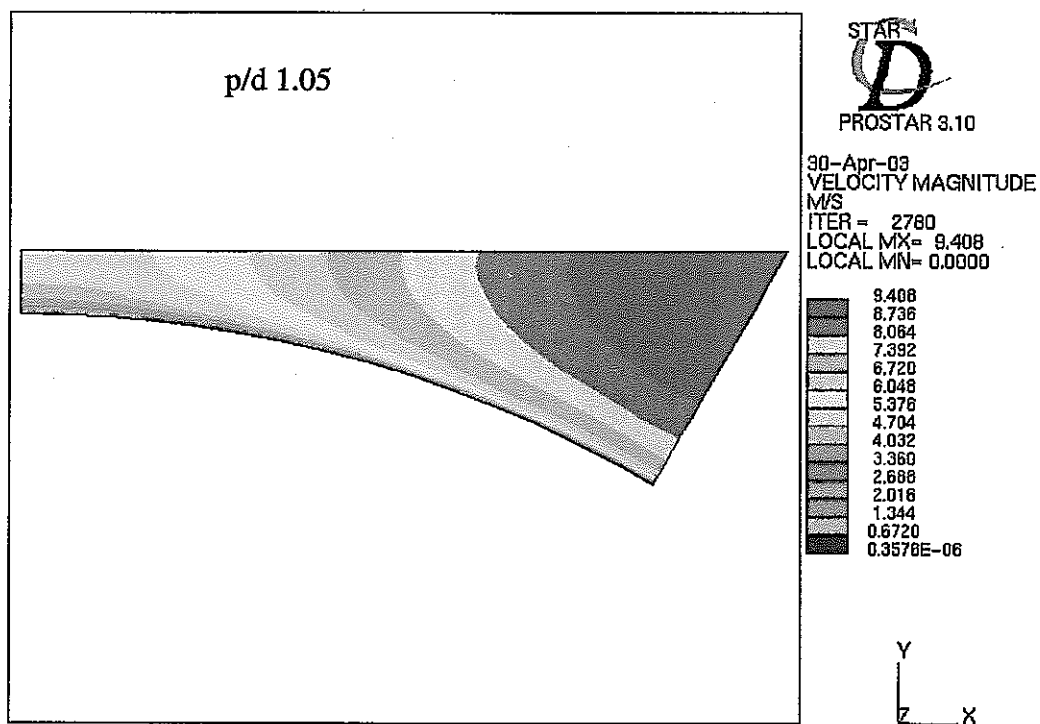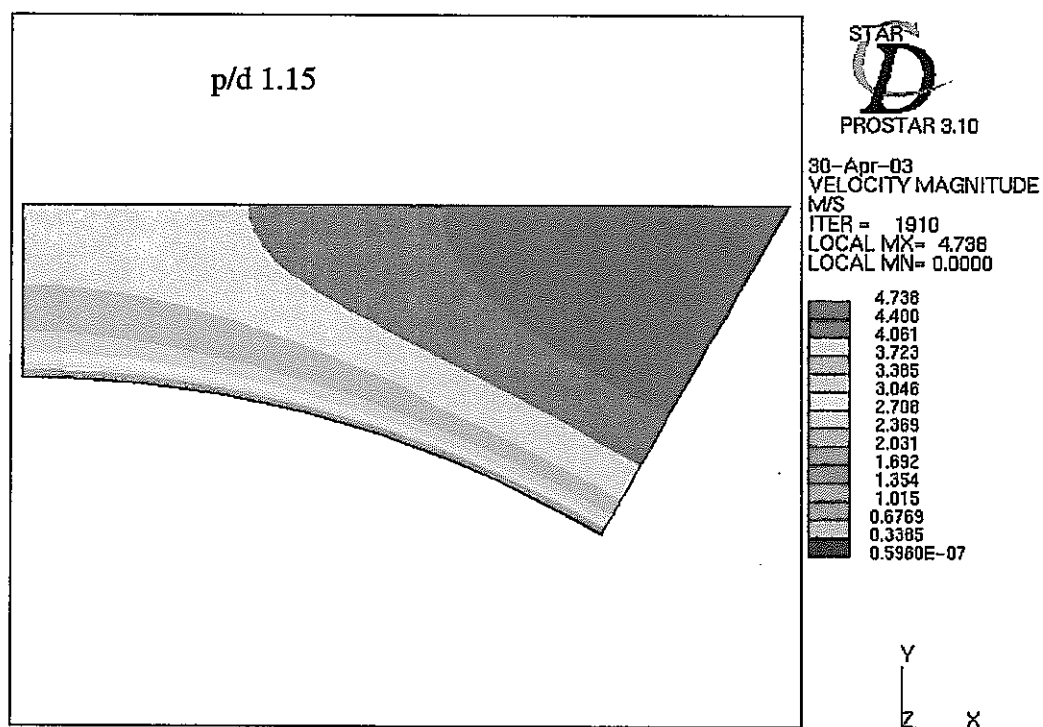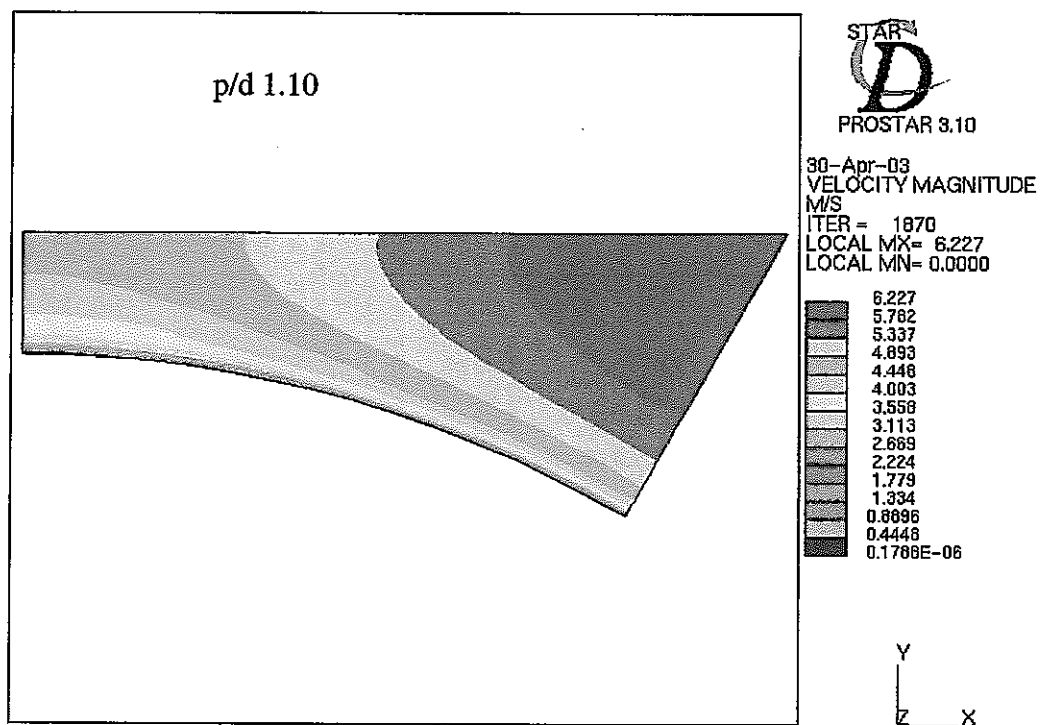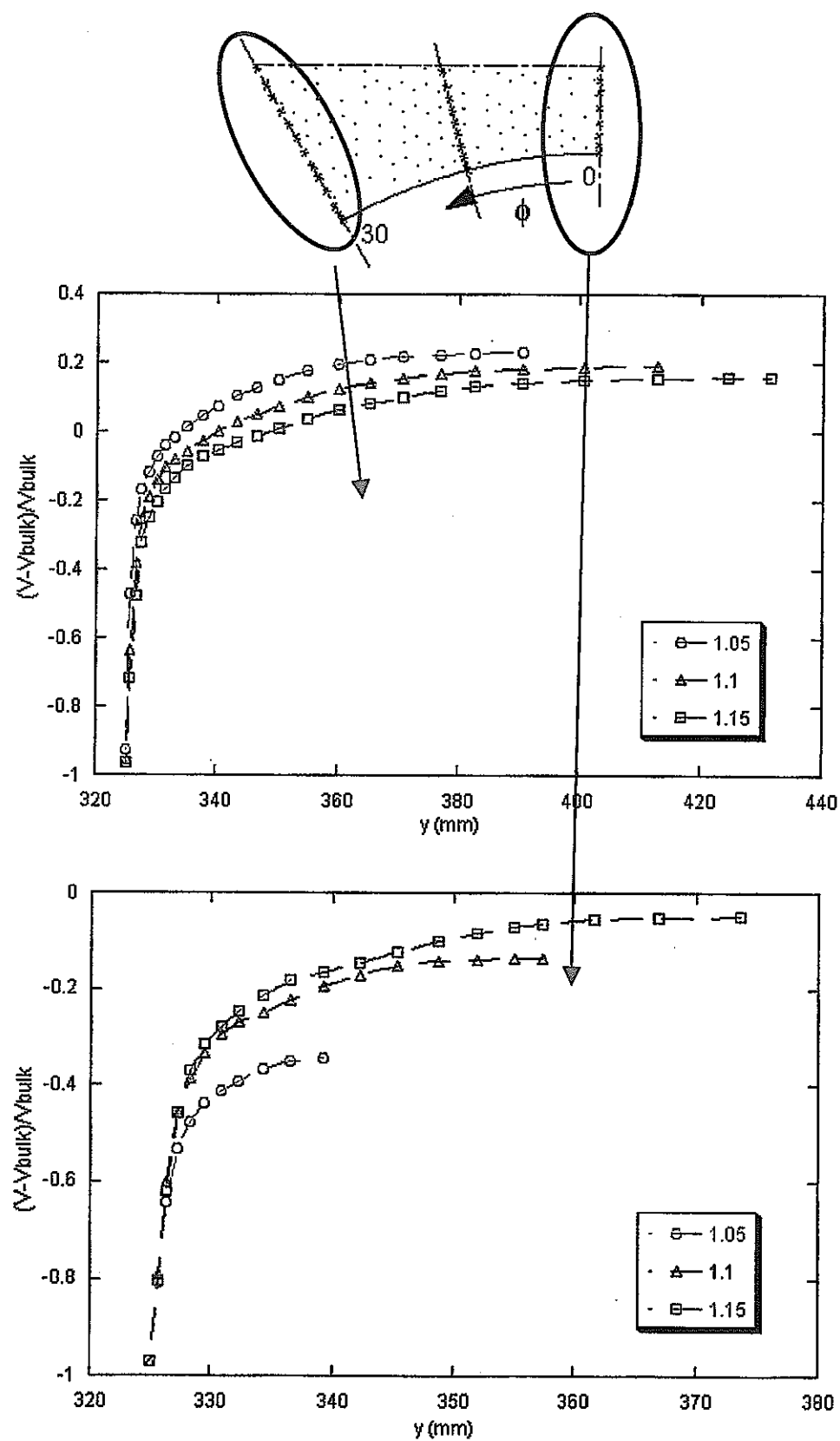
Temperature Distributions

p/d 1.15
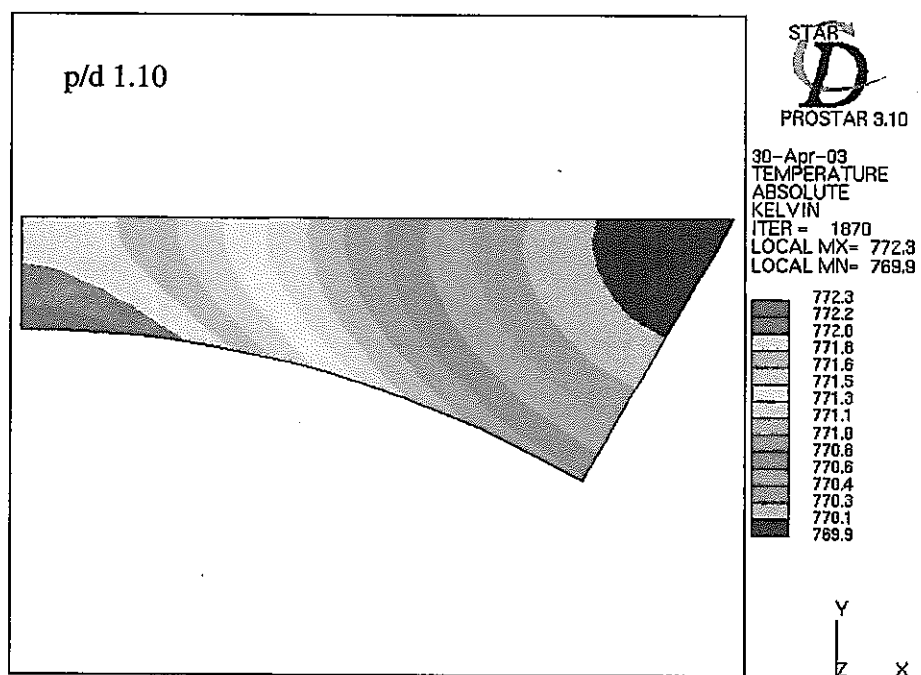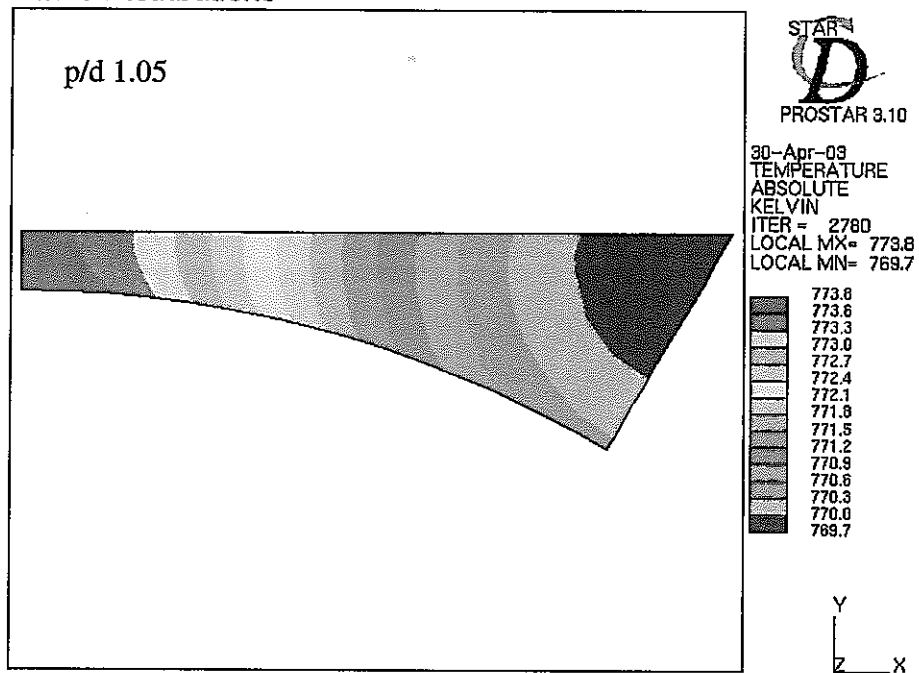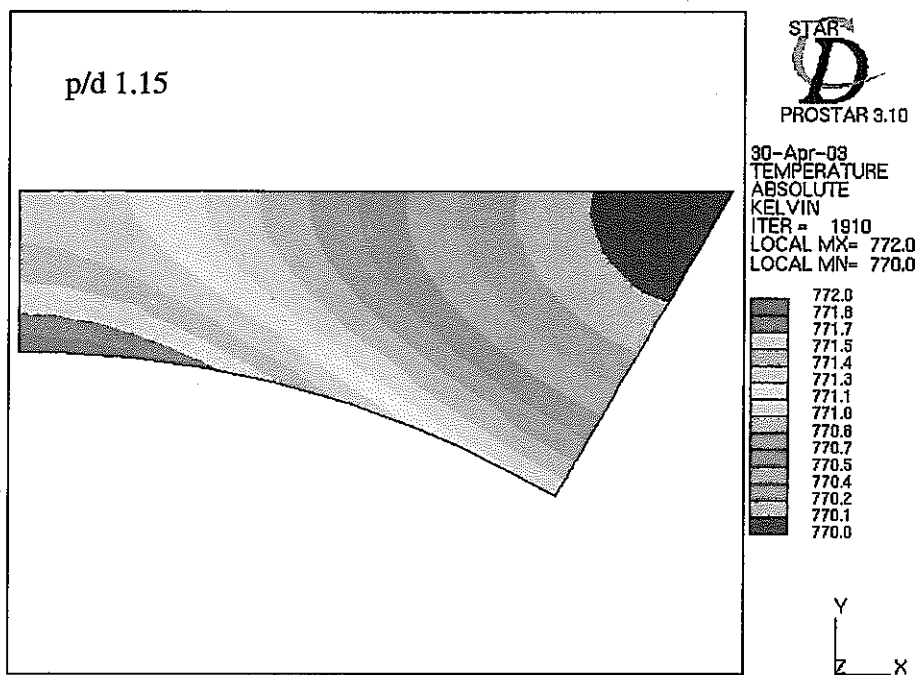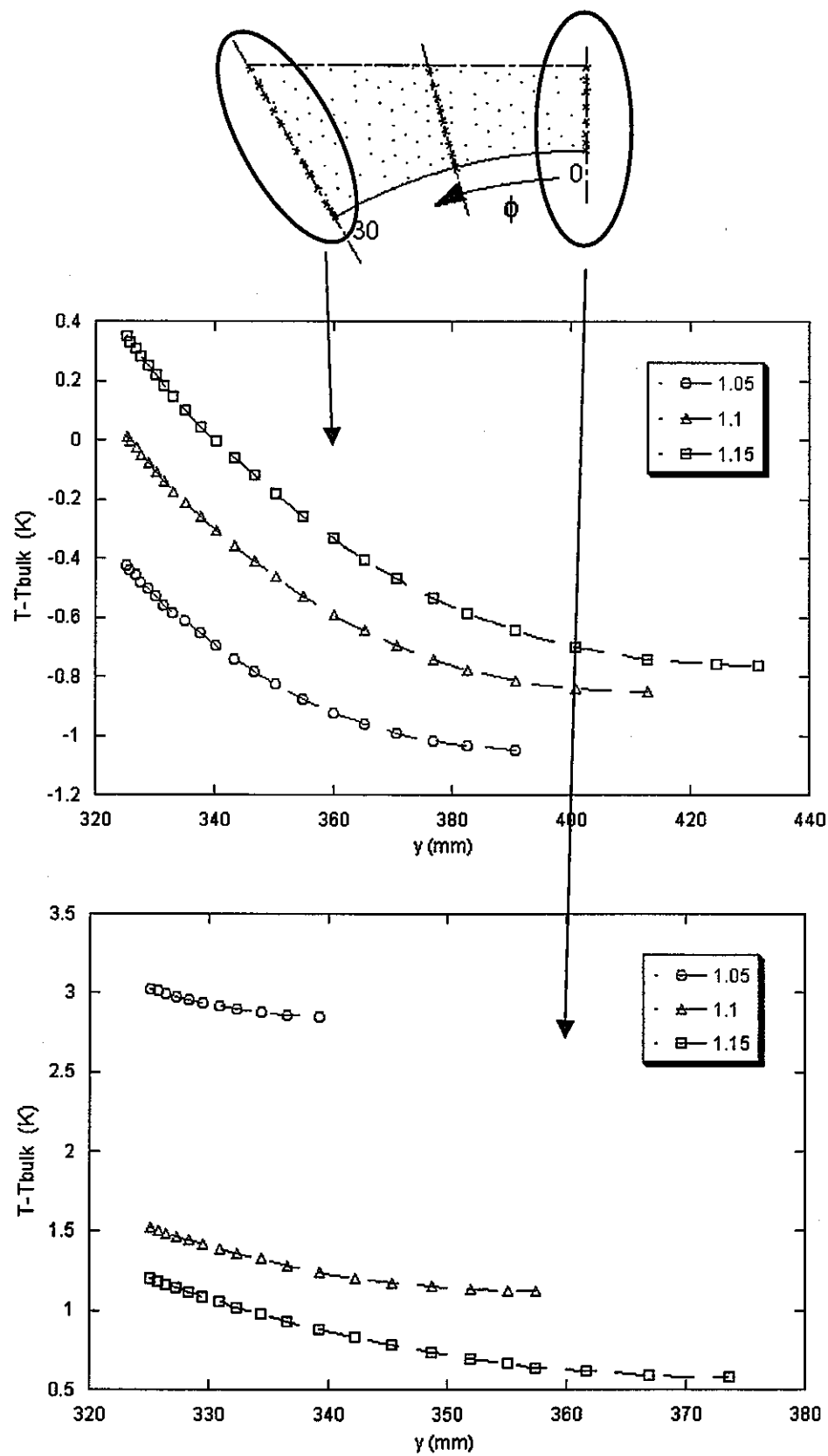
Pressure Drops

The pressure drops obtained from the CDF calculation are compared with those predicted adopting classical friction correlations:

Blasius

$$f = \frac{0.316}{Re^{0.25}}$$

Cheng Todreas

$$f_T = \frac{C'_{fT}}{(Re'_T)^n} \qquad n=0.18$$

$$C'_{fT} = a + b_1\left(\frac{p}{d}-1\right) + b_2\left(\frac{p}{d}-1\right)^2$$

1 ≤ p/d ≤ 1.1   **1.1 < p/d < 1.5**

a	b1	b2	a	b1	b2
0.09378	1.398	-8.664	0.1458	0.03632	-0.03333
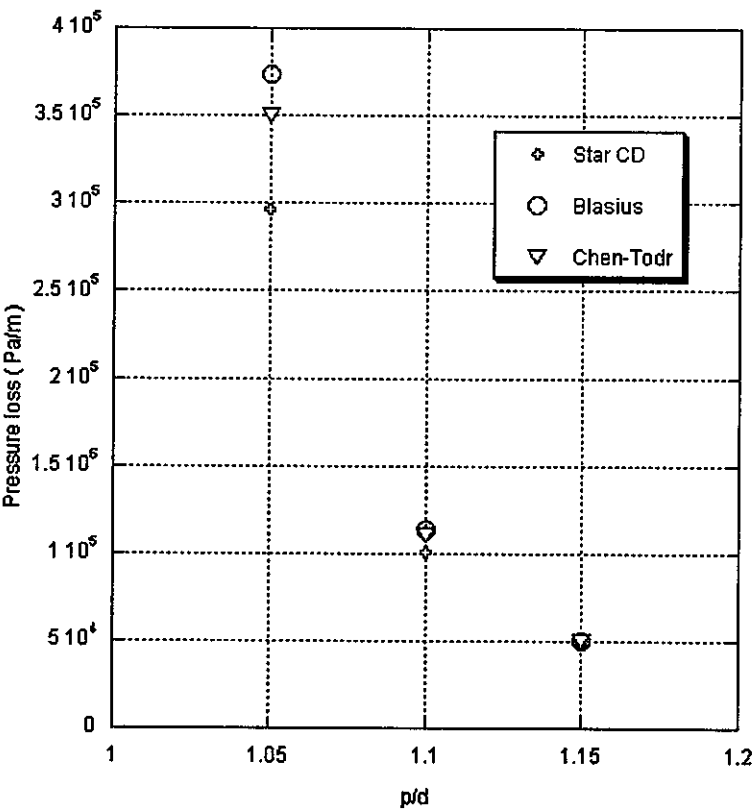
Appendix G

Turbulence Models Evaluation for Heat Transfer Simulation in Tight Lattice Fuel Bundles

The 10th International Topical Meeting on Nuclear Reactor Thermal Hydraulics (NURETH-10), Seoul, Korea, October 5-9, 2003

The 10th International Topical Meeting on Nuclear Reactor Thermal Hydraulics (NURETH-10)
Seoul, Korea, October 5-9, 2003.

TURBULENCE MODELS EVALUATION FOR HEAT TRANSFER SIMULATION IN TIGHT LATTICE FUEL BUNDLES

Emilio Baglietto , Hisashi Ninokata
Tokyo Institute of Technology
2-12-1 O-Okayama, Meguro-Ku, Tokyo, 152-8550, Japan
Phone/Fax +81-3-5734-3056, E-mail: 01d51276@ nr.titech.ac.jp

KEY WORDS

Turbulence, tight lattice, non-linear models, secondary flow

ABSTRACT

A comparative evaluation of different turbulence models is presented in this work, to select which one could be adopted for the evaluation of thermo-hydraulic performances of tight lattice fuel bundles. The individual models are briefly introduced and discussed; they comprehend linear, quadratic and cubic version of the k-ε model, the k-ω model, and the SST model by Menter. The capabilities of the various turbulence closures are evaluated on a benchmark describing a heated bundle, containing four rods arranged in one row, with sodium cooling. The coolant temperatures from the experiment are compared with the computed values, for the region between the rods, and near the channel periphery. The results show that linear k-ε, k-ω and SST model, obtain a very close agreement with each other, but are not capable of correctly predicting the temperature field, due to their inability to account for anisotropy. Quadratic and cubic models are instead capable to produce a close agreement with experimental data, being able to account, in some extent, for anisotropy.

1. INTRODUCTION

The International Reactor Innovative and Secure (IRIS) is an advanced, light water reactor being developed by an international consortium of industry, laboratory, university and utility establishments, led by Westinghouse. The reactor design is based on proven LWR technology, so that no new technology development is needed and near term deployment is possible (Carelli et al., 2002). At the same time evolutionary solutions are being developed for future reloads (Petrovic et al., 2002).

An ultra-long life, high conversion, core design is currently under development. This core will be characterized by a very tight lattice, with relatively small water volume fraction. It is therefore clear that the termohydraulic design will represent a key point in the development of such a solution. In order to successfully tackle this challenge we must introduce innovative fuel configurations, to obtain a more uniform utilization of the coolant. A main undesirable aspect of classic triangular lattice is in fact the non-optimal distribution of water around fuel pins, which leads to a non uniform circumferential clad temperature and wall shear stress distribution (Romano et al., 2001). The target is therefore to minimize the maximum clad and fuel centerline temperatures, keeping at the same time the pressure drops through the core as low as possible.

A large range of arrangements is taken into consideration for the design of the future core. In particular evolutionary and exotic fuel pin designs are considered promising and have shown the possibility of highly increasing fuel performances (Romano and Todreas, 2000). Performances of these new designs need to be evaluated and compared with a detailed analysis, capable of correctly modeling three dimensional phenomena. Classical lumped parameters codes adopted in nuclear industries, such as subchannel analysis codes are not appropriate for our purpose, being calibrated on specific geometries and operational conditions. As it is well known, the finest instruments for modeling turbulence are DNS and LES. The computing requirements however are extremely high; in the DNS case for example they scale as $Re^{9/4}$, making them, at the moment, unsuitable for our analysis. Modern CFD codes of practical use are based on the so-called Reynolds Averaged Navier Stokes equations (RANS) models, where the terms representing turbulence interactions are modeled in terms of the mean flow variables, as for example in the widely used k-. approach. However, the reliability and accuracy of the results cannot easily be assured (Freitas, 1995). Turbulence modeling is usually considered the weakest point in CFD analysis.

For this reason we are performing a profound and critical analysis of the modern turbulence models, to evaluate their capabilities and limitations in describing flow in a tight lattice geometry. The first results of this research come from the evaluation of various low Reynolds k-. models on an isothermal benchmark (Baglietto and Ninokata, 2003). They have shown that quadratic and cubic closure relationships offer higher fidelity in predicting wal stresses and velocity fields in tight lattice rod bundles. The higher accuracy is due to the ability of these models to account, to some extent, for the anisotropy of the flow, as opposed to classical linear models, where, being viscosity a scalar, each component of the stress affects its strain to the same extent. This capability is clearly shown by the existence of a secondary flow field in the subchannel.

As next step we focus in this work on the performances of various turbulence closures in predicting the temperature fields in a tight lattice geometry. In particular attention is concentrated on the relation between accuracy and computational requirements of the various models. In addition to classical low and high Reynolds formulation of the k-ε model, we analyze the behavior of two alternative approaches, the k-ω and the Shear Stress Transport (SST) model. In the k-ω model, instead of the equation for the turbulent dissipation rate, ε, an equation for the turbulent frequency, ω, of the large scales is used. The ω-equation is claimed to have significant advantages near the surface and to correctly predict the turbulent length scale, leading to improved wall shear stress and heat transfer predictions. This model should also offer the advantage of reduced resolution demands for an integration to the wall (Vieser et al., 2002). The SST model is aimed at avoiding the possible limitations of the k-ω model in the region distant from the wall, adopting the k-ε description for this region.

2. TURBULENCE MODELS

2.1 Linear and non-linear k-ε models

It is well known that, despite of the large variety of available models, the standard k -ε is nevertheless the most popular and applicable to a large variety of flow cases with reasonable prediction accuracy. However, there still are fundamentals problems that need to be resolved. In particular, it is well known that the usual formulations of the model assume an isotropic eddy diffusivity in modeling the Reynolds stress tensor. One important deficiency of such a model is the fact that anisotropic effects are not accounted for. In simple terms, since the viscosity is a scalar, each component of the stress affects its strain to the same extent. For this reason, flows where turbulent intensity gradients, and hence the augmentation effects of secondary strain rates, are important cannot be accurately predicted. The most quoted example is the secondary flow that originates in a square duct due to the gradients of the turbulent shear stresses (Myong, 1991).

Consequently our attention in this work is directed not only to the standard approach but also to a non-linear formulation of the k-ε model. This approach is intended to realistically describe the effects of anisotropy in the flow through a non-linear extension of the stress-strain relation. This approach forms a Non-Linear Eddy Viscosity Model (NLEVM) sometimes also refereed to as an Explicit Algebraic Reynolds Stress Model (Suga, 1998).

The formulation of the k-ε model has been presented in many papers and will not be repeated here, for conciseness, but can be found in reference (Launder and Spalding, 1974). We instead briefly present the turbulence closure correlations for the linear and non-linear formulations.

Linear Model

For the standard linear k-ε model, the constitutive relations for the Reynolds stresses are as follows:

$$-\overline{\rho u_i' u_j'} = 2\mu_t s_{ij} - \frac{2}{3}\left(\mu_t \frac{\partial u_k}{\partial x_k} + \rho k\right)\delta_{ij} \qquad (1)$$

where, due to the linear correlation, each component of the shear stress influences only one component of the velocity gradient, therefore being unable to account for anisotropy. Non linear models try to cater for this defect by adopting non-linear relationships between Reynolds stresses and the rate of strain.

Quadratic Model

For the quadratic model, the constitutive relations for the Reynolds stresses are as follows:

$$-\overline{\rho \frac{u_i' u_j'}{k}} = \frac{2}{3}\left(\frac{\mu_t}{k}\frac{\partial u_k}{\partial x_k} + \rho\right)\delta_{ij} - \frac{\mu_t}{k}S_{ij} + C_1 \frac{\mu_t}{\varepsilon}\left[S_{ik}S_{kj} - \frac{1}{3}\delta_{ij}S_{kl}S_{kl}\right] + C_2 \frac{\mu_t}{\varepsilon}\left[\Omega_{ik}S_{kj} + \Omega_{jk}S_{kl}\right] +$$

$$C_3 \frac{\mu_t}{\varepsilon}\left[\Omega_{ik}\Omega_{jk} - \frac{1}{3}\delta_{ij}\Omega_{kl}\Omega_{kl}\right] \qquad (2)$$

where

$$C_1 = \frac{c_{NL1}}{\left(c_{NL6} + c_{NL7}S^3\right)C_\mu} \qquad (3)$$

$$C_2 = \frac{c_{NL2}}{\left(c_{NL6} + c_{NL7}S^3\right)C_\mu} \qquad (4)$$

$$C_3 = \frac{c_{NL3}}{\left(c_{NL6} + c_{NL7}S^3\right)C_\mu} \qquad (5)$$

and

$$C_\mu = \frac{A_0}{A_1 + A_2 S + A_3 \Omega} \qquad (6)$$

where $A_0, A_1, A_2, A_3, c_{NL1}, c_{NL2}, c_{NL3}, c_{NL6}, c_{NL7}$ are empirical coefficients whose values are shown in table 1. S_{ij} and Ω_{ij} are elements of the mean strain and vorticity tensors, respectively, and are given by:

$$S_{ij} = \frac{\partial u_i}{\partial x_j} + \frac{\partial u_j}{\partial x_i} \qquad (7)$$

$$\Omega_{ij} = \frac{\partial u_i}{\partial x_j} - \frac{\partial u_j}{\partial x_i} \qquad (8)$$

The other two terms required to complete the definition of $C\mu$ are as follows:

$$S = \frac{k}{\varepsilon}\sqrt{\frac{1}{2}S_{ij}S_{ij}} \qquad (9)$$

$$\Omega = \frac{k}{\varepsilon}\sqrt{\frac{1}{2}\Omega_{ij}\Omega_{ij}} \qquad (10)$$

The introduction of these quadratic terms has shown to be able to successfully reproduce turbulence driven secondary flows in various cases. Anyhow the various quadratic models have shown limits in the sensitivity to minor strains. The quadratic models in particular do not have sensitivity to streamline curvature.

Cubic Model

In order to capture the streamline curvature effects it is necessary to introduce further terms. A cubic term is therefore added to correlation (2), as follows:

$$-\overline{\rho}\frac{\overline{u_i' u_j'}}{k} = \frac{2}{3}\left(\frac{\mu_t}{k}\frac{\partial u_k}{\partial x_k}+\rho\right)\delta_{ij} - \frac{\mu_t}{k}S_{ij} + C_1\frac{\mu_t}{\varepsilon}\left[S_{ik}S_{kj} - \frac{1}{3}\delta_{ij}S_{kl}S_{kl}\right] + C_2\frac{\mu_t}{\varepsilon}\left[\Omega_{ik}S_{kj}+\Omega_{jk}S_{ki}\right]+$$

$$C_3\frac{\mu_t}{\varepsilon}\left[\Omega_{ik}\Omega_{jk} - \frac{1}{3}\delta_{ij}\Omega_{kl}\Omega_{kl}\right] + C_4\mu_t\frac{k}{\varepsilon^2}\left(S_{ki}\Omega_{lj}+S_{kj}\Omega_{li}\right)S_{kl} + +C_5\mu_t\frac{k}{\varepsilon^2}\left(S_{kl}S_{kl}-\Omega_{kl}\Omega_{kl}\right)S_{ij} \qquad (11)$$

$$C_4 = c_{NL4}C_\mu^2 \qquad (12)$$

$$C_5 = c_{NL5}C_\mu^2 \qquad (13)$$

C_4 and C_5 are again empirical coefficients given in table 1.

Table 1 Coefficient for turbulence closures

A_0	A_1	A_2	A_3	c_{NL1}	c_{NL2}	c_{NL3}	c_{NL4}	c_{NL5}	c_{NL6}	c_{NL7}
0.667	1.25	1.0	0.9	0.75	3.75	4.75	-10.0	-2.0	1000	1.0

2.2 Wall Treatment

The commonly used high Reynolds number versions of the k-ε model, as well known, cannot be applied near the vicinity of the wall since the model neglects the effects of viscosity. The typical approach to avoid modeling these effects is through the use of empirical wall functions, to bridge the gap between the solid boundary and the turbulent core. However, the universality of such functions breaks down for complex flows. Another common approach is the use of a two-layer formulation, where the ε-equation is only solved in the outer part of the boundary layer, whereas the inner portion of the logarithmic layer, and the viscous sub-layer, are treated by a mixing length formulation (Patel et al., 1985). Again, for complex flows, the coupling between the mixing length and the ε-equation becomes problematic, and the solution depends strongly on the specification of the matching location; the uniqueness of the solution can therefore not be guaranteed.

Since our study will deal with analyzing complex geometries, both these approaches cannot be considered acceptable for our intent. Hence, near wall k-ε models or low Reynolds number models, which attempt to model the direct influence of viscosity, are the only suitable approach. This formulation uses the standard transport equation for k, but augments the equation for ε with an extra term, which depends on the distance to the wall, to render the model valid up to solid wall. Details of the implemented scheme are not given for brevity, but can be found in reference (CDL, 1999).

Such a technique is anyhow computationally more intensive and in particular requires the values of the y+ in the near wall cell to be of the order of 1. This condition produces extremely high meshing requirements making the simulation of large geometries problematic. For this reason, in the work, particular attention is posed on the balance between accuracy and mesh requirements of the different low Reynolds approaches, as compared to the high Reynolds form.

2.3 k-ω and SST models

For the k-ω model, the general forms of the k and ω equations are as follows (Wilcox, 1998):

Turbulence Energy

$$\frac{1}{\sqrt{g}}\frac{\partial}{\partial t}\left(\sqrt{g}\,\rho k\right)+\frac{\partial}{\partial x_j}\left(\rho\tilde{u}_j k-\left(\mu+\frac{\mu_t}{\sigma_k^\omega}\right)\frac{\partial k}{\partial x_j}\right)=\rho P_k-\rho\beta^*k\omega \tag{14}$$

Specific dissipation rate

$$\frac{1}{\sqrt{g}}\frac{\partial}{\partial t}\left(\sqrt{g}\,\rho\omega\right)+\frac{\partial}{\partial x_j}\left(\rho\tilde{u}_j\omega-\left(\mu+\frac{\mu_t}{\sigma_\omega^\omega}\right)\frac{\partial\omega}{\partial x_j}\right)=\rho\alpha\frac{\omega}{k}P_k-\rho\beta\omega^2+\rho S_\omega \tag{15}$$

Standard

For the standard model the closure coefficients and auxiliary relations are:

$$\alpha=\frac{13}{25}\ ,\quad \beta=\beta_0 f_\beta\ ,\quad \beta^*=\beta_0^* f_\beta^*\ ,\quad \sigma_k^\omega=\sigma_\omega^\omega=2\ ,$$

$$\beta_0=\frac{9}{125}\ ,\quad f_\beta=\frac{1+70\chi_\omega}{1+80\chi_\omega}\ ,\quad \chi_\omega=\left|\frac{\omega'_{ij}\omega'_{jk}s'_{ki}}{\left(\beta_o^*\omega\right)^3}\right|\ ,$$

$$\beta_0=0.09\ ,\quad f_\beta^*=\begin{cases}1 & ,\ \chi_k\le 0 \\ \dfrac{1+680\chi_k^2}{1+400\chi_k^2} & ,\ \chi_k>0\end{cases}\ ,$$

$$\chi_k=\frac{1}{\omega^3}\frac{\partial k}{\partial x_j}\frac{\partial\omega}{\partial x_j}\ ,\quad S_\omega=0 \tag{16}$$

where $s'_{ij}=\dfrac{1}{2}S_{ij}$ and the eddy viscosity is given by

$$\mu_t=\rho\frac{k}{\omega} \tag{17}$$

SST model

The SST model implemented is that proposed by Menter (1993), the coefficients in this case are expressed in the following general form:

$$C_\phi=F_1 C_{\phi 1}+\left(1-F_1\right)C_{\phi 2} \tag{18}$$

where

$$F_1=\tanh\left(\arg_1^4\right) \tag{19}$$

$$\arg_1=\min\left[\max\left(\frac{\sqrt{k}}{0.09\omega y};\frac{500\nu}{y^2\omega}\right);\frac{4\rho k}{\sigma_{\omega 2}^\omega CD_{k\omega}y^2}\right] \tag{20}$$

$$CD_{k\omega} = \max\left(\frac{2\rho}{\omega\sigma_{\omega2}^{\omega}}\frac{\partial k}{\partial x_j}\frac{\partial \omega}{\partial x_j}, 10^{-20}\right) \tag{21}$$

The coefficient set 1 is

$$\sigma_{k1}^{\omega} = 1.176 \ , \ \sigma_{\omega1}^{\omega} = 2 \ , \ \beta_1 = 0.075 \ , \ \beta_1^* = 0.09 \ ,$$

$$\alpha_1 = \frac{\beta_1}{\beta_1^*} - \frac{1}{\sigma_{\omega1}^{\omega}}\frac{\kappa^2}{\sqrt{\beta_1^*}} \ , \ \kappa = 0.41 \tag{22}$$

and the coefficient set 2 is

$$\sigma_{k2}^{\omega} = 1 \ , \ \sigma_{\omega2}^{\omega} = 1.176 \ , \ \beta_2 = 0.0828 \ , \ \beta_2^* = 0.09 \ ,$$

$$\alpha_2 = \frac{\beta_2}{\beta_2^*} - \frac{1}{\sigma_{\omega2}^{\omega}}\frac{\kappa^2}{\sqrt{\beta_2^*}} \ , \tag{23}$$

$$S_\omega = 2\left(1 - F_1\right)\frac{1}{\sigma_{\omega2}^{\omega}}\frac{1}{\omega}\frac{\partial \omega}{\partial x_j}\frac{\partial k}{\partial x_j} \tag{24}$$

The eddy viscosity for this model is

$$\mu_t = \rho\frac{a_1 k}{\max\left(a_1\omega, \Omega^* F_2\right)} \tag{25}$$

where

$$a_1 = 0.31 \ , \ F_2 = \tanh\left(\arg_2^2\right) \ , \arg_2 = \max\left(2\frac{\sqrt{k}}{0.09\omega y}, \frac{500\nu}{y^2\omega}\right)$$

$$\Omega^* = \sqrt{\frac{1}{2}\Omega_{ij}\Omega_{ij}} \tag{26}$$

2.4 k-ω Wall Treatment

Both k-ω models are adopted in the low Reynolds number form, for which ω at the near-wall cell is fixed algebraically according to:

$$\omega_p = \frac{60\nu}{\beta_1 y^2} \tag{27}$$

where ν is the kinetic viscosity, y the normal distance from the wall and β_1=0.075.

3. SOLUTION METHOD

3.1 Code Description

The commercial code Star-CD is adopted for our simulations. The presented models are available as already implemented. The differential equations governing the conservation of mass, momentum, energy, etc. within the fluid, are discretized by the finite volume (FV) method Thus, they are first integrated over the individual computational cells and then approximated in terms of

the cell-centered nodal values of the dependent variables. This approach has the merit, amongst others, of ensuring that the discretized forms preserve the conservation properties of the parent differential equations.

3.2 Discretization Practice and Solution Scheme

The manner in which the convective and diffusive fluxes are expressed in terms of nodal values is one of the key factors determining accuracy and stability of the calculations. The choice of convective flux approximation is particularly important. There are essentially two main classes of convective flux approximation in widespread use, namely:

Low-order schemes, which characteristically generate discretized equation forms that are easy to solve, produce solutions which obey the expected physical bounds, but sometimes give rise to smearing of gradients, also known as numerical diffusion.

Higher-order schemes, which better preserve steep gradients, but may result in equations that are more difficult to solve (and, in extreme cases, may provoke numerical instabilities) or have solutions exhibiting non-physical spatial oscillations. These oscillations may, in some cases, lead to spurious values, e.g. negative species concentration or turbulent kinetic energy. This phenomenon is often termed numerical dispersion.

In this work a first order upwind differencing (UD) scheme is considered sufficient, due to the good quality of the mesh adopted, and to the forced convection regime of the considered case. A Quadratic Upstream Interpolation of Convective Kinematics (QUICK) is nevertheless furthermore applied to assess the independency of results from discretization practices.

The discretized equations are then solved in a segregated manner with the SIMPLE (Semi-Implicit Method for Pressure-Linked Equations) algorithm (Patankar and Spalding, 1972). In particular, for our steady-state calculations it is adopted in an iterative mode, i.e. the time derivative terms are deleted from the FV equations. For this reason, in order to avoid instability, we must introduce under-relaxation. Thus, if the iteration counter is k, the solution for the selected variable ϕ^k is taken as a weighted mean of the previous iterate ϕ^{k-1} and the current one, denoted by ϕ^{k*}, as follows:

$$\phi^k = \alpha_\phi \phi^{k*} + (1 - \alpha_\phi)\phi^{k-1} \tag{28}$$

where α_ϕ, the under-relaxation factor, lies in the range $0 < \alpha_\phi \leq 1$

4. BENCHMARK PROBLEM

4.1 Experiment description

The experiment adopted as a benchmark was performed at the Karlsruhe Nuclear Research Center in 1989, and is named TEGENA (Moller, 1989). Since considerable variations in temperature occur in the bundle boundary zone, and this zone has shown to be the most critical for a correct numerical prediction, the experiments were performed in typical subchannels of the bundle boundary zone. The selected geometry is in fact a 4-rod in one row inside a rectangular channel box. The pitch to diameter ratio of the rod, p/d=1.147, was selected as typical of an advanced reactor concept.

Sodium was chosen as the liquid-metal coolant because a suitable test bench and practical experience had been available.
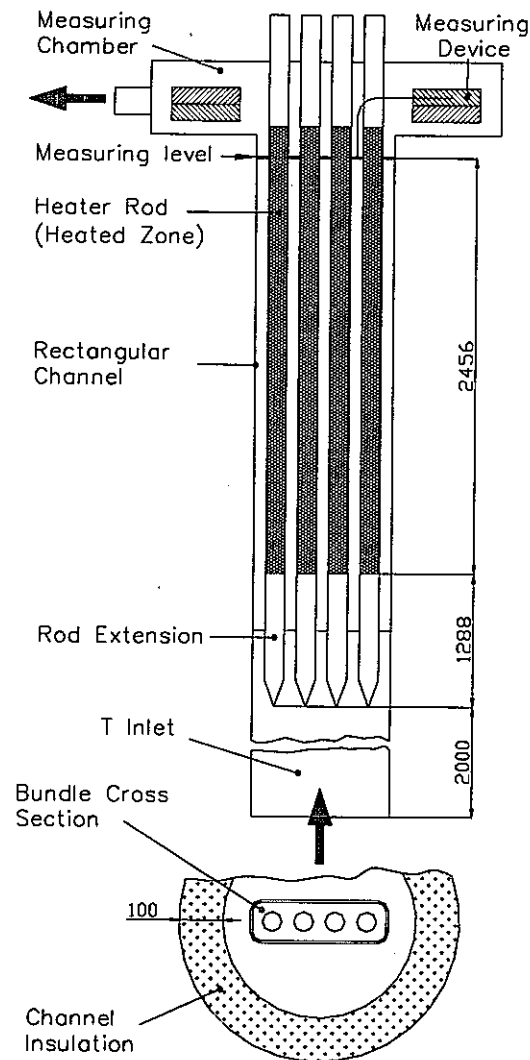
Figure 1. TEGENA Test Geometry

The test section is schematically represented in figure 1. The heater rods are 25 mm in diameter and about 4 m in length, 2.5 m of them heated. The sodium flows from an inlet section in the open rectangular channel into the 4-rod bundle. It first passes an unheated zone of 1288 mm length, it is then heated and leaves the cylindrical measuring chamber through a nozzle provided on its site. The maximum heat flux densities generated on the rod surfaces are 60 W/cm^2. The selected heated length of 2456 mm (201 hydraulic diameters) is sufficient to obtain thermally developed flow conditions during uniform heating.

The temperatures in the sodium flowing through the bundle subchannels are carefully measured in the horizontal main measuring level, 29 mm ahead of the end of the rectangular channel. A measuring probe is fixed to an externally adjustable measuring slides in such a manner that it can be moved in X and Y direction within the subchannels. Four miniature thermocouples protrude from the end of the vertical probe. They are designated TE21, TE22, TE23 and TE24. The geometry is shown in figure 2.
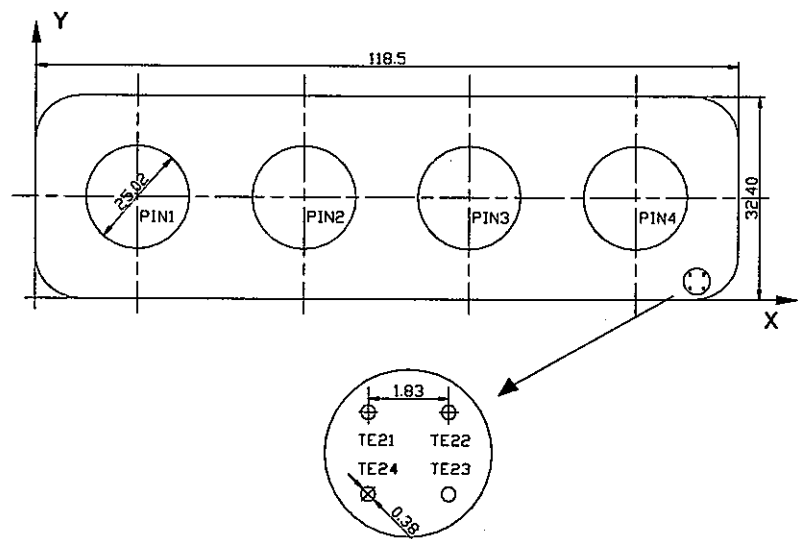
Figure 2. TEGENA Measuring Probe

4.2 Operational Conditions

Among the numerous experiments of TEGENA we select two cases. For these, the sodium temperature distributions are known along a line, as shown in figures 3 and 4. The Flow conditions are very similar, the Reynolds number is around 60,000, with a heat flux density generated on the rod surfaces of about 50 W/cm². Detailed data of the two cases considered are presented in table 2.
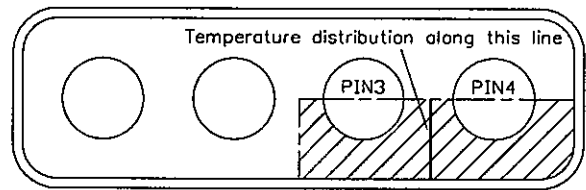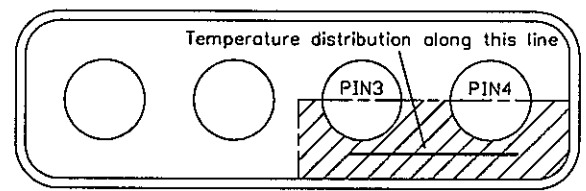

Figure 3. CASE 1 Measuring Location

Figure 4. CASE 2 Measuring Location

Table 2   TEGENA Experimental Parameters

CASE	Re	Mass Flow	Inlet Temp	Outlet Temp	Heat Flux PIN1	Heat Flux PIN2	Heat Flux PIN3	Heat Flux PIN4
1	60,100	3.12 kg/s	257.98 C	350.74 C	49.38 W/cm²	49.00 W/cm²	49.42 W/cm²	49.74 W/cm²
2	61,300	3.19 kg/s	256.55 C	350.74 C	51.01 W/cm²	50.59 W/cm²	50.02 W/cm²	51.37 W/cm²

4.3 Simulation Model

Due to the geometrical symmetry, only ¼ of the bundle has been modeled in our calculations, as can be seen in figure 5. Since our intention has been to adopt low Reynolds number form of the turbulence model, and being for these the meshing requirements extremely severe, we limited the height of the modeled region. The lower part of the rectangular channel and the unheated rod bundle zone have not been modeled, and a preliminary calculation has been run to evaluate the minimum height required to obtain thermally fully developed flow conditions.
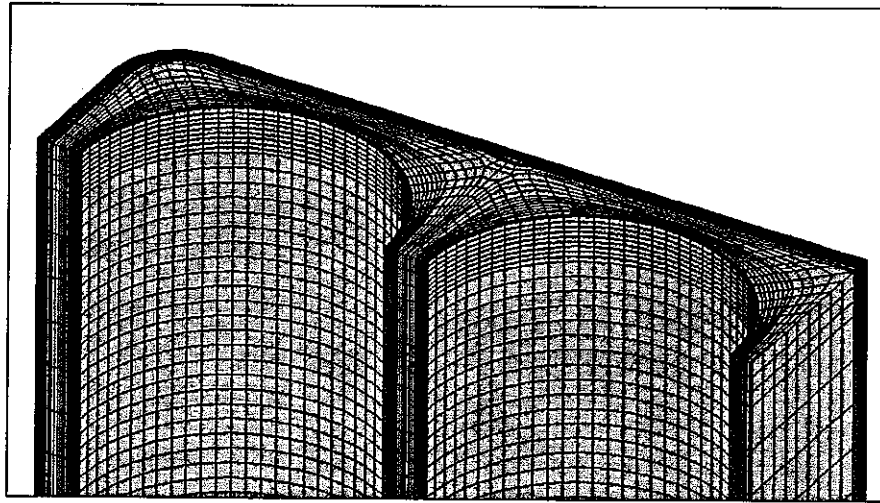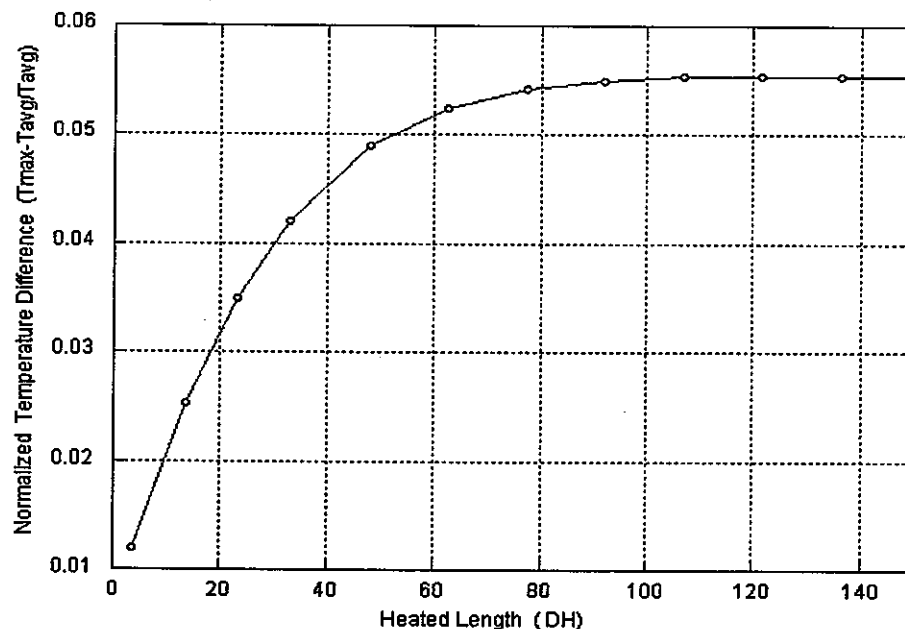

Figure 5. Bundle Modeled Region

Figure 6. Thermal Development of the Flow

As shown in figure 6, the normalized temperature difference, i.e. the maximum temperature minus the flow averaged temperature divided the flow averaged temperature in the plane, has been evaluated at growing elevations in the model. As we can see the thermal field is largely fully developed after 110 hydraulic diameters. We therefore adopted a model with a height of 120 hydraulic diameters, which corresponds to 1466 mm.

Since it is very important to study the dependency of the results on the grid resolution, to demonstrate the grid-convergence of the solution, three different grid resolutions have been used in our analysis, and are shown in figure 7. The total number of nodes varies from 800,000, for the coarse grid, to 3,000,000 for the superfine one.
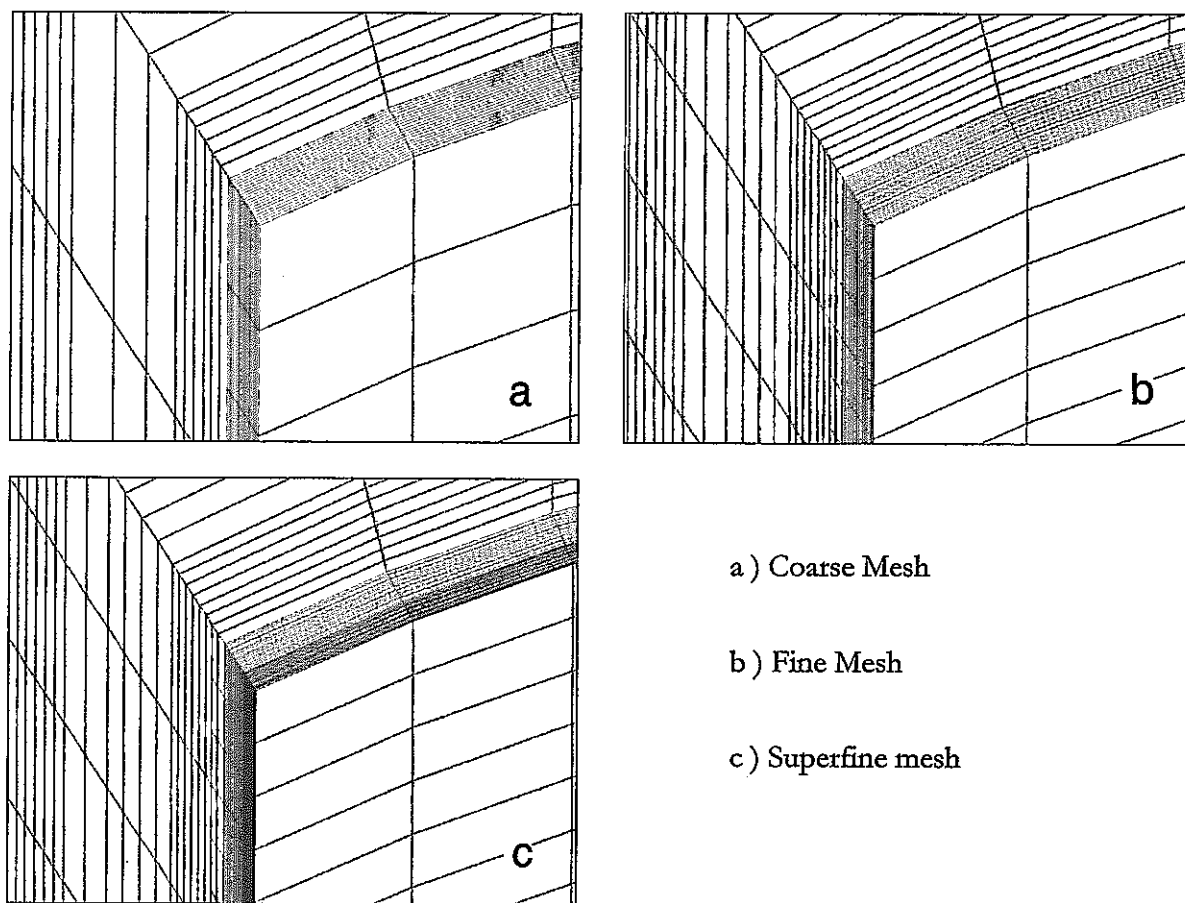
a) Coarse Mesh

b) Fine Mesh

c) Superfine mesh

Figure 7. Calculational Grids

5. PRESENTATION AND DISCUSSION OF RESULTS

5.1 Numerical and grid convergence

The calculations performed are extremely requiring from the numerical point of view. The adoption of a model with a tall and narrow geometry puts a strong challenge on the convergence of the calculation, and requires the adoption of a very low under-relaxation coefficient for the pressure solution, of the order of 0.1. When adopting fine and superfine meshes the convergence of the enthalpy solution is too slow if adopting a typical under-relaxation of 0.95. We must adopt a coefficient of 0.99 to effectively reach convergence.

As previously discussed all calculations have been performed adopting both the first order Upwind Differential (UD) scheme and the higher order QUICK scheme. The results have shown that in all cases the two schemes produce the same results. The UD scheme is as expected more stable but requires a much higher number of iterations when dealing with fine mesh. The QUICK scheme on the other hand is less stable but much less sensible to the quality of the grid, requiring anyhow an increased calculation time for each step.

Figure 8 presents the residuals histories of some of the analyzed cases. It is also interesting to note that the k-ω model, when dealing with fine meshes shows a much quicker convergence as compared to k-ε models.
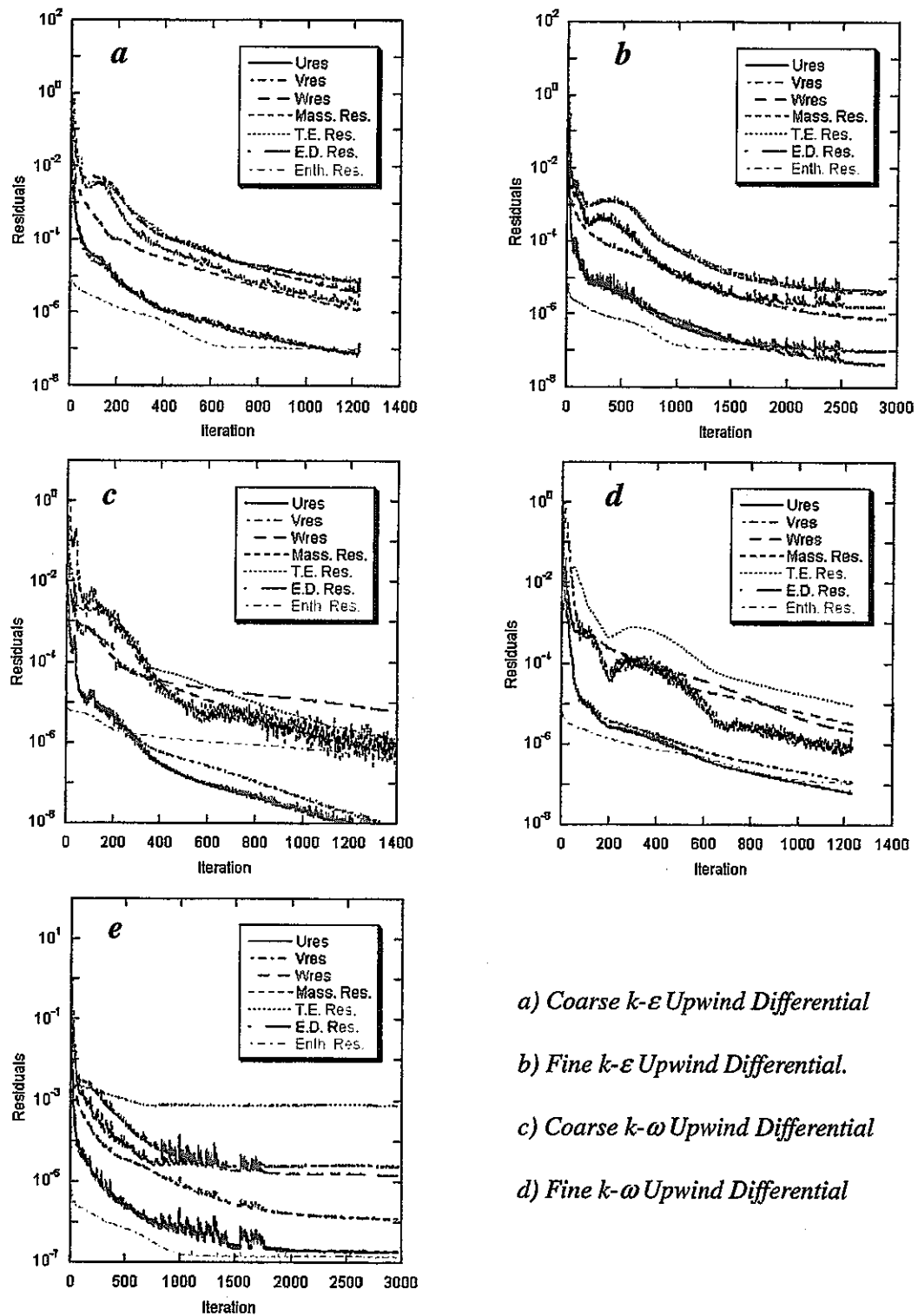
Figure 8. Normalized Residuals

All turbulence models have been tested on the different meshes, previously presented, to analyze grid dependency. In general, for all models the results obtained for the fine and refined grids provided the same values, showing that the quality of the fine grid is sufficient for our analysis. The results for the coarse grid case show little difference, and in particular, if adopting a high Reynolds number k-ε model, this difference is not relevant. The k-w and the SST models did not present the expected advantage for the mesh requirement, even for these models the y+ values in the first cell attached to the wall must be of the order of 1.0.

5.2 CASE 1 Temperature distribution

The temperature distributions calculated for the case 1 are presented in comparison with the experimental values, along the line shown in figure 3. The values X21 through X24 represent the temperatures measured by the thermocouples, shown in figure 2.
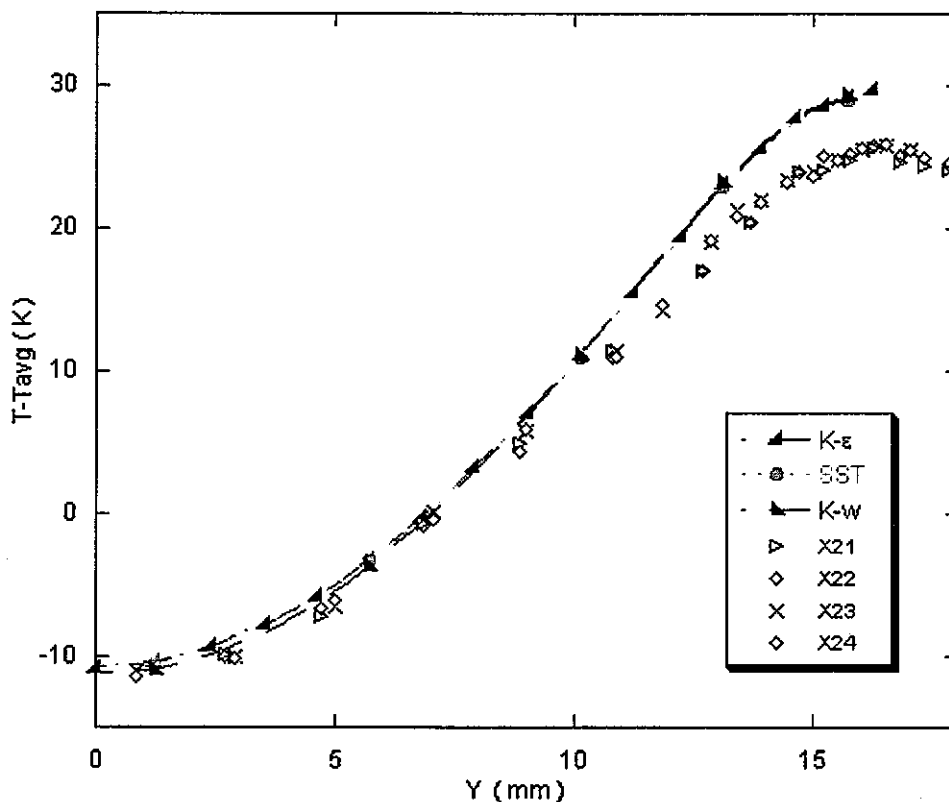

Figure 9.   k-ε, k-ω and SST Models

Figure 9 clearly shows that the linear k-ε, the k-ω, and the SST model produce closely the same temperature distribution. All models over predict in the same measure the temperature values in the narrow gap region between the heated rods. The difference in the peak temperature is in the order of 5 K. These predictions, adopting linear turbulence models do show a strong consistency, proving the maturity of the implementations, for the high Reynolds flow conditions analyzed. At the same time anyhow they prove how, their inability to account for anisotropy render them unable to produce a qualitatively and quantitatively correct prediction.

In this respect figure 10 shows the comparison between the linear and non-linear modeling approach. The quadratic non-linear model only, is presented, since the cubic model presents exactly the same outcome. In fact the cubic term, which is introduced to account for curvature of the streamline, does not produce, as expected, difference in the evaluated geometry.
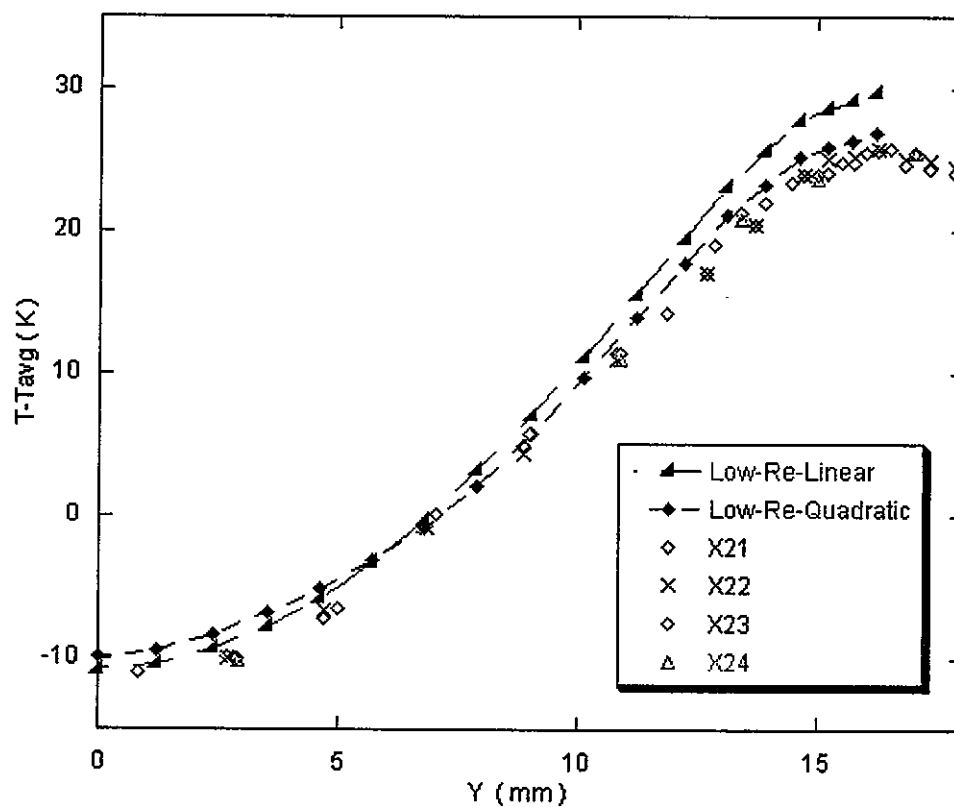
Figure 10. Linear and Quadratic k-ε Models
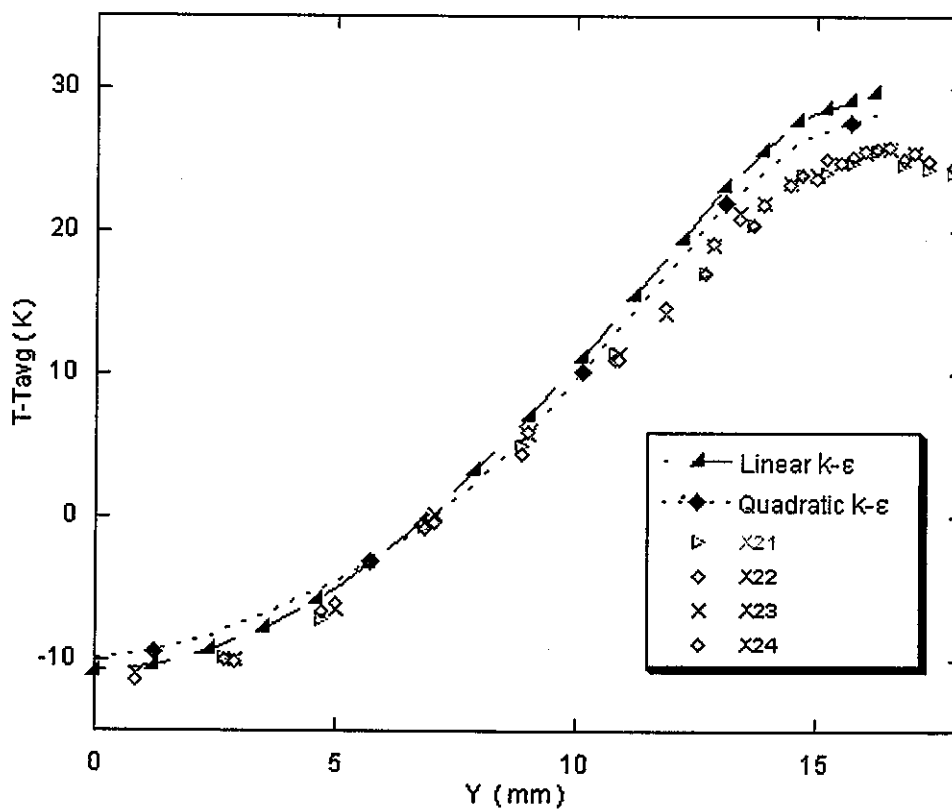
Figure 11. Linear and Quadratic high-Re k-ε Models

The agreement is indeed rather satisfactory, and the small over prediction in the region close two the wall of the rectangular channel, might be a model limitations, but is considered by the authors, most likely related to the non-perfectly adiabatic experimental conditions.

In figure 11 we have presented a comparison between the linear and the quadratic model, as applied in the high Reynolds k-ε formulation, with the adoption of a law-of-the-wall for the near wall region. Such treatment allows to drastically reduce the number of nodes required for the calculation, and radically increases the speed of the calculations. For this reason such an approach is, at present, the only acceptable to model large geometries, as for example a whole fuel assembly. The comparison shows how, although we cannot correctly describe the near wall region, the model can anyway benefit from the non-linear modeling, producing a somehow smaller over prediction of the maximum sodium temperature.

Figure 12 in addition shows the present of a secondary flow field in the flow, caused by the gradients of the shear stresses. The magnitude of such a motion is extremely low, less than 1% of the coolant velocity, but, as shown, it is capable of strongly influencing the temperature distribution in the bundle.
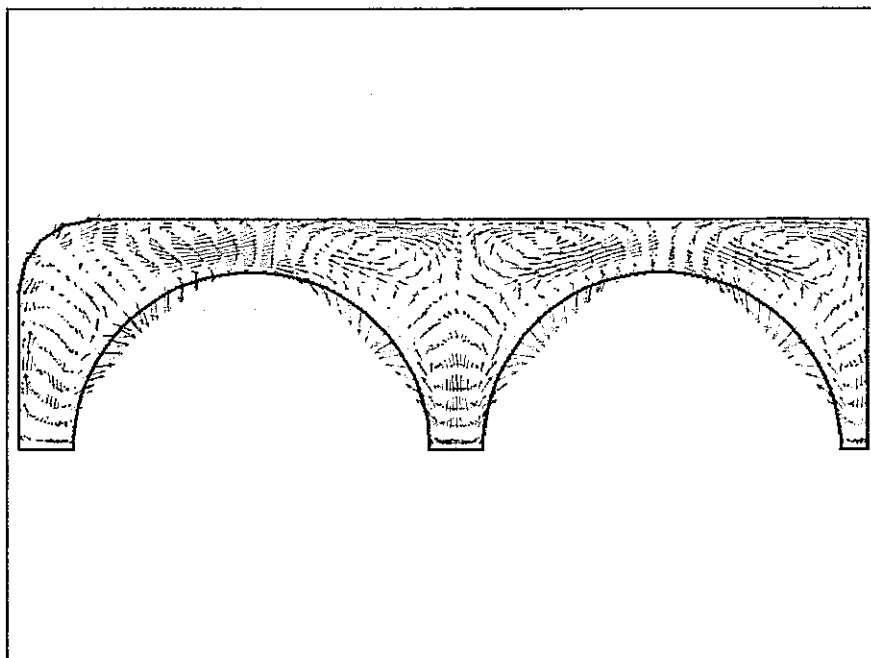

Figure 12.   Secondary flow field

5.3   CASE 2 Temperature distribution

The second case, considered in our work, compares the temperature distribution along a line close to the channel box, as shown in figure 3. As for case 1, the predictions of all linear models were in very close agreement, and therefore only the k-ε is shown, as representative. In figure 13 we compared the results of the linear and quadratic closure for the low Reynolds k-ε model. We clearly see that our results have a large qualitative difference in the two peaks as compared with the experiment. The TEGENA data present a difference in the temperature between the two peaks of about 5 K. This difference is related to the different heat flux in the pin3 and 4, that, as shown in table 2, is of the order of 3%. Since in our calculations we did not modeled the complete heated length, the difference in the peak for the calculation results is very small, only about 1 K. Furthermore, this difference could be in part related to the different isolations around the rectangular channel, shown in figure 1, which could cause a higher heat dispersion in the region close to the pin3.
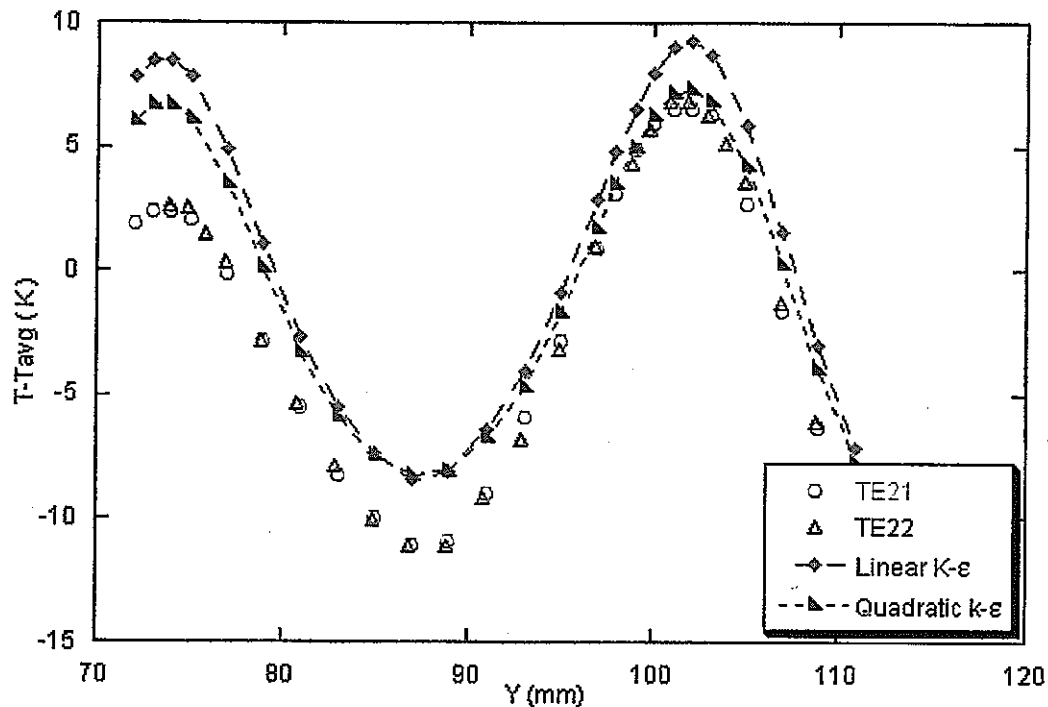
Figure 13.   Linear and Quadratic k-ε Models

The results anyhow seem once again to show the importance of the anisotropic modeling which can produce a flatter temperature distribution, which better conforms to the experimental one. The case anyhow would require further investigations for a correct analysis.

3.   CONCLUSIONS

A comparative study between different turbulence models has been presented in this work. The different turbulence closures have been applied to a benchmark referring to the TEGENA experiment, performed at the Karlsruhe Nuclear Research Center in 1989. The work was intended to evaluate the model performances in predicting the temperature distributions in a tight lattice rod bundle.

The comparisons firstly show the maturity of the implementations of the different models. All linear models, k-ε, k-ω and SST, in fact produced the same predictions. These models indeed over predict the temperature values in the narrow gap region between pins, due to their inability to account for anisotropy. The secondary flows, which arise from the gradients of the shear stresses, produce a flattening in the temperature field, in the same extents of the flattening for the velocity field that we discussed in a previous work (Baglietto and Ninokata, 2003). In this respect the non-linear models are therefore capable of reproducing the temperature field with a higher accuracy.

The work therefore confirms the necessity of accounting for anisotropy in the models to obtain a correct analysis of flow in a tight lattice geometry. At the same time, the low-Reynolds models adopted in the work showed extremely high mesh requirements for a correct analysis, which makes them, at present, unsuitable for modeling large geometries, as for example fuel bundles.

Correct comparisons between different fuel designs can therefore be obtained, on smaller domains, with quadratic and cubic k-ε models. These models, after a further refinement, will be adopted in the first part of our fuel design. More extensive work is instead required to select a model that could be successfully applied for a correct simulation of a complete fuel assembly. At present the high Reynolds version of the non-linear models has shown relatively good performances in the

predictions and the very low meshing and computational requirements and makes it appealing. At the same time, the adoption of an empirical law, for the near wall region, does not guarantee the applicability of such an approach to generic geometries, and complex flows.

It is intention of the authors to evaluate, in future work, the performances of the V2F model by Durbin (1995) in this respect. The V2F model avoids explicit low-Re terms in the e equation by using an elliptic relaxation equation near the wall in addition, an equation for the fluctuating $\bar{v}2$ is introduced. This model does not require the calculation of wall distance, and does not require the use of dumping functions or wall functions to adjust the behavior of turbulence quantities. It should therefore present reduced computational overhead, and in particular reduced meshing requirements, which are key points of our investigation. At the same time it is claimed to produce better friction and heat transfer predictions through the correct modeling of the viscous sub-layer.

NOMENCLATURE

d_{ij}	=	*Kronecker delta*	ε	=	*Turbulent dissipation rate*
k	=	*Turbulent kinetic energy*	μ_t	=	*Turbulent viscosity*
S_{ij}	=	*Element of the mean strain tensor*	ν	=	*Kinematic viscosity*
s_{ij}	=	*Rate of strain tensor*	*D.N.S.*	=	*Direct numerical simulation*
y	=	*Normal distance from the wall*	*L.E.S.*	=	*Large eddy simulation*
Ω_{ij}	=	*Element of the mean vorticity tensor*	*R.A.N.S.*	=	*Reynolds Averaged Navier Stokes equations*

REFERENCES

1. E. Baglietto, H. Ninokata, 2003, "Selection of an Appropriate Turbulence Model to Evaluate Performances of Novel Fuel Geometries for the "IRIS" Reactor". Selected for presentation at the *4th ASME/JSME Joint Fluids Engineering Conference*, Honolulu, Hawaii.
2. M. D. Carelli, K. Miller, C. V. Lombardi, N. Todreas, E. Greenspan, H. Ninokata, F. Lopez, L. Cinotti, J.Collado, F.Oriolo, 2002, "IRIS: Proceeding Towards the Preliminary Design " *Proceedings of the 10th International Conference on Nuclear Engineering*, Arlington, VA, April 14-18, 2002, 10-22947.
3. P. A. Durbin, 1995, "Separated Flow Computations with the k-e-v2f model", *AIAA Journal*, **Vol. 33**, No. 4.
4. B. E. Launder, D.B. Spalding, 1974, 'The numerical computation of turbulent flows', *Comp. Meth. in Appl. Mech. and Eng.*, 3, pp. 269-289.
5. F. R. Menter, 1993, "Zonal two equation k-ω turbulence models for aerodynamic flows", *Proc. 24th Fluid Dynamics Conf.*, Orlando, Florida, USA, 6-9 July, Paper No. AIAA 93-2906.
6. R. Moller, 1989, *"TEGENA: Detailed Experimental Investigations of Temperature and Velocity Distributions in Rod Bundle Geometries with Turbulent Sodium Flow"*, Kernforschungszentrum Karlsruhe.
7. H. K. Myong, 1991, "Numerical Investigation of Fully Developed Turbulent Fluid Flow and Heat Transfer in a Square Duct" *Int. J. Heat and Fluid Flow*, **Vol. 12**, No. 4.
8. Patankar, S.V., and Spalding, D.B.1972.'A calculation procedure for heat, mass and momentum in three-dimensional parabolic flows', *Int. J. Heat Mass Transf*, **Vol. 15**.

9. V. C. Patel, W. Rodi, G. Scheuerer, 1985, "Turbulence Models for Near-Wall and Low Reynolds Number Flows – a review", *AIAA Journal* **23**, 1308.

10. B. Petrovic, M. D. Carelli, E. Greenspam, M. Milosevic, J. Vujic, E. Padovani, F. Ganda, 2002, "First Core and Refueling Options for IRIS" *Proceedings of the 10th International Conference on Nuclear Engineering*, Arlington, VA, April 14-18, 2002, 10-22581.

11. A. Romano, N. E. Todreas, 2000, *"Analysis of Novel Fuel Geometries for the Geneartion IV "IRIS" Reactor "* Department of Nuclear Engineering, Massachusetts Institute of Technology, MIT-ANP-TR-073.

12. A. Romano, V. Kriventsev, H. Ninokata, N.E. Todreas, 2001, "Novel Fuel Geometries for the Generation IV IRIS Reactor" *Proceedings of the 9th International Conference on Nuclear Engineering*, Nice, France, April 8-12, 2001.

13. K. Suga, 1998, "Recent Developments in Eddy Viscosity Modelling of Turbulence", *R&D Review of Toyota CRDL*, **Vol. 33**, No 1.

14. Vieser, W., Esch, T., Menter, F., 2002, "Heat Transfer Predictions using Advanced Two-Equation Turbulence Models". *CFX Technical Memorandum.*

15. D. C. Wilcox, 1998, *"Turbulence Modelling for CFD"*, 2nd edition, DCW Industries, Inc.

16. *"STAR-CD Version 3.10 Manual, Methodology"* Computational Dynamics Limited, (1999).

Appendix H

Calculation of Heat Transfer Coefficients on a Flat Plate by Pseudo Direct Numerical Simulation of Turbulence

Calculation of Heat Transfer Coefficients on A Flat Plate by Pseudo Direct Numerical Simulation of Turbulence

Takeharu MISAWA[1*] , Isamu MAEKAWA[2], and Hisashi NINOKATA[1]

[1]*Tokyo Institute of Technology, 2-12-1 O-Okayama, Meguro-Ku, Tokyo, 152-8550*

[2]*Kawasaki Heavy Industries, ltd. 2-6-5, Minamisuna, Koto-Ku, Tokyo, 136-8588*

(Received   )

The pseudo direct numerical simulation using finite difference method has been carried out for fully-developed turbulent flows through heated paralleled flat plates. Uniform heat flux is applied to both walls. The main objectives of this paper are to investigate the validity of the numerical method, and the influence of the spatial resolution in the streamwise and spanwise directions upon the turbulent field. The Reynolds number, based on the friction velocity and the channel half-width is 180, and the Prandtl numbers are 5.9, 1.0, 0.72, 0.025, and 0.0045. The good results for the mean profile and the second-correlation of velocity and temperarure, and the Nusselt number for various Prandtl numbers are obtained, and the spatial resolution, in this paper, scarcely affected the calculated results.

KEYWORDS: pseudo direct numerical simulation, forced convection, finite difference method, thermal transfer coefficient, flat plate, turbulent statistics

I. Introduction

It is necessary to perform detailed turbulent heat transfer analysis in a fuel assembly. The attempt was made to use a pseudo direct numerical simulation using finite difference method, in the hope that this method could replace a past empirical approaches based on experiments or statistics. In this paper, we describe the pseudo direct numerical simulation of fully-developed turbulent flow through heated paralleled flat plates.

It is discussed that the finer grid size, which can resolve the minimum scale turbulent eddy, is necessary to perform the direct numerical simulation. However, for the application of the thermal direct numerical simulation to engineering, it is significant to investigate grid size affects necessary in estimating the mean velocity and temperature profiles, and their second-order correlations.

The purpose of this work is to test the method to be applied for rod-bundle thermal

*Corresponding author, Tel. +81-3-5734-3062, Fax. +81-3-5734-3056, E-mail: 01d19077@nr.titech.ac.jp

hydraulic analysis, and to investigate the influence of a grid size on calculating the thermal turbulent field.

II. Numerical Method and Parameters

1. Computational Domain

Figure.1 shows the computational domain. The size of the domain is given by *3.2 δ*, *2.0 δ*, and *6.4 δ*, in the spanwise, wall-normal, and streamwise directions, respectively, where *δ* denotes the channel half-width. The fluid is incompressible Newtonian fluid of constant density ρ, constant viscosity μ, constant thermal conductivity λ, and constant thermal capacity C_p. Uniform heat flux q_w is applied to both walls.

The friction Reynolds number $Re_\tau (= w_\tau \, \delta / \nu)$, is *180*, and the Prandtl numbers $Pr (= \mu C_p / \lambda)$ are *5.9* (water in normal temperature), *1.0* (water in 15MPa, 330℃), *0.72* (air in normal temperature and pressure), *0.025* (NaK, 100℃), *0.0045* (sodium in normal pressure, 500℃), where w_τ denotes the friction velocity $(\equiv \sqrt{\tau_{wall}/\rho})$, ν the kinetic viscosity, and τ_{wall} the wall shear stress.

2. Basic Equations

The flow variables and the equations are made dimensionless using the channel half-width δ, the density ρ, the friction velocity w_τ, and the friction temperature T_τ $\{ \equiv q_w / (\rho C_p \cdot w_\tau) \}$.

The governing equations for the simulations are the mass continuity equation:

$$\frac{\partial u_j^+}{\partial x_j^*} = 0 \qquad\qquad .(.1)$$

Navier-Stokes equation:

$$\frac{\partial u_i^+}{\partial t^+} + u_j^+ \frac{\partial u_i^+}{\partial x_j^*} = -\frac{\partial p^+}{\partial x_i^*} + \frac{1}{Re_\tau} \frac{\partial^2 u_i^+}{\partial x_j^{*2}} - \frac{\overline{\partial p}^+}{\partial x_i^*} \delta_{iz} \qquad (.2)$$

and the energy equation:

$$\frac{\partial T^+}{\partial t^+} + u_j^+ \frac{\partial T^+}{\partial x_j^*} = \frac{1}{Pr \cdot Re_\tau} \frac{\partial^2 T^+}{\partial x_j^{*2}}. \qquad (.3)$$

In Eqs. (1)-(3), the following definitions are employed:

$u_j^+ \equiv u_j / w_\tau$

$t^+ \equiv t \cdot w_\tau / \delta$

$p^+ \equiv p / (\rho w_\tau^2)$

$T^+ \equiv T / T_\tau \quad and$

$x_j^* \equiv x_j / \delta.$

Here the averaged value is indicated by $(^-)$.

The fluid is driven by a mean pressure difference in the streamwise direction. The third term of the left-hand side in Eq. (2) is the mean constant pressure gradient term $\partial \overline{p}^+/\partial z^*$, and the first term of the left-hand side is the fluctuation component from the mean pressure difference.

The mixed mean temperature increases linearly in the streamwise direction. Then the temperature T^+ is divided into two parts:

$$T^+(x^*, y^*, z^*) = \frac{d\overline{T}_m^+}{dz^*} z^* - \theta^+(x^*, y^*, z^*) \qquad (.4)$$

where $\overline{T}_m^+$ is the mixed mean temperature:

$$\overline{T}_m^+ = \frac{\int \overline{W}^+ \overline{T}^+ dy^*}{\int \overline{W}^+ dy^*}. \qquad (.5)$$

In the present condition, this streamwise gradient becomes:

$$\frac{d\overline{T}_m^+}{dx^*} = \frac{1}{\overline{W}_{bulk}^+}. \qquad (.6)$$

where $\overline{W}_{bulk}^+$ is the bulk mean velocity:

$$\overline{W}_{bulk}^+ = \int \overline{W}^+ dy^*. \qquad (.7)$$

With the above transformation, the energy equation (3) becomes:

$$\frac{\partial \theta^+}{\partial t^+} + u_j^+ \frac{\partial \theta^+}{\partial x_j^*} = \frac{1}{Pr \cdot Re_\tau} \frac{\partial^2 \theta^+}{\partial x_j^{*2}} + \frac{W^+}{\overline{W}_{bulk}^+}. \qquad (.8)$$

3. Numerical Method

Non-slip boundary conditions are imposed to velocities, Neumann condition to pressure, and the transformed temperature $\theta = 0$ on the both walls. Periodic conditions are imposed to the velocities, pressure, and transformed temperature in the spanwise and streamwise directions.

The numerical method is based on the fractional step method, with the staggered grid. For the spatial derivatives, the consistent scheme [1] is applied for the convection terms, the second order accurate central scheme for other terms. An explicit Adamus-Bashforth scheme is used for time-advancement of convection and dissipation terms. However, for the simulation of low Prandtl number fluids, an implicit Crank-Nicolson scheme is applied for dissipation term in energy equation (8) to avoid the restriction of time-interval by explicit description of dissipation term. The Poisson-type pressure equation is solved by the scaling

CG method using FFT in the streamwise direction.

4. Solution Prodedure

In this work, both the fine-grid and coarse-grid computations are performed, in order to investigate the influence of spatial resolutions in the spanwise and streamwise direction upon calculated thermal turbulent flow. The computational domain is divided into *128x64x128* grids in the fine-grid computation, and *64x64x64* grids in coarse-grid computation, in the spanwise, wall-normal, streamwise direction. Non-uniform grids, which are concentrated on the walls, are used in the wall-normal direction in order to resolve viscous sublayer. The minimum and maximum grid sizes in wall units, which are defined by yw_τ / ν, are *1.1* and *11.0*. In this paper, the wall-normal mesh size is not varied between fine-grid and coarse-grid computation. Uniform grids are applied in the streamwise and spanwise direction. The grid sizes of the coarse-grid computation in wall units are *9.0* in the spanwise direction, *18.0* in the streamwise direction. Those of the fine-grid computation in wall units are 4.5 in the spanwise direction, *9.0* in the streamwise direction.

The time interval, which is defined by $\Delta t^+ \equiv \Delta t \cdot w_\tau / \nu$, is 0.0005.

First, isothermal simulation is carried out. Fully-developed flow is reached after $t^+=25$, and is judged by a linear shear stress in **Fig.2**, and by the fact that the sample data, which is time-averaged for every 10000 time steps or for $\Delta t^+=5$, shows stationary state behaviors. The results of velocity are time-averaged over $t^+=25$-50, and spatial-averaged over streamwise and spanwise directions. After that, the heat transfer simulations for various Prandtl numbers are performed. Fully-developed flow is reached after $t^+=80$. It is identified by the fact that the sample data, which is time-averaged for every 10000 time steps, shows stationary state behaviors. The results of temperature are time-averaged over $t^+=80$-110, and spatial-averaged.

The computations are performed with the vector computer. Total CPU time of fine-grid cases is, for example, about 80 hours.

III. Computational Results

1. Velocity Field

The mean streamwise velocity profile is shown in **Fig.3**, and is compared with the results using the spectral method by Kim et al (1987) [2], and the finite difference method by Kawamura et al (1998) [3]. While the agreement of the fine-grid computation is good enough, the coarse-grid case underestimates about 4% in the center of the channel.

The calculated bulk-Reynolds numbers Re_{bulk} ($=\overline{W}_{bulk}D_h / \nu$), where D_h denotes the equivalent diameter defined by $D_h = 4(S/L_w)$, S the cross-sectional area, and L_w the wetted length, are 11400 in the fine-grid computation, and 11000 in the coarse-grid computation. The trend is the same as for the streamwise velocity profiles. .

The root-mean square of velocity variance is shown in **Fig.4**. The agreement of the results of V^+_{rms} is satisfactory. However, the coarse resolution case underestimates the peak U^+_{rms} of about 2%, and W^+_{rms} of about 4%.

The Reynolds shear stress is shown in **Fig.5**. While the coarse grid computation overestimates near the wall, agreement is satisfactory in the region of $y^+>30$.

These results show that, the fine- and coarse-grid computations give a slight difference on the streamwise velocity profile, U^+_{rms} and W^+_{rms}, and on the Reynolds shear stresses near the wall, but are calculated to be both in good agreement with results of Kim *et al*, and Kawamura *et al*.

2. Temperature field

The mean temperature profiles are shown in **Fig.6** for various Prandtl numbers, and are compared with Kader's correlation (1981)[4] and the results by Kawamura *et al* (1998)[3] with $Re_r=180$, $Pr=0.71$ and 0.025. The calculation results are in good agreement with Kader's correlations. The coarse-grid computation estimates the peak value about 5% less than the fine-grid computation for $Pr=5.9$, about 4% for $Pr=1.0$, and about 3% for $Pr=0.72$. Both the fine- and coarse-grid cases show agreement within 1% for $Pr=0.025$, 0.0045. In comparison with the result of Kawamura *et al*, the coarse-grid computation for $Pr=0.72$ underestimates the peak temperature θ^+ of about 3%, while the fine-grid case shows agreement within 1%. Both the fine- and coarse grid computation for $Pr=0.025$ show agreement with the result of Kawamura *et al* within 1%. The difference of the results of the fine- and coarse grid case decreases with a decrease of Prandtl number. It is well known that the smallest scale of the temperature fluctuation decreases with an increase of Prandtl number. Therefore, for high Prandtl number, because coarse grid case does not have enough grid size, the spatial resolution affects the calculated results. For low Prandtl number, in particular $Pr=0.025$, 0.0045, the influence of spatial resolution upon the results hardly find, and the coarse-grid case can obtain the same accurate results as the fine-grid case.

The root-mean square of the temperature variance, and the turbulent heat flux for $Pr=0.72$ and 0.025 are shown in **Figs.7 and 8**, compared with the results of Kawamura *et al* for $Pr=0.71$ and 0.025. Both figures show that, while the coarse-grid case slightly overestimates it near the wall, both fine- and coarse grid computations are in good agreement with the result of Kawamura *et al*.

3. Heat Transfer Coefficient

The calculated Nusselt numbers for various Prandtl number are given in **Fig.9**, compared with Dittus-Boelter correlation (1945)[5], Seban correlation (1950)[6], and the result of Kawamura *et al for $Pr=0.71$ and 0.025. The calculated Nusselt numbers are given by:

$$Nu \equiv \frac{h \cdot D_h}{\lambda} = \frac{4\,\mathrm{Re}_\tau\,\mathrm{Pr}}{\bar{\theta}_m^+}. \quad (.9)$$

where h denotes the heat transfer coefficient.

The difference of the results of the fine- and coarse-grid case is about 5% for Pr=5.9, about 4% for Pr=1.0, about 3% for Pr=0.72. Both the fine- and coarse grid computations show agreement within 1% for Pr=0.025, 0.0045. The trend is the same as for the mean temperature profiles. The fine-grid case is in good agreement with the result of Kawamura *et al* for *Pr=0.71* within 1%, while coarse-grid case within 4%. Both the fine-grid and coarse-grid cases for *Pr=0.025, 0.0045* are in agreement with Seban correlation within 15-20%, and those for *Pr=5.9, 1.0, 0.72* are in agreement with Dittus-Boelter correlation within 15%, in spite of the fact that these correlations were originally for circular tube.

IV. Conclusions

The pseudo direct numerical simulation for the heated parallel flat plates for various Prandtl numbers was performed, and the influence of the spatial resolutions in the streamwise and spanwise direction upon the thermal turbulent field, was investigated.

It is confirmed that the calculated results by the numerical method describes in this paper gave good results for the mean profiles, second-order correlations of the velocity and temperature, especially for the estimation of the Nusselt numbers in various Prandtl number fluids, and that the spatial resolution, in the streamwise and spanwise directions, scarcely affects those within the grid sizes, in particular for low Prandtl number fluids.

We will make the best use of the knowledge of those for rod-bundle analysis, in the future.

Aknowledgement

References

1) Suzuki, T. and Kawamura, N.,. "Consistency of Finite-Difference Scheme in Direct Numerical Simulation of Turbulence", *Trans. JSME*, **60B**, 578, [in Japanese] (1994).

2) Kim, J., Moin, P. & Moser, R., "Turbulence statistics in fully developed channel flow at low Reynolds number", *J.Fluid Mech.*, **177**, 133-166, (1987).

3) Kawamura, H., Ohsaka, K., Abe, H., Yamamoto, K., "DNS of turbulent heat transfer in

channel flow with low to medium-high Prandtl number", *Int.J.Heat. Fluid. Flow*, **19**, 482-491, (1998).

4) Kader, B. A,, "Temperature and concentration profiles in fully turbulent boundary layers", *Int.J.Heat. Mass. Transfer.*, **vol.24, No.9**, 1541-1544, (1981).

5) Dittus, F. W.,and Boelter, L. M. K., "Transfer in Automobile Radiators of the Turbulent Type", Univ. of California Publications in Engineering, (1947).

6) Seban, R. A., "Heat Transfer to a Fluid Flowing Turbulently between Parallel Walls with Asymmetric Wall Temperatures", *Trans. ASME*, **vol.72**, 789, (1950).
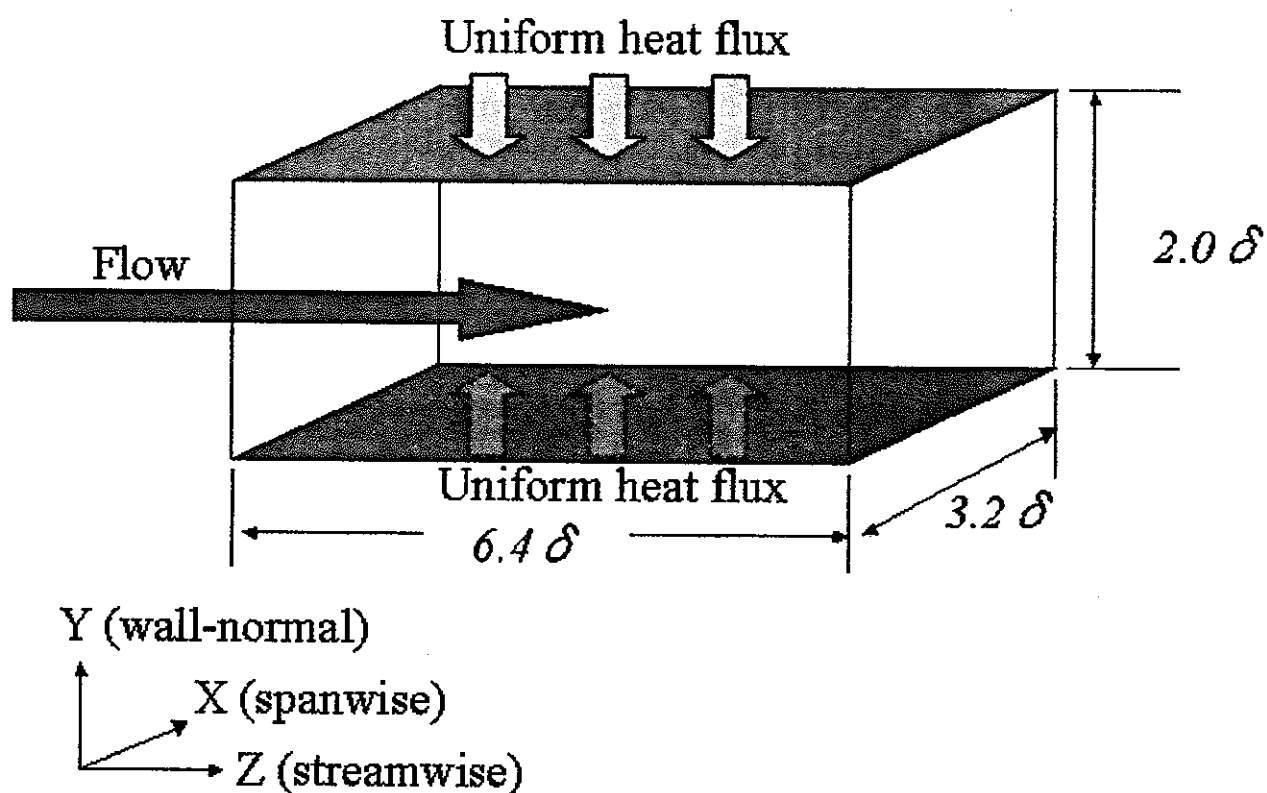
Fig.1, Computational geometry

T. Misawa
Calculation of Heat Transfer Coefficients on A Flat Plateby Pseudo Direct Numerical
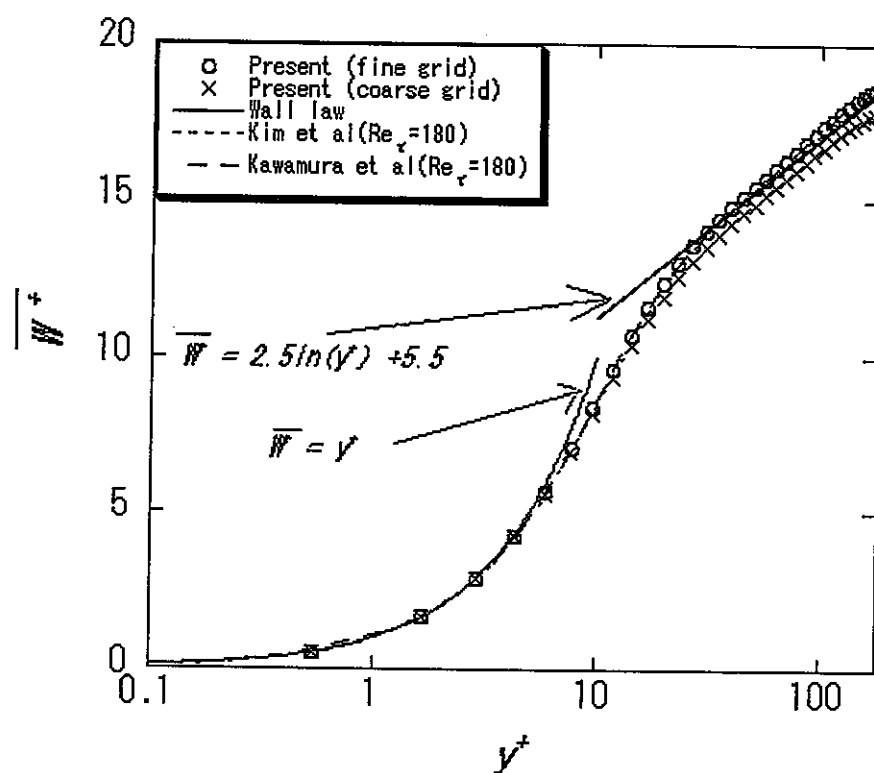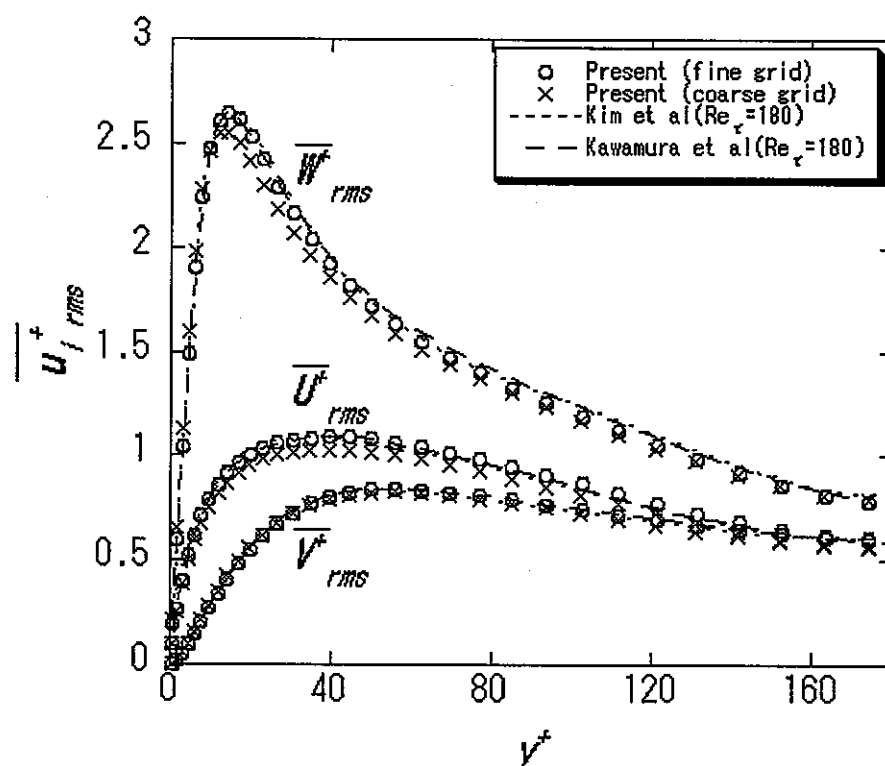Simulation of Turbulence
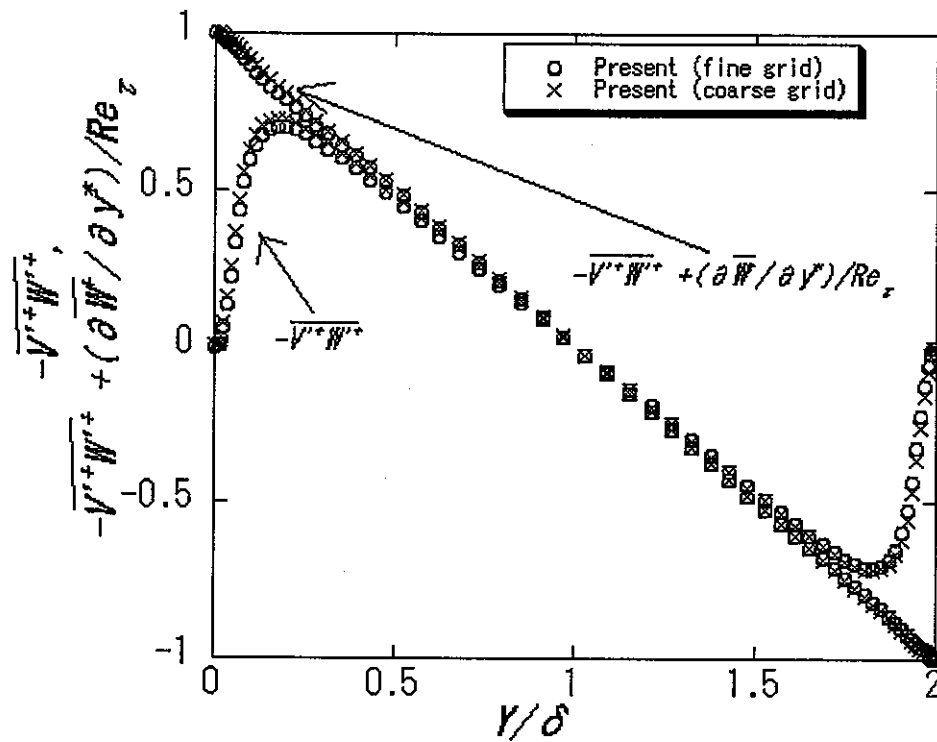
Fig.2 Total shear stress normalized by the friction velocity. $-\overline{v'^+w'^+}$ **denote the Reynolds shear stress, and** $(\partial \overline{W}^+/\partial y^*)/\mathrm{Re}_\tau$ **the viscous shear stress.**

T. Misawa

Calculation of Heat Transfer Coefficients on A Flat Plateby Pseudo Direct Numerical Simulation of Turbulence

Fig.3 Mean streamwise velocity profiles normalized by the friction velocity.

T. Misawa

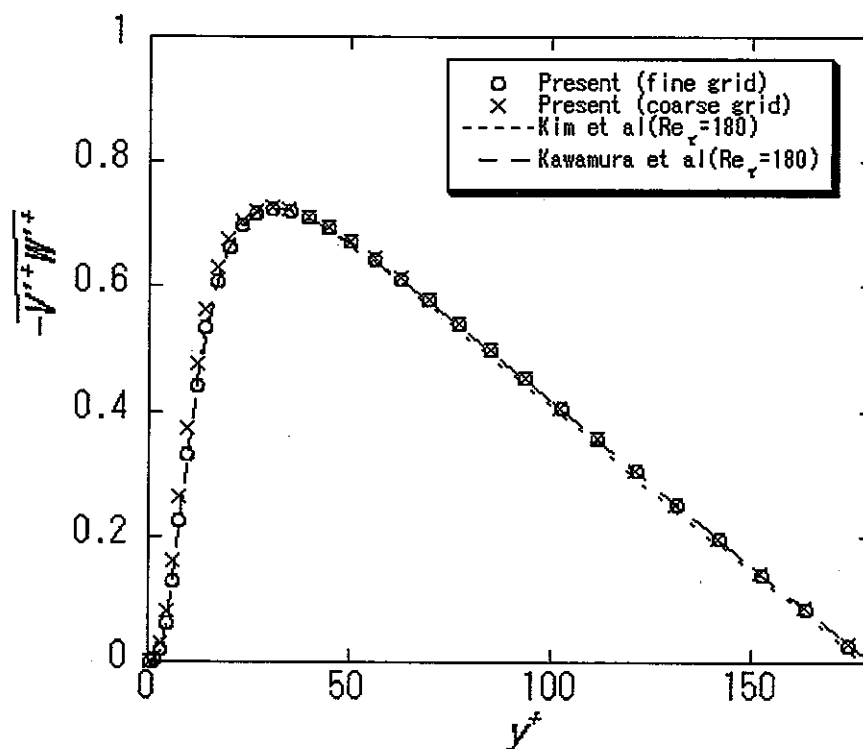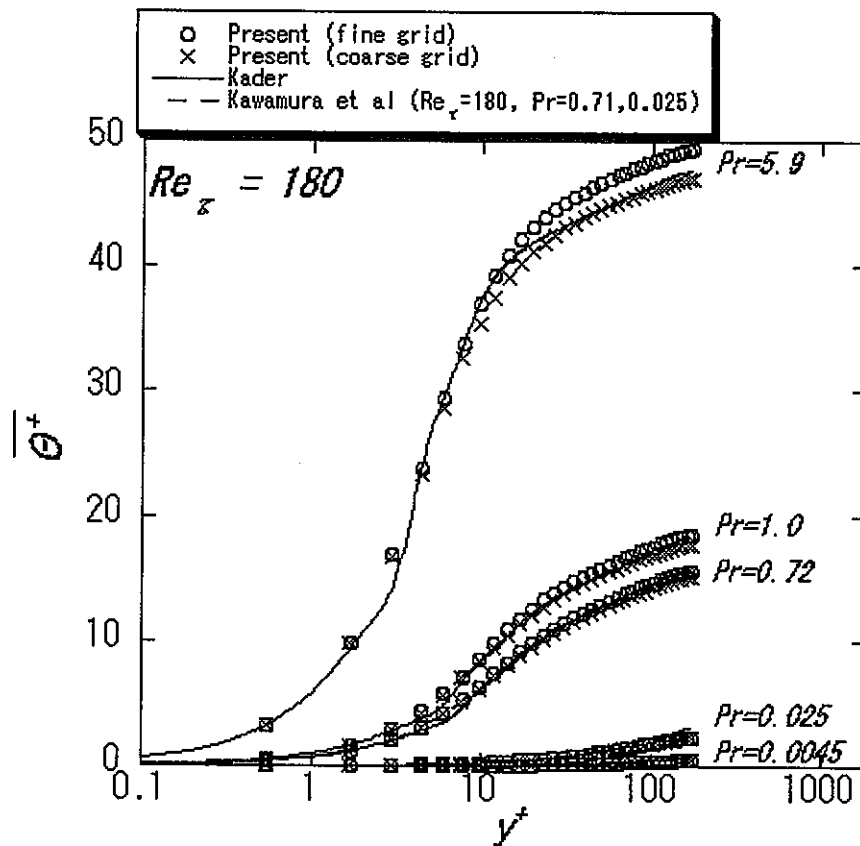Calculation of Heat Transfer Coefficients on A Flat Plateby Pseudo Direct Numerical Simulation of Turbulence

Fig.4 Turbulent intensities of velocity normalized by the friction velocity.

T. Misawa

Calculation of Heat Transfer Coefficients on A Flat Plate by Pseudo Direct Numerical Simulation of Turbulence

Fig.5　Reynolds shear stress normalized by the friction velocity.

T. Misawa

Calculation of Heat Transfer Coefficients on A Flat Plateby Pseudo Direct Numerical Simulation of Turbulence

Fig.6 Mean temperature profiles normalized by the friction temperature.

T. Misawa

Calculation of Heat Transfer Coefficients on A Flat Plateby Pseudo Direct Numerical Simulation of Turbulence
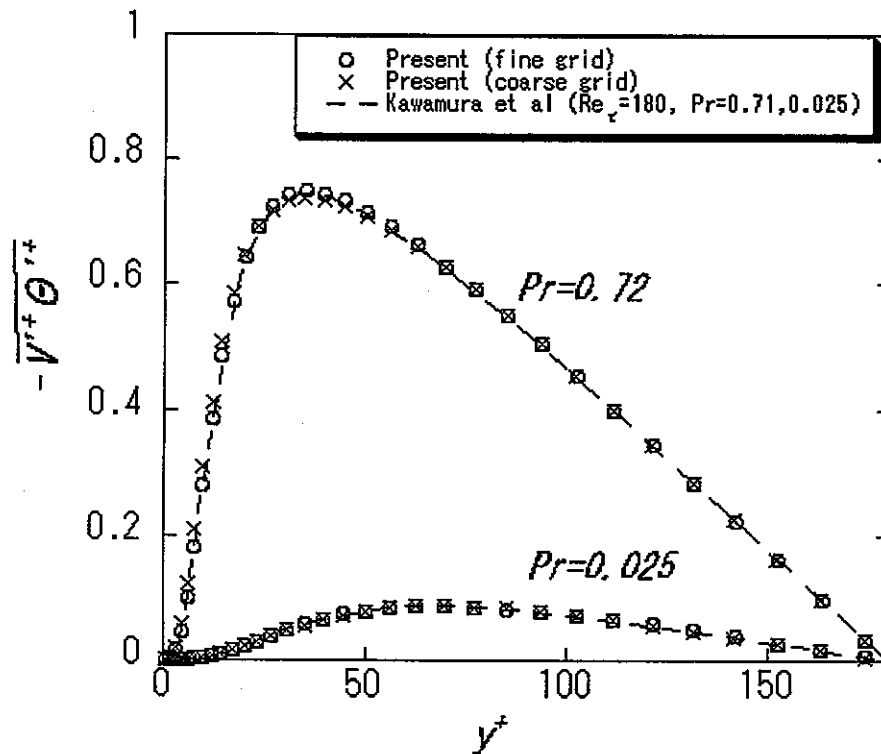
Fig.7 Turbulent heat flux normalized by the friction temperature.

T. Misawa

Calculation of Heat Transfer Coefficients on A Flat Plateby Pseudo Direct Numerical Simulation of Turbulence
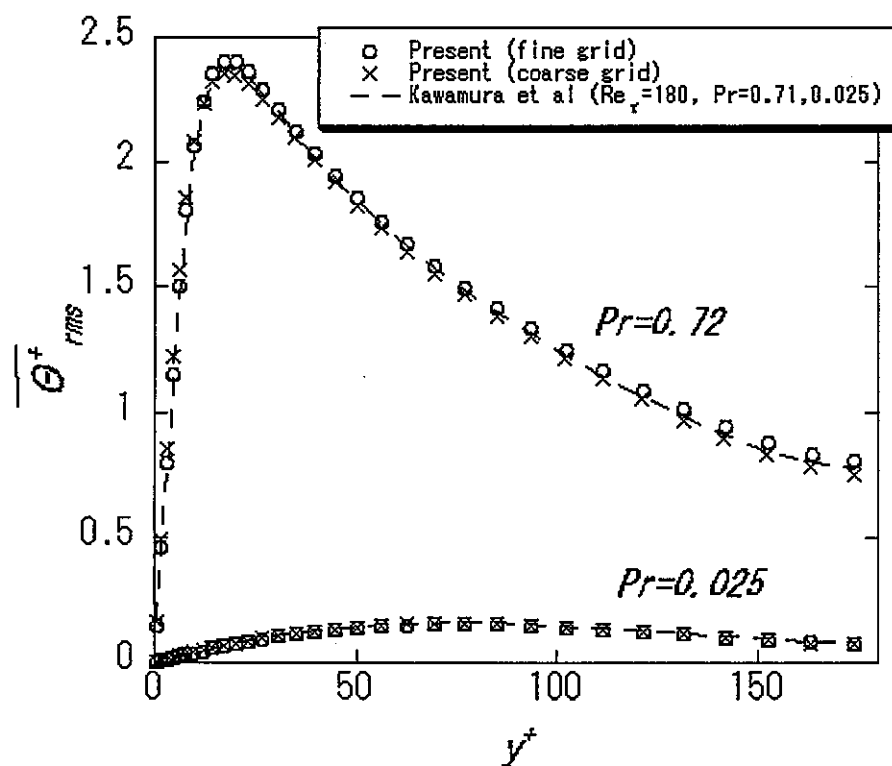
Fig.8 Turbulent intensities of temperature normalized by the friction temperature.

T. Misawa
Calculation of Heat Transfer Coefficients on A Flat Plateby Pseudo Direct Numerical Simulation of Turbulence
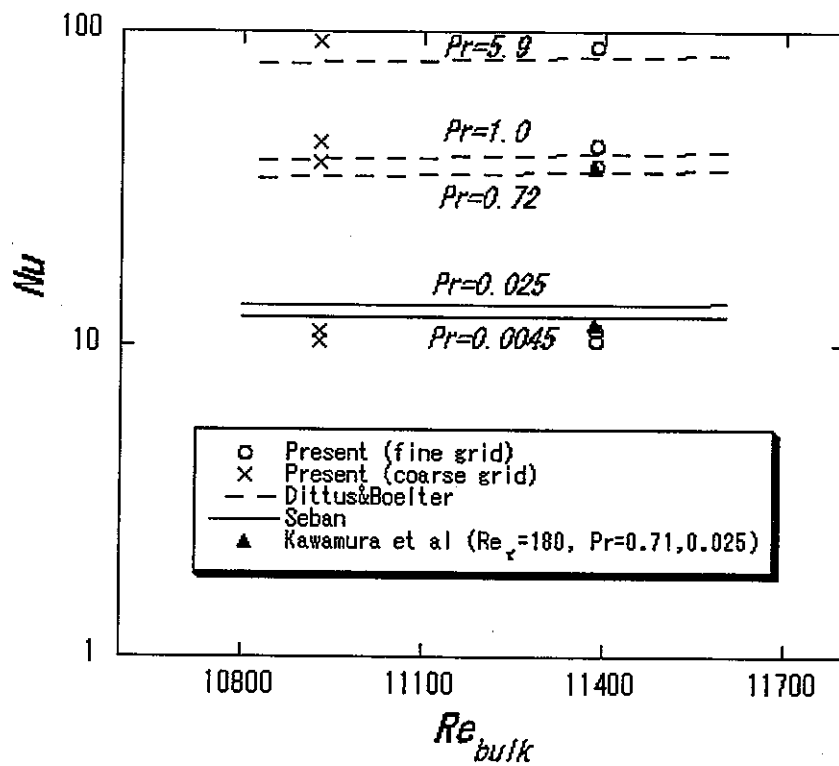
Fig.9　Nusselt numbers.

T. Misawa

Calculation of Heat Transfer Coefficients on A Flat Plateby Pseudo Direct Numerical Simulation of Turbulence